



UNIVERSITY OF ILLINOIS
URBANA

AERONOMY REPORT NO. 76

MIDLATITUDE SPORADIC-E LAYERS

(NASA-CR-153057) MIDLATITUDE SPORADIC-E
LAYERS (Illinois Univ.) 257 p HC A12/MF A01
CSCL 04A

N77-24683

HC A12/MF A01

Unclas
G3/46 29123

by
K. L. Miller
L. G. Smith

December 1, 1976

Library of Congress ISSN 0568-0581



Supported by
National Aeronautics and Space Administration
Grant NGR 14-005-181
National Science Foundation
Grants ATM 75-15523 and GA 27295

Aeronomy Laboratory
Department of Electrical Engineering
University of Illinois
Urbana, Illinois

A E R O N O M Y R E P O R T

N O 76

MIDLATITUDE SPORADIC-E LAYERS

by

K. L. Miller
L. G. Smith

December 1, 1976

Supported by
National Aeronautics and
Space Administration
Grant NGR 14-005-181
National Science Foundation
Grants ATM 75-15523 and GA 27295

Aeronomy Laboratory
Department of Electrical Engineering
University of Illinois
Urbana, Illinois

ABSTRACT

The starting point of this investigation is the partially transparent echo from midlatitude sporadic-*E* layers as recorded by ionosondes; this is the range of frequencies between the blanketing frequency and the maximum frequency. One interpretation is that it is a partial reflection at the steep gradients of electron density which characterize the vertical profile of the layers as recorded in rocket flights. The theory of reflection at gradients is developed and evaluated in the case of five layers. It is found that this mechanism is not sufficient to explain the phenomenon. An alternative explanation is that the midlatitude sporadic-*E* layers are not uniform in the horizontal plane but contain localized regions of high electron density. This is investigated using data obtained by incoherent-scatter radar and is found to provide a satisfactory explanation.

The main features of midlatitude sporadic-*E* layers are consistent with the convergence of metallic ions as described by the wind-shear theory applied to gravity waves and tides. The interference of gravity waves with other gravity waves and tides can be recognized in the altitudes of occurrence and the structure of the layers. The small-scale horizontal irregularities are attributed in some cases to critical level effects and in others to fluid instabilities. The convergence of a meteor trail can, under some circumstances, account for localized enhancement of the electron density in the layer.

TABLE OF CONTENTS

ABSTRACT.	iii
TABLE OF CONTENTS	v
LIST OF TABLES.	ix
LIST OF FIGURES	x
1. INTRODUCTION.	1
1.1 <i>General Introduction</i>	1
1.2 <i>Partially Transparent Echoes from Midlatitude Sporadic-E Layers</i>	7
1.3 <i>Objectives of this Study</i>	8
2. THEORY OF FORMATION OF SPORADIC-E LAYERS.	11
2.1 <i>Introduction</i>	11
2.2 <i>Wind-Shear Theory</i>	13
2.2.1 <i>E-region winds</i>	13
2.2.2 <i>The equation of motion of a charged particle</i>	18
2.2.3 <i>The polarization electric field</i>	21
2.2.4 <i>The formation of ionized layers</i>	22
2.3 <i>Metallic Ions</i>	24
2.3.1 <i>Introduction</i>	24
2.3.2 <i>General characteristics of metallic ions</i>	25
2.3.3 <i>Production rates of metallic atoms and ions</i>	26
2.3.4 <i>Lifetimes of metallic ions</i>	28
2.3.5 <i>Diurnal variation</i>	29
2.3.6 <i>Effect of heavy ions</i>	36
3. REFLECTION OF RADIO WAVES BY SPORADIC-E LAYERS.	39
3.1 <i>Introduction</i>	39
3.2 <i>Ionosonde Observations of Sporadic E</i>	39

PRECEDING PAGE BLANK NOT FILMED

3.3	<i>Reflection Coefficients.</i>	42
3.3.1	<i>Introduction.</i>	42
3.3.2	<i>Propagation of radio waves in the ionosphere.</i>	42
3.3.3	<i>Approximate solutions</i>	47
3.3.4	<i>Full-wave solution.</i>	53
3.3.5	<i>Solution using a digital computer</i>	57
3.3.6	<i>Description of sporadic-E layer by a mathematical function.</i>	60
3.3.7	<i>Performing the integration.</i>	61
3.4	<i>Results of Reflection Coefficient Calculations</i>	64
3.4.1	<i>Comparison with independent solutions</i>	64
3.4.2	<i>The effect of ionosonde sensitivity</i>	65
3.4.3	<i>Results of reflection coefficient analysis.</i>	71
4.	<i>OBSERVATION OF SPORADIC-E LAYERS BY INCOHERENT-SCATTER RADAR.</i>	84
4.1	<i>Introduction</i>	84
4.2	<i>Incoherent Scatter</i>	85
4.2.1	<i>Introduction.</i>	85
4.2.2	<i>Scattering of radio waves</i>	86
4.2.3	<i>Autocorrelation analysis.</i>	88
4.2.4	<i>Pulse compression</i>	92
4.3	<i>The Arecibo Observatory.</i>	98
4.4	<i>Experimental Techniques.</i>	100
4.4.1	<i>Electron density.</i>	100
4.4.2	<i>Ion drift velocity.</i>	103
4.4.3	<i>Data collection and presentation.</i>	105
4.5	<i>Observations</i>	111
4.5.1	<i>Introduction.</i>	111

4.5.2	14 January 1974, 14:11-15:03 AST	111
4.5.3	17 January 1974, 20:06-22:15 AST	112
4.5.4	18 January 1974, 12:38-14:02 AST	117
4.5.5	19 January 1974, 12:53-14:56 AST	117
4.5.6	24 January 1974, 18:03-19:01 AST	120
4.5.7	28 January 1974, 12:52-14:58 AST	123
4.5.8	10 July 1975, 11:31-13:33 AST	132
4.5.9	16 July 1975, 12:14-18:58 AST	134
4.5.10	17 July 1975, 03:33-08:20 AST	139
4.5.11	19 July 1975, 11:05-14:22 AST	141
4.5.12	20 July 1975, 10:55-15:23 AST	145
4.5.13	21 July 1975, 19:52-24:00 AST	147
4.5.14	23 July 1975, 03:11-08:05 AST	153
4.5.15	26 July 1975, 09:07-16:47 AST	153
4.5.16	26 July 1975, 19:44-21:37 AST	158
4.5.17	27 July 1975, 11:25-15:02 AST	158
4.6	<i>Comparison of Ionosonde and Incoherent-Scatter-Radar</i>	
	<i>Observations</i>	163
4.6.1	<i>Effect of volume averaging</i>	163
4.6.2	<i>Effect of limited sampling</i>	164
4.7	<i>Summary</i>	168
5.	DISCUSSION	170
5.1	<i>Introduction</i>	170
5.2	<i>Ion Drift Velocity and the Formation of Sporadic-E Layers . . .</i>	170
5.3	<i>Altitudes of Sporadic-E Layers</i>	174
5.3.1	<i>Combined effects of gravity waves and tides</i>	174
5.3.2	<i>Components of tidal modes</i>	178

5.3.3	<i>Standing waves</i>	179
5.3.4	<i>Quasi-stagnation levels</i>	179
5.4	<i>Boundaries of Sporadic-E Layers</i>	182
5.5	<i>Wave-like Structure in Sporadic-E Layers</i>	186
5.6	<i>Irregular Structure Associated with Critical Levels</i>	189
5.6.1	<i>Introduction</i>	189
5.6.2	<i>Critical levels</i>	189
5.6.3	<i>Effect on sporadic-E layer formation</i>	191
5.7	<i>Irregular Structure Caused by Fluid Instabilities</i>	194
5.8	<i>Irregular Structure Caused by Plasma Instabilities</i>	197
5.9	<i>Irregular Structure Attributed to Meteor Trails</i>	198
5.9.1	<i>Irregular source function</i>	198
5.9.2	<i>Individual meteor trails</i>	198
5.9.3	<i>Convergence of a meteor trail</i>	199
5.9.4	<i>Correlations with meteor activity</i>	201
5.10	<i>Summary</i>	203
6.	SUMMARY AND CONCLUSIONS	205
6.1	<i>Summary</i>	205
6.2	<i>Conclusions</i>	207
6.3	<i>Suggestions for Future Work</i>	208
APPENDIX I	THE EFFECT OF THE POLARIZATION ELECTRIC FIELD ON THE FORMATION OF SPORADIC-E LAYERS	210
APPENDIX II	APPROXIMATE DERIVATIONS OF REFLECTION COEFFICIENTS	216
II.1	<i>Approximation of a Layer by Multiple Thin Films</i>	216
II.2	<i>W.K.B. Solution</i>	218
II.3	<i>Solution Using Hypergeometric Functions</i>	222
REFERENCES.		231

LIST OF TABLES

<u>Table</u>	<u>Page</u>
4.1 Observations during January, 1974, at Arecibo, P. R.	106
4.2 Observations during July, 1975, at Arecibo, P. R..	107

LIST OF FIGURES

Figure		Page
1.1	Electron density of the <i>E</i> region at 10:05 EST on 10 August 1973 measured by a rocket-borne Langmuir probe	2
1.2	Ionograms recorded at Wallops Island: (a) 3 August 1973 at 11:01 EST during flight of Nike Apache 14.513; (b) 10 August 1973 at 10:06 EST during flight of Nike Apache 14.514	4
1.3	An idealized ionogram illustrating sporadic- <i>E</i> nomenclature [URSI, 1972].	5
2.1	Schematic representation of atmospheric regions [Whitten and Poppoff, 1971].	12
2.2	Wind component velocity versus altitude [Rosenberg, 1968] . .	14
2.3	Wind shear versus altitude [Rosenberg, 1968].	15
2.4	Diurnal variation of the metallic ion concentration for various values of q_A and q_I with a residence time due to transport of 12 hr.	33
2.5	Diurnal variation of the metallic ion concentration for various values of q_A and q_I with a residence time due to transport of 24 hr.	34
2.6	Time variation of metallic atom and ion concentration shown for transport lifetimes of 12 hr and 24 hr. The concentration of metallic atoms is not affected by the transport lifetime	35
2.7	Effect of ionic mass on the efficiency of the wind-shear mechanism. Altitudes indicated along the curve mark the location where, for atmospheric conditions at that altitude, M is equal to an ion mass of 30 amu	38

Figure		Page
3.1	Variation of the real part of n^2 with X , where n is the refractive index of a magnetoionic medium and X is the square of the ratio of the plasma frequency of the medium to the incident frequency of an electromagnetic wave	46
3.2	Representative electron-density profile for a sporadic- E layer	48
3.3	Altitudes at which the index of refraction vanishes for the modes of propagation, for the case of the electron density profile of Figure 3.2	49
3.4	Symmetric and transitional Epstein profiles	52
3.5	The set of mathematical functions and their sum, used to describe the electron density profile of a sporadic- E layer observed at Wallops Island, 16 July 1970.	62
3.6	Comparison of the full-wave solution with the W.K.B. solution of the reflection coefficients of a symmetric Epstein layer having a full-width at half-maximum of 352.6 m.	66
3.7	Comparison of full-wave solutions with solutions of the reflection coefficients of symmetric Epstein profiles using hypergeometric functions. Widths of the layers are 352.6 m and 705.2 m	67
3.8	Comparison of full-wave solutions with solutions of the reflection coefficients of transitional Epstein profiles using hypergeometric functions. Widths of the layers are 176.3 m and 352.6 m	68
3.9	Comparison of full-wave solutions of reflection and transmission coefficients developed in this study with full-wave	

Figure		Page
	solutions from <i>Chesell</i> [1971b] (solid lines). The layer used was a parabola with a half-width of 477 m.	69
3.10	Electron-density profile of sporadic-E layer observed at Wallops Island, 24 July 1968. The fitted curve used in the analysis is the dashed profile.	73
3.11	Reflection and transmission coefficients of sporadic-E layer, 24 July 1968	74
3.12	Electron-density profile of sporadic-E layer observed at Wallops Island, 16 July 1970, with the fitted curve used in the analysis.	75
3.13	Reflection and transmission coefficients of sporadic-E layer, 16 July 1970.	76
3.14	Electron-density profile of a nighttime sporadic-E layer observed at Wallops Island, 22 June 1965, with the fitted curve used in the analysis.	78
3.15	Reflection and transmission coefficients of sporadic-E layer, 22 June 1965	79
3.16	Electron-density profiles of two sporadic-E layers observed at Wallops Island, 3 August 1973 and 10 August 1973, with the fitted curves used in the analysis. Altitude scale is relative to the center of each layer.	80
3.17	Reflection and transmission coefficients of sporadic-E layer, 3 August 1973.	81
3.18	Reflection and transmission coefficients of sporadic-E layer, 10 August 1973	82
4.1	Incoherent-scatter power spectrum for O^+ ions where the	

Figure

Page

	wavelength is much greater than the Debye length. The spectrum is shown only for positive Doppler shifts [after Hagfors, 1961].	89
4.2	Real and imaginary autocorrelation functions measured using the five-pulse technique with a 30-min integration time and a 16 μ s pulse. The solid curves show a fitted theoretical autocorrelation function corresponding to $T_i = 250$ K, $v_{in} = 300$ s ⁻¹ , and a radial drift velocity of 14 m s ⁻¹ away from the radar [Zamlutti and Farley, 1975].	91
4.3	The 13-bit Barker code and its autocorrelation function . . .	93
4.4	The time (range) variation of $\langle G(t) ^2 \rangle$ in dB below maximum value for the 13-baud Barker code for various T_p/T_x with $T_e/T_i = 1.0$ [Gray and Farley, 1973]	96
4.5	The scattered-power profile of a meteor trail. Secondary maxima are artifacts of the pulse-compression technique . . .	97
4.6	Effect of volume averaging of the electron density in 600-m range gates. Parabolas have been fit to average densities for two cases	102
4.7	An illustration of the method used in the experiment and the effects of winds on the data [Miller and Smith, 1975] . .	109
4.8	Illustration of a scan of the radar by drawing contours on a computer array of electron densities printed as functions of altitude and azimuth.	110
4.9	Electron density (10^5 cm ⁻³) of a sporadic-E layer observed during successive 90 deg scans on 14 January 1974. The motion of the radar beam is clockwise in the first scan and	

Figure		Page
	counterclockwise in the second.	113
4.10	<i>fbEs</i> and <i>foEs</i> on 14 January 1974.	114
4.11	Representation of maximum density of the sporadic-E layer observed on 17 January 1974. The altitude of the layer is 97 km. The direction of odd numbered scans is toward lower values of azimuth; even numbered scans toward greater azimuth	115
4.12	<i>fbEs</i> and <i>foEs</i> on 17 January 1974.	116
4.13	Electron density (10^5 cm^{-3}) above Arecibo, 18 January 1974, between 12:59 and 13:13 AST. Each scan represents approxi- mately 3 min.	118
4.14	<i>fbEs</i> and <i>foEs</i> on 18 January 1974. Shaded area represents limits of plasma frequencies derived from incoherent scatter data.	119
4.15	Electron density (10^5 cm^{-3}) above Arecibo, 19 January 1974, between 14:21 and 14:25 AST (upper two scans) and between 14:29 and 14:32 AST (lower two scans). Each scan represents approximately 3 min	121
4.16	Electron column densities through a sporadic-E layer at an altitude of 100 km observed on 24 January 1974. The radar beam was held in a fixed vertical position [Miller and Smith, 1975].	122
4.17	<i>fbEs</i> and <i>foEs</i> on 24 January 1974 [Miller and Smith, 1975] . .	124
4.18	Electron-density profiles observed on 24 January 1974	125
4.19	Electron-density profiles observed between 18:00 and 19:00 AST on 24 January 1974.	126

Figure		Page
4.20	Representation of maximum density of the sporadic-E layer observed on 28 January 1974 between 12:52 and 14:58 AST. The altitude of the layer is 105 km. The direction of odd-numbered scans is from left to right, even-numbered scans from right to left [Miller and Smith, 1975]	128
4.21	Electron density (10^5 cm^{-3}) above Arecibo, 28 January 1974, between 13:40 and 13:54 AST. Each scan represents approximately 3 min.	129
4.22	Electron density above Arecibo, 28 January 1974, between 14:14 and 14:28 AST. Each scan represents approximately 3 min	130
4.23	$f_b E_s$ and $f_o E_s$ on 28 January 1974. Shaded area represents limits of plasma frequencies derived from the incoherent-scatter data [Miller and Smith, 1975]	131
4.24	Ion drift velocities, 10 July 1975. The solid line shows velocities from incoherent-scatter measurements between 11:31 and 12:39 AST, the dashed line from measurements between 11:56 and 13:07 AST	133
4.25	$f_b E_s$ and $f_o E_s$ on 16 July 1975	135
4.26	Line-of-sight ion drift velocities at altitudes of 100.4, 104.0 and 107.5 km, measured by incoherent-scatter radar on 16 July 1975.	136
4.27	Components of the ion drift velocity at 13:12 AST, 16 July 1975. Uncertainties are based on least-squares fit of the data to theoretical autocorrelation functions	137
4.28	Ion drift velocities, 16 July 1975. The altitude of a	

Figure	Page
sporadic-E layer is indicated by the circled points.	
Parentheses indicate a weak layer	138
4.29 Electron density observed on 17 July 1975. Contours are at 10^4 and 10^5 cm^{-3} . Each scan of the radar beam was between approximately 270 and 310 deg azimuth	140
4.30 <i>fbEs</i> and <i>foEs</i> on 17 July 1975	142
4.31 <i>fbEs</i> and <i>foEs</i> on 19 July 1975. Shaded area represents limits of plasma frequencies derived from incoherent-scatter data.	143
4.32 Electron density (10^6 cm^{-3}) from a sequence of 12 scans of the radar beam on 19 July 1975. The horizontal distance represented in each frame is approximately 10 km.	144
4.33 Representation of maximum density (10^6 cm^{-3}) of a portion of the sporadic-E layer observed on 19 July 1975 between 12:52 and 13:00 AST. The direction of the odd-numbered scans is toward increasing azimuth; even numbered scans are toward decreasing azimuth.	146
4.34 Ion drift velocities, 20 July 1975.	148
4.35 Electron density (10^5 cm^{-3}) from a sequence of scans of the radar beam on 20 July 1975.	149
4.36 <i>fbEs</i> and <i>foEs</i> on 21 July 1975	150
4.37 Electron density (10^4 cm^{-3}) from a sequence of scans of the radar beam on 21 July 1975.	151
4.38 Ion drift velocity, 23 July 1975.	154
4.39 <i>fbEs</i> and <i>foEs</i> on 26 July 1975	155
4.40 Electron-density profile measured by incoherent scatter radar at 09:12 AST on 26 July 1975. A three-point weighted	

Figure		Page
	average was used to smooth the profile.	156
4.41	Ion drift velocities, 26 July 1975.	157
4.42	<i>fbEs</i> and <i>foEs</i> on 26 July 1975. Shaded area represents limits of plasma frequencies derived from incoherent-scatter data.	159
4.43	Electron density from a sequence of scans of the radar beam on 26 July 1975. Contours are at intervals of $1 \times 10^4 \text{ cm}^{-3}$ in electron density. The contour at $1 \times 10^5 \text{ cm}^{-3}$ has been darkened.	160
4.44	Electron density from a sequence of scans of the radar beam on 26 July 1975. Contours are at intervals of $5 \times 10^3 \text{ cm}^{-3}$	161
4.45	Electron density profile measured by incoherent-scatter radar at 12:55 AST on 27 July 1975. A three-point weighted average was used to smooth the profile.	162
4.46	Beam pattern in the reference frame of the sporadic-E layer observed on 28 January 1974. Motion of the layer is 85 m s^{-1} at an azimuth of 190 deg. The radar is scanning between 210 and 270 deg	165
4.47	Frequency of occurrence of peak electron densities between 13:45 and 13:50 AST on January 1974 (circles), and pre- diction based on maximum <i>ftEs</i> (square).	167
5.1	Vertical ion drift velocities (m s^{-1}) deduced from the horizontal components of the ion drift velocity measured on 16 July 1974 by incoherent-scatter radar	173
5.2	Electron-density profiles observed at Arecibo, 19 July 1975 .	175

Figure		Page
5.3	Vertical ion drift caused by two superimposed sinusoidal wind systems: one in the east-west plane with a vertical wavelength of 10 km and a constant phase, the other with a vertical wavelength of 12.5 km and a downward phase velocity. The phase of the second wave changes by 2π radians in the sequence shown.	177
5.4	Electron density observed on 17 July 1975 (see Figure 4.29). Contours are at intervals of $1 \times 10^4 \text{ cm}^{-3}$, with contours at multiples of $5 \times 10^4 \text{ cm}^{-3}$ darkened	183
5.5	Sketch of possible configuration of winds producing the electron-density distribution shown in Figure 5.4. (a) Direction of sinusoidal east-west horizontal winds, (b) Ion drift velocities and locations of sporadic-E layers	185
5.6	Electron density (10^5 cm^{-3}) observed by a single-pulse experiment on 16 July 1975 between 14:37 and 14:47 AST. The direction of scan is from right to left	188
5.7	Electron density observed on 17 July 1975 (see Figure 4.29). Contours are at intervals of $1 \times 10^4 \text{ cm}^{-3}$, with contours at multiples of $5 \times 10^4 \text{ cm}^{-3}$ darkened.	195
5.8	Electron density observed on 17 July 1975 (see Figure 4.29). Contours are at intervals of $1 \times 10^4 \text{ cm}^{-3}$, with contours at multiples of $5 \times 10^4 \text{ cm}^{-3}$ darkened.	196
5.9	Initial and final configuration of an ionized trail in the presence of a wind shear.	200

1. INTRODUCTION

1.1 *General Introduction*

The ionosphere, a region of partially-ionized gases in the earth's upper atmosphere, has been the subject of much research in the past years. Among the most striking features encountered in nearly every technique by which the ionosphere is studied are sporadic-*E* layers.

Sporadic-*E* layers are common features in the region of the ionosphere between the altitudes of 95 and 120 km. This is the lower part of the *E* region, an ionospheric region extending from 90 to 160 km in altitude. An electron-density profile of the *E* region containing a sporadic-*E* layer is shown in Figure 1.1. Detailed vertical electron-density profiles measured by sounding rockets show midlatitude sporadic *E* to be thin layers of enhanced ionization [Smith and Mechtly, 1972]. The layers are usually only one or two kilometers thick, but may extend horizontally over hundreds of kilometers.

The ionosphere at altitudes where sporadic *E* occurs contains high concentrations of metallic ions with complementary electrons to preserve charge neutrality [Narcisi, 1973; Zbinden *et al.*, 1975]. The metallic ions are presumed to be of meteoric origin. Most are ionized either by collisional processes as the meteor enters the atmosphere, or by charge exchange with ambient molecular ions. The lifetime with respect to recombination of a metallic ion in the *E* region is several months.

The most widely held theory of the formation of midlatitude sporadic-*E* layers is that of vertical convergence of the long-lived metallic ions by the combined action of the horizontal neutral wind and the geomagnetic field. The ions collect in thin layers determined by vertical shears in the horizontal wind.

Layers of metallic ions are apparently a constant feature of the *E* region. However, the concentration in the layers is not always enough in daytime to

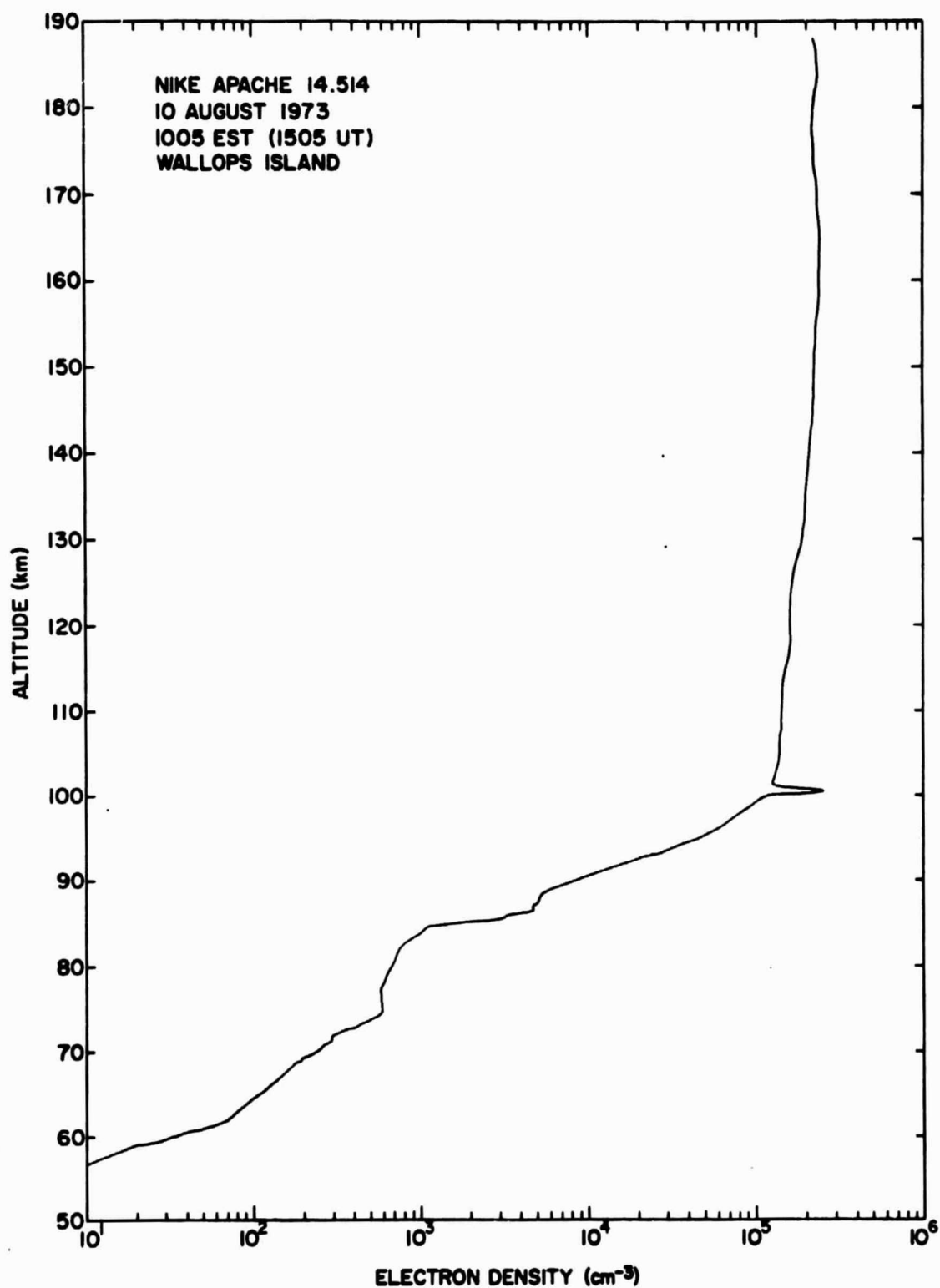


Figure 1.1 Electron density of the E region at 10:05 EST on 10 August 1973, measured by a rocket-borne Langmuir probe.

produce layering in the electron density. *LaLonde* [1966] observed layers of ionization being exposed at sunset as the *E* region ionization density decayed. This was also observed during a solar eclipse by *Narcisi* [1966]. Layering of the electron concentration is nearly always in evidence in the nighttime ionosphere [*Smith and Mechtly*, 1972].

Sporadic *E* was first studied by reflecting radio waves from the ionosphere and examining the characteristics of the reflected wave. It is seen as a strong reflection from the *E* region at a virtual height that is constant with frequency. The echoes from sporadic *E* are detected at frequencies much greater than the plasma frequency of the normal *E* region. As these echoes are not always present, appearing in fact to occur randomly, they were given the name, "sporadic *E*".

Most observations have been made using an ionosonde, a type of ionosphere sounder which measures the time it takes a transmitted pulse of electromagnetic radiation to be reflected by the ionosphere and return. The time delay gives a measure of the virtual height of the reflecting ionization, which can be related to the true height of reflection by considering the retardation of the group velocity of the radiation passing through the ionized medium. The height of reflection is the height at which the local plasma frequency of the ionosphere equals the frequency of the incident radiation. By varying the frequency of the pulse, the height and electron density of the underside of the ionosphere can be measured. The ionosonde typically makes a record of the virtual height of reflection versus frequency. Examples of this type of record, called ionograms, are shown in Figure 1.2.

As early studies of sporadic *E* were done, for the most part, with ionosphere sounders, the terminology describing sporadic *E* describes its appearance on ionograms. An idealized ionogram illustrating sporadic-*E* nomenclature is shown in Figure 1.3. The blanketing frequency (f^bEs) is defined as that frequency below

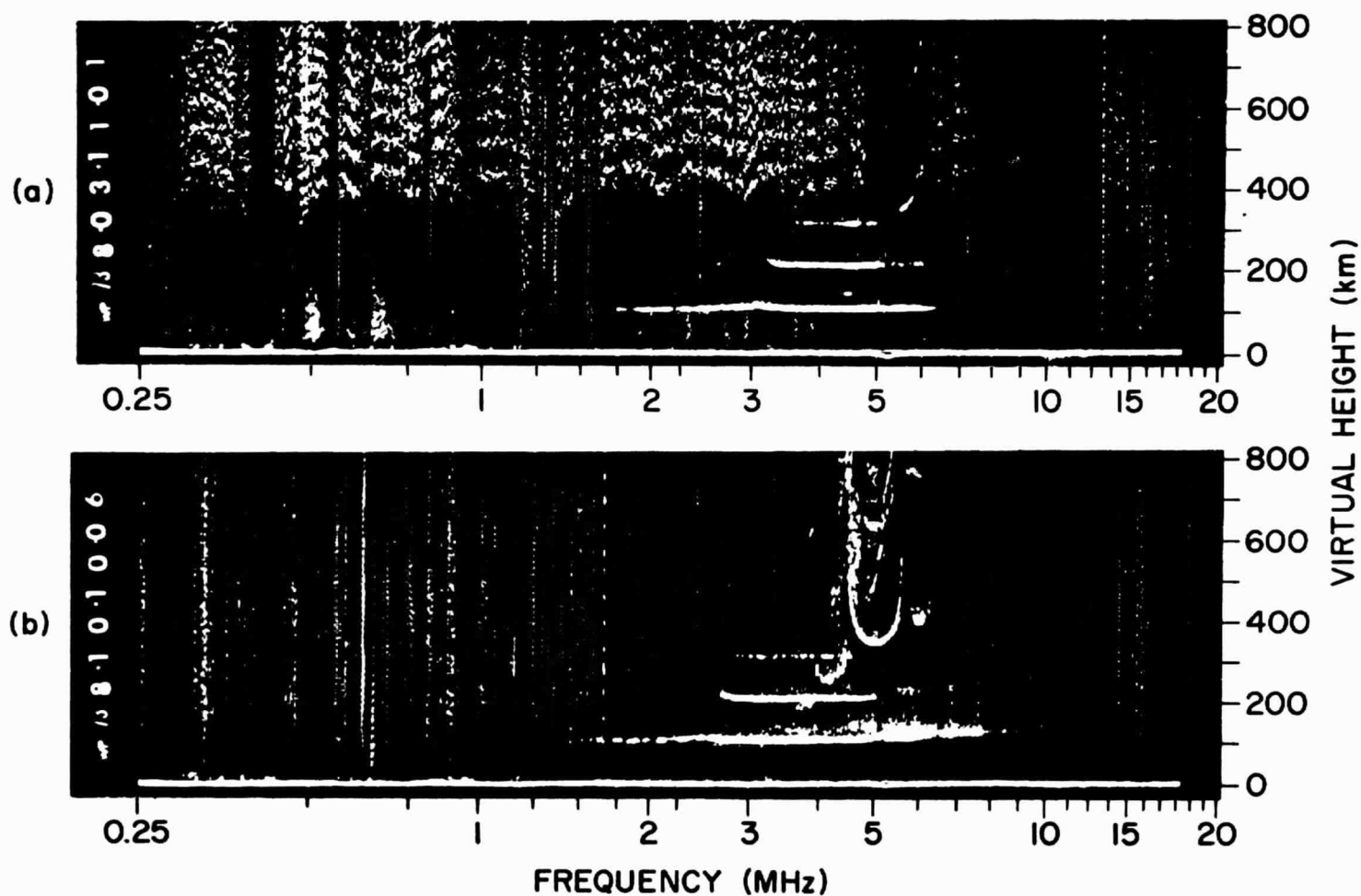


Figure 1.2 Ionograms recorded at Wallops Island: (a) August 3, 1973 at 11:01 EST during flight of Nike Apache 14.513; (b) August 10, 1973 at 10:06 EST during flight of Nike Apache 14.514.

ORIGINAL PAGE IS
OF POOR QUALITY

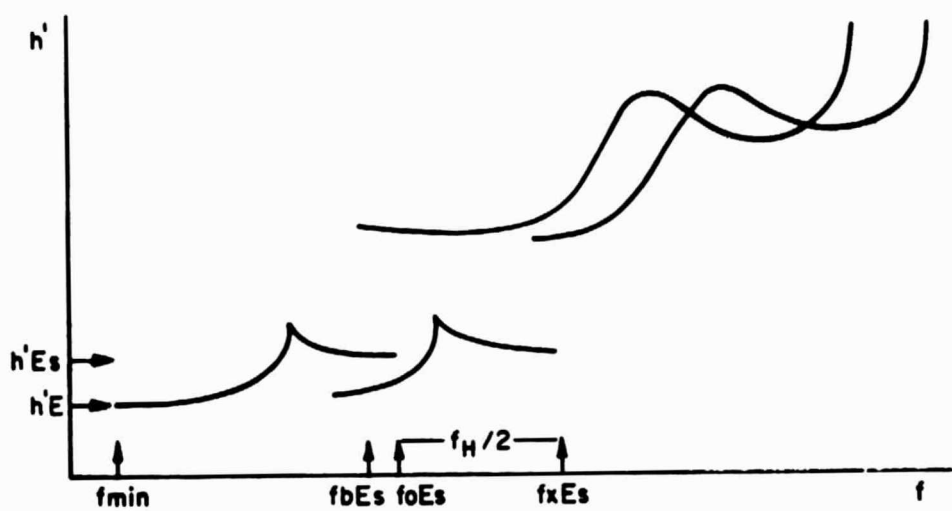


Figure 1.3 An idealized ionogram illustrating sporadic- E nomenclature [URSI, 1972].

which no traces are seen of reflections from above the sporadic- E layer. The top frequency (f^oE_s), sometimes called the critical or maximum frequency (f^xE_s), is the frequency above which no echo is detected from the sporadic- E layer. If the maximum frequencies of reflection of ordinary and extraordinary waves can be resolved, they are designated by f^oE_s and f^xE_s respectively. It must be emphasized that these conventions were developed to document features on ionograms, and do not explain the physical features of the sporadic- E layers.

Other nomenclature has been adopted to describe the appearance and time development of the echoes from sporadic E [Smith, 1957]. The various types of sporadic E are grouped into three major categories: auroral, equatorial, and midlatitude. Although ionograms of these three types of sporadic E share many characteristics, the physical phenomena involved are quite different. Auroral sporadic E is caused by ionization of the atmosphere by auroral particle precipitation [Hunsucker, 1972], while equatorial sporadic E is the result of the scattering of radio waves by the electron-density irregularities of the unstable plasma of the electrojet [Balsley et al., 1976]. In this study, only sporadic E occurring at midlatitudes will be considered.

The detailed vertical structure of sporadic- E layers has been observed using sounding rockets. This is usually done by measuring the current to a Langmuir probe operated at a fixed voltage [Smith, 1969]. The layers are usually Gaussian-shaped, but more complex structures are sometimes observed [Smith and Mechtly, 1972].

In spite of the many observations of sporadic E by these and other techniques, many features of sporadic- E layers remain unexplained. It is the purpose of this work to examine the structure and motion of sporadic- E layers in detail, both in the vertical and horizontal planes, in the context of the present theory of the formation of these layers.

1.2 Partially Transparent Echoes from Midlatitude Sporadic-E Layers

On an ionogram there is a frequency range between $f_b E_s$ and $f_t E_s$ where the sporadic-E layer is partially transparent to radio waves. Often this range is too large to be explained on the basis of the different reflection frequencies of the ordinary and extraordinary modes. Models proposed to account for this effect have been discussed by *Reddy and Rao* [1968] and by *Whitehead* [1972a]. In one model the echo is attributed to partial reflection at the large vertical gradients of electron density that characterize the upper and lower boundaries of a sporadic-E layer. Calculations by *Reddy* [1968] and by *Chessell* [1971a,b] indicated that partial reflections from thin layers can occur over a large range of frequency and provide an explanation for the effect. However, re-examination of this model in the present work using observed electron-density profiles of sporadic-E layers shows that this explanation is, in fact, inadequate.

In another model, the partial transparency is attributed to high electron density in regions of limited horizontal extent in the sporadic-E layer. In this model the maximum frequency of the sporadic-E reflection, $f_t E_s$, corresponds to total reflection from the regions of enhanced ionization illuminated by the ionosonde. The blanketing frequency $f_b E_s$ then corresponds to the peak plasma frequency of the layer in which these regions are embedded.

The presence of irregularities of this type within sporadic-E layers has not been substantiated by rocket observations. *Reddy and Rao* [1968] showed that the peak plasma frequency of sporadic-E layers measured from rockets usually approximated $f_b E_s$, and was never as large as $f_t E_s$. Further, it was shown by *Smith and Mechtly* [1972] that the sporadic-E electron-density profile measured during the descent of the rocket usually matches the profile from the ascent in both shape and altitude, even though a distance of 100 km or more often separates the two points on the trajectories. However, this in itself is not sufficient to

exclude the idea of horizontal variability in sporadic-E layers. It does support the idea that, if there are irregularities in sporadic-E layers with the required electron densities, they must be of small horizontal extent and sparsely scattered throughout the layer; the probability of a rocket passing through an irregularity must be very small.

In a variation of this second model, the irregularities are small-scale fluctuations appearing in the vertical electron-density profile. Data of nighttime sporadic E taken by rocket-borne probes have indicated the presence of irregularities such as these which could scatter radio waves with frequencies much higher than would be reflected. *Bowhill* [1966] has shown that the partially transparent sporadic-E echo observed by the ionosonde on those occasions can be accounted for theoretically by scattering from the irregularities on the electron-density profile. However, this fine structure is not generally observed by rocket probes when $f_{TEs} \gg f_{bEs}$.

1.3 Objectives of this Study

The main objectives of this investigation are to explain the partial transparency of midlatitude sporadic-E layers to radio waves, and to evaluate the results with respect to the dominant physical processes involved in the formation and maintenance of sporadic-E layers.

Chapter 2 starts with the development of the general theory of the formation of sporadic-E layers by wind shears. This includes a critical review of the important physical and chemical processes in the lower E region of the ionosphere as they apply to sporadic E.

Because of their apparent importance to sporadic E, a section of this chapter is devoted to consideration of metallic atoms and ions. The basic chemical reactions involved are discussed and an estimate made of the production rate of metallic ions. A new simplified description is developed of the

diurnal variation of the metal content at sporadic-*E* altitudes.

Chapter 3 deals with the first of the models for the partial transparency of sporadic-*E* echoes. This is the model which attributes the partial reflections to the large electron-density gradients that characterize the vertical profile of the layers as recorded in rocket flights. The theory of reflection at gradients is developed and evaluated in the case of five sporadic-*E* layers. It is found that this mechanism is not sufficient to explain the phenomenon.

The alternative model, that sporadic-*E* layers are not uniform in the horizontal plane but contain localized regions of enhanced electron density, is then investigated. As described in Chapter 4, this is done using data taken by the incoherent-scatter radar at the Arecibo Observatory in Puerto Rico. The structure of many of the layers observed is complex, and includes irregularities of the magnitude required to account for the partial transparency of the sporadic-*E* layers.

Various interpretations of the observed irregularities in sporadic *E* are discussed in Chapter 5. The complex structure of sporadic-*E* layers is interpreted in terms of the effects of motions of the neutral atmosphere. Evidence is shown that internal gravity waves play a major role in the development of this structure and are potentially able, in a region of high wind shears, to converge ionization horizontally and form highly enhanced irregularities in the electron density. The action of wind shears on meteor trails in the vicinity of sporadic-*E* layers is also shown to be one possible source of isolated regions of enhanced electron density.

It is shown that sporadic-*E* layers do contain highly enhanced electron-density irregularities which are apparently responsible for the partial transparency of the layers to radio waves. The complexity observed in the electron-density distribution is interpreted in most cases as a complexity in

the motion of the neutral atmosphere. It is also concluded that in spite of the complexity of the sporadic-*E* layers, the features observed can be explained by applying wind-shear theory to metallic ions.

2. THEORY OF FORMATION OF SPORADIC-E LAYERS

2.1 Introduction

Nearly all sporadic-*E* layers that are observed occur in the altitude region between 95 and 120 km. This is an interesting region of transition where the relative importance of many processes is changing. In the context of electrical conductivity it is sometimes called the dynamo region. It will be shown later that the mechanism producing vertical ion drifts, which lead to the formation of sporadic-*E* layers, is based on the same concepts as are used in deriving the conductivity tensor.

The atmosphere of the earth is divided into natural regions by various parameters such as ionization density and temperature. The relative locations of several of these regions are shown in Figure 2.1. The lower thermosphere, where sporadic *E* is observed, is a region of transition between dynamic regimes. The turbopause, shown in Figure 2.1 at 105 km, marks a division between turbulent mixing of the gases below, and non-turbulent gravitational (diffusive) separation above.

The ionospheric *D*, *E*, and *F* regions are determined by layers of ionization which are not always well defined. The layering is the result of the photoionization of different atmospheric species. As the optical depth of the atmosphere increases and the composition changes, the primary species being photoionized and the ion production rate also change. The ionization of the daytime *E* region is predominantly O_2^+ and NO^+ , with O^+ reaching comparable concentrations above 110 km [Whitten and Poppoff, 1971]. The basic theory of the formation of a layer by photoionization was first developed by Chapman [1931].

The lower *E* region also contains metallic ions and atoms. The average concentration of ionized metals is small compared with O_2^+ and NO^+

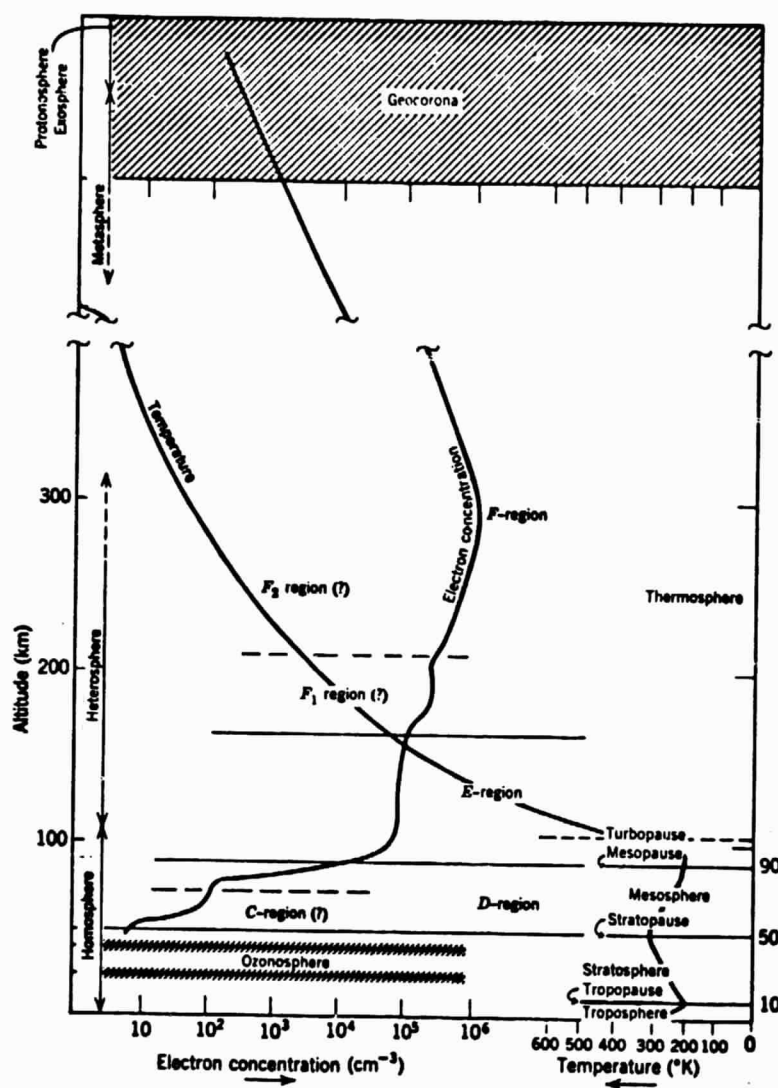


Figure 2.1 Schematic representation of atmospheric regions [Whitten and Poppoff, 1971].

concentrations. However, the recombination rate of metallic ions is very small, allowing the convergence of the metallic ions into thin layers with peak densities much greater than that of O_2^+ and NO^+ . At night, the decrease in ionization density from the recombination of the molecular ions reveals layering in the electron-density profile characteristic of metallic ions on essentially every occasion [Smith and Mechtly, 1972].

The formation of sporadic-E layers by wind shears was first suggested by Dungey [1956; 1959]. The theory has been developed by several authors, including Whitehead [1961], Axford [1963], MacLeod [1966], and Kato [1966]. The layering of metallic ions is the subject of discussion of this chapter. The theory of formation of sporadic-E layers by wind shears will be developed, together with a discussion of the source and characteristics of the metallic ions. We begin with a discussion of the motions of the neutral atmosphere, which is the driving force for the formation of these layers.

2.2 Wind-Shear Theory

2.2.1 *E-region winds.* The lower *E* region has been found to be characterized by variable winds and large wind shears [Bedinger et al., 1968; Rosenberg and Zimmerman, 1972]. From a series of vapor-trail releases from rockets, Rosenberg [1968] found an r.m.s. wind speed at sporadic-E altitudes of 70 m s^{-1} , and an r.m.s. wind shear of 120 m s^{-1} per scale height, or approximately 0.02 s^{-1} . Results of the Rosenberg study, plotted in Figures 2.2 and 2.3, give an indication of some of the characteristics of *E*-region winds. The mean vertical wavelength of the dominant wave was found to be 3.4 scale heights, or about 21 km at an altitude of 100 km, with no vertical dependence of the amplitude. No significant seasonal dependence of either the speed or the vertical shear was detected.

It is difficult to determine the prevailing winds because of the

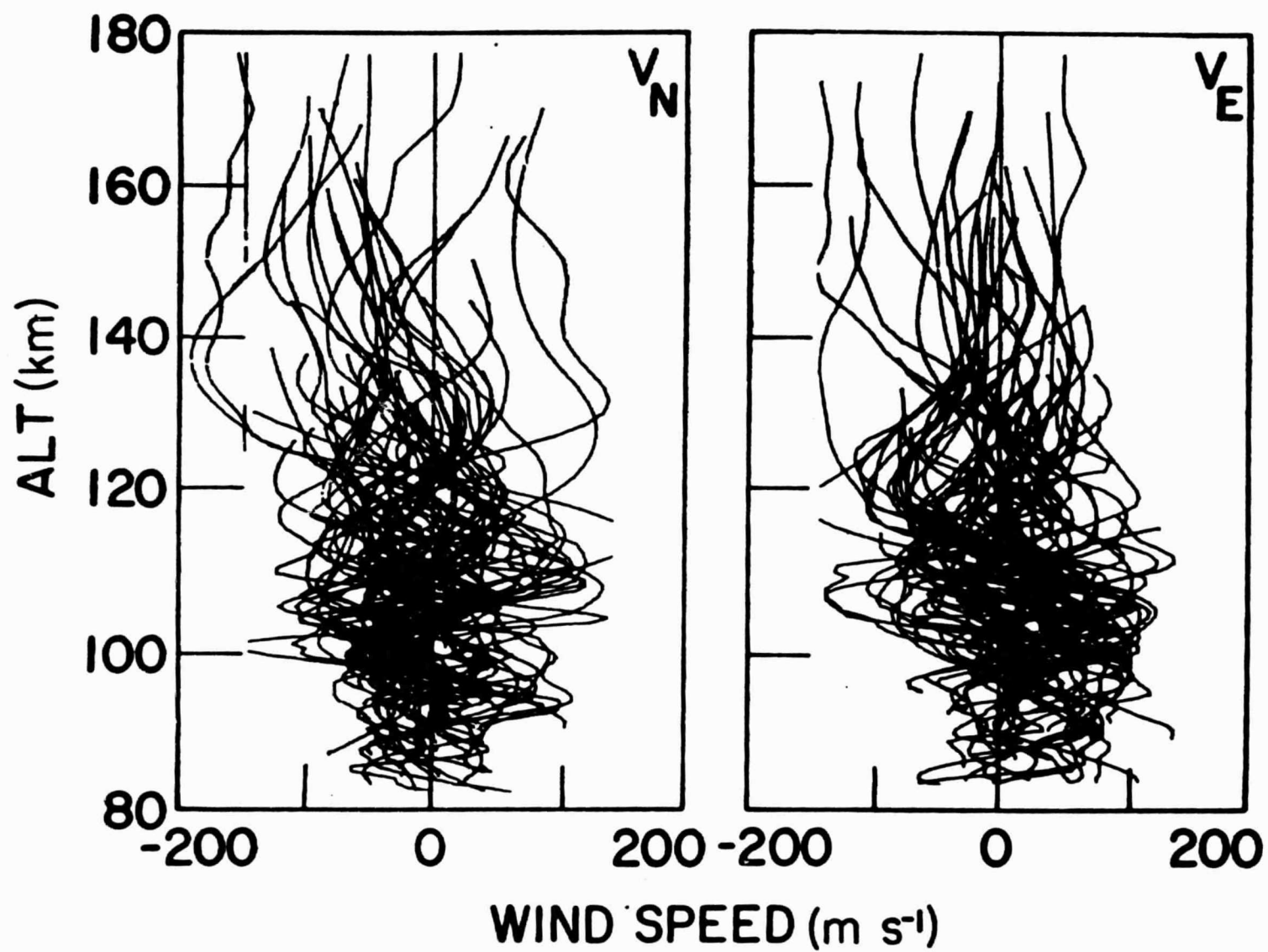


Figure 2.2 Wind component velocity versus altitude [Rosenberg, 1968].

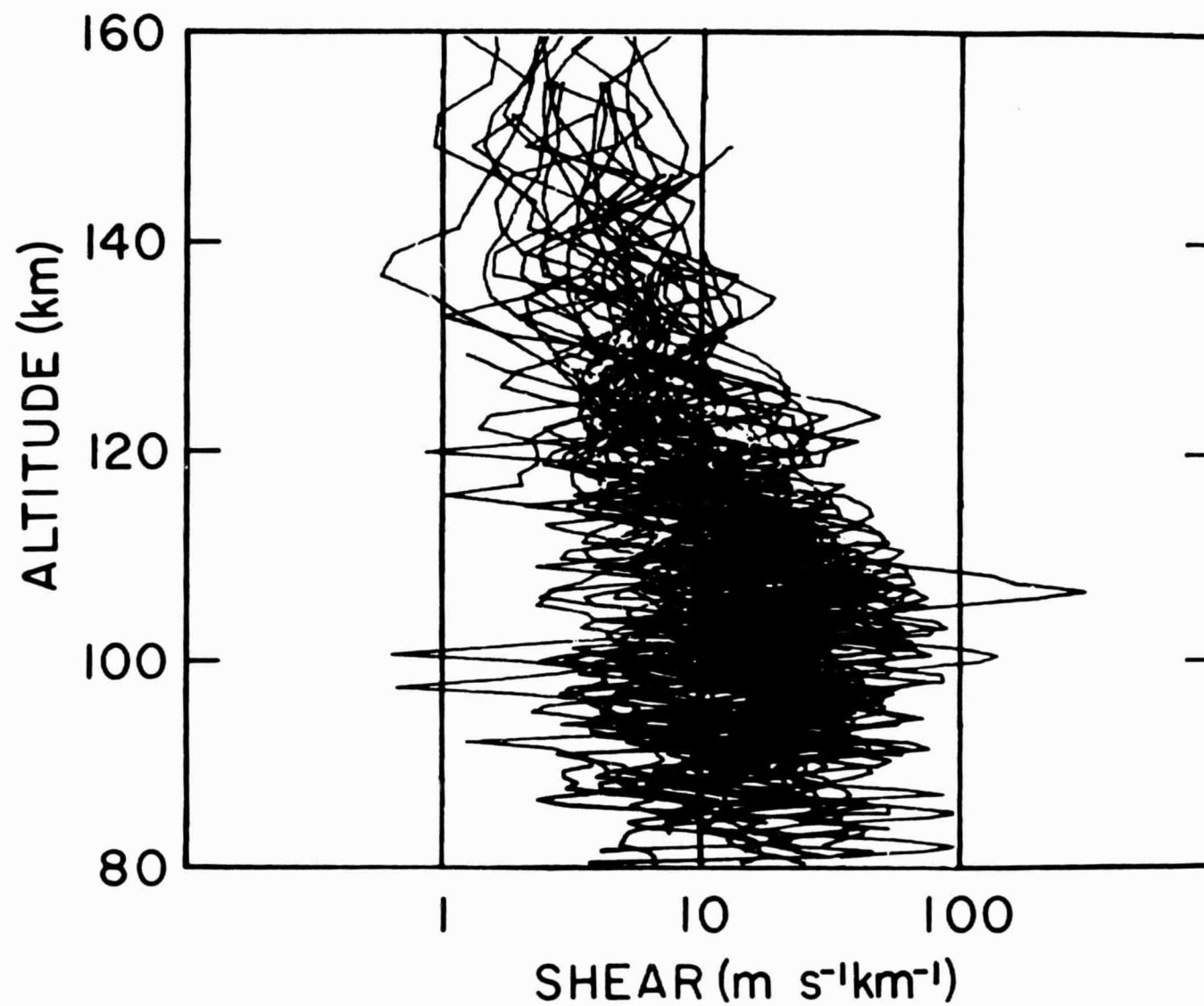


Figure 2.3 Wind shear versus altitude [Rosenberg, 1968].

variability of this region of the atmosphere. Meteor radar experiments indicate that prevailing winds are eastward in midlatitudes, increasing with altitude in the summer and decreasing with altitude in the winter. There is evidence that at certain latitudes the prevailing winds become westward at higher altitudes in the winter [Hines, 1963].

The motions of the atmosphere at sporadic-E altitudes are found to include tidal oscillations and gravity waves [Hines, 1974; Francis, 1975]. The two types of oscillations are actually very similar, differing mainly in period and horizontal wavelength. The main energy source for tides is solar heating, with some small effect contributed by the lunar gravitational field. Sources of gravity waves are not well known, but are more localized and are thought to include geographic features, shear instabilities in the atmosphere, turbulence, auroras, and solar eclipses [Hines, 1974--Preamble to paper 22].

Expressions describing both tides and gravity waves are derived [Rishbeth and Garriott, 1969] by combining the equation of motion of the neutral atmosphere, the continuity equation, the adiabatic gas equation, and the perfect gas law. In the case of tides the equations are solved in spherical coordinates. It is found, for example, that tidal oscillations of solar origin can be written in polar coordinates (r, θ, ϕ) as

$$\chi_s = \sum_m \sum_n R_{mn}(r) \Theta_{mn}(\theta) e^{im\phi} \quad (2.1)$$

where χ_s is the velocity divergence. The angular functions in equation (2.1) are Hough functions and can be written in terms of spherical harmonics (Y_{lm}) as

$$\Theta_{mn}(\theta) e^{im\phi} = \sum_{l=m}^{\infty} a_{lmn} Y_{lm}(\theta, \phi) \quad (2.2)$$

The radial term, $R(r)$, can be approximated locally by

$$R_{mn}(r) \sim \exp(ik_{mn}r) \quad (2.3)$$

where the wave number k_{mn} is given by

$$k_{mn}^2 = \left(\frac{1}{Hh_{mn}} \right) \left[\frac{(\gamma-1)}{\gamma} + \frac{dH}{dh} \right] - \frac{1}{4H^2} \quad (2.4)$$

The scale height of the neutral atmosphere is represented by H , and h_{mn} is the "equivalent depth" given by the eigenvalues of the various modes. If k_{mn} is real, the wave is internal and propagates vertically. If k_{mn} is imaginary, the wave is evanescent. k_{mn} is imaginary for all waves in which the subscript n is less than zero. For $n > 0$, k_{mn} can become imaginary at certain heights, for example where dH/dh becomes sufficiently negative, indicating that the wave is reflected.

The energy density of the wave can be shown to be independent of height. Since the energy density can be expressed as

$$E = \frac{1}{2} d |\vec{u}|^2 \quad (2.5)$$

where d is the mass density and \vec{u} is the velocity amplitude, the amplitude of the tidal oscillations is inversely proportional to the square root of the density. This increase in amplitude with height is known as tidal amplification. A similar effect can also be derived for gravity waves. However, this increase of amplitude with height is not evident in the wind reported by Rosenberg [1968].

The behavior of internal gravity waves is described by the same equations. However, since the periods of gravity waves are much less than the earth's rotational period and their wavelengths are much less than the radius of the earth, both tidal and Coriolis effects can be neglected. The dispersion relation can then be expressed as

$$(\omega^2 - \omega_a^2) \omega^2 / c^2 - \omega^2 (k_x^2 + k_z^2) + \omega_g^2 k_x^2 = 0 \quad (2.6)$$

where k_x and k_z are the horizontal and vertical components of the wave number and

$$\omega_a = \gamma g / 2c \quad (2.7)$$

$$\omega_g = (\gamma - 1)^{1/2} g / c \quad (2.8)$$

$$c = (\gamma g H)^{1/2} \text{ (speed of sound)} \quad (2.9)$$

The dispersion relation, equation (2.6), shows that propagating solutions can exist only for waves with frequencies either greater than ω_g , in which case they are known as acoustic gravity waves, or less than ω_g , which are known as internal gravity waves. At sporadic-E altitudes, ω_a corresponds to a period of about 4.5 min, and ω_g to a period of about 5 min.

Although gravity waves have greater downward phase velocities than tides, the vertical wavelength of both tides and gravity waves are similar. This is also true of velocity amplitudes. *Hines* [1966] found a peak amplitude of about 40 m s^{-1} . *Kochanski* [1964] estimates the amplitudes of gravity waves to be 55 m s^{-1} . *Whitehead* [1972b] considers this value of the amplitude of gravity waves to be an underestimate, since meteor-radar observations show the amplitude of the irregular winds to be greater than that of either tidal modes. In any case the amplitudes are roughly comparable, and very complex wind patterns and changes can arise from the superposition of the two types of oscillations.

2.2.2 The equation of motion of a charged particle. The motion of a charged particle in the E region is, to a large degree, influenced by the effects of its collisions with neutral atoms and molecules, by electric fields and by the geomagnetic field. The equation of motion can be written

$$m \frac{d\vec{v}}{dt} = m\vec{v}(\vec{\omega} - \vec{v}) + q\vec{v} \times \vec{B} + q\vec{E} + m\vec{g} - \frac{1}{n} \nabla p \quad (2.10)$$

where

q , m , \vec{v} = charge, mass, and velocity of the charged particle

\vec{w} = velocity of the neutral wind

ν = effective collision frequency

\vec{E} = electric field

\vec{B} = geomagnetic field

\vec{g} = gravitational acceleration

n, p = number density and partial pressure of the particular charged species.

The electric field, \vec{E} , is the sum of any external electric fields and the internal (polarization) electric field resulting from forces acting with different effects on the electrons and ions. Thus,

$$\vec{E} = \vec{E}_{\text{ext}} + \vec{E}_{\text{pol}} \quad (2.11)$$

In this analysis, the magnetic and gravitational fields are assumed to be constant for a limited range of altitude. The geomagnetic field is written

$$\vec{B} = B_0 \hat{\Gamma} \quad (2.12)$$

where $\hat{\Gamma}$ is a unit vector in the direction of the field.

The effective collision frequency is a simplified expression, and is used in the sense that $m\nu(\vec{w}-\vec{v})$ represents the force per unit volume exerted on the ions by collisions with the neutral gas. The large ratio of neutral-to-ionized particle concentrations in the dynamo region justifies neglecting collisions between ionized particles. The force due to the partial-pressure gradient is also a macroscopic property of the gas, and can be written as $n^{-1}\nabla(nkT)$, where k is Boltzmann's constant and T is the temperature of the ionized species. This term is much smaller than the other terms in equation (2.10) and is usually neglected [MacLeod et al., 1975].

It is convenient, in solving equation (2.10) for the drift velocity of

the ionization, to define

$$\rho \equiv v/\omega_H \quad (2.13)$$

where ω_H is the gyrofrequency, given by

$$\omega_H \equiv \frac{qB_0}{m} \quad (2.14)$$

and to combine all terms not containing \vec{v} in the following manner

$$\vec{u} \equiv \vec{w} + \frac{1}{\rho q B_0} [q\vec{E} + m\vec{g} - \frac{1}{n} \nabla (nkT)] \quad (2.15)$$

Equation (2.10) can now be written, assuming steady state conditions,

$$0 = \rho(\vec{u} - \vec{v}) + \vec{v} \times \hat{\Gamma} \quad (2.16)$$

which can be solved for \vec{v} by taking, respectively, the dot product and the cross product with $\hat{\Gamma}$ and then combining the results, giving

$$\vec{v} = \frac{1}{1+\rho} [\rho^2 \vec{u} + \rho \vec{u} \times \hat{\Gamma} + (\vec{u} \cdot \hat{\Gamma}) \hat{\Gamma}] \quad (2.17)$$

Equation (2.17) represents the most concise formulation of wind-shear theory, including the effects of the neutral wind system and of external electric fields. From equation (2.15) it can be seen that the electric field, if known, can be easily incorporated into the calculation of ion velocities.

This expression shows the relative importance of the various components of the velocity of the neutral wind and of the electric field at different altitudes. In the case of ions ρ is equal to one near an altitude of 120 km [Wright and Fedor, 1970]. At this altitude, the three terms in equation (2.17) are of equal magnitude. At lower altitudes, collisions with the neutral gas become more important, and the first term dominates. At higher altitudes, the third term dominates and the ions are constrained to move parallel to the

magnetic field. In the case of electrons, ρ is much less than one throughout the region of interest, and the electron velocity is dominated by the third term in equation (2.17).

The analysis so far has been perfectly general. If winds are neglected (i.e. $\omega = 0$ in equation 2.15) and only the electric field is considered, coefficients of equation (2.17) give expressions proportional to elements of the conductivity tensor. Thus, equation (2.17) can be written

$$\vec{v} = \frac{1}{ne} [\sigma_P \vec{E} + \sigma_H \vec{E} \times \hat{r} + (\sigma_0 - \sigma_P) (\vec{E} \cdot \hat{r}) \hat{r}] \quad (2.18)$$

where [Whitten and Poppoff, 1971]

$$\begin{aligned} \sigma_P &= \frac{\epsilon_0 \omega_p^2 v}{2v + \omega_H} & (\text{Pedersen conductivity}) \\ \sigma_H &= \frac{\epsilon_0 \omega_p^2 \omega_H}{2v + \omega_H} & (\text{Hall conductivity}) \\ \sigma_0 &= \frac{\epsilon_0 \omega_p^2}{v} & (\text{longitudinal conductivity}) \end{aligned} \quad (2.19)$$

and ω_p is the plasma frequency. By choosing a coordinate system with the magnetic field oriented along the z -axis equation (2.18) leads to the familiar form

$$\vec{j} = ne\vec{v} = \begin{pmatrix} \sigma_P & \sigma_H & 0 \\ -\sigma_H & \sigma_P & 0 \\ 0 & 0 & \sigma_0 \end{pmatrix} \vec{E} \quad (2.20)$$

where \vec{j} is the current density.

2.2.3 The Polarization electric field. The equations derived above have neglected any interactions between electrons and ions. However, when

equation (2.17) is applied separately to ions and electrons it is seen that they move in different directions creating a polarization electric field. This is usually neglected in calculating vertical drifts for midlatitude conditions because of the greater mobility of electrons parallel to the magnetic field; when ions move vertically, the electrons are able to follow.

Explicit expressions for the components of the polarization field are given in Appendix I. The field is shown to be negligible at midlatitudes. However, the effect of the polarization field becomes appreciable at low latitudes, preventing the formation of sporadic-E layers by vertical shears in the horizontal wind at the geomagnetic equator.

The correlation of sporadic E with latitude was suggested by *Smith* [1957] and shown by *Heisler and Whitehead* [1960; 1964] using data from the study by *Smith* [1957]. The absence of blanketing sporadic E at the magnetic equator was noted during the I.G.Y. by *Bowles and Cohen* [1962] from vertical incidence ionograms.

2.2.4 *The formation of ionized layers.* Vertical ion drift velocities can be calculated using equation (2.17) if the neutral wind velocity and the external electric field are known. The neutral wind is usually determined by the motion of vapor trails from rockets, as described in Section 2.2.1. The electric field in the midlatitude ionosphere has been measured by balloon- and rocket-borne probes [*Mozzer*, 1972; *Schutz et al.*, 1973], and inferred from incoherent scatter observations [*Harper et al.*, 1976]. The field is horizontal and equal to or less than 1 or 2 mV m⁻¹.

Equation (2.15) shows that an external electric field has the same effect on the ionization as does a neutral wind with a velocity of $\vec{E}/\rho B_0$. For an electric field of 1 mV m⁻¹, this term would be equal to 25/ ρ m s⁻¹, or 8 m s⁻¹ at an altitude of 110 km. Although the external electric field is small, it can

change the altitude of a sporadic-E layer by a few kilometers [Macleod et al., 1975].

Once the vertical ion velocities are found, the ion-density profile can be determined using the continuity equation

$$\partial n / \partial t = Q - L + \nabla \cdot (D \nabla n - n \vec{v}) \quad (2.21)$$

where D is the coefficient of diffusion, and Q and L are production and loss terms for the species being considered. In the case of metallic ions, the production and loss by chemical reactions are small compared with the effects of diffusion and transport [Ferguson, 1972; Brown, 1973]. Thus, for steady-state conditions, equation (2.21) can be written

$$\frac{1}{n} \nabla n = \vec{v} / D \quad (2.22)$$

If, for example, horizontal stratification is assumed and the vertical ion drift changes linearly with altitude as

$$v_z = a(z - z_0) \quad (2.23)$$

and assuming the diffusion coefficient to be constant through the region, the solution of equation (2.23) is

$$n = n_0 \exp \left(\frac{a(z - z_0)^2}{2D} \right) \quad (2.24)$$

Equation (2.5) describes an electron-density profile with a simple Gaussian shape, which is similar to many of the observed sporadic-E profiles.

Because of the complex wind structure and chemistry occurring in the lower E region, ionization-density profiles are usually found numerically using a digital computer. In this case, equation (2.21) can be solved for all species, including those for which production and loss terms are important

[MacLeod *et al.*, 1975]. *Axford and Cunnold* [1966] discussed the effect of a wind shear on two ionized species with differing recombination coefficients. They showed that, while the slowly-recombining species formed a layer at the wind shear, the density of the ion with the fast recombination rate was actually depleted at the wind shear. This is attributed to the increased recombination loss rate resulting from the enhanced electron density at the layer. The effect has been observed in ion mass spectrometer measurements [Narcisi, 1968; Zbinden *et al.*, 1975].

The requirement that the ionized species from which sporadic-*E* layers are formed have a small recombination rate leads to the consideration of metallic ions. The presence of metallic ions in the *E* region, and their role in the formation and maintenance of sporadic-*E* layers will be discussed in the following section.

2.3 *Metallic Ions*

2.3.1 *Introduction.* In the previous section the theory of formation of sporadic-*E* layers by wind shear was described. One of the major problems encountered in the early development of wind-shear theory of sporadic *E* was the lifetime of the ions in the layer [Layzer, 1964a]. It was assumed that sporadic-*E* layers would contain the same ionic constituents as the rest of the lower *E* region, predominantly O_2^+ and NO^+ . However, the rapid recombination rates of O_2^+ and NO^+ would prevent the peak electron density in the layer from reaching the observed values. In response to this problem, a model was developed of sporadic-*E* layers formed of metallic ions [Axford and Cunnold, 1966]. The presence of metallic ions in a sporadic-*E* layer had been shown by Istomin [1963] using a rocket-borne mass spectrometer.

In this section, various sources and sinks of metallic ions are discussed. It is suggested that direct ionization of metal atoms at the time a meteoroid

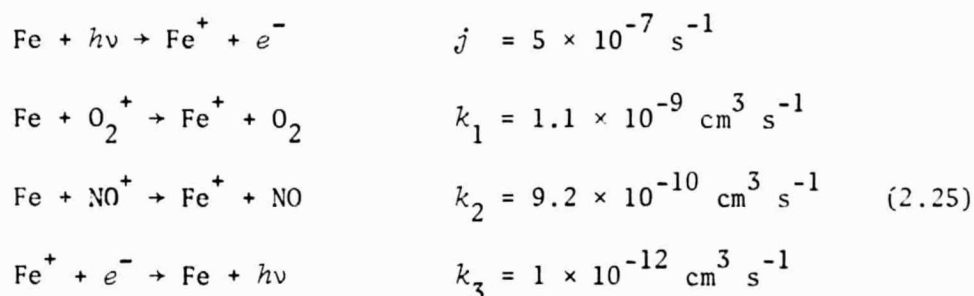
enters the earth's atmosphere is an important source of metallic ions. A model is developed describing the diurnal variation in metallic ion concentration to conform with a similar behavior in sporadic-E peak electron density. The model considers charge-exchange reactions between metal atoms and the major ionospheric constituents, as well as the direct contribution by ablating meteors. The ionization is removed by transport downward out of the lower E region.

2.3.2 *General characteristics of metallic ions.* Mass-spectrometer measurements have shown the presence of layers of metallic ions in the region between about 85 and 130 km [Istomin, 1963; Narcisi and Bailey, 1965; Narcisi, 1968, 1972; Young et al., 1967; Anderson and Barth, 1971; Johanessen and Krankovsky, 1972; Zbinden et al., 1975; Goldberg, 1975]. The most common ions in these layers are Fe^+ and Mg^+ . Also present are Si^+ , Na^+ , Ca^+ , K^+ , and traces of others. Si^+ has the same mass as N_2^+ but is identified above 100 km by the low recombination rate required for the formation of layers and at lower altitudes by its chemical properties [Goldberg, 1975].

It is generally accepted that the metal ions are of meteoric origin, although the relative abundances of the metals in meteors are not reflected in the metallic ions. Baggeley and Cumack [1974] calculate the relative abundances of the four main ions expected to form initially by collisions with the atmosphere as Fe^+ , 48%; Si^+ , 34%; Mg^+ , 10%; and Na^+ , 7%. Other theories now discounted of the source of the metal ions include the transport to high altitudes of particles initially found in sea spray [Allen, 1970], and the evaporation from aerosols of both terrestrial and extraterrestrial origin in the ionosphere [Donahue and Meier, 1967].

Considering ablation from meteors as the source, metal atoms are ionized

by three processes: collisions with the ambient atmosphere as the meteor impacts; charge exchange with O_2^+ and NO^+ ; and photoionization. Detailed chemical reaction schemes have been outlined in several papers [Swider, 1969; Ferguson, 1972; Brown, 1973; Baggaley and Cumack, 1974; Poole and Nicholson, 1975]. Using iron as an example, the important reactions involving metals at sporadic-E altitudes, with rate constants as quoted in Brown [1973], are



Rate constants for magnesium are approximately the same as those for iron [Brown, 1973].

2.3.3 *Production rates of metallic atoms and ions.* The production rate of metal ions by the initial collisions with atmospheric molecules has been computed by Lebedinets and Shushkova [1970]. They find a peak production rate of $10^{-1} \text{ cm}^{-3} \text{ s}^{-1}$ occurring at about 105 km.

The ionization rate due to meteor trails can be estimated from meteor radar observations of line electron density. The number $N(m^{-2} \text{ s}^{-1})$ of meteor trails exceeding a line electron density $\Lambda(m^{-1})$ is represented by

$$N(>\Lambda) = K\Lambda^{-1} \quad (2.26)$$

with $K \approx 1.3 \times 10^2 \text{ m}^{-3} \text{ s}^{-1}$ [Sugar, 1964]. This is established over the range $10^{10} < \Lambda < 10^{18} \text{ m}^{-1}$. The differential flux is given by

$$dN/d\Lambda = -K\Lambda^{-2} \quad (2.27)$$

Assuming all trails are vertical, the ionization production rate q_I ($m^{-3} s^{-1}$) is given by

$$q_I = \int_{N_1}^{N_2} \Lambda \, dN = K \int_{\Lambda_2}^{\Lambda_1} \Lambda^{-1} \, d\Lambda = K \ln \left(\frac{\Lambda_1}{\Lambda_2} \right) \quad (2.28)$$

Thus, for each decade in line electron density, $q_I \approx 3 \times 10^2 m^{-3} s^{-1}$. For the range of Λ from 10^{10} to 10^{18} then, $q_I \approx 2.5 \times 10^3 m^{-3} s^{-1}$.

In addition there is an obliquity factor resulting from the distribution of zenith angles of the trails. Assuming this to be of the order of a factor of 10, the ionization rate due to metal ions formed directly in meteor trails is $q_I \approx 3 \times 10^4 m^{-3} s^{-1}$ or $0.03 cm^{-3} s^{-1}$.

A check on this estimate of q_I is found in data from the daytime equatorial ionosphere. *Woodman* [1970] quotes the upward vertical ion velocities in the upper *E* region as approximately $20 m s^{-1}$. *Aiken and Goldberg* [1973] show daytime concentrations of individual metal ion species at heights above the meteor region of about $10 cm^{-3}$. If all metal ions produced in the meteor region are transported upward, the total production rate of metal ions in that region can be found. From the continuity equation (2.21),

$$q_{I_{total}} = \frac{nv_z}{\Delta z} \sim 10^{-2} cm^{-3} s^{-1} \quad (2.29)$$

which is consistent with the production rates given above.

Another estimate may be obtained from the total amount of metal deposited in the ionosphere by meteors. The amount is not well known. A representative estimate of the total mass of the matter deposited by ablation from meteoroids is $9 \times 10^{10} g yr^{-1}$ [*Gadsden*, 1968] which corresponds to a column influx of metallic atoms and ions of approximately $2 \times 10^6 cm^{-2} s^{-1}$

[Brown, 1973]. If the effective depth of deposition of meteoric material is 30 km, this estimate gives a combined production rate of atoms and ions as $0.7 \text{ cm}^{-3} \text{ s}^{-1}$. Comparing this to the production rate of metallic ions discussed above gives the fraction of metallic atoms which are ionized directly in meteor trails as approximately 5%.

Little is known of the neutral metal concentrations. Sodium has been measured more successfully than other metals, but only at altitudes near 90 km. There are many opinions of the relative production rates of atoms and ions by meteor ablation. Based on measured cross sections for ionizing collisions between neutral species, Brown [1973] concluded that thermalization of the atoms by kinetic energy transfer is much more important than ionization by the collisions. However, Lebedinets and Shushkova [1970] found that, based on their calculations, ionization by meteors is an important source of metallic ions in the upper atmosphere. The ionization of metal atoms in meteor trails by enhanced NO^+ concentrations and increased radiation levels may also contribute significantly. Anderson and Barth [1971] compared day airglow measurements of Mg and Mg^+ , and concluded that the ratio, Mg^+/Mg , has a lower limit of 22.2. Gadsden [1972], on the other hand, held that the measurement of Anderson and Barth might be low by as much as a factor of 20. If meteor ablation and transfer processes are neglected, it can be shown using the reactions of equation (2.25) that over 99% of the metal atoms would be ionized under either daytime or nighttime conditions [Brown, 1973].

2.3.4 *Lifetimes of metallic ions.* Recombination rate constants of the metallic ions are on the order of $10^{-12} \text{ cm}^3 \text{ s}^{-1}$. The time rate of change of the concentration of metal ions by recombination is given by

$$\frac{d[M^+]}{dt} = -k_3[M^+][e^-] \quad (2.30)$$

where $[M^+]$ is the metallic ion concentration and k_3 is the recombination coefficient. For the situation in which $[M^+] \ll [e^-]$ this can be solved for $[M^+]$ giving

$$[M^+] = [M^+]_0 \exp(k_3 [e^-] t) \quad (2.31)$$

The time constant for recombination is then expressed as

$$\tau_R = \frac{1}{k_3 [e^-]} \quad (2.32)$$

Assume, for example, that $[e^-]$ is constant at the daytime value of 10^5 cm^{-3} and $[M^+]_0$ is 10^3 cm^{-3} , then it is seen that $\tau_R = 10^7 \text{ s}$, or approximately 16.5 weeks.

The residence time of metallic ions due to transport processes, τ_T , can be estimated by the ion production rates discussed previously. If an average metallic ion concentration of 10^3 cm^{-3} is assumed, then if the ion production rate is $0.025 \text{ cm}^{-3} \text{ s}^{-1}$, τ_T is 11.1 hr; and for a production rate of $0.01 \text{ cm}^{-3} \text{ s}^{-1}$, 27.8 hr.

The only effective loss process at midlatitudes is thus the downward transport of the ions by the effects of the neutral wind. Long-lived ions trapped at a null point in a gravity wave follow the downward-moving phase of the wave until the ions are "dumped" in the region below 90 or 95 km where collisions with the neutral atmosphere inhibit their motion and other chemical reactions become important [Chimonas and Axford, 1968]. The predominance of either the diurnal or semidiurnal tide in the transport of metallic ions from the E region would be allowed by the range of residence times of metallic ions discussed above.

2.3.5 Diurnal variation. The diurnal variations in the concentrations of metallic atoms and ions may be obtained as the solutions of

$$\frac{d[M]}{dt} = q_A - K[M] \quad (2.33)$$

and

$$\frac{d[M^+]}{dt} = q_I + K[M] - T[M^+] \quad (2.34)$$

where

$$K = j + k_1[O_2^+] + k_2[NO^+] \quad (2.35)$$

In these equations, $[M]$ and $[M^+]$ are the concentrations of metallic atoms and ions, and q_A and q_I are the rates of production of atoms and ions by meteors. The term $K[M]$ represents the combined effects of photoionization and charge-exchange with the ambient ionization. For a metallic ion profile that decreases exponentially with height, the loss process (downward transport) is proportional to $[M^+]$, T being the constant of proportionality.

The diurnal variation is mainly the result of the variation of the charge-exchange process contained in the coefficient K . This varies continuously during a 24-hour period in a way determined by the concentrations of O_2^+ and NO^+ . A simple model is used in the following analysis in which K is approximated by a constant nighttime value between sunset (18 hr) and sunrise (06 hr) and is set equal to a constant value, representative of average daytime conditions, between sunrise and sunset. The time constants are such that this model gives a representation of the day-to-night change in concentrations of metallic ions and atoms but does not reproduce accurately the transition periods near sunrise and sunset.

For the situation discussed above the concentrations of metallic atoms and ions can be found as the solution of equations (2.34) and (2.35)

$$[M] = ([M]_0 - q_A/K) e^{-Kt} + q_A/K \quad (2.36)$$

$$[M^+] = \left(\frac{K[M]_0 - q_A}{T-K} \right) e^{-Kt} + \left([M^+]_0 - \frac{K[M]_0 - q_A}{T-K} - \frac{q_A + q_I}{T} \right) e^{-Tt} + \frac{(q_A + q_I)}{T} \quad (2.37)$$

where $[M]_0$ and $[M^+]_0$ are the concentrations of atoms and ions at the beginning of the time period being considered. The concentrations at the end of the half-day period are found by putting $t = 12$ hr in these equations. The four equations for the concentrations at sunrise, $[M]_1$ and $[M^+]_1$, and at sunset, $[M]_2$ and $[M^+]_2$, may then be solved simultaneously in terms of the quantities q_A , q_I , $K(\text{day})$, $K(\text{night})$, and T .

Possible values of the sunrise and sunset concentrations are illustrated by the following examples. From equations (2.25) values of K can be found by estimating concentrations of O_2^+ and NO^+ . These concentrations are quite uncertain at the present time. For this example $[O_2^+]$ and $[NO^+]$ will be taken to be $4 \times 10^4 \text{ cm}^{-3}$ and $2 \times 10^4 \text{ cm}^{-3}$ in the daytime; $3 \times 10^2 \text{ cm}^{-3}$ and $6 \times 10^2 \text{ cm}^{-3}$ at night. The corresponding values of K are $6.3 \times 10^{-5} \text{ s}^{-1}$ in the daytime and $8.8 \times 10^{-7} \text{ s}^{-1}$ at night. The concentrations of metallic atoms at sunrise and sunset are then

$$[M]_1 = 6.05 \times 10^4 q_A \quad (2.38)$$

and

$$[M]_2 = 1.88 \times 10^4 q_A \quad (2.39)$$

The concentration of metallic atoms is not affected by the residence time of the metallic ions. If this residence time (T^{-1}) is taken to be 12 hr, then the concentrations of metallic ions at sunrise and sunset are

$$[M^+]_1 = (2.19 \times 10^4)q_A + (4.32 \times 10^4)q_I \quad (2.40)$$

$$[M^+]_2 = (5.67 \times 10^4)q_A + (4.32 \times 10^4)q_I \quad (2.41)$$

For $T^{-1} = 24$ hr,

$$[M^+]_1 = (6.30 \times 10^4)q_A + (8.64 \times 10^4)q_I \quad (2.42)$$

$$[M^+]_2 = (1.02 \times 10^5)q_A + (8.64 \times 10^4)q_I \quad (2.43)$$

Curves showing the dependence of the diurnal variation in the metallic ion concentration on q_A and q_I are plotted in Figure 2.4 for $T^{-1} = 12$ hr and in Figure 2.5 for $T^{-1} = 24$ hr. The observed diurnal variation of $[M^+]$ and the value of q_I matching the estimates of the preceding discussion are approximated where $q_A = 10^{-1} \text{ cm}^{-3} \text{ s}^{-1}$ and $q_I = 10^{-2} \text{ cm}^{-3} \text{ s}^{-1}$. These values for q_A and q_I are consistent with calculations of the fraction of atoms ionized during ablation [Sida, 1969; Lebedinets, 1973].

The estimated values for q_I and q_A are used in equations (2.36) and (2.37) with values of $[M]_1$, $[M]_2$, $[M^+]_1$, and $[M^+]_2$ based on equations (2.38) through (2.43) and using values of T^{-1} of 12 and 24 hr, representing the diurnal and semidiurnal tides. The resulting diurnal behavior of $[M^+]$ and $[M]$ is plotted in Figure 2.6.

In the model described above, curves similar to Figure 2.6 can be found using any combination of q_I , q_A , and T . The basic diurnal trends are not dependent on the current estimates of the relative importance of the three processes since changes in their relative values would affect only the magnitude of the diurnal variation. If $q_A \gg q_I$, the diurnal variation would be negligible; while if $q_I \ll q_A$, $[M^+]_1/[M^+]_2 \approx e^{-T\tau}$, where $\tau = 12$ hr. Also, larger values of T result in larger diurnal

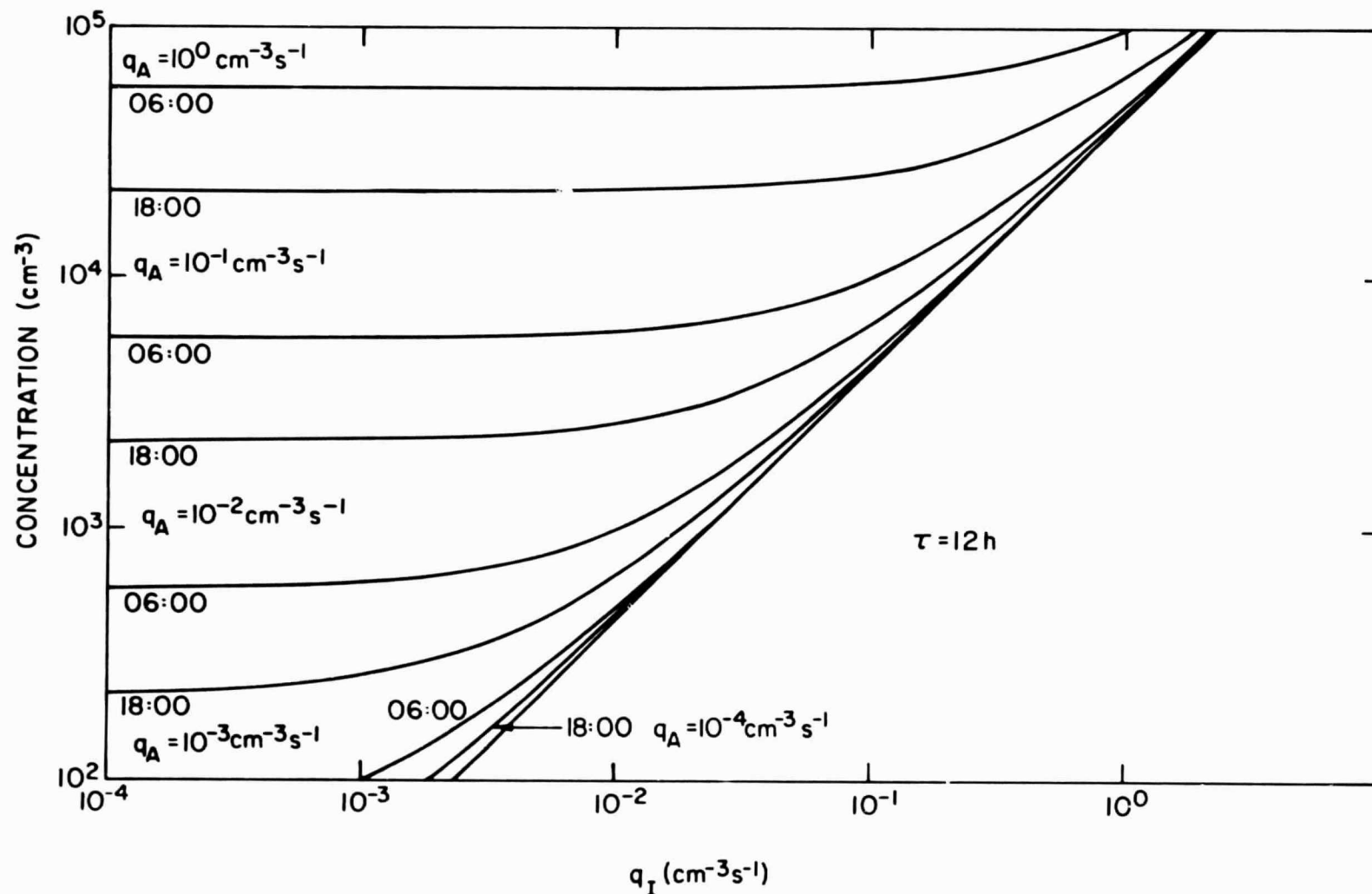


Figure 2.4 Diurnal variation of the metallic ion concentration for various values of q_A and q_I with a residence time due to transport of 12 hr.

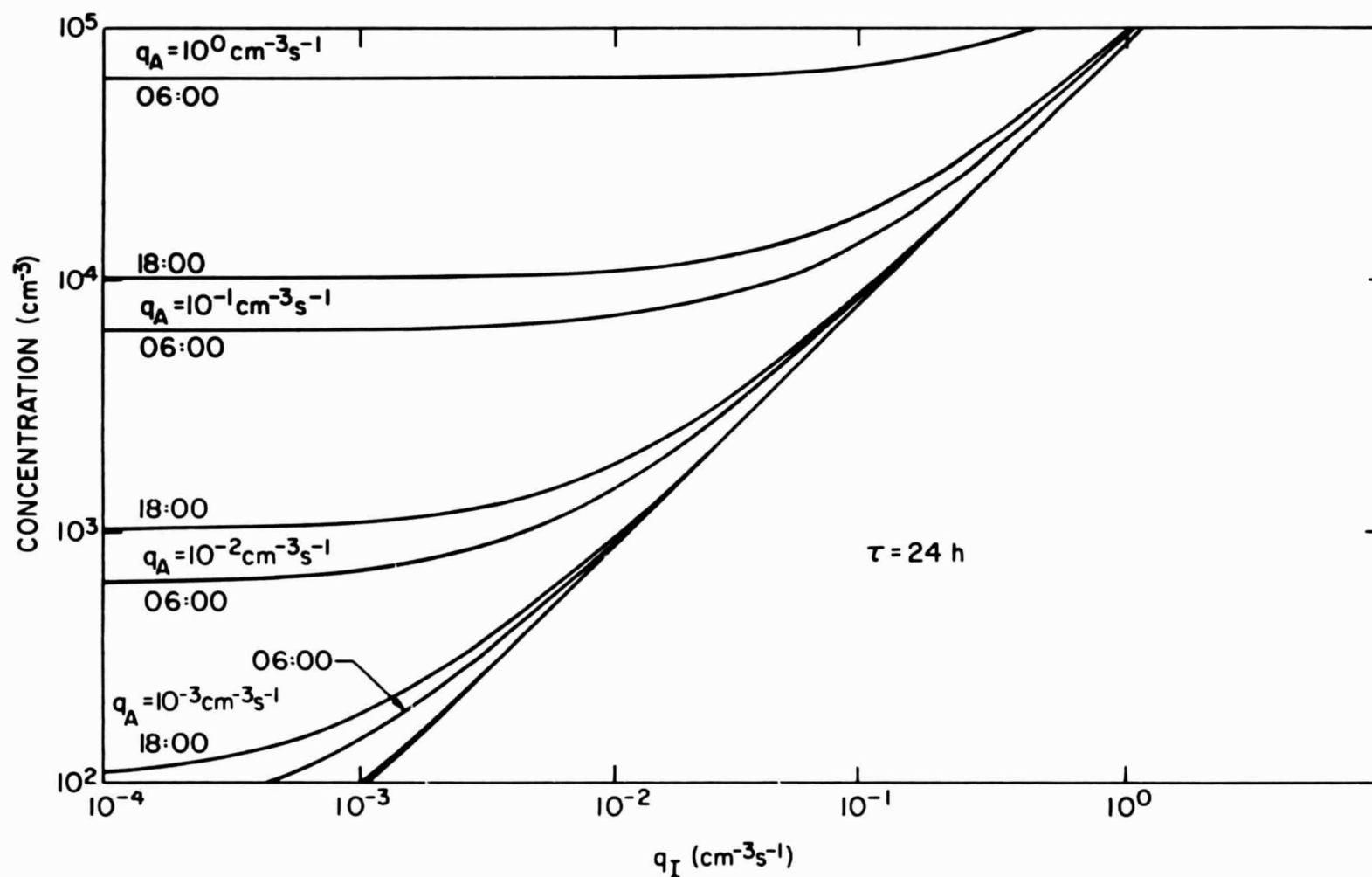


Figure 2.5. Diurnal variation of the metallic ion concentration for various values of q_A and q_I with a residence time due to transport of 24 hr.

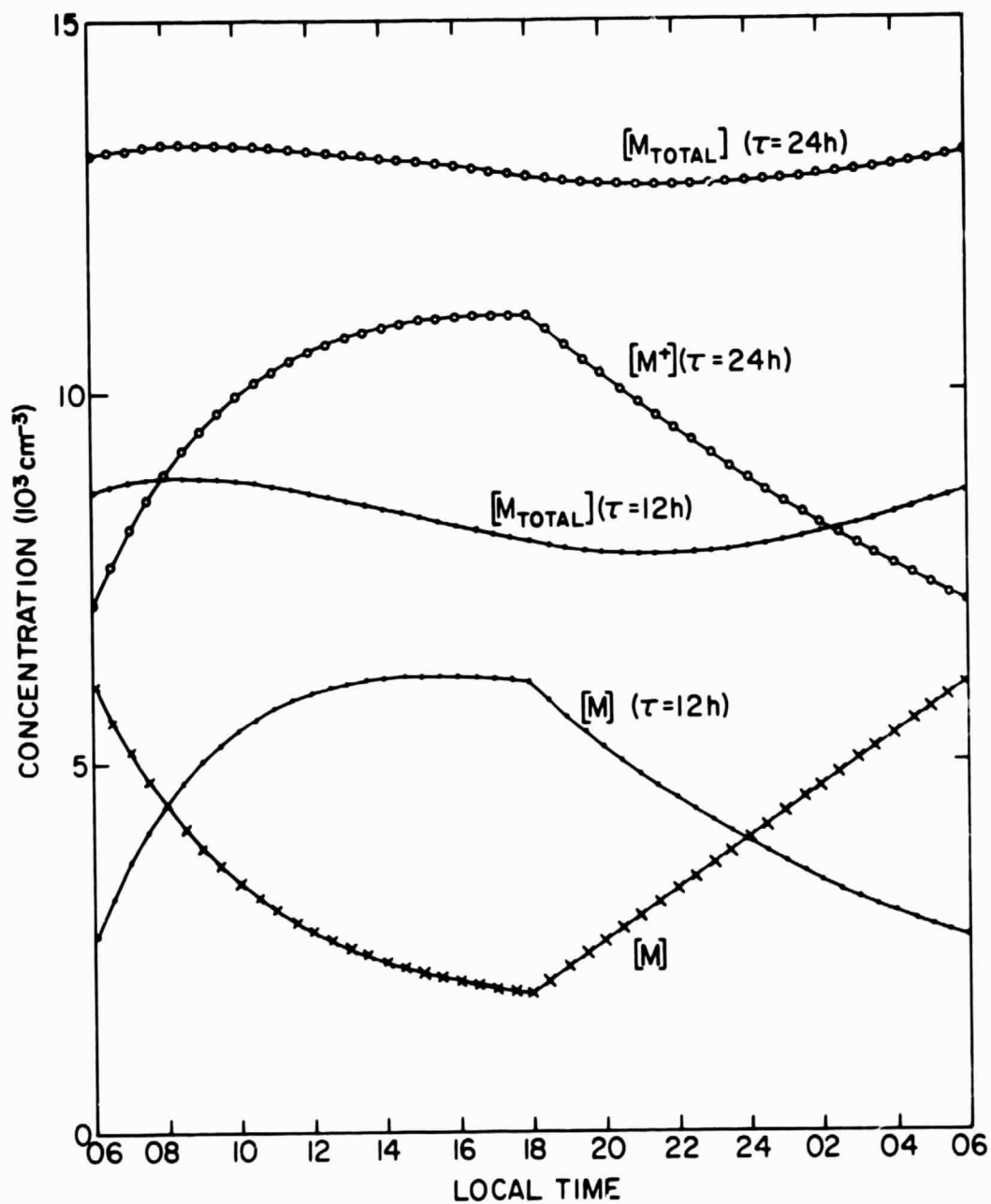


Figure 2.6. Time variation of metallic atom and ion concentrations shown for transport lifetimes of 12 hr. and 24 hr. The concentration of metallic atoms is not affected by the transport lifetime.

variations of $[M^+]$, but do not affect $[M]$. A model similar to this was developed by *Gadsden* [1970] to explain the observed distribution of sodium.

2.3.6 *Effect of heavy ions.* Meteor trails probably contain a continuum of particle masses. In studies of twilight luminescence, *Link* [1973] found evidence of meteoric aerosols at altitudes near 100 km. These metallic particles can also become ionized and would be acted upon by the neutral wind as described by wind-shear theory.

The efficiency of the wind-shear mechanism in converging ionization increases as the mass of the ions increases. An estimate of the effectiveness of a wind shear in maintaining a density gradient against diffusion is given by the ratio v_z/D (see equation 2.22).

The effect of the mass of an ionized particle on the vertical drift induced by the motion of the neutral wind is found by equation (2.17). The ion-neutral collision frequency is proportional to $M^{-1/2}$ [*Ratcliffe*, 1972], where M is the mass of the ion. Thus the ratio of the ion-neutral collision frequency to the ion gyrofrequency can be expressed as

$$\rho = (CM)^{1/2} \quad (2.44)$$

where C is a constant.

The molecular diffusion coefficient is given by

$$D = kT/mv \quad (2.45)$$

so that, for an east-west horizontal wind, equations (2.17) and (2.45) give the dependence of v_z/D on the mass of the ionized particle as

$$\frac{v_z}{D} \propto \frac{M}{1+CM} \quad (2.46)$$

The dependence of v_z/D on the mass of the particles is shown in Figure 2.7. The altitudes indicated along the curve mark the location where, for the atmospheric conditions at that altitude, M is equal to an ion mass of 30 amu. This figure shows that the effect of the wind-shear mechanism is independent of mass at altitudes below about 105 km. At an altitude of 120 km, if the mass of the ions is increased by a factor of 10, the ratio v_z/D increases by a factor of 1.8, from 0.5 to 0.9 in the units shown in Figure 2.7. This effect would be enhanced if the particles were more than singly charged.

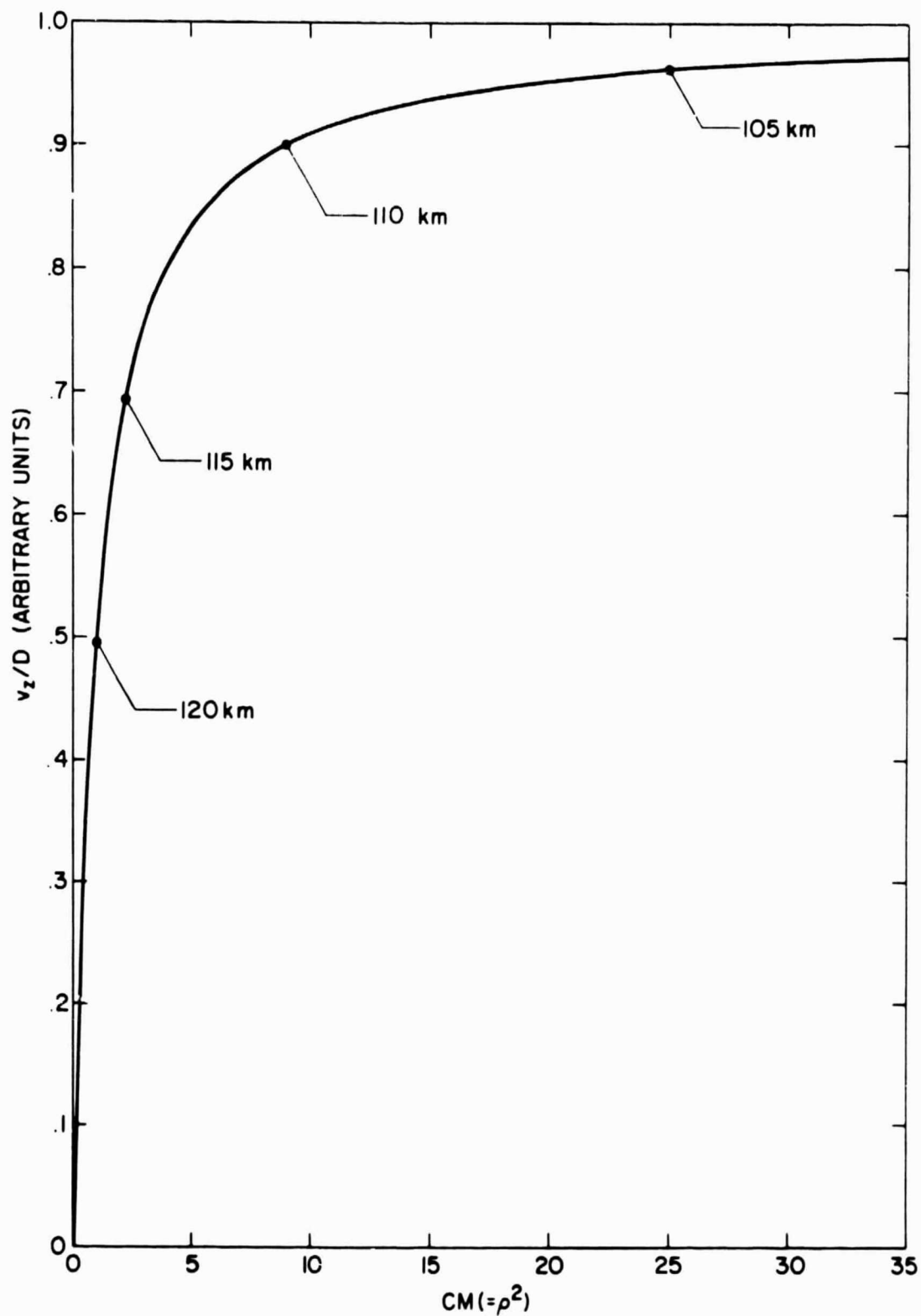


Figure 2.7 Effect of ionic mass on the efficiency of the wind-shear mechanism. Altitudes indicated along the curve mark the location where, for atmospheric conditions at that altitude, M is equal to an ion mass of 30 amu.

3. REFLECTION OF RADIO WAVES BY SPORADIC-E LAYERS

3.1 Introduction

In this chapter, the observation of sporadic-E layers by reflection of radio waves is discussed. A full-wave analysis of the reflection coefficient is developed and applied to electron-density profiles measured by rocket probes. It is shown that partial reflections from the steep gradients at the upper and lower boundaries of sporadic-E layers cannot account for the partial transparency.

3.2 Ionosonde Observations of Sporadic E

Most observations of sporadic-E layers are made by the reflection of radio waves from free electrons in the layer. However, information on the small-scale structure of sporadic-E layers gained by the reflection of radio waves is limited by poor horizontal resolution, and by the fact that only the part of the layer below the electron-density peak can be investigated. These limitations have thus far prevented the resolution of the source of partial transparency at frequencies between $fbEs$ and $ftEs$.

Vertical-incidence ionosphere sounders, or ionosondes, have been used extensively in the study of the ionosphere. The first measurements using an ionosonde-like device were made by *Breit and Tuve* [1926]. The technique developed rapidly after the initial experiments, and by the 1950's, ionosondes were being operated routinely in most parts of the world [*Smith*, 1957].

Today there are several variations of the basic ionosonde. One employs three or more spaced receivers to record phase information in order to determine the position and velocity of the ionization at the point of reflection [*Wright*, 1968; *Wright and Fedor*, 1969]. Scale sizes of ionospheric irregularities are estimated from the diffraction patterns of the

reflected radiation [Beynon and Wright, 1969; Armstrong and Lue, 1970; Goodwin and Summers, 1970]. Another variation involves the separate detection of the ordinary and extraordinary reflections [Whitehead, 1972a; Chessell et al., 1973].

Ionograms are recorded routinely at many stations, usually at intervals of 15 min or 1 hr. Examples were shown in Figure 1.2. Various parameters, including f_bE_s and f_tE_s , are scaled according to internationally accepted guidelines [URSI, 1972]. The parameters relating to sporadic E which are scaled from ionograms are sketched in an idealized ionogram in Figure 1.3

The recording of ionograms at regular intervals has made possible statistical studies that have revealed many of the characteristics of sporadic E . World-wide maps of the frequency of occurrence of intense sporadic E show a strong maximum in the area of Japan and the Philippines, and a weaker minimum over South Africa [Smith, 1957; Leighton et al., 1962]. Diurnal and seasonal variations are apparent, with maximum values of f_bE_s and f_tE_s occurring at midday and during local summer [Thomas and Smith, 1959; Raver, 1962]. In an observation quite relevant to this study, Heisler and Whitehead [1962] found that f_tE_s increased before and decreased after corresponding changes in f_bE_s . They also noted that large differences between f_tE_s and f_bE_s were most likely to occur during periods where either or both of the frequencies were changing.

In Chapter 1 two models were suggested as possible sources of the partial transparency of sporadic- E layers. In one the source is considered to be reflection or scattering from irregularities embedded within the layers; the other holds that gradient reflections from thin, horizontally-stratified layers are responsible. There is evidence supporting both

positions [Smith, 1968].

Rawer [1962] concluded from a statistical study of sporadic-E that $ftEs$ represents the plasma frequency of the maximum electron density of the layer, while $fbEs$ is the plasma frequency of the smallest value of the peak electron density. He determined on the basis of the 1962 study and earlier calculations [Rawer, 1939] that partial reflections can be neglected in interpreting ionograms. The same conclusion was reached by *Whitehead* [1972a] through an evaluation of the reflection characteristics of the ordinary and extraordinary components of the reflected wave. Spaced ionosondes have shown evidence of irregularities with scale sizes varying from one to a few tens of kilometers [DeGregorio et al., 1962; Armstrong and Lue, 1970; Goodwin and Summers, 1970]. *Goodwin and Summers* interpreted the irregularities to be frontal irregularities in the form of ridges and troughs usually travelling to the north-west or south-east. However, these measurements may be affected by gravity-wave oscillations in the height of the layer focusing or defocusing the reflected radiation and giving the illusion of movement [Hines and Reddy, 1967].

Reddy and Rao [1968] observed that $fbEs$ more closely matches the peak plasma frequency of sporadic-E layers measured by rockets than does $ftEs$. They also observed that while $fbEs$ is generally smaller, by about 10%, than the peak plasma frequency indicated by the rocket measurement, $foEs$ is much larger. This behavior is characteristic of reflections from thin layers. *Chessell* [1971a] showed that the frequency region in which a thin layer is partially transparent is increased by magnetoionic coupling of the two characteristic modes of propagation at frequencies below the peak plasma frequency of the layer.

The coherent scattering of radiation from small electron-density

irregularities has been considered by *Tao and Wait* [1962] and *Reddy* [1968] and will not be treated in this work. *Bowhill* [1966] showed that scattering can account for the partially transparent echo on some occasions.

The status of the two models discussed above when this work was begun was that the validity of neither could be established definitively. As will be shown later, previous studies of reflections from sporadic-*E* layers had deficiencies which left the question open. The purpose of the following analysis is to determine conclusively whether gradient reflections from sporadic-*E* layers are of sufficient magnitude to be the source of the observed partial transparency of the layers.

3.3 *Reflection Coefficients*

3.3.1 *Introduction.* This section presents a discussion of the propagation of electromagnetic radiation through a magnetoionic medium. The basic equations governing propagation are developed in a form readily suited to the derivation of reflection and transmission coefficients. Approximate methods of derivation of reflection coefficients from ionized layers are discussed and shown to be inadequate for this study. However, the approximate expressions are used to check the validity of the full-wave analysis.

A scheme is described whereby the full-wave reflection and transmission coefficients are programmed on a digital computer. This requires the description of sporadic-*E* electron-density profiles by mathematical functions. The results of this full-wave analysis are discussed in Section 3.4.

3.3.2 *Propagation of radio waves in the ionosphere.* As most observations of sporadic *E* are made by experiments involving radio waves, it is appropriate that the effect that gradients in the ionosphere have on radio waves be examined. This development is an extension of the work of *Budden* [1961] and *Pitteway* [1965].

The matrix differential equation describing a vertically-incident electromagnetic wave in the ionosphere is [Budden, 1961]

$$\frac{d\tilde{e}}{dz} = -ikT\tilde{e} \quad (3.1)$$

where k is the magnitude of the free space wave number,

$$\tilde{e} = \begin{bmatrix} E_x \\ E_y \\ (\mu_0/\epsilon_0)^{1/2} H_x \\ (\mu_0/\epsilon_0)^{1/2} H_y \end{bmatrix} \quad (3.2)$$

and

$$T = \begin{bmatrix} 0 & 0 & 0 & 1 \\ 0 & 0 & 1 & 0 \\ -M_{yx} + \frac{M_{yz} M_{zx}}{(1+M_{zz})} & -1 - M_{yy} + \frac{M_{yz} M_{zy}}{(1+M_{zz})} & 0 & 0 \\ 1 + M_{xx} - \frac{M_{xz} M_{zx}}{(1+M_{zz})} & M_{xy} - \frac{M_{xz} M_{zy}}{(1+M_{zz})} & 0 & 0 \end{bmatrix} \quad (3.3)$$

\underline{M} is the susceptibility tensor of the ionosphere.

By an appropriate choice of the orientation of the coordinate system, \underline{T} can be written simply in terms of the actual components of \underline{M} . The coordinate system will be oriented so that the geomagnetic field lies in the y - z plane, with z vertically upward and x in an eastward direction. The susceptibility tensor is written in this coordinate system as

$$M = - \frac{X}{U(U^2 - Y^2)} \begin{bmatrix} U^2 & -iUY_L & iUY_T \\ iUY_L & U^2 - Y_T^2 & Y_T Y_L \\ iUY_T & -Y_T Y_L & U^2 - Y_L^2 \end{bmatrix} \quad (3.4)$$

where

$$X \equiv \frac{Nq^2}{\epsilon_0 m \omega^2} \equiv \frac{\omega_p^2}{\omega^2} \quad (3.5)$$

$$\vec{Y} \equiv \frac{q\vec{B}}{m\omega} \equiv - \frac{\omega_H}{\omega} \hat{\Gamma} \quad (3.6)$$

and

$$U \equiv 1 - i\nu/\omega \quad (3.7)$$

The transverse (Y_T) and longitudinal (Y_L) components of \vec{Y} are given by Y_y and Y_z . $\hat{\Gamma}$ is a unit vector in the direction of the magnetic field. q and m are the charge and mass of the electron, N is the electron number density, and ν is the electron-neutral collision frequency. The plasma frequency of the medium and the electron gyrofrequency are, respectively, ω_p and ω_H .

The solution of equation (3.1) provides expressions for the components of the electromagnetic fields in the ionosphere as a function of altitude for a given electron-density profile. This is called a "full-wave" solution, and involves the simultaneous solution of four coupled complex differential equations for each mode. A method of solution using a digital computer is described later in this chapter. Once the total electromagnetic field is known, it can be separated into upward and downward travelling waves from which the reflection coefficient can be calculated.

In order to derive reflection and transmission coefficients using the equations of this section, the polarization of an electromagnetic wave and the refractive index of the medium must be known. The polarization, ρ , of a progressive wave travelling in the $+z$ direction is defined as

$$\rho \equiv E_y/E_x \quad (3.8)$$

In terms of the magnetoionic parameters defined in equations (3.5), (3.6), and (3.7), the polarization of the wave in the ionosphere is

$$\rho = \frac{-iY_T^2}{2Y_L(U-X)} \pm i \left[\frac{Y_T^4}{4Y_L^2(U-X)^2} + 1 \right]^{1/2} \quad (3.9)$$

The refractive index of the ionized medium is given by

$$n^2 = 1 - \frac{X}{U - \frac{Y_T^2}{2(U-X)} \pm \left[\frac{Y_T^4}{4(U-X)^2} + Y_L^2 \right]^{1/2}} \quad (3.10)$$

It will be noticed that (3.9) and (3.10) are double-valued. In each case the upper sign applied to the ordinary mode of propagation and the lower sign to the extraordinary mode. The refractive indices will be designated n_o and n_x respectively. The real part of n^2 is plotted in Figure 3.1 for conditions at an altitude of 100 km. The values used are $\nu/2\pi = 0.02$ MHz and $\omega_H/2\pi = 1.4$ MHz.

Figure 3.1 shows that there are values of X and corresponding electron densities at which the refractive index vanishes. The effective wavenumber (kn) also vanishes and the wave is reflected. In the absence of collisions, these points occur at $X = 1$ for the ordinary mode, and $X = 1 \pm Y$ for the extraordinary mode. At greater electron densities the refractive index is

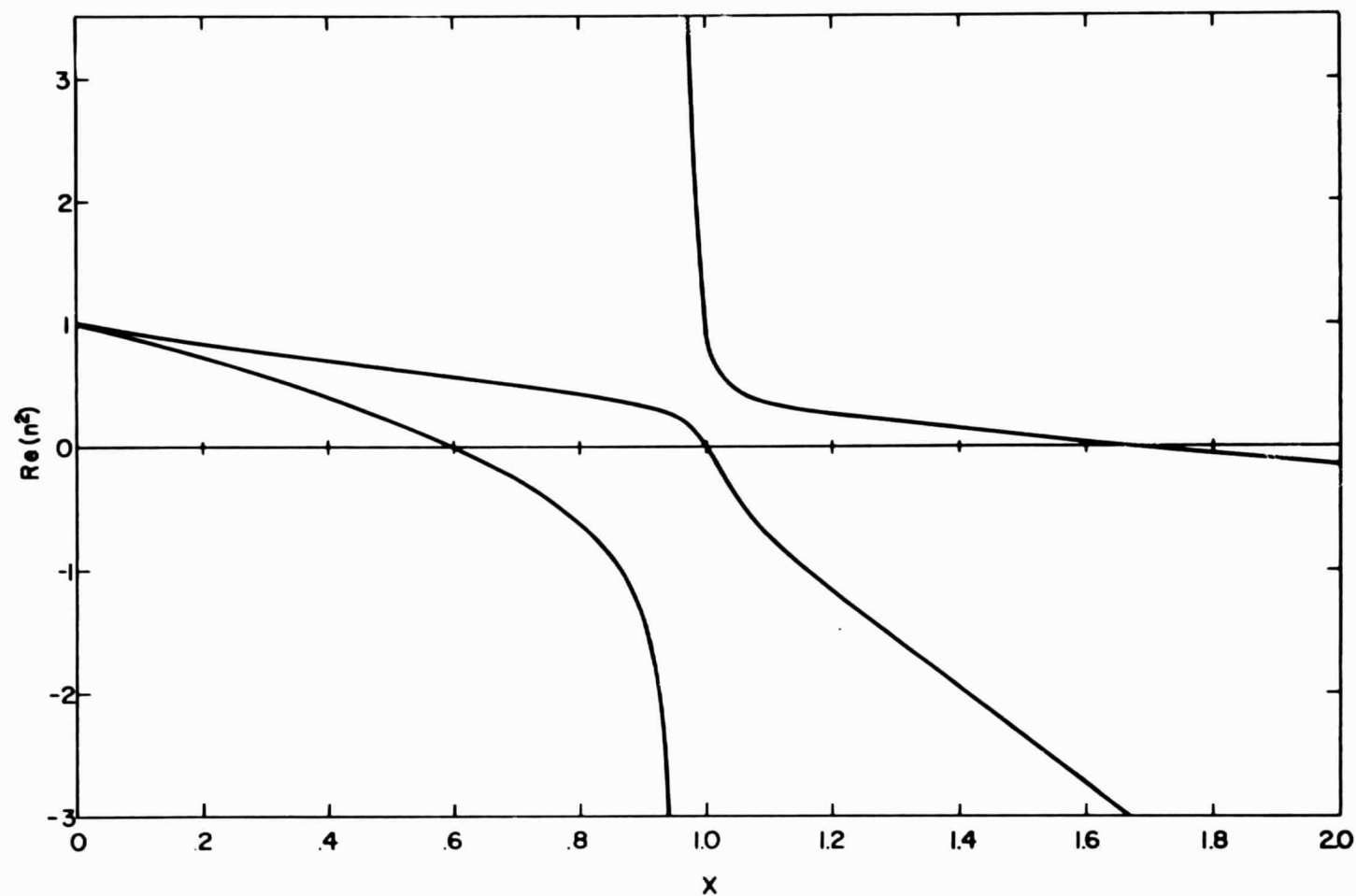


Figure 3.1 Variation of the real part of n^2 with X , where n is the refractive index of a magnetoionic medium and X is the square of the ratio of the plasma frequency of the medium to the incident frequency of an electromagnetic wave.

imaginary, and the wave is evanescent. Figure 3.2 shows a representative electron-density profile for a sporadic-E layer. Figure 3.3 shows, for this layer, the altitudes at which the index of refraction vanishes for the modes of propagation.

There is a singularity in the refractive index at $X = \frac{1-Y^2}{1-Y_L^2}$, which is just less than $X = 1$. In this region, the change in the elliptical polarization of the wave is very rapid, resulting in strong magnetoionic coupling between the modes [Budden, 1961]. The location of this singularity is indicated in Figure 3.3 by a dashed line. In the region between the infinity in n_x and the zero in n_o , both refractive indices are real. A wave with extraordinary polarization resulting from magnetoionic coupling in this region would propagate past the point where $X = 1$ and, depending on its frequency, reflect where $X = 1 + Y$ or propagate through the layer. The so-called Z-trace, seen at times on ionograms, is the result of this reflection.

3.3.3 Approximate solutions. Several approximate expressions for reflection coefficient are used in optics and electrodynamics. Three of these expressions provide useful checks on the accuracy of the full-wave solutions. Derivations of the three approximate solutions are presented in Appendix II.

The most direct approach to an estimation of the reflection coefficient is to approximate the ionized layer by a series of vertically thin layers (Section II.1). The electron density is assumed constant within each layer.

Denoting the refractive index in the regions below and above the series of layers respectively as n_i and n_t , the reflection and transmission coefficients are given by, from equations (II.15) and (II.16),

$$R = \frac{an_i + bn_i n_t - c - \frac{dn_t}{dn_i}}{an_i + bn_i n_t + c + \frac{dn_t}{dn_i}} \quad (3.11)$$

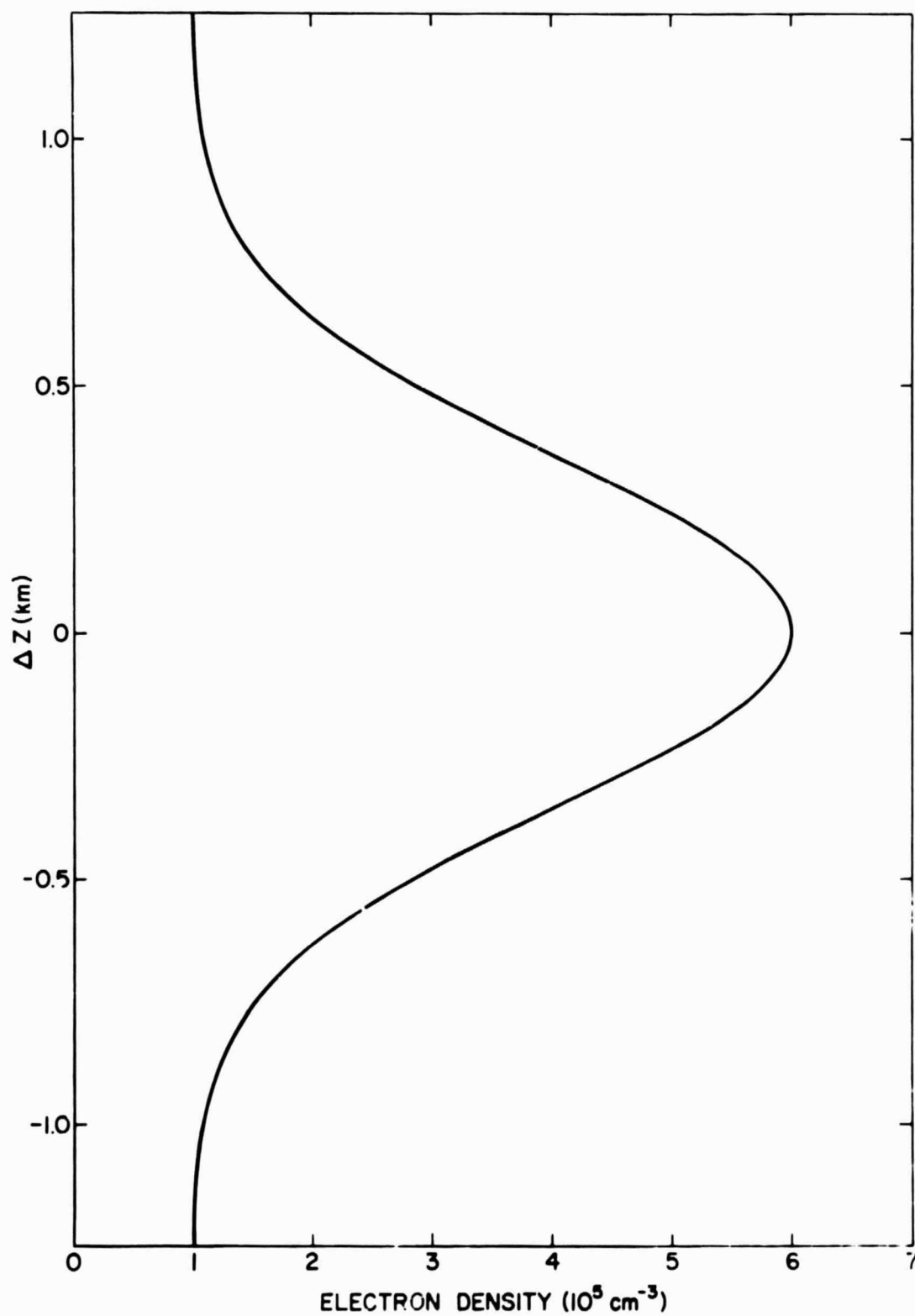


Figure 3.2 Representative electron-density profile for a sporadic-E layer.

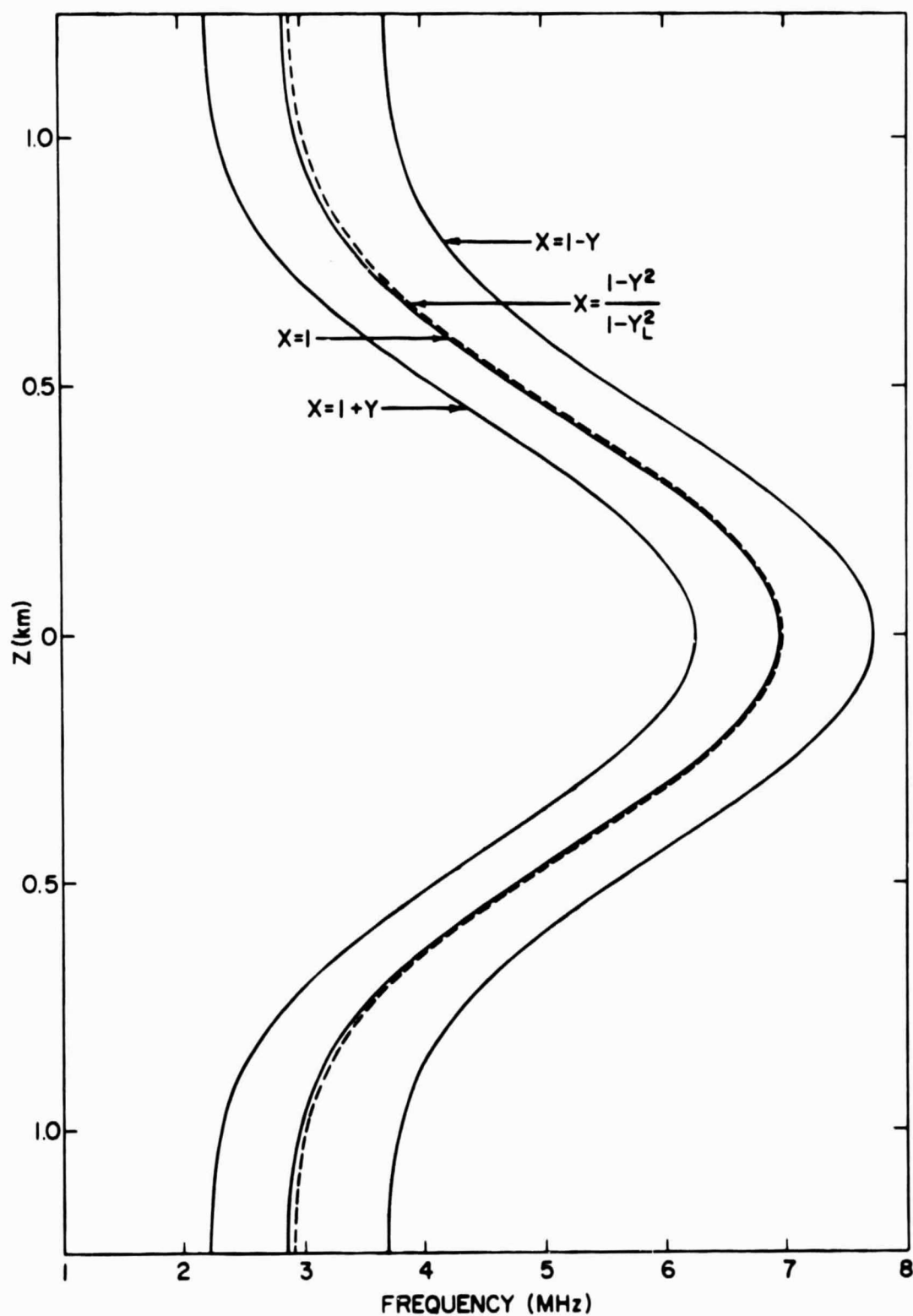


Figure 3.3 Altitudes at which the index of refraction vanishes for the modes of propagation, for the case of the electron-density profile of Figure 3.2.

$$T = \frac{2n_i}{an_i + bn_i n_t + c + dn_t} \quad (3.12)$$

where a , b , c , and d are constants that depend on the thickness and refractive indices of the layers in the reflecting medium. In the case of a single layer these become the Fresnel formulas.

These equations are invalid where the frequency of the wave is at or below the plasma frequency of the medium. Also, reflections generated by the discontinuities at the boundaries between levels make it impossible to examine small reflection coefficients from a continuous medium using the approximation.

Another solution, valid in a slowly varying medium where the frequency of radiation does not approach the plasma frequency, is the W.K.B. approximation (Section II.2). In this method, the wave equation

$$\frac{d^2 E_y}{dz^2} + k^2 n^2 E_y = 0 \quad (3.13)$$

is solved by substituting an arbitrary function of height for knz , where k is the wave number of the vertically-propagating wave, and n is the height-dependent refractive index. The refractive index is assumed to vary slowly with height, and several approximations are possible by virtue of its small second derivative. The reflection coefficient for an ionized layer is found to be, equation (II.32)

$$R = -\frac{1}{2} \int_{-\infty}^{\infty} n^{-1/2} \frac{dn}{dz} \exp -2ik \int_0^z n(z') dz' dz \quad (3.14)$$

This approximation is valid in sporadic-E layers unless the frequency of the incident radiation approaches the plasma frequency of the medium. However,

it is unacceptable for the present study because of the desire to examine the reflection coefficient at frequencies near and below the peak plasma frequency of the layer.

The third approximate solution assumes the ionization profile to be in the shape of a so-called Epstein profile [Budden, 1961]. For this case, exact expressions for the reflection coefficient can be derived using solutions of the hypergeometric equation (Section II.3).

For a symmetric layer of ionization, the magnitude of the reflection coefficient is found to be, equation (II.85)

$$|R| = \left[\frac{\cos^2(\pi d)}{\cos^2(\pi d) \cosh^2(\pi S) + \sin^2(\pi d) \sinh^2(\pi S)} \right]^{\frac{1}{2}} \quad (3.15)$$

where

$$d = (\frac{1}{4} - S^2 M)^{\frac{1}{2}}$$

$$S = \frac{2k}{m}$$

$$M = X_{\max} = \frac{f_p^2}{f_{\text{incident}}^2}$$

and m is a dimensionless parameter related to the full-width at half-maximum (Δz) of the layer by $\Delta z = 3.526/m$ meters.

The reflection coefficient of a transition region between low and high electron density is, equation (II.82)

$$|R| = \frac{\sinh\left[\frac{\pi k}{m}(1-n_{\infty})\right]}{\sinh\left[\frac{\pi k}{m}(1+n_{\infty})\right]} \quad (3.16)$$

Examples of symmetric and transition Epstein layers are shown in Figure 3.4.

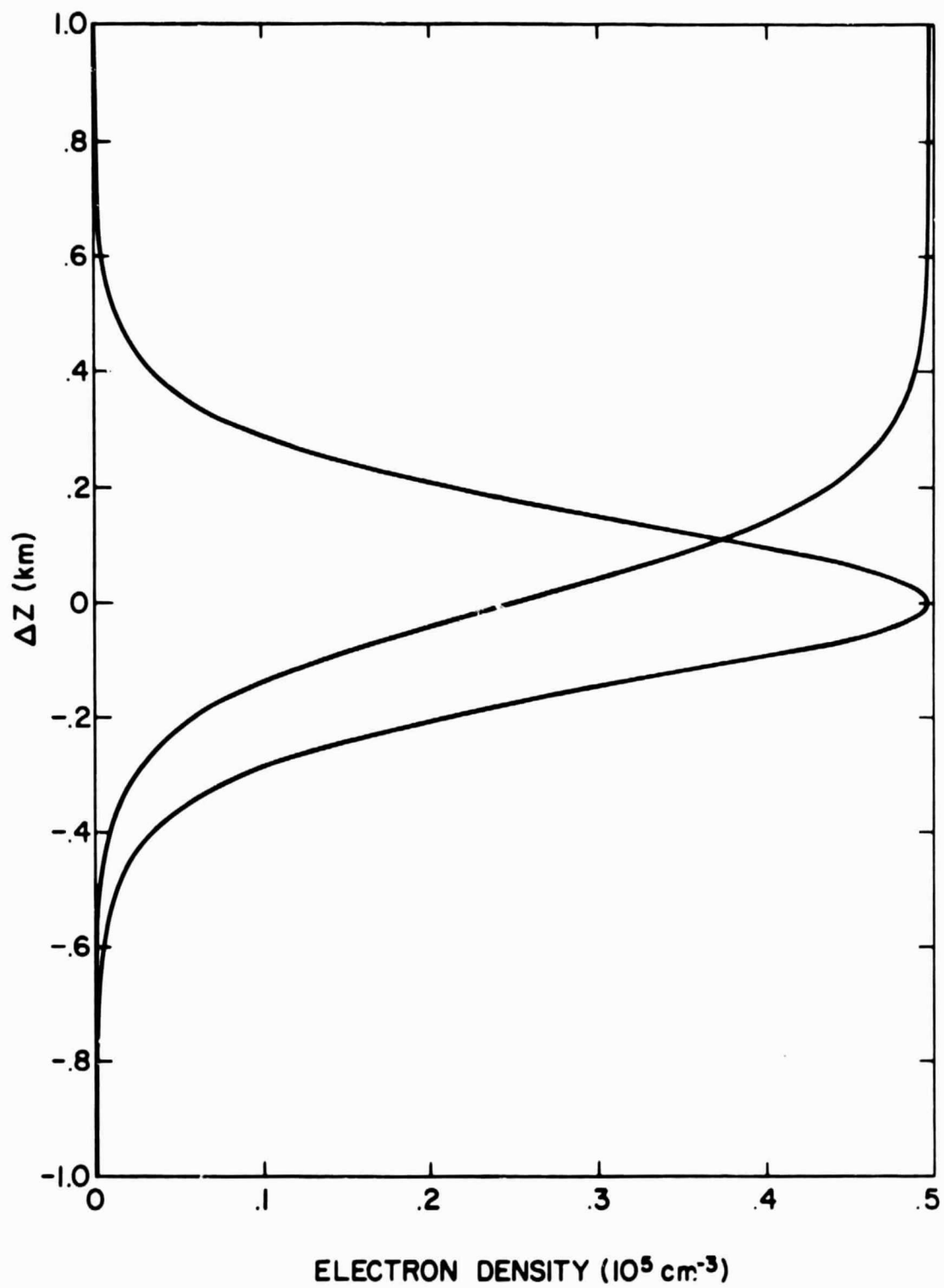


Figure 3.4 Symmetric and transitional Epstein profiles.

Reflection coefficients calculated by these approximate methods will later be compared with full-wave solutions in cases where the approximations are valid.

3.3.4 *Full-wave solution.* The mathematical development of the equations describing the propagation of electromagnetic waves in an ionized medium were discussed in Section 3.2.1. It is the purpose of this section to derive reflection and transmission coefficients that accurately described the actual reflection and transmission by a sporadic-E layer. Because of coupling between modes of the incident radiation by the geomagnetic field, some transmission through the layer at frequencies below the peak plasma frequency is expected. Therefore, a full-wave analysis is necessary. The results of this analysis will be checked against approximate methods and also against independent derivations of full-wave solutions.

The full-wave solution of the reflection and transmission coefficients builds directly on the derivation in Section 3.3.1, where it was shown that the electromagnetic fields in the wave and their derivatives are related by

$$\frac{d\mathbf{e}}{dz} = -ikT\mathbf{e} \quad (3.1)$$

This equation is integrated through the region of ionization for each of two independent modes of \mathbf{e} . The initial conditions for each mode specify an ordinary or extraordinary upward travelling wave above the layer of ionization. Thus, from Maxwell's equations and equation (3.8),

$$\begin{aligned} E_x &= E_{x0} e^{-iknz} \\ E_y &= \rho E_x \\ H_y &= (\mu_0/\epsilon_0)^{-1/2} n E_x \\ H_x &= -\rho H_y \end{aligned} \quad (3.17)$$

so that

$$e = \begin{bmatrix} 1 \\ \rho \\ -(\mu_0/\epsilon_0)^{1/2} n \rho \\ (\mu_0/\epsilon_0)^{1/2} n \end{bmatrix} \quad (3.18)$$

The polarization of the wave is specified in the expressions used for ρ and n , equations (3.9) and (3.10).

By integrating equation (3.1) using the ordinary wave polarization in equation (3.18) as the initial condition, and again, using the extraordinary wave polarization, two independent solutions, $e^{(1)}$ and $e^{(2)}$, are formed below the layer. Each solution can be separated into upward and downward travelling parts. Then, by taking the appropriate ratios, the reflection and transmission coefficients can be derived.

The electric field can be expressed as the superposition of upward (U) and downward (D) travelling waves in the following manner:

$$\vec{E} = \vec{E}_U e^{-iknz} + \vec{E}_D e^{iknz} = \vec{U} + \vec{D} \quad (3.19)$$

from which

$$\frac{d\vec{E}}{dz} = -ikn\vec{U} + ikn\vec{D} \quad (3.20)$$

These two equations can be solved for the upward and downward travelling waves,

$$\vec{U} = \frac{1}{2} \left(\vec{E} - \frac{1}{ikn} \frac{d\vec{E}}{dz} \right) \quad (3.21)$$

$$\vec{D} = \frac{1}{2} \left(\vec{E} + \frac{1}{ikn} \frac{d\vec{E}}{dz} \right) \quad (3.22)$$

In general, the ordinary and extraordinary waves are elliptically polarized. The angle formed by their major axes in the x - y plane is bisected by a line rotated clockwise 45° from magnetic north [Budden, 1961]. Thus, in order to compare electric fields of the two modes with each other the x component of one must be compared with the y component of the other [Chessel, 1971b].

Using the definition of polarization, equation (3.8),

$$\begin{aligned}
 E_x &= E_{ox} + E_{xx} \\
 E_y &= \rho_o E_{ox} + \rho_x E_{xx} \\
 H_x &= -\rho_o H_{oy} - \rho_x H_{xy} \\
 H_y &= H_{oy} + H_{xy}
 \end{aligned}
 \tag{3.23}$$

where the subscripts o and x refer to the ordinary and extraordinary modes.

The simultaneous solutions of equations (3.23) are

$$\begin{aligned}
 E_{ox} &= \frac{-\rho_x E_x + E_y}{\rho_o - \rho_x} \\
 E_{xy} &= \frac{E_x - \rho_x E_y}{\rho_o - \rho_x} \\
 H_{oy} &= \frac{H_x - \rho_x H_y}{\rho_o - \rho_x} \\
 H_{xx} &= \frac{\rho_x H_x + H_y}{\rho_o - \rho_x}
 \end{aligned}
 \tag{3.24}$$

Then, by substituting equations (3.24) into (3.21) and (3.22), the desired components of the incident and reflected waves can be written

$$\begin{aligned}
U_{ox} &= \frac{1}{2(\rho_o - \rho_x)} \left[-\rho_x E_x + E_y - \left(\frac{\mu_o}{\epsilon_o} \right)^{1/2} \left(\frac{1}{n_o} H_x + \frac{\rho_x}{n_o} H_y \right) \right] \\
U_{xy} &= \frac{1}{2(\rho_o - \rho_x)} \left[E_x - \rho_x E_y - \left(\frac{\mu_o}{\epsilon_o} \right)^{1/2} \left(\frac{\rho_x}{n_x} H_x + \frac{1}{n_x} H_y \right) \right] \\
D_{ox} &= \frac{1}{2(\rho_o - \rho_x)} \left[-\rho_x E_x + E_y + \left(\frac{\mu_o}{\epsilon_o} \right)^{1/2} \left(\frac{1}{n_o} H_x + \frac{\rho_x}{n_o} H_y \right) \right] \\
D_{xy} &= \frac{1}{2(\rho_o - \rho_x)} \left[E_x - \rho_x E_y + \left(\frac{\mu_o}{\epsilon_o} \right)^{1/2} \left(\frac{\rho_x}{n_x} H_x + \frac{1}{n_x} H_y \right) \right]
\end{aligned} \tag{3.25}$$

The transmitted waves have been specified by the initial conditions of the integration, equation (3.18), to be purely ordinary and purely extraordinary upward travelling waves, and will be represented by V_o and V_x .

The reflection and transmission coefficients are determined by

$$\begin{bmatrix} D_{ox}^{(1)} & D_{ox}^{(2)} \\ D_{xy}^{(1)} & D_{xy}^{(2)} \end{bmatrix} = \begin{bmatrix} {}_oR_o & {}_oR_x \\ {}_xR_o & {}_xR_x \end{bmatrix} \begin{bmatrix} U_{ox}^{(1)} & U_{ox}^{(2)} \\ U_{xy}^{(1)} & U_{xy}^{(2)} \end{bmatrix} \tag{3.26}$$

$$\begin{bmatrix} V_{ox}^{(1)} & V_{ox}^{(2)} \\ V_{xy}^{(1)} & V_{xy}^{(2)} \end{bmatrix} = \begin{bmatrix} {}_oT_o & {}_oT_x \\ {}_xT_o & {}_xT_x \end{bmatrix} \begin{bmatrix} U_{ox}^{(1)} & U_{ox}^{(2)} \\ U_{xy}^{(1)} & U_{xy}^{(2)} \end{bmatrix} \tag{3.27}$$

where, for example, ${}_oR_x$ describes the reflection of incident extraordinary radiation as ordinary radiation. The superscripts indicate the independent solutions of equation (3.1). The solution of equations (3.26) and (3.27) give

$$\tilde{R} \equiv \begin{bmatrix} {}_oR_o & {}_oR_x \\ {}_xR_o & {}_xR_x \end{bmatrix} = \frac{1}{|U|} \begin{bmatrix} (U_{xy}^{(2)} D_{ox}^{(1)} - U_{xy}^{(1)} D_{ox}^{(2)}) & \rho_o (U_{ox}^{(1)} D_{ox}^{(2)} - U_{ox}^{(2)} D_{ox}^{(1)}) \\ \rho_x (U_{xy}^{(2)} D_{xy}^{(1)} - U_{xy}^{(1)} D_{xy}^{(2)}) & (U_{ox}^{(1)} D_{xy}^{(2)} - U_{ox}^{(2)} D_{xy}^{(1)}) \end{bmatrix} \tag{3.28}$$

and

$$\tilde{T} \equiv \begin{bmatrix} T_o & T_x \\ x^T_o & x^T_x \end{bmatrix} = \frac{1}{|U|} \begin{bmatrix} (U_{xy}^{(2)} V_{ox}^{(1)} - U_{xy}^{(1)} V_{ox}^{(2)}) & \rho_o (U_{ox}^{(1)} V_{ox}^{(2)} - U_{ox}^{(2)} V_{ox}^{(1)}) \\ \rho_o (U_{xy}^{(2)} V_{xy}^{(1)} - U_{xy}^{(1)} V_{xy}^{(2)}) & (U_{ox}^{(1)} V_{xy}^{(2)} - U_{ox}^{(2)} V_{xy}^{(1)}) \end{bmatrix} \quad (3.29)$$

where

$$|U| = U_{ox}^{(1)} U_{xy}^{(2)} - U_{ox}^{(2)} U_{xy}^{(1)}$$

The expressions describing the reflection and transmission of radio waves by a magnetoionic medium are now in a form whereby they can be solved by computer techniques. This solution, described in the following section, involves the use of a Runge-Kutta integration routine to solve equation (3.1) for components of E and H . These components can be readily transformed using equations (3.28) and (3.29) into reflection and transmission coefficients of circularly-polarized radiation.

3.3.5 Solution using a digital computer. The full-wave solution of the wave equation in an ionized medium requires the integration of four complex differential equations, equation (3.1), through the region of ionization. A Runge-Kutta 4th-order integration routine developed by Gill [1951] provides a relatively simple but accurate way to perform the integration.

The derivation of the Runge-Kutta algorithm can be found in several texts [Stanton, 1961; Antosiewicz and Gautschi, 1962]. At each step in the integration, the value of the function is found from the previous value using a Taylor expansion

$$e(z+h) = e(z) + he'(z) + \frac{h^2}{2!} e''(z) + \frac{h^3}{3!} e'''(z) + \dots \quad (3.30)$$

This is applied to each of the four differential equations (3.1), expressed as

$$\frac{de}{dz} = f(z, e) \quad (3.31)$$

with the result that, keeping terms up to fourth order in h ,

$$\begin{aligned} \Delta e = & hf + \frac{h^2}{2!} (f_z + ff_e) + \frac{h^3}{3!} [f_{zz} + 2ff_{ze} + f^2 f_{ee} + f_e (f_z + ff_e)] \\ & + \frac{h^4}{4!} [f_{zzz} + 3ff_{zze} + 3f^2 f_{zee} + f^3 f_{eee} + f_e (f_{zz} + 2ff_{ze} + f^2 f_{ee}) \\ & + (2f_{ze} + 3ff_{ee} + f_e^2) (f_z + ff_e)] \end{aligned} \quad (3.32)$$

in which the subscripts denote differentiation. This equation is to be expressed in the form

$$\Delta e = aK_w + bK_2 + cK_3 + dK_4 \quad (3.33)$$

where

$$\begin{aligned} K_1 &= hf(z, e) \\ K_2 &= hf(z+mh, e+nK_1) \\ K_3 &= hf(z+ph, e+qK_1+rK_2) \\ K_4 &= hf(z+sh, e+tK_1+uK_2+vK_3) \end{aligned} \quad (3.34)$$

To do this, equations (3.34) are expanded about z and e again using a Taylor series. To simplify the resulting series, define

$$\begin{aligned} F_{\alpha 1} &\equiv i_\alpha f_z + j_\alpha ff_e \\ F_{\alpha 2} &\equiv i_\alpha^2 f_{zz} + 2i_\alpha j_\alpha ff_{ze} + j_\alpha^2 ff_{ee} \\ F_{\alpha 3} &\equiv i_\alpha^3 f_{zzz} + 3i_\alpha^2 j_\alpha ff_{zze} + 3i_\alpha j_\alpha^2 f^2 f_{zee} + j_\alpha^3 f^3 f_{eee} \end{aligned} \quad (3.35)$$

where $\alpha = 1, 2, 3$; and

$$\begin{aligned} i_1 &= m & j_1 &= n \\ i_2 &= p & j_2 &= q + r \\ i_3 &= s & j_3 &= t + u + v \end{aligned}$$

Using these definitions, (3.34) becomes

$$\begin{aligned} K_1 &= hf \\ K_2 &= hf + h^2 F_{11} + \frac{h^3}{2} F_{12} + \frac{h^4}{6} F_{13} \\ K_3 &= hf + h^2 F_{21} + \frac{h^3}{2} (F_{22} + 2rF_{11}f) \\ &\quad + \frac{h^4}{6} \{F_{23} + 3rF_{12}f_e + 6rF_{11}[pf_{ze} + (q+r)ff_{ee}]\} \\ K_4 &= hf + h^2 F_{31} + \frac{h^3}{2} [F_{32} + 2(uF_{11} + vF_{21})f_e] \\ &\quad + \frac{h^4}{6} \{F_{33} + 3(uF_{12} + vF_{22})f_e + 6(uF_{11} + vF_{21})[sf_{ze} + (t+u+v)ff_{ee}] \\ &\quad + 6rvF_{11}f_e^2\} \end{aligned} \tag{3.36}$$

Now, equations (3.36) are substituted into (3.33), which is equated with equation (3.32). By matching coefficients of like powers of h , one can write thirteen independent equations and solve for the thirteen coefficients in equations (3.33) and (3.34). Thus,

$$\Delta e = \frac{1}{6} K_1 + \frac{1}{3} (1 - 2^{-\frac{1}{2}}) K_2 + \frac{1}{3} (1 + 2^{-\frac{1}{2}}) K_3 + \frac{1}{6} K_4 \tag{3.37}$$

and

$$\begin{aligned}
 K_1 &= hf(z, y) \\
 K_2 &= hf(z + \frac{1}{2}h, y + \frac{1}{2}K_1) \\
 K_3 &= hf(z + \frac{1}{2}h, y - (\frac{1}{2} - 2^{-\frac{1}{2}})K_1 + (1 - 2^{-\frac{1}{2}})K_2) \\
 K_4 &= hf(z + h, y - 2^{-\frac{1}{2}}K_2 + (1 + 2^{-\frac{1}{2}})K_3)
 \end{aligned}
 \tag{3.38}$$

The value of each component of \underline{e} is given at each step by

$$e(z) = e(z - \Delta z) + \Delta e(z) \tag{3.39}$$

The above set of equations is in a form which is easily adapted for use on a digital computer. In this study, the version contained in the IBM Scientific Subroutines Package was used. This routine allows the simultaneous solution for both independent modes. Also, each step in the integration is done for two different step sizes, thus testing the accuracy. If the error exceeds a given value, the step size is halved. This is repeated until the desired accuracy is attained.

3.3.6 *Description of a sporadic-E layer by a mathematical function.*

The electron-density profiles of sporadic-E layers have been measured by Langmuir probes carried by sounding rockets [Smith, 1969]. This technique provides a continuous measure of current to the probe. Over a limited height range the current is proportional to the electron density. The nature of digital computers requires that the electron density be either stored as a discrete array or generated at each step. Because of the uncertainty associated with the step size and the possibility of fictitious reflections

being generated by discontinuities in the slope, the latter option was taken. This meant that each layer to be studied first had to be described by a mathematical function.

Functions describing the layers were found using a least squares technique which optimized the fit to a given series of functions by varying the parameters within these functions [Bevington, 1969]. A trial function was constructed for a layer, and the best fit of that particular function to the data was found. This function would then be subtracted from the data giving a new data set. A new function was then fitted to the new data set and the difference determined. This process was repeated until a good fit was obtained. The final electron-density profile would be the sum of the functions that best fit the original data. For example, Figure 3.5 shows the set of functions used to describe a sporadic-E layer observed at Wallops Island on 16 July 1970. This profile provides a good test for the method of curve fitting, as it is more complex than most sporadic-E layers. It was possible by this method to model each of the sporadic-E profiles used in this study to a high degree of accuracy.

3.3.7 Performing the integration. The solution of equation (3.1) is found for various sporadic-E profiles using the Runge-Kutta method of integration through the layer. The starting values for two independent modes are presented in equation (3.18), and describe upward-travelling ordinary and extraordinary waves. The integration is started and ended in regions of the profile where the gradient of electron density is small, thus avoiding the introduction of apparent reflections from discontinuities in the gradient. Double precision variables are employed throughout the computer program.

Pitteway [1965] showed analytically that the independence of the two solutions should be preserved throughout the integration. It is found that,

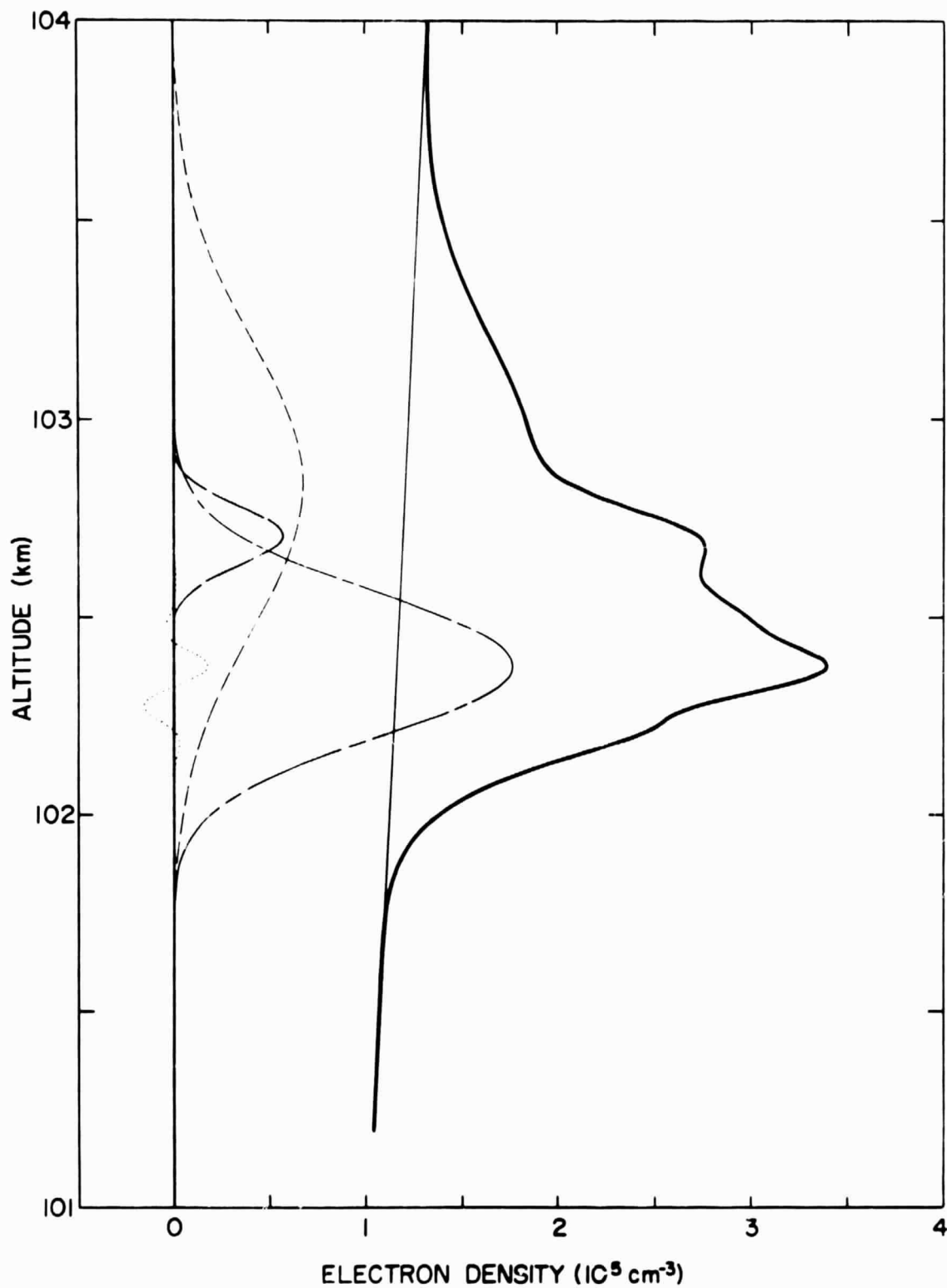


Figure 3.5 The set of mathematical functions and their sum, used to describe the electron-density profile of a sporadic-E layer observed at Wallops Island, 16 July 1970.

during the course of the integration, the two modes, which were originally independent, lose their independence. The loss of their independence can be attributed to the finite accuracy of the digital computer. The truncation of the components of the solutions has the effect of introducing elements of one solution into the other, with the effect that as the integration proceeds, the two solutions will be dominated by the most rapidly growing eigenmode.

Following the suggestion of *Pitteway* [1965], a constraint is introduced at regular intervals through the integration which insures that the two solutions are Hermitian orthogonal. This is done by replacing the second solution, $\underline{e}^{(2)}$, by a new solution, $\underline{e}^{(2')}$, which is made up of a linear combination of the two solutions, but defined so as to be Hermitian orthogonal to the first solution, $\underline{e}^{(1)}$. Thus,

$$\underline{e}^{(2')} = \underline{e}^{(2)} - \frac{\underline{e}^{(1)*} \cdot \underline{e}^{(2)}}{\underline{e}^{(1)*} \cdot \underline{e}^{(1)}} \underline{e}^{(1)} \quad (3.40)$$

The rapid growth of evanescent modes was limited by the following procedure: if the value of any component of either solution became larger than ten, all components of both solutions and their derivatives were reduced by a factor of ten. The number of times this operation was done was recorded for subsequent use.

Neither the orthogonality constraint nor the reduction of the size of the components and derivatives affects the reflection coefficient since for this calculation upward and downward travelling waves are compared with each other at the same level. All that is required is that there are two independent solutions.

For transmission coefficients, upward travelling waves below the layer are compared with upward travelling waves above the layer. Because of the

addition of solutions to preserve orthogonality, information of transmission resulting from mode coupling is not preserved. Therefore, upgoing ordinary and extraordinary waves below the layer are compared respectively with ordinary and extraordinary waves above the layer to get ${}_o^T{}_o$ and ${}_x^T{}_x$. The waves below the layer are multiplied by the appropriate factors of ten to compensate for the procedure used to limit the evanescent modes.

3.4 Results of Reflection Coefficient Calculations

3.4.1 *Comparison with independent solutions.* The validity of the derived reflection and transmission coefficients discussed above and the accuracy of the computer program employed are now tested against some of the approximate solutions of Section 3.3.2. In each case the full-wave solution is found to be consistent with the result of the approximate method. The solutions are also compared with full-wave solutions published in the literature.

As an initial test, the analysis was made using a constant electron density and an incident frequency of radiation well above the plasma frequency of the medium. To the accuracy of the computer, the result showed total transmission with no reflection. The electron-density profile was then modified so as to describe a semi-infinite region of constant electron density bounded below by free space. The reflection and transmission coefficients of a wave incident on this boundary, as given by the full-wave solution, were equal to the values given by equations (3.11) and (3.12).

The next approximate solution was derived using the W.K.B. method. The reflection coefficient was calculated from equation (3.14) and compared with the full-wave solution. A symmetric Epstein profile used in the comparison is shown in Figure 3.4, and is described by

$$n^2 = 1 - 4X_p \frac{e^{m(z-z_o)}}{[1+e^{m(z-z_o)}]^2} \quad (3.41)$$

where X_p is the value of X at the peak of the layer and $m = 0.01$. The full-width at half-maximum of this Epstein profile is 352.6 meters. The results of this calculation, showing good agreement between the two methods, are plotted in Figure 3.6.

The symmetric electron-density profile of Figure 3.4 is also used to test the full-wave solution against the solution derived from the hypergeometric equation. In this case, the reflection coefficient is given by equation (3.15). As is shown in Figure 3.7, there is good agreement between the two methods. The result is also shown for a thicker profile with $m = 0.005$. The reflection coefficients of transition layers with $m = 0.01$ and $m = 0.02$ are shown in Figure 3.8. The difference between the value of the reflection coefficient from the W.K.B. method and from the hypergeometric function is the result of neglecting the geomagnetic field in the latter case.

Chessell [1971b] has calculated reflection and transmission coefficients of several types of profiles using a full wave analysis. Chessell's results were used to check the full-wave solution used in this study. This comparison is shown in Figure 3.9.

The electron-density profile used in this comparison with Chessell's work is a parabola with a half-width of 477 m, measured to the point where the electron density is zero. This profile can be used effectively to study strong reflections from sporadic-E layers. However, the discontinuities in electron-density gradient at the upper and lower boundaries of the layer give rise to reflections that mask any gradient reflections.

3.4.2 *The effect of ionosonde sensitivity.* The results of this study are to be compared with ionograms recorded at Wallops Island at the time the profiles were measured by rocket-borne probes. In this connection it is necessary to discuss the effect of ionosonde sensitivity on the ionograms.

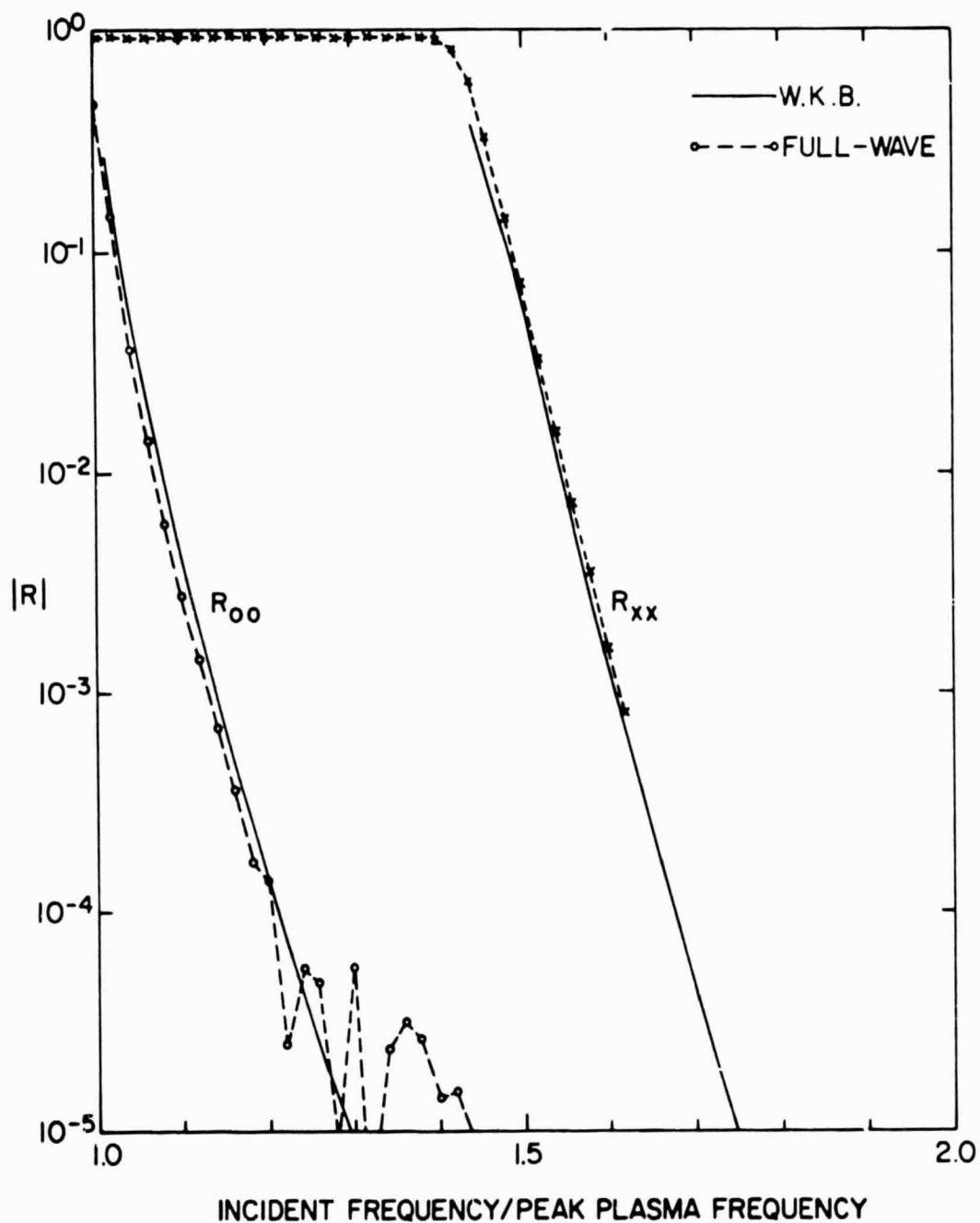


Figure 3.6 Comparison of a full-wave solution with a W.K.B. solution of the reflection coefficients of a symmetric Epstein layer having a full-width at half-maximum of 352.6 m.

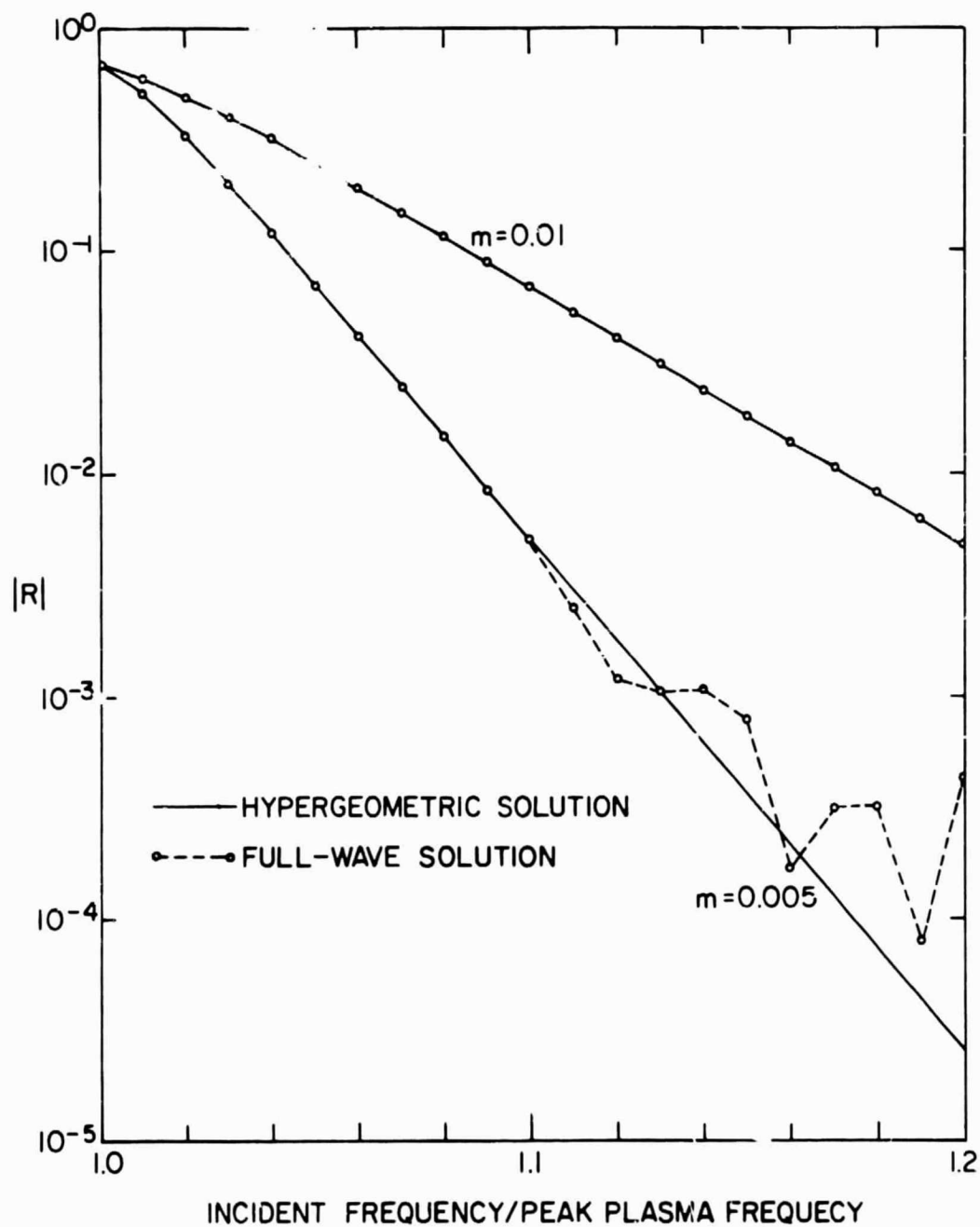


Figure 3.7 Comparison of full-wave solutions with solutions of the reflection coefficients of symmetric Epstein profiles using hypergeometric functions. Widths of the layers are 352.6 m and 705.2 m.

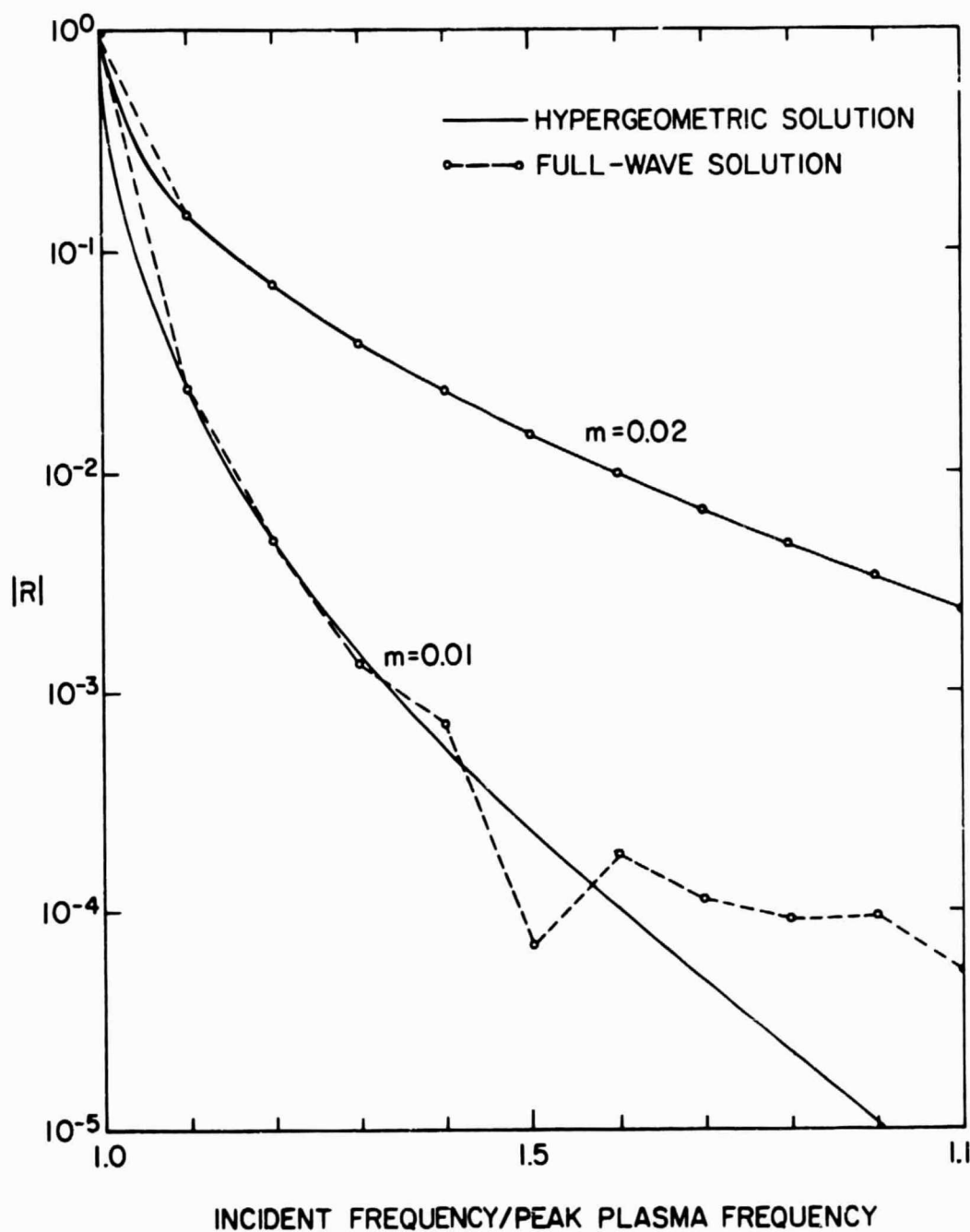


Figure 3.8 Comparison of full-wave solutions with solutions of the reflection coefficients of transitional Epstein profiles using hypergeometric functions. Widths of the layers are 176.3 m and 352.6 m.

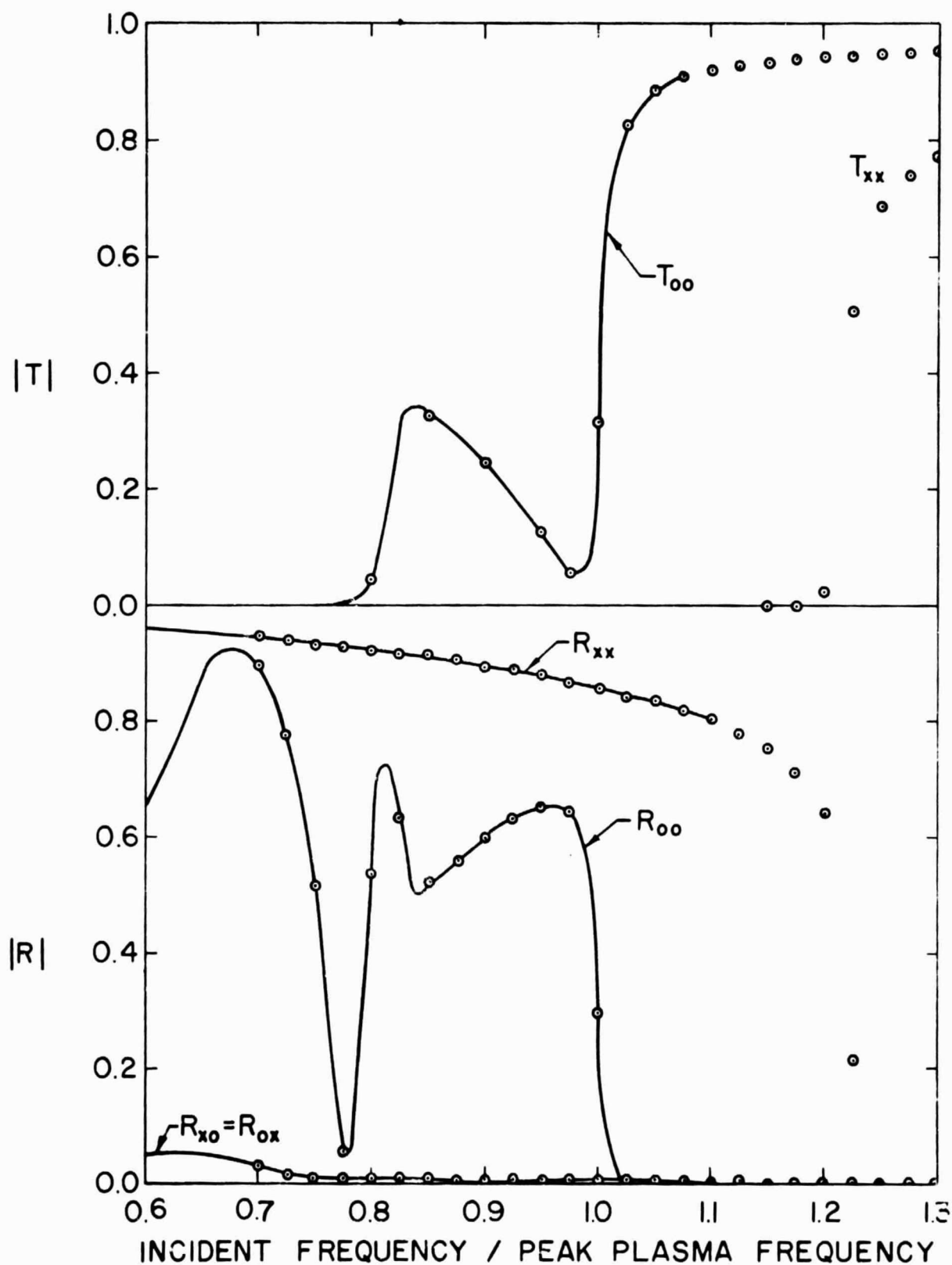


Figure 3.9 Comparison of full-wave solutions of reflection and transmission coefficients developed in this study with full-wave solutions from Chesell [1971b] (solid lines). The layer used was a parabola with a half-width of 477 m.

As the signal to an ionosonde becomes weaker, the gain is automatically increased. Also, the standard methods of recording ionograms by photographing oscilloscope screens or burning paper with a spark convey limited amplitude information. The effect is that a weak echo appears to be no different from a strong echo on the ionogram.

The sensitivity of the ionosonde at Wallops Island was measured by attenuating the signals received by the ionosonde. The attenuation was increased until the trace disappeared from the ionogram. These tests showed that a layer at sporadic-E altitude with a reflection coefficient greater than 10^{-3} would be recorded on the ionogram. Other researchers estimate this threshold reflection coefficient to be between 10^{-3} and 10^{-2} [Smith, 1957; Reddy, 1968].

Because of this automatic adjustment of sensitivity the partial transparency indicated in Figure 3.9, for example, at frequencies below the plasma frequency is not observed. This partial transparency in the frequency range $f = f_p$ to $f = f_p - f_H/2$ results from magnetoionic mode coupling (as discussed at the end of Section 3.3.2). Based on the calculations of this study and assuming similar transmission coefficients for waves travelling either direction through the layer, it appears likely that reflections from layers above the sporadic-E layer would be recorded on the ionogram. For example, a signal reflecting totally at an altitude of 300 km which twice penetrates a layer with a transmission coefficient of 9.5×10^{-2} would have the same amplitude at the ground as if it had reflected at an altitude of 100 km from a layer with a reflection coefficient of 10^{-3} . It is not likely, however, that this echo from the F region would be detected by an ionosonde. At frequencies just below the peak plasma frequency there would be a strong return from the sporadic-E layer, and the automatic gain control would set

the gain of the ionosonde at a low value so that the *F*-region echo would not be received.

As noted in the previous section care has to be taken in the full-wave analysis to avoid discontinuities in the electron-density gradient. The apparent reflection coefficient from a discontinuous gradient will easily exceed 10^{-3} . If it were real, this reflection would be recorded on an ionogram. The problem of apparent reflections from discontinuous electron-density gradients has often been overlooked in the past in studies of reflection coefficients. For example, the conclusion of Reddy [1968] that gradient reflection is an important source of partial reflections from sporadic-*E* layers is based on apparent reflections from the two gradient discontinuities in the electron-density profile used.

When actual electron-density profiles are used, it is usually impossible to begin and end the integration through the layer at altitudes where the gradient is zero. In this study, the end points were carefully chosen to minimize this effect. Reflections from the two discontinuities interfere destructively and constructively. The result is that the reflection coefficient becomes periodic as a function of incident frequency, with the maxima giving a measure of the magnitude of the error introduced into the reflection coefficient. This periodicity makes for easy recognition, as can be seen in Figures 3.6, 3.7, and 3.8.

3.4.3 Results of reflection coefficient analysis. A number of sporadic-*E* profiles have been measured by rocket probes. It is estimated that, excluding flights with the specific purpose of studying sporadic *E*, 50% of the daylight rocket launches and virtually all of the nighttime launches in the Aeronomy Laboratory program have shown sporadic-*E* layers [Smith and Mechtly, 1972]. Four daytime profiles and one nighttime profile

have been selected for analysis of reflection coefficients.

The first daytime profile is shown in Figure 3.10 together with the fitted curve used in the full-wave analysis. The circumstances of the layer are described by *Smith and Mechtly* [1972]. Ionograms recorded during the launch at noon (EST) on 24 July 1968, showed $f_b E_s$ to be 6.70 MHz and $f_t E_s$ to be 7.65 MHz.

The reflection and transmission coefficients calculated from this profile are plotted in Figure 3.11. No echoes attributable to gradient reflections would be expected on the ionogram. The difference in frequency of $f_b E_s$ and $f_t E_s$ in this case (0.94 MHz) is accounted for by the different reflection frequencies of the ordinary and extraordinary waves. The calculated difference, based on the difference between the frequency at which ${}_x R_x$ becomes less than 10^{-3} and the peak plasma frequency of the layer, is 0.90 MHz.

The second daytime profile is shown in Figure 3.12, again with the fitted curve used in the analysis. For this layer, at 11:00 EST on 16 July 1970, $f_b E_s$ was 5.35 MHz and $f_t E_s$ was 10.70 MHz, a difference of 5.35 MHz, much greater than in the previous case. The calculated reflection and transmission coefficients are shown in Figure 3.13. The blanketing frequency agrees well with the reflection of the ordinary wave. The gradient of the lower boundary of this layer is rather steeper than the previous case and, indeed, stronger gradient reflections can be noted. At $|R| = 10^{-3}$, the limit of sensitivity of the ionosonde, the expected difference in $f_b E_s$ and $f_t E_s$ is 1.39 MHz, greater than for the previous example, but not large enough to account for the observations.

Sporadic-E layers are almost always present at night. *Keddy* [1968] reports a tendency for the difference between $f_b E_s$ and $f_t E_s$ to be greater at night than in the day. In most instances nighttime sporadic-E layers are

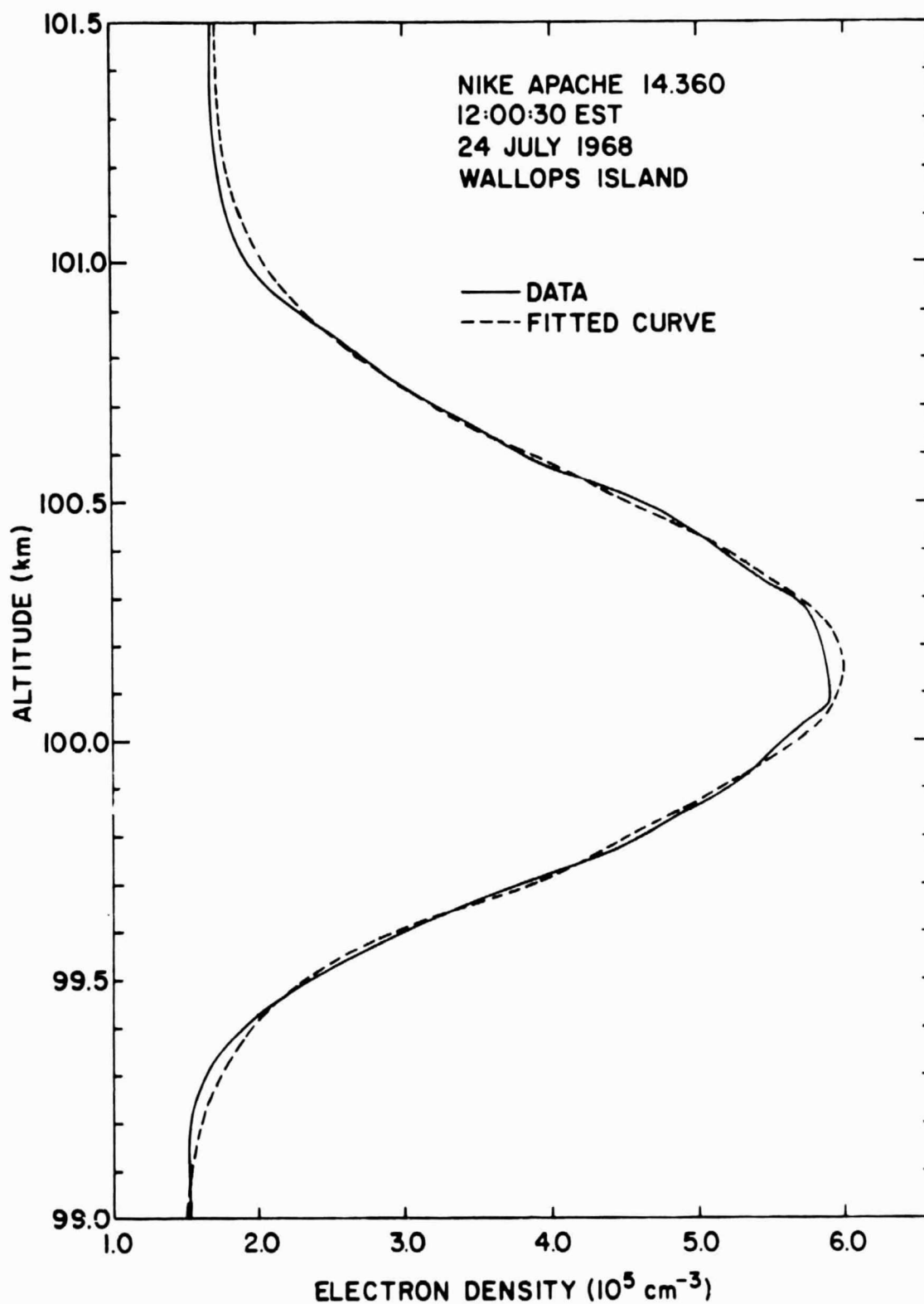


Figure 3.10 Electron-density profile of sporadic-E layer observed at Wallops Island, 24 July 1968. The fitted curve used in the analysis is the dashed profile.

24 JULY 1968

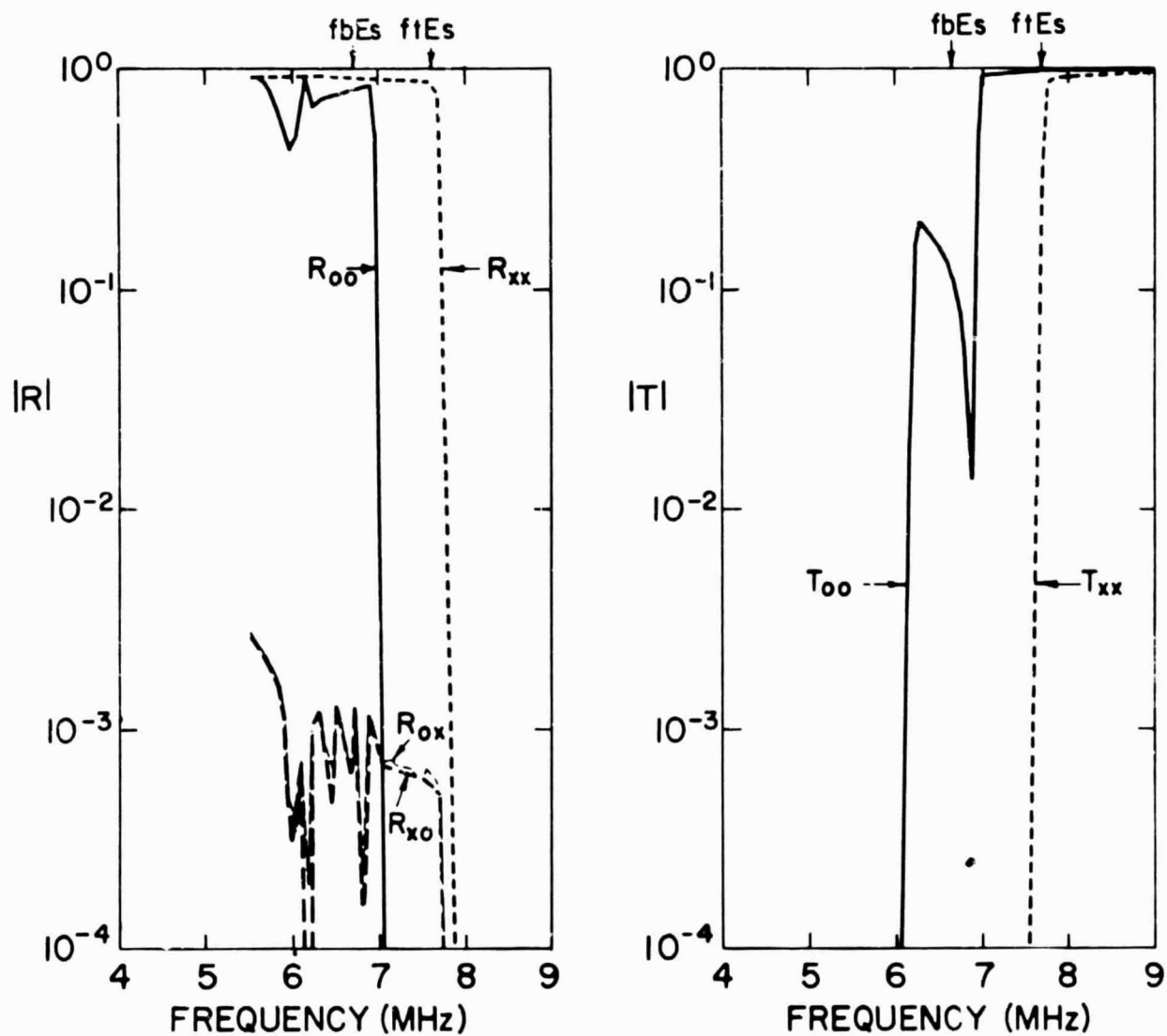


Figure 3.11 Reflection and transmission coefficients of sporadic-F layer, 24 July 1968.

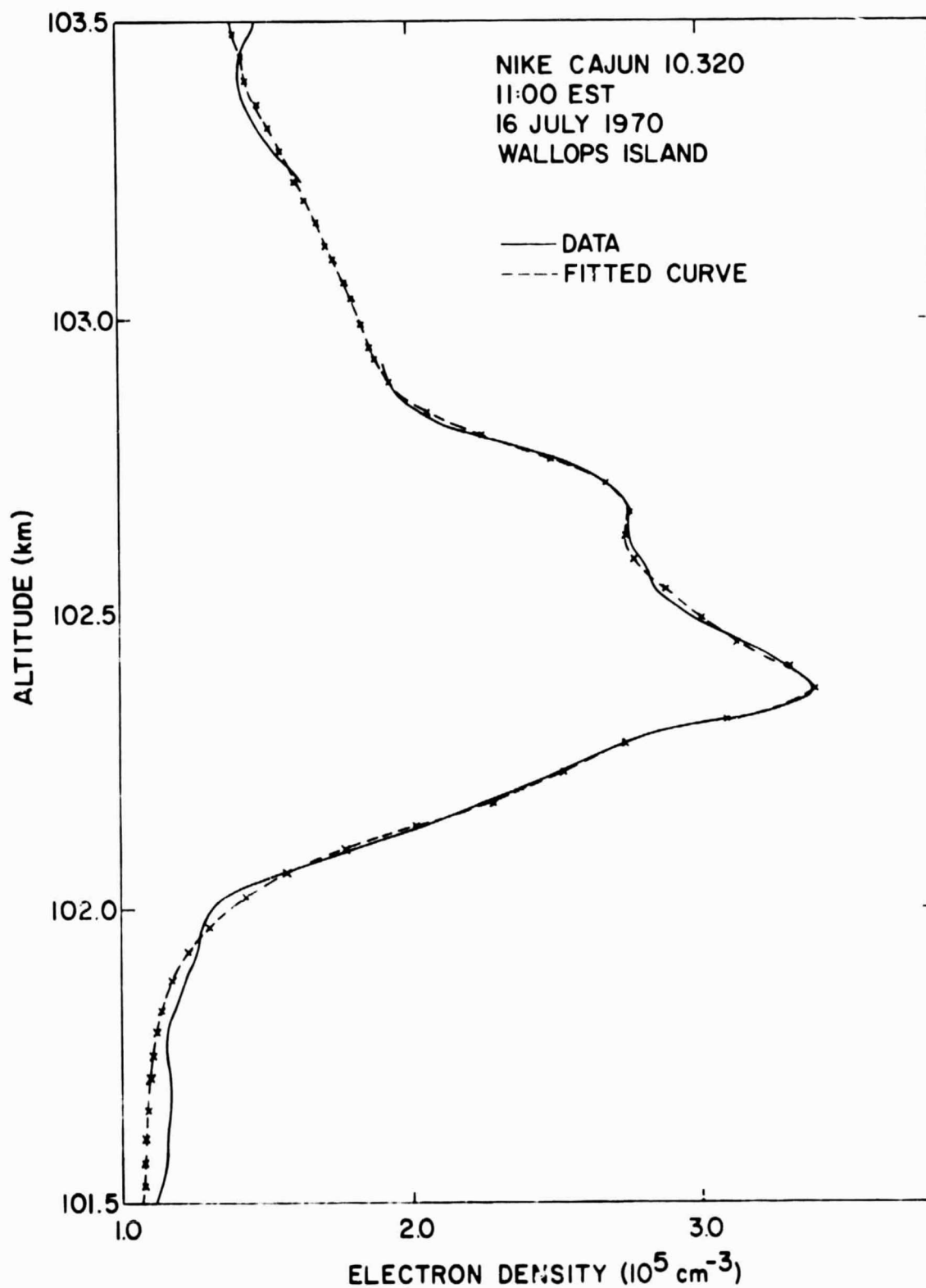


Figure 3.12 Electron-density profile of sporadic-E layer observed at Wallops Island, 16 July 1970, with the fitted curve used in the analysis.

16 JULY 1970

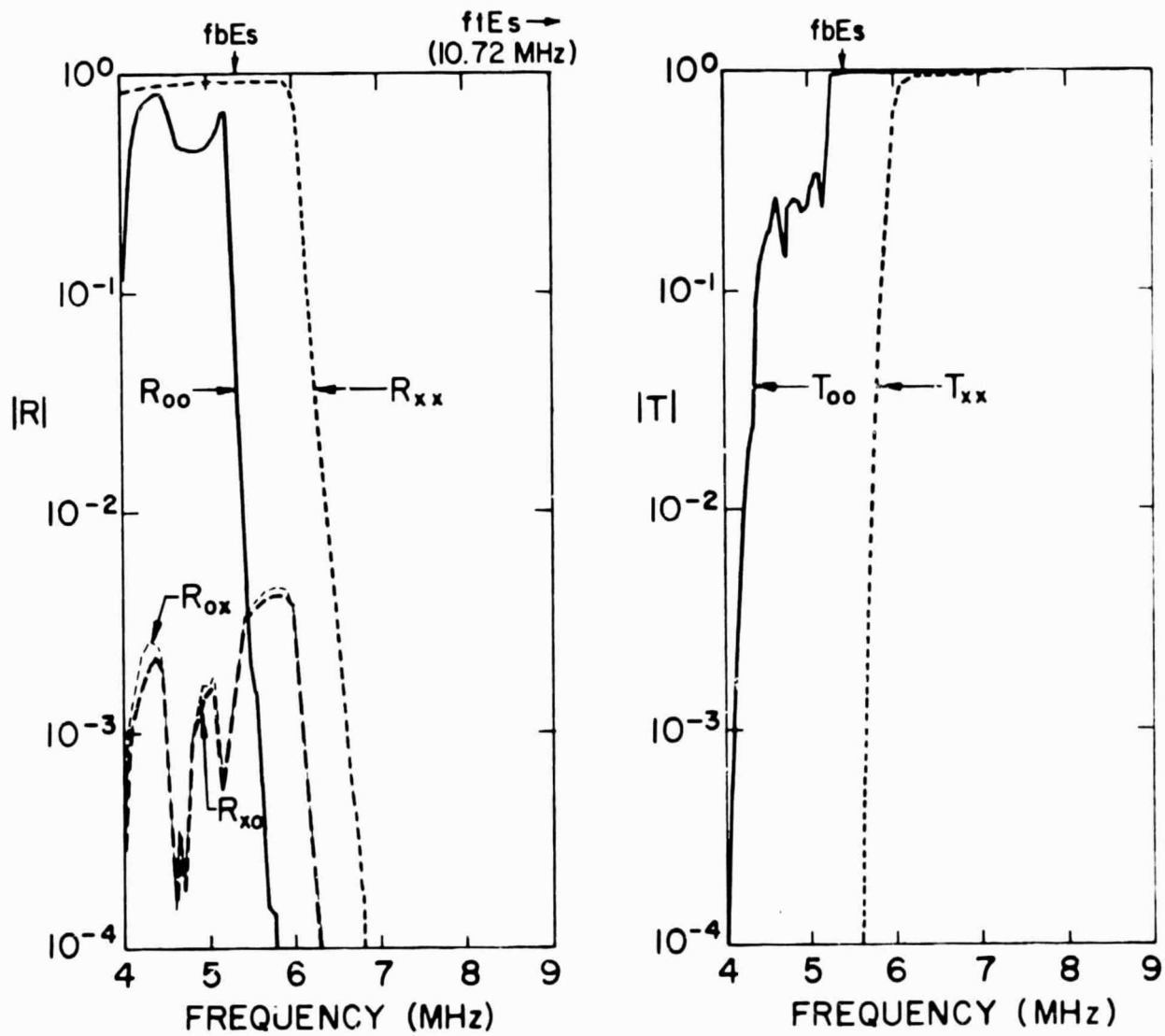


Figure 3.13 Reflection and transmission coefficients of sporadic-E layer, 16 July 1970.

thinner than daytime layers and have a lower peak electron density. The electron-density profile of a particularly intense nighttime layer is shown in Figure 3.14, again with the mathematical function used in the analysis. Its reflection and transmission coefficients are plotted in Figure 3.15. In this case $f_b E_s$ was 1.7 MHz and $f_t E_s$ was 4.6 MHz. Again, the top frequency of reflection cannot be explained on the basis of gradient reflections, the calculated value of $f_t E_s - f_b E_s$ being 1.07 MHz.

Two rocket launches have been made during this study of the partial transparency of sporadic-E layers. The first was launched on 3 August 1973 into an intense sporadic-E layer when the range of partial transparency was small: $f_b E_s$ was 5.5 MHz and $f_t E_s$ was 6.3 MHz. At the time of the second launch, on 10 August 1973, partial transparency was detected over a large range of frequencies: $f_b E_s$ was 4.0 MHz and $f_t E_s$ was 8.0 MHz. Ionograms recorded at the times of the two launches were shown in Figure 1.2.

The electron-density profiles of these two layers are plotted together in Figure 3.16 together with the fitted curves. Initially the difference between the electron-density gradients in the two profiles encouraged the idea that the partial transparency results from gradient reflection. However, calculation of the reflection coefficients of the layers show that this is not the case. The reflection and transmission coefficients of the August 3 layer are shown in Figure 3.17, and of the August 10 layer in Figure 3.18. They appear to be very similar. In neither case can either $f_t E_s$ or $f_b E_s$ be explained on the basis of reflection coefficients. In the case of the layer observed on 3 August 1973, the value of $f_t E_s - f_b E_s$ based on the full-wave analysis is 0.95 MHz; while, for the 10 August 1973, it is 0.97 MHz.

The lack of exact coincidence between $f_t E_s$ and the peak plasma frequency of the layers studies here is probably the result of the measurements being

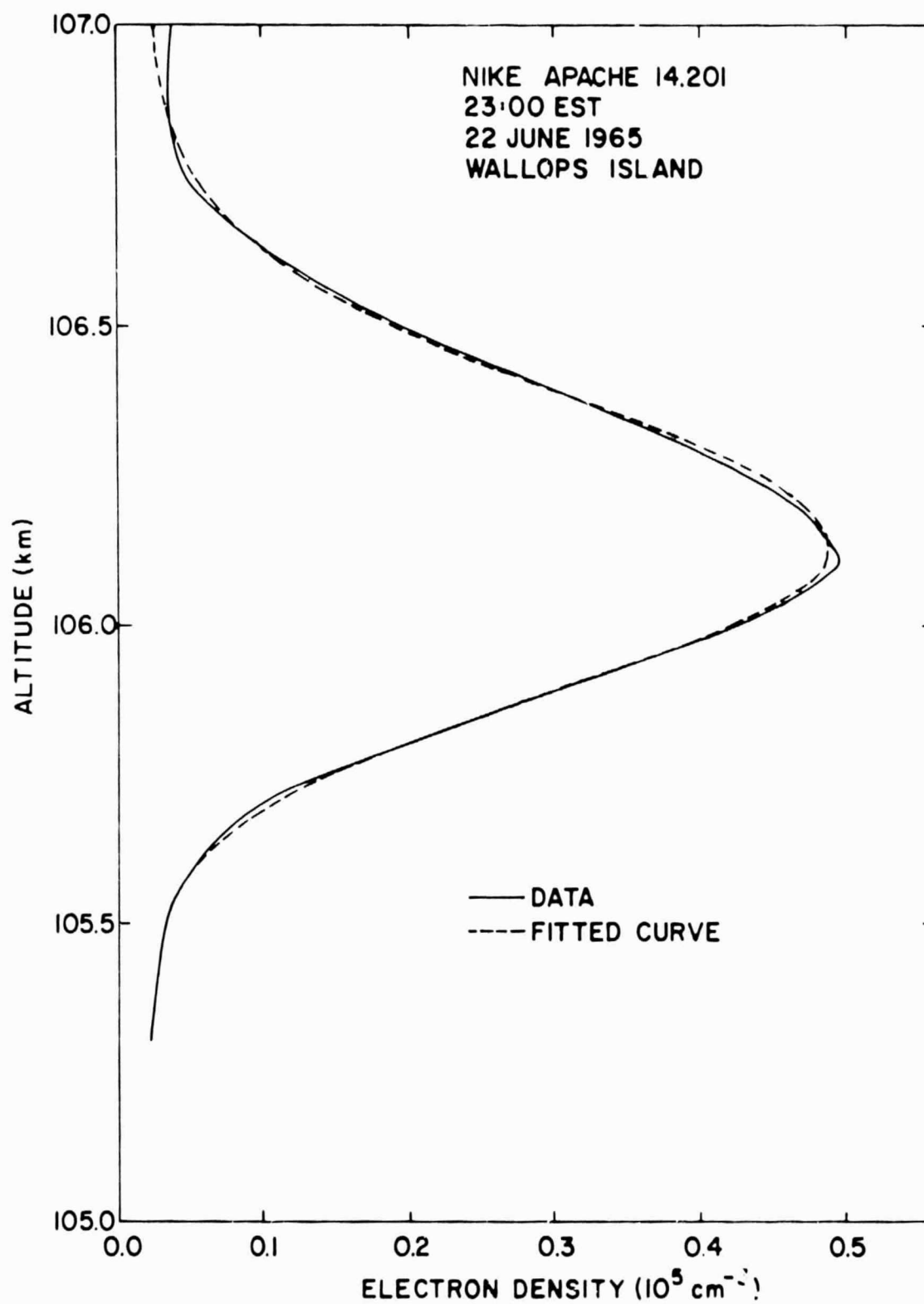


Figure 3.14 Electron-density profile of a nighttime sporadic-E layer observed at Wallops Island, 22 June 1965, with the fitted curve used in the analysis.

22 JUNE 1965

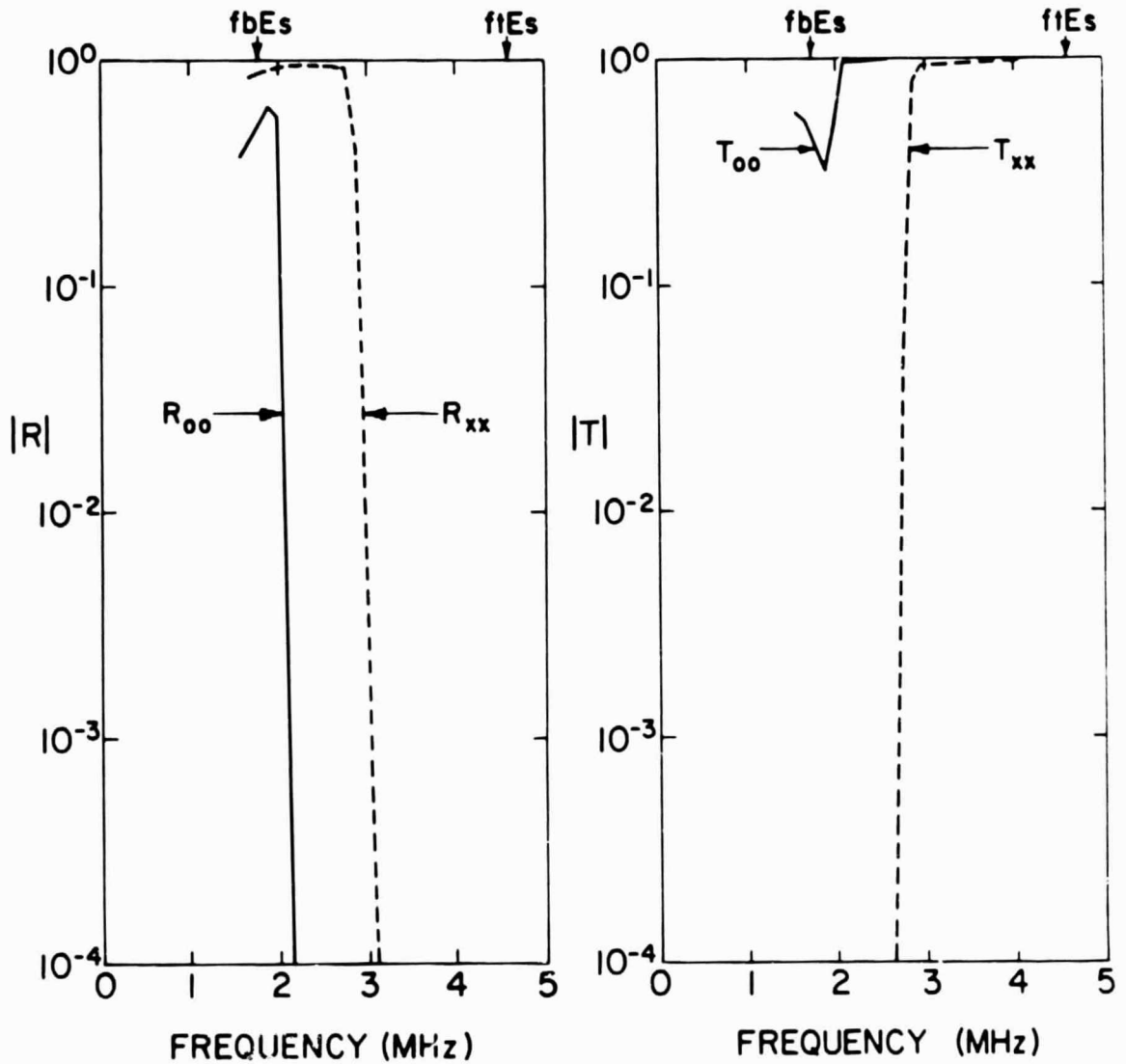


Figure 3.15 Reflection and transmission coefficients of sporadic-E layer, 22 June 1965.

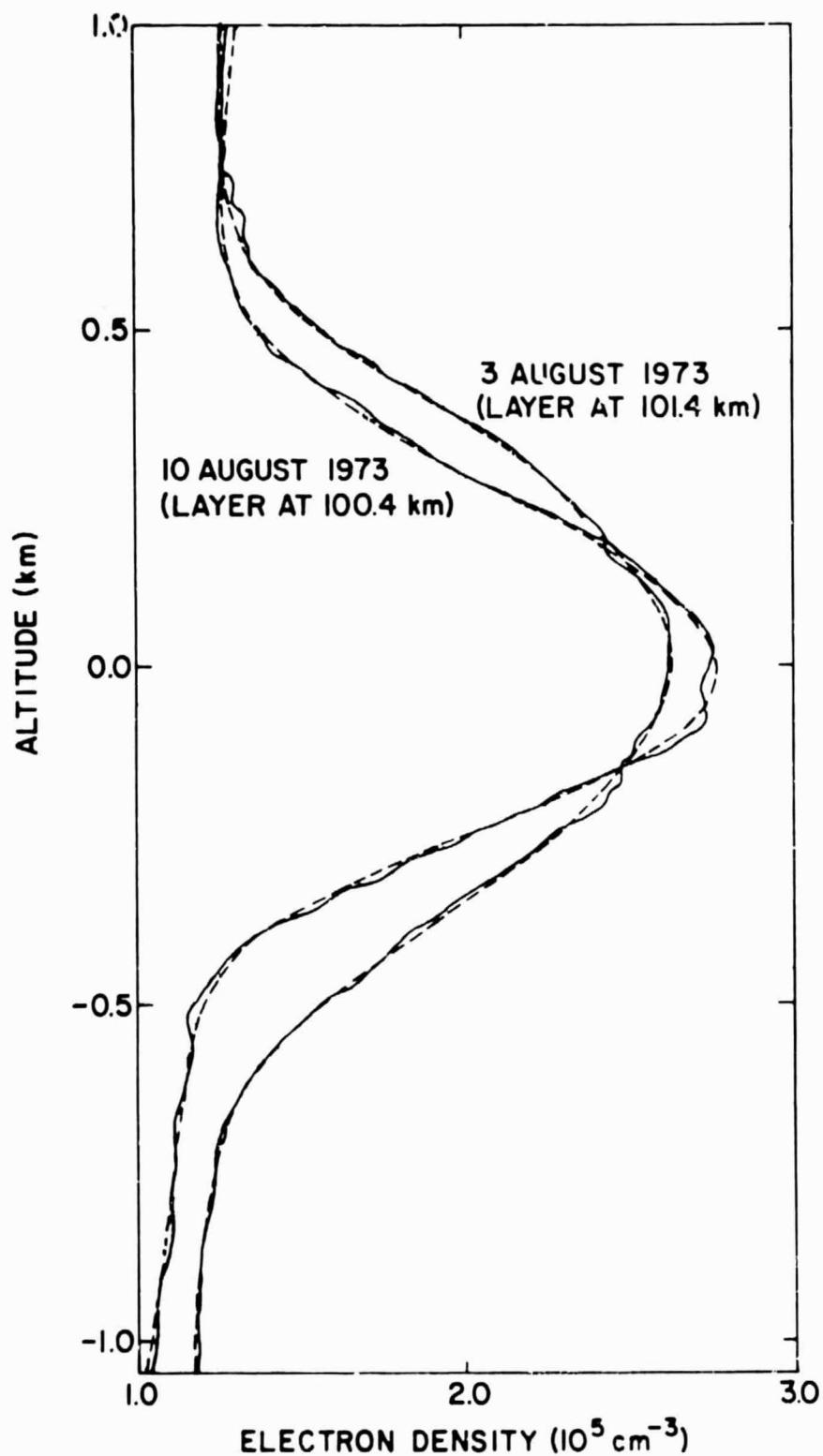


Figure 3.16 Electron-density profiles of two sporadic-E layers observed at Wallops Island, 3 August 1973 and 10 August 1973, with the fitted curves used in the analysis. Altitude scale is relative to the center of each layer.

3 AUGUST 1973

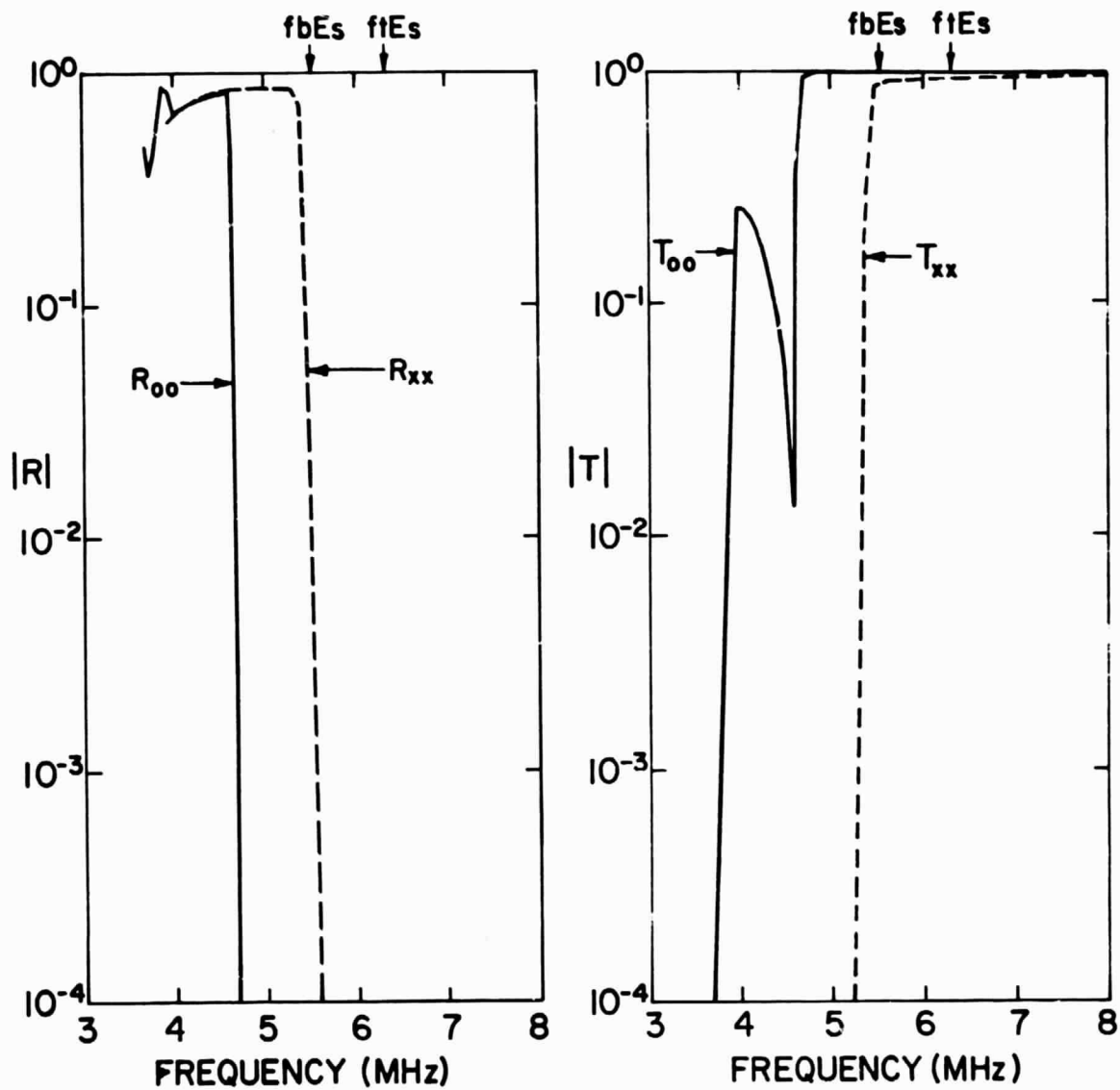


Figure 3.17 Reflection and transmission coefficients of sporadic-E layer, 3 August 1973.

C-2

10 AUGUST 1973

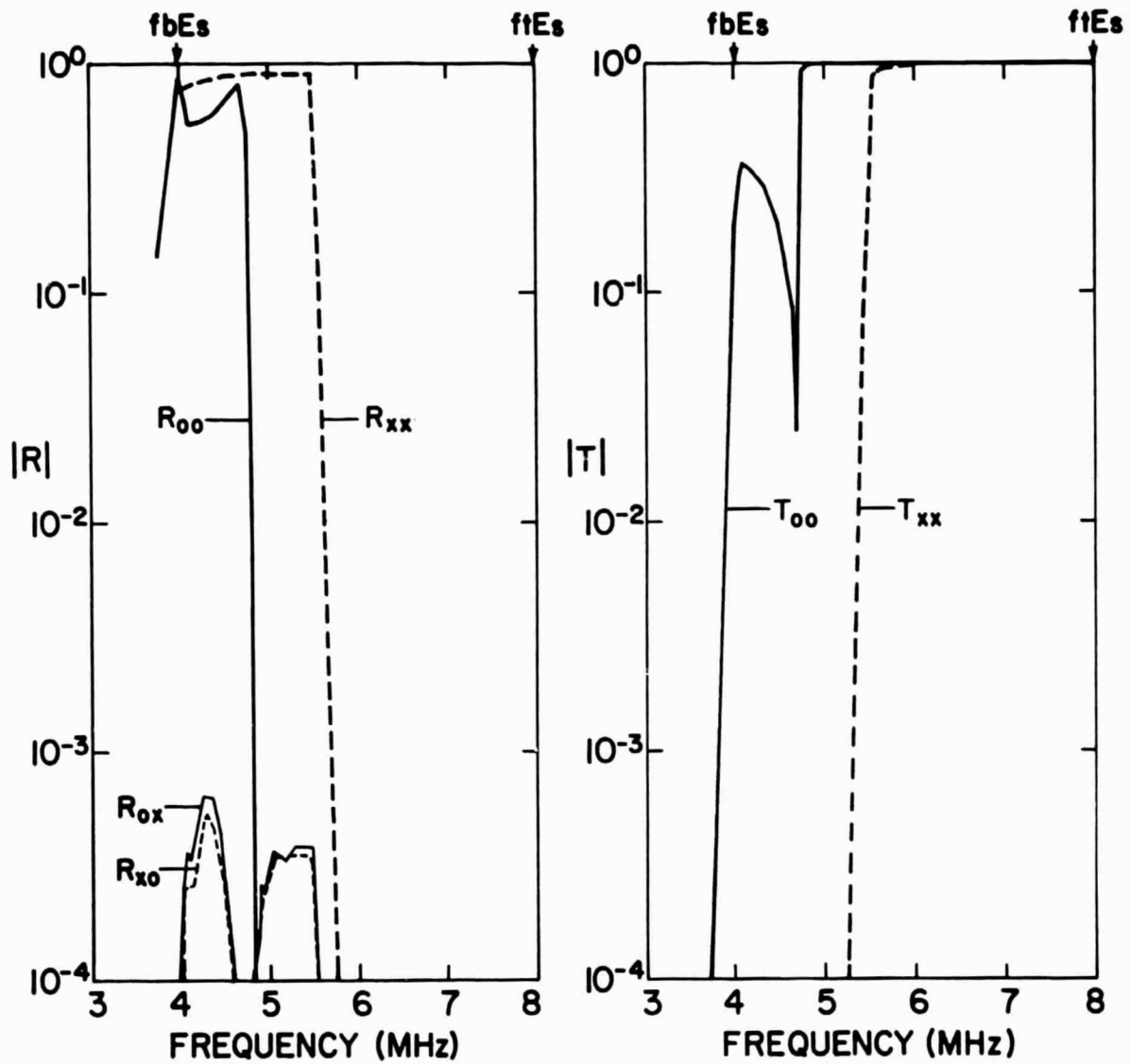


Figure 3.18 Reflection and transmission coefficients of sporadic-E layer, 10 August 1973.

made at different locations. The F region echo from which f^oE_s is determined is reflected in the first Fresnel zone at the F region. At an altitude of 300 km, the first Fresnel zone has a diameter of 8.5 km. Thus the radiation reflecting from the F region and detected at the ionosonde illuminates a circular section of the sporadic- E layer which is only approximately 2.8 km in diameter. The conditions in this small region may be quite different from the conditions along the path of the rocket, which is typically separated by a distance on the order of 100 km. *Smith and Mechtly* [1972] also note cases in which simultaneous comparisons give disagreement, yet which can be reconciled by geographic considerations.

The reflection coefficients of sporadic- E layers described in this section present convincing evidence that the partial transparency over a range of frequency greater than 1 MHz cannot be explained on the basis of gradient reflection. Although there is a small dependence on electron-density gradient, it is insufficient to account for the characteristics of the reflection from the layers studied.

4. OBSERVATION OF SPORADIC-*E* LAYERS BY INCOHERENT-SCATTER RADAR

4.1 *Introduction*

The previous chapter dealt with the possibility of gradient reflections being observed from sporadic-*E* layers. It was shown that the range of frequencies at which observed gradients of sporadic-*E* layers partially reflect radio waves is too small to account for the large differences between $f_b E_s$ and $f_t E_s$ that have been observed.

According to a second model, partially transparent sporadic-*E* echoes are the result of reflections from regions of high electron density scattered throughout the horizontal plane of the layer. Measurements by radio reflection have been interpreted to show the existence of irregular structure in sporadic-*E* layers, but the implied structure has never been directly observed.

Recent developments in incoherent-scatter radar have led to an increased resolution in range which now makes it possible to make effective measurements of sporadic-*E* layers. With the use of pulse-compression techniques, a resolution of 600 m in range is now being achieved; the thickness of a sporadic-*E* layer is generally between one and three kilometers.

In this chapter, experiments will be described which exploit the technique of incoherent-scatter radar in the investigation of sporadic-*E* layers. The observations were taken during January, 1974, and July, 1975, at the Arecibo Observatory located in Puerto Rico. In one type of experiment, pulse compression techniques were used to gain the best possible space and time resolution of sporadic-*E* ionization. It will be shown that small regions of enhanced electron density do indeed exist at times in sporadic-*E* layers,

providing an explanation of the partial transparency of the sporadic-E echoes observed simultaneously by the local ionosonde.

In the other experiment ion drift velocities were measured by a multiple-pulse technique. These data, in addition to indicating the motion of the layer, also allow investigation of the mechanism of formation of the layer.

The main features of the observations are presented in this chapter. Their interpretation in terms of current theories of sporadic-E layers is considered in the subsequent chapter.

A preliminary account of the experiments of January 1974 has been given by *Miller and Smith* [1975]. The material of that paper is included, properly identified, in this chapter.

4.2 *Incoherent Scatter*

4.2.1 *Introduction.* The development of high-power radar in the past three decades has enabled the scattering of radio waves from the ionosphere to become a powerful tool in the study of the atmosphere. The technique known as incoherent scatter provides the ability to measure continuously such atmospheric quantities as electron density, electron and ion temperatures, ion composition, and ion velocities.

The rapid advance of radar technology during and immediately following World War II lead to the active study of scattering of radio waves by the lower ionosphere. The first efforts had the purpose of either reducing interference on military radars or developing long-range communication systems [*Booker and Gordon*, 1950; *Bowles*, 1964]. *Gordon* [1958] proposed that radar technology was sufficiently advanced that incoherent backscatter could be detected from free electrons in the ionosphere. The first incoherent-scatter measurement was made in the same year by *Bowles* [1958]

at Long Branch, Illinois, using a 41-MHz radar. A review of the present status of incoherent scatter is presented by *Evans* [1975].

4.2.2 *Scattering of radio waves.* Incoherent scatter is used at frequencies much greater than the plasma frequency of the ionosphere. The radio waves are scattered by variations in the permittivity caused by random fluctuations in the electron density. The scattered power received at the ground from incoherent scatter is shown by *Evans* [1969] to be

$$P_s = \frac{C n \sigma}{R^2} \quad (4.1)$$

where R is the range from the receiver to the region where the radiation is scattered, n is the electron density of the scattering medium, and C is a constant which is dependent on various parameters associated with the radar itself. The scattering cross section, σ , is given by

$$\sigma = \frac{\sigma_e}{(1+\alpha^2) [1+(T_e/T_i)+\alpha^2]} \quad (4.2)$$

where $\alpha = 4\pi D/\lambda$, D is the Debye length, and the ratio of electron temperature to ion temperature, T_e/T_i , is less than about 3. The radar cross section of an electron, σ_e , is equal to $4\pi r_e^2$, where r_e is the classical electron radius. In practice, the power received is usually separated into range gates of length corresponding to the pulse length, and converted to electron density by calibrating it with the peak electron density of the F region, as measured by an ionosonde.

The power received also contains an undesired noise component, P_N . The signal-to-noise ratio, P_S/P_N , is only of the order of unity in most incoherent-scatter experiments. To improve the accuracy of the power measurement, a series of measurements are integrated [*Evans and Loewenthal*, 1964]. The noise power can be estimated by measuring the power at a number (m) of

time delays from which no incoherent-scatter echo is expected,

$$\bar{P}_N = \frac{1}{m} \sum_{i=1}^m P_i \quad (4.3)$$

This is then subtracted from the power measured at time delays where signal is expected, giving P_S . The accuracy of the measurement integrated over n sweeps of the radar time base is given by

$$\Delta P_S = \pm [(\Delta P)^2 + (\Delta \bar{P}_N)^2]^{\frac{1}{2}} \quad (4.4)$$

where

$$\Delta P = \pm \frac{P_S + P_N}{n^{\frac{1}{2}}} \quad (4.5)$$

$$\Delta \bar{P}_N = \pm \frac{\bar{P}_N}{(nm)^{\frac{1}{2}}} \quad (4.6)$$

Information can be deduced on electron and ion temperatures and ion composition from the shape of the frequency spectrum of scattered radiation [Ratcliffe, 1972; Evans, 1969]. The scattering of radiation is strongly controlled by fluctuations with wave number equal to twice the wave number of the incident radiation. Two types of longitudinal waves are mainly responsible for the scattering: ion-acoustic waves and electron plasma waves. Features in the spectrum of the returned signal can be identified with each type.

For the incident wavelengths much longer than the Debye length used in incoherent-scatter measurements the contribution of the ion-acoustic waves is centered at the incident frequency, with maxima Doppler shifted to greater and lower frequencies by the mean speeds of the ions. An ion-acoustic wave of length Λ has a frequency of [Ratcliffe, 1972]

$$\Omega = \frac{2\pi\nu_i}{\Lambda} [1 + (T_e/T_i)]^{\frac{1}{2}} \quad (4.7)$$

For thermal ion velocities of

$$v_i = \left[\frac{k_B T_i}{m_i} \right]^{1/2} \quad (4.8)$$

the Doppler shift of the backscattered signal is

$$\Omega = \frac{4\pi}{\lambda} \left[\frac{k_B T_i [1 + (T_e/T_i)]}{m_i} \right]^{1/2} \quad (4.9)$$

where k_B is Boltzmann's constant and m_i is the ionic mass.

The component in the incoherent-scatter spectrum due to electron plasma waves, has its frequency shifted by the plasma frequency, regardless of the incident wavelength. This component is called the plasma line, and has been used in measurements of electron density.

An example of the scattered-power spectrum, adapted from Hagfors [1961], is shown in Figure 4.1. The shape of the spectrum is determined by the quantities T_i , T_e/T_i , and m_i [Evans, 1969]. By assuming a value for one of the quantities, the other two can be determined by comparing the shape of the measured spectrum with theoretical spectra.

The velocity of the ionization, if there is no net electric current, shifts the entire spectrum by

$$\Delta f_d = \frac{2v_d}{\lambda} \quad (4.10)$$

where v_d is the component of the ionization velocity toward the radar. If there is motion of the electrons with respect to the ions, the spectrum becomes asymmetric [Evans, 1969]. This effect is important in equatorial and auroral regions, but is not significant at midlatitudes.

4.2.3 *Autocorrelation analysis.* In incoherent-scatter observations, it is more often the practice to measure the autocorrelation function of the signal than the frequency spectrum [Farley, 1969]. Autocorrelation

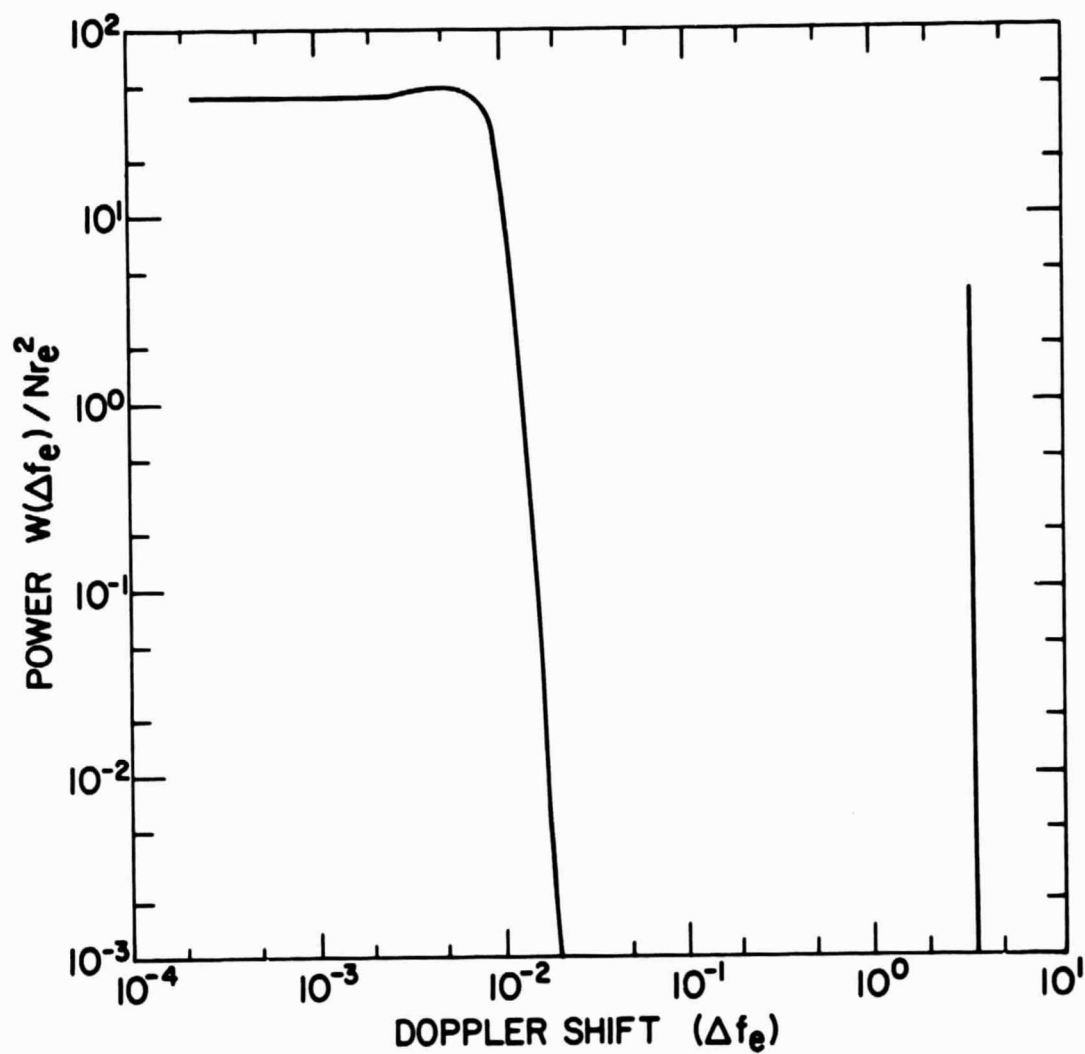


Figure 4.1 Incoherent-scatter power spectrum for O^+ ions where the wavelength of the incident radiation is much greater than the Debye length. The spectrum is shown only for positive Doppler shifts [after Hagfors, 1961].

functions are measured by transmitting a series of pulses, either as a pair separated by a varying multiple of a time delay, τ , or as a sequence of unevenly-spaced pulses from which different combinations give different time delays. The autocorrelation function is then constructed as

$$R(z, t) = \frac{\langle V(z, t) V^*(z, t + \tau) \rangle}{\langle |V(z, t)|^2 \rangle} \quad (4.11)$$

where $V(z, t)$ is the complex signal (i.e. amplitude and phase information) received from a range z at time t .

As in the case of the frequency spectrum, the shape of the autocorrelation function contains information on the several ionospheric properties (Figure 4.2). The time delay for the first zero-crossing in the autocorrelation function is less for higher ion temperatures or lighter ions. The shape of the curve is affected by the electron-ion temperature ratio, ion-neutral collisions, and the magnetic field. If there is either a net plasma drift or an electric current, the frequency spectrum is asymmetric and the autocorrelation function is complex.

After the autocorrelation function is measured, it is compared with theoretical autocorrelation functions generated from various combinations of physical quantities [Farley, 1969; Zamlutti and Farley, 1975].

The main advantage in measuring the autocorrelation function rather than the frequency spectrum is that the required accuracy can be attained using a shorter pulse. The increased height resolution resulting from the shorter pulse is gained at the expense of time resolution. Since the frequency spectrum can be obtained by a Fourier transform of the autocorrelation function, information of atmospheric properties is not lost by the use of this technique.

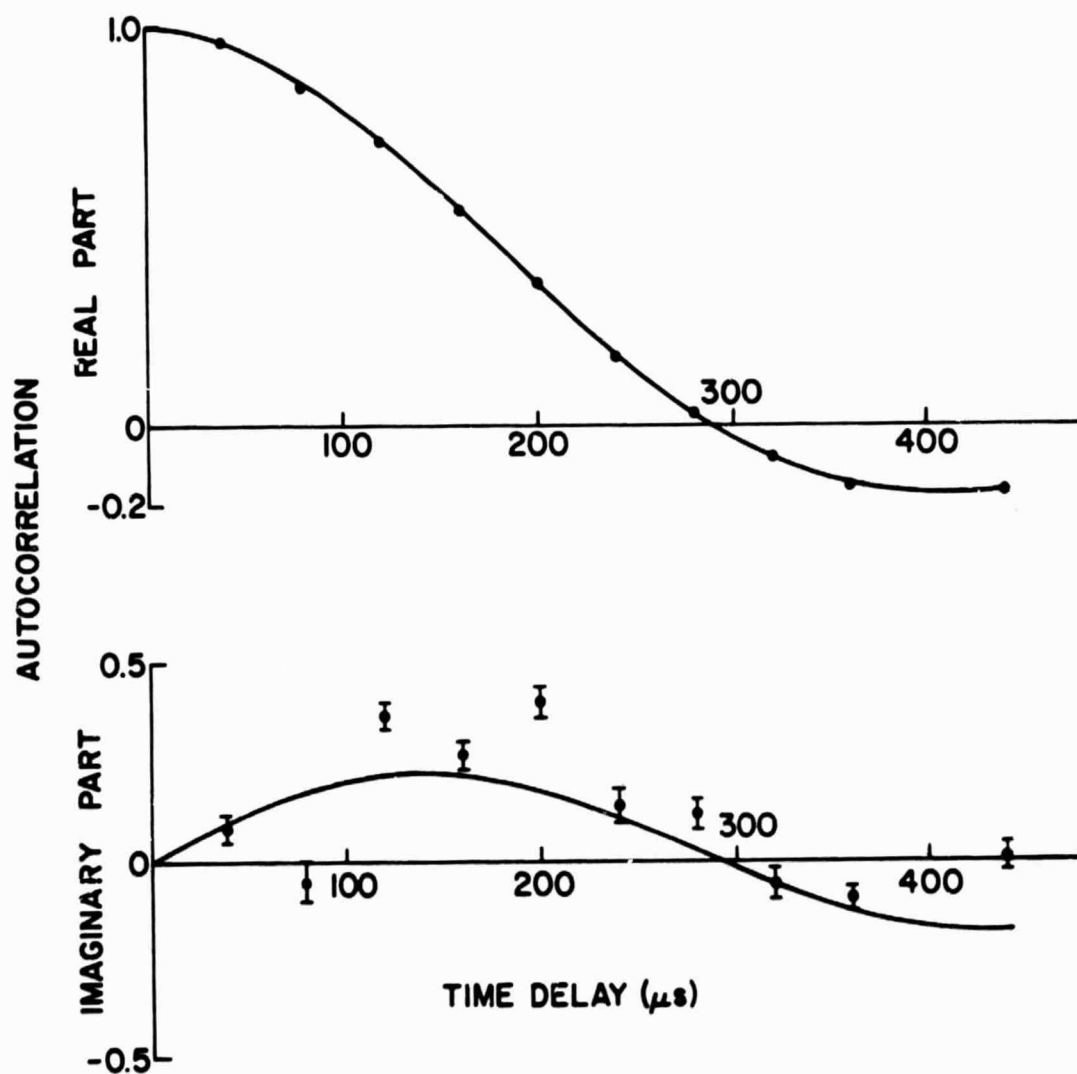


Figure 4.2 Real and imaginary autocorrelation functions measured using the five-pulse technique with a 30-min integration time and a 16 μs pulse. The solid curves show a fitted theoretical autocorrelation function corresponding to $T_i = 250$ K, $v_{in} = 300$ s $^{-1}$, and a radial drift velocity of 14 m s $^{-1}$ away from the radar [Zanlutti and Farley, 1975].

4.2.4 *Pulse compression.* Another method of increasing height resolution without increasing transmitted power is known as pulse compression. Although this technique has been used in radio astronomy for several years, it has only recently been used successfully in incoherent scatter measurement [Ioannidis and Farley, 1972]. It is through the development of pulse-compression capabilities at the Arecibo Observatory that the height resolution was increased to the point where sporadic-E layers could be effectively studied.

Using pulse compression, segments of a transmitted pulse are reversed in phase in such a way that the resulting frequency spectrum resembles that of a much shorter pulse. When the scattered pulse is received and decoded it is approximately the same as would be received from a short pulse with the energy of the complete long pulse that was transmitted [Gray and Farley, 1973].

At Arecibo a 13-bit Barker-coded pulse is used, shown with its autocorrelation function in Figure 4.3. The autocorrelation functions of Barker codes are characterized by uniform side lobes and a central maximum with an amplitude n times greater than the amplitude of the side lobes, where n is the number of bits in the code.

A phase-coded pulse, $b(t)$, after being scattered by a thin slab in the ionosphere and received at the ground, can be represented by $b(t)f(t)$ [Gray and Farley, 1973]. When the signal is received it is cross-correlated with a replica of the transmitted pulse, so that the final signal can be written as

$$G(t) = \int_{-\infty}^{\infty} b(t_1)f(t_1)b(t_1-t)dt_1 \quad (4.12)$$

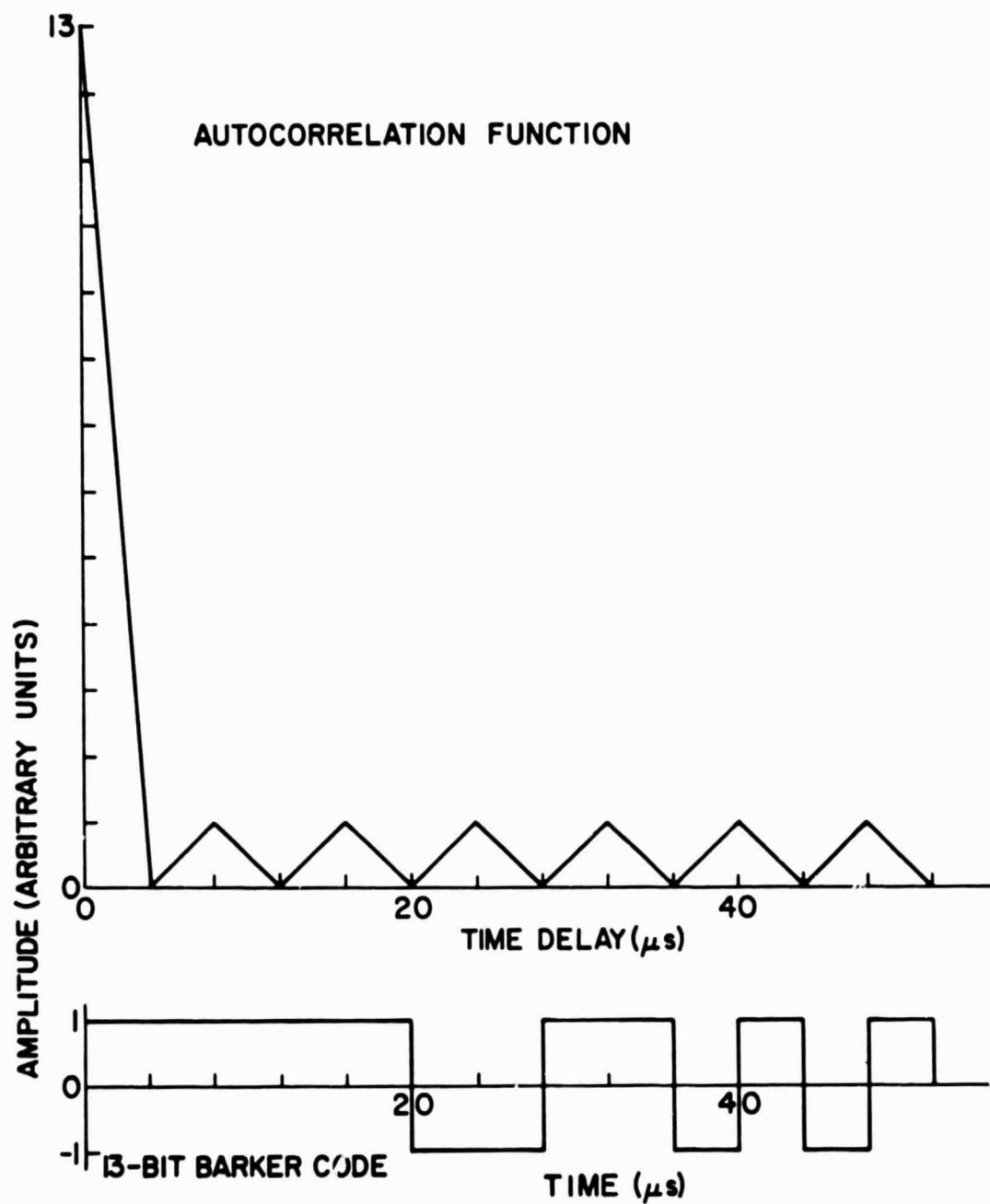


Figure 4.3 The 13-bit Barker code and its autocorrelation function.

Then the ensemble average of the power is

$$\langle |G(t)|^2 \rangle = \int_{-\infty}^{\infty} \int_{-\infty}^{\infty} b(t)b(t_2) \langle f(t_1)f^*(t_2) \rangle b(t_1-t)b(t_2-t) dt_1 dt_2 \quad (4.13)$$

If $t_1 - \tau$ is substituted for t_2 , $\langle f(t_1)f^*(t_2) \rangle$ becomes the autocorrelation function of the scattering medium, equation (4.11). Since the autocorrelation term at $\tau = 0$ is proportional to the electron density, equation (4.13) can be written

$$\langle |G(t)|^2 \rangle \propto n \int_{-\infty}^{\infty} R(\tau) F(t, \tau) d\tau \quad (4.14)$$

where

$$F(t, \tau) = \int_{-\infty}^{\infty} b(t_1)b(t_1+\tau)b(t_1-t)b(t_1+\tau-t) dt_1 \quad (4.15)$$

The value of $F(t, \tau)$ is not affected by the characteristics of either the receiver or the scattering medium, but only by the particular pulse compression scheme used.

For perfect correlation, $R(\tau)$ is equal to one and $\langle |G(t)|^2 \rangle$ is proportional to the square of the autocorrelation function of the phase-coded pulse. This is approximately true also for cases where the length of the pulse is small compared with the correlation time of the scattering medium. The power measured at $t = 0$, i.e. the center peak of the autocorrelation function of the pulse, depends only on the total length of the pulse relative to the correlation time of the medium.

One of the limitations in the use of this technique in incoherent scatter is that the phase coherence of the signal is partially lost during scattering. *Gray and Farley [1973]* showed that the loss of phase coherence is not significant as long as the total length of the pulse is less than the

time to the first zero crossing of the autocorrelation function of the scattering medium shown as approximately 300 μ s in Figure 4.2.

A detailed consideration of the measured signal in pulse compression experiments can be found in *Gray and Farley* [1973]. The range variation of $\langle |G(t)|^2 \rangle$ for various values of the ratio of total pulse length to correlation time of the medium is shown in Figure 4.4. The side lobes show the relative influence of echoes from other altitudes on the measurement of electron density. The contribution from other altitudes is not important if the electron density varies slowly on the scale of the altitude resolution. However, in the case of sporadic-E layers the difference in electron density from one altitude measured to the next can be quite significant. The effect is to decrease the apparent peak density of the layer and to increase the apparent density immediately above and below the layer.

This smearing can be seen in an electron-density profile measured in this study that apparently includes a meteor trail, shown in Figure 4.5. As in the above derivation, the only scattering is from a very small altitude region. The positions of the side lobes with respect to the height gates compare with the range variation shown in Figure 4.4. In most sporadic-E layers, the peak electron density does not approach the value relative to the background ionization shown in Figure 4.5, and side lobes are not apparent in the data.

The main effect of the contribution of side lobes to the scattered power is at altitudes immediately above and below the sporadic-E layer. At the peak of the layer, the relative contribution from other altitudes is decreased, with the result that the observed electron density relative to that of the E region is too low by approximately 10 % [*Gray and Farley*, 1973]. The reduction in signal from the sporadic-E layer depends on the thickness

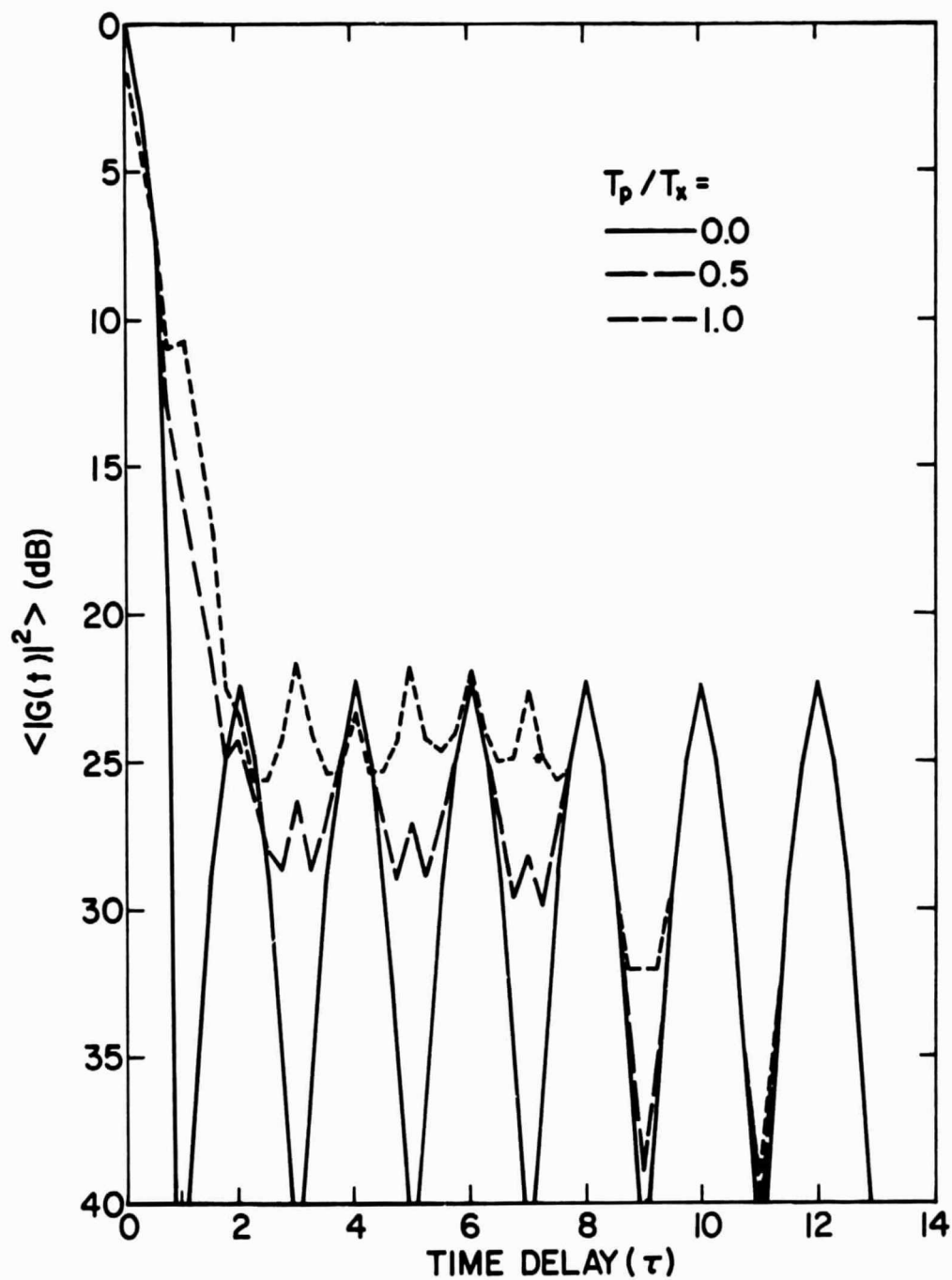


Figure 4.4 The time (range) variation of $\langle |G(t)|^2 \rangle$ in dB below maximum value for the 13-baud Barker code for various T_p/T_x with $T_e/T_i = 1.0$ [Gray and Farley, 1973].

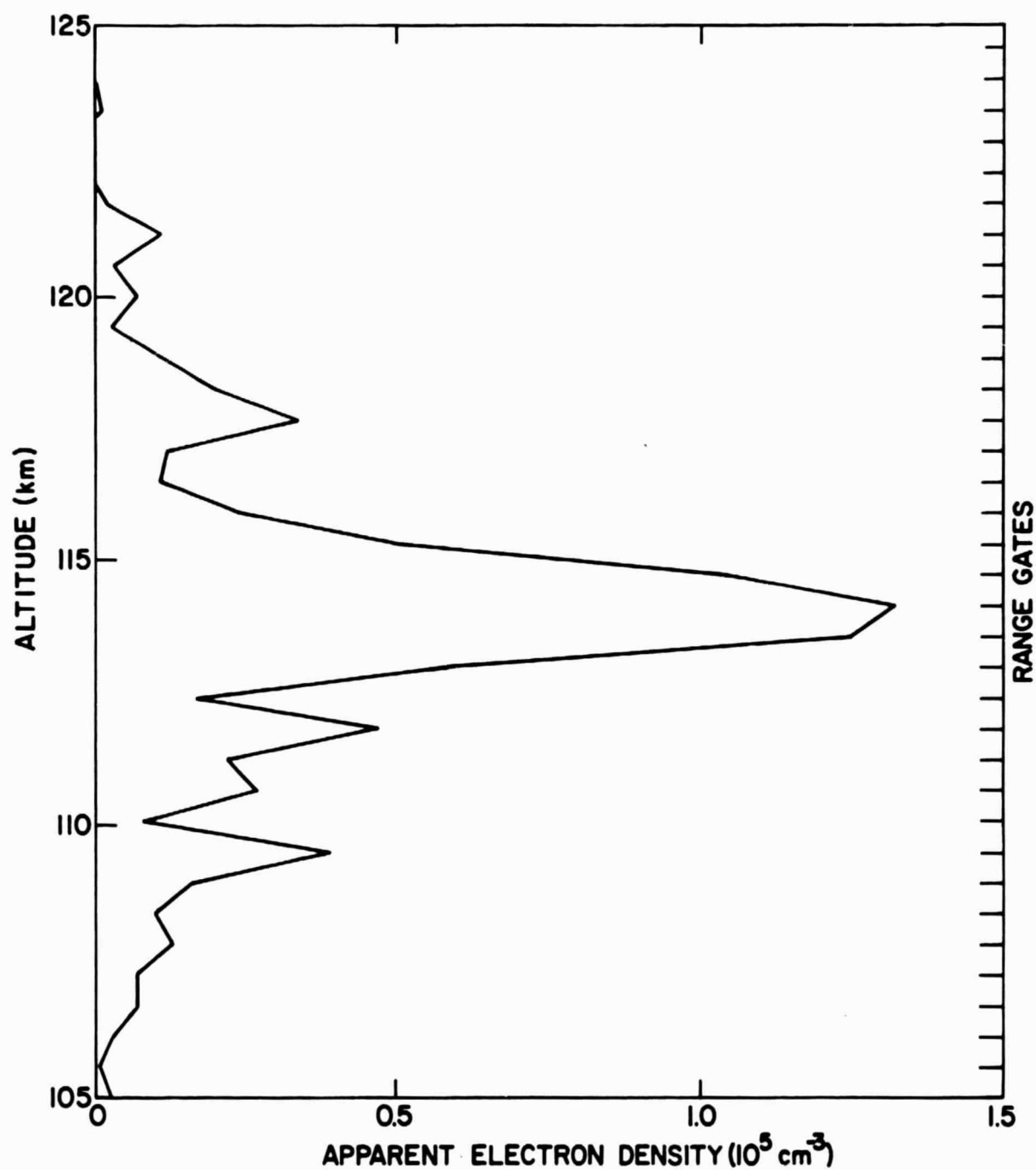


Figure 4.5 The scattered-power profile of a meteor trail. Secondary maxima are artifacts of the pulse-compression technique.

of the layer and its position with respect to the range gates, and can not be determined accurately. For this reason, no correction was made for this effect in the analysis of the data.

The electron-density profile is determined from the received power in the same way as in the single- and multiple-pulse experiments described earlier, with the height resolution being determined by the baud length of the phase-coded pulse instead of by the total pulse length. Theoretically, it would also be possible to measure other atmospheric properties by forming autocorrelation functions from sets of phase-coded pulses. The pulse-compression technique has been used to estimate the concentration of Fe^+ in a sporadic-E layer [Behnke and Vickrey, 1975]. However, more development is needed to extend the technique to other properties.

4.3 *The Arecibo Observatory*

The incoherent-scatter facility used in this study is located at the National Astronomy and Ionosphere Center, 15 km south of Arecibo, Puerto Rico. The geographic coordinates of the observatory are $18^\circ 21'$ North, $66^\circ 45'$ West. It is at a geomagnetic latitude of 30° North. The dip angle of the magnetic field is 50° ; its magnetic declination is $8^\circ 30'$ West.

The antenna system is a fixed spherical reflector below a movable feed. The aperture has a diameter of 305 m and a radius of curvature of 265 m. A 430-MHz transmitter is used in the experiment, giving a beam width of approximately 300 m at an altitude of 100 km. The power output of the transmitter, when pulsed, is 2.5 MW. The maximum average transmitted power in a pulsed mode is 150 kW. The pulse width has a range of from 2 μs to 10 ms, with a pulse repetition period of from 1 ms to 1 s. For all experiments described here, the transmitter is controlled by an on-line digital computer.

The spherical shape of the reflector causes the radiation to be focused into a line. For the 430-MHz transmitter a 30 m-long line feed is used. The feed is a waveguide suspended from a carriage house mounted on a curved track with a radius that coincides with the radius of the reflector. The position of the feed on the curved track determines the zenith angle. This track is suspended from a circular horizontal track, so the line feed can also be moved in azimuth.

The steerability of the radar beam is of major importance to the experiments described here. The maximum slew rate of the beam is about 23 deg min^{-1} in azimuth, and 2.5 deg min^{-1} in elevation. Limits of the feed are 0 to 540 deg in azimuth and 0 to 20 deg in zenith angle. Because of the change in gain when the elevation is changed, the zenith angle of the beam was held constant in each experiment. The feed illuminates the complete surface of the reflector when it is vertical, but at a zenith angle of 20 deg the signal is reduced by about 4 dB. This reduction in signal becomes important only when the zenith angle approaches 20 deg. The gain does not change significantly with azimuth.

When the scattered signal is received, it is first heterodyned to a center frequency of 30 MHz at the receiver located in the carriage house and then sent to the operations building, where further analog processing is accomplished. Depending on the requirements of the experiment this may include decoding and autocorrelation.

The signal is then sampled by analog-to-digital converters, and immediately processed by the computer. Finally, the results, usually in the form of autocorrelation functions or scattered-power profiles, are stored on magnetic tape.

4.4 Experimental Techniques

4.4.1 *Electron density.* Data were taken in the form of scattered-power profiles using a 13-bit Barker-coded pulse with a 4- μ sec baud length [Gray and Farley, 1973]. The power profiles are converted to electron-density profiles by calibration of the radar to the electron density at the peak of the *F* region obtained by the ionosonde. In this calibration the echo power is corrected for the effect of the value of T_e/T_i being different in the *E* and *F* regions. For the set of experiments done in 1974, the value of T_e/T_i in the *F* region is taken from Evans [1967]. In 1975, T_e and T_i were measured in the multi-pulse experiment described above and assumed to have the same variation from one day to the next. In the *E* region adjacent to the sporadic-*E* layer T_e/T_i is assumed to be equal to one.

The data must also be corrected for range effects which include both the decrease in signal strength with the square of the range, and, for *D*- and *E*-region observations, a near-field correction to the gain [Rowe, 1974].

Data were taken on one occasion with the beam held in a vertical position and on other occasions with the beam scanning in azimuth at a fixed zenith angle. The two modes were used to evaluate the potential of the radar for studies of horizontal structure.

The 600-m resolution in range made possible by the Barker coding is important because of the anticipated thinness of the layers. Intense daytime sporadic-*E* layers observed in rocket measurements are typically 1.5 to 3 km in total thickness while layers at night may be 1 km in total thickness [Smith, 1966; Smith and Mechtly, 1972].

The height resolution of 600 m attainable using Barker-coded pulses is not sufficient to determine accurately the peak electron density of a

sporadic-*E* layer. The result is that the peak electron density measured by incoherent scatter is consistently below the density expected, based on ionosonde measurement. Estimates of the effect of this volume averaging were obtained using electron-density profiles of sporadic-*E* layers from rocket-based measurements. This is illustrated in Figure 4.6 by the electron-density profile of a sporadic-*E* layer measured from a sounding rocket on 10 August 1973. To simulate the effect of volume averaging the electron density has been averaged over altitude regions of 600 m, giving approximately the same effect as the incoherent-scatter measurement. The averaging is done for two extreme cases, and a parabolic fit is made to the highest three points. It is seen that, even in the best case where the 600-m gate is exactly centered on the layer, the value of electron density given by incoherent scatter is less than the actual peak electron density. In the four layers examined, the ratio of the peak electron density obtained by the parabolic fit to the true peak electron density of the layers varied from 0.6 to 0.9.

Since the horizontal variation of the electron density is of more importance to this study than the peak electron density of a layer, the problem of smearing the profile by the 600-m resolution in range is not critical. However, two effects of this smearing should be noted. First, if there is a change in the altitude of a layer, the apparent peak density will be affected. This can be seen by comparing the peak densities given by the two averaging configurations in Figure 4.6. The farther the peak of a layer is from the center of a range gate, the smaller the apparent peak electron density will be. Also as *J. D. Whitehead* [personal communication, 1974] has pointed out, regions of small horizontal extent would be unresolved if they fail because of size or position to fill the radar beam

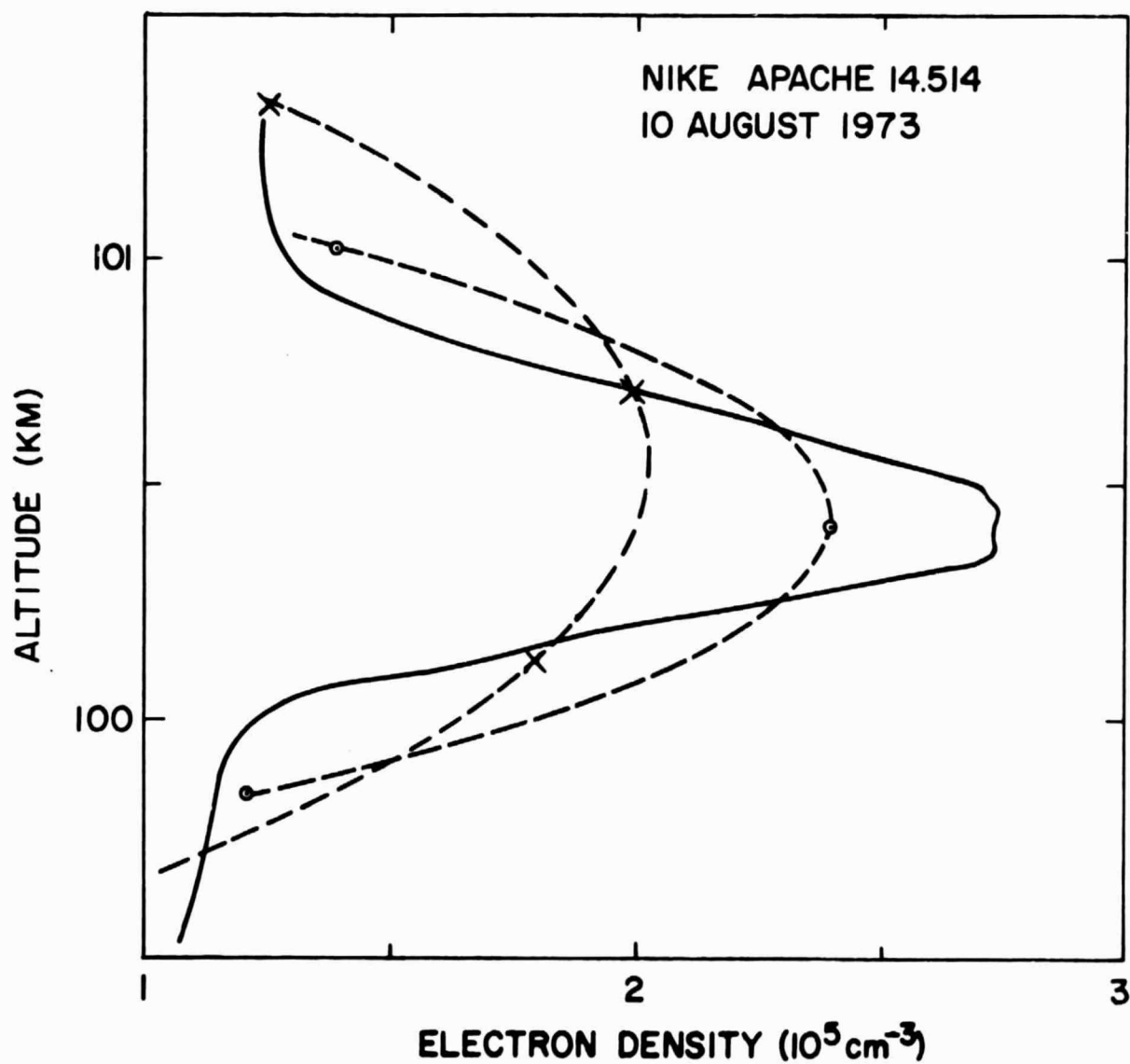


Figure 4.6 Effect of volume averaging of the electron density in 600-m range-gates. Parabolas have been fit to average densities for two cases.

throughout the entire integration time.

Another major difficulty in using the Arecibo Observatory to study sporadic-E by this method is the turn-on time delay of at least 15 min. When the detection of an intense sporadic-E layer by the ionosonde was used as a criterion for making an observation, the transmitter could not in many instances be brought up in time to observe the peak of the event.

4.4.2 *Ion drift velocity.* Ion drift velocities in the altitude region 100 to 167 km were measured by incoherent scatter using a five-pulse technique described by *Zamlutti and Farley* [1975]. Autocorrelation functions are found from a series of five 8- μ s pulses at relative times of 0, 120, 160, 360, and 440 sec. Various combinations of the pulses gave points of the autocorrelation function at intervals of 40 μ s to a maximum time delay of 440 μ s, excluding the point at 400 μ s, Figure 4.2. Above 167 km, a single-pulse experiment with a pulse length of 296 μ s was used.

In order to construct an ion drift velocity vector, measurements were made at three positions of the radar beam. The positions used were at 180, 270, and 0 deg azimuth. The components of the ion velocity can be found from the line-of-sight velocities by

$$v_E = \frac{v_0 + v_{180} - 2v_{270}}{2 \sin \theta} \quad (4.16)$$

$$v_N = \frac{v_0 - v_{180}}{2 \sin \theta} \quad (4.17)$$

$$v_Z = \frac{v_0 + v_{180}}{2 \cos \theta} \quad (4.18)$$

where θ is the zenith angle of the radar beam. For these observations, $\theta = 15$ deg.

The measured autocorrelation functions from each position of the beam are fit by a least-squares method to a library of functions stored in the observatory computer system giving electron and ion temperature, collision frequency, and line-of-sight drift velocities. Error estimates are based on the accuracy of the least-squares fit. Estimated errors in T_e and T_i are of the order of 5%. Drift-velocity errors are typically between 5 and 10 m s^{-1} . Errors were found to become very large for measurements taken in early morning or late evening, when the electron densities are small. No measurements are possible at night.

Scattered-power profiles were measured during the five minutes required to swing the beam through the 90 deg between positions. The measurement used single 8- μs pulses, giving a height resolution of 1.2 km. The profiles were stored on magnetic tape after integrating 300 samples, or every 3.5 sec, for a resolution in azimuth of about 1 deg.

The measurement of winds at sporadic-E altitudes by the method of *Zamlutti and Farley* [1975] is limited by the minimum altitude at which measurements can be made. The correlation time in the E region is of the order of 500 μs . Because of ground clutter, no signal can be used until the echo height of the last pulse of the set is above about 30 km, a time delay of 200 μs . This means that to measure autocorrelation functions with time lags of up to 500 μs the minimum range that can be used is 105 km, representing a time delay of 700 μs . Even with the radar beam at a zenith angle of 15 deg, the minimum altitude is higher than the altitude of occurrence of many sporadic-E layers.

The correlation of wind data with sporadic-E layers was also hampered by the inability to make simultaneous measurements of the electron density and the ion velocities. The electron densities were measured with good

height and time resolution using Barker-coded pulses and short integration times. The ion velocity measurement, on the other hand, used a five-pulse autocorrelation scheme which required long (~15 min) integration times during which no electron-density profiles were recorded. Various combinations of these two experiments were used in an effort to correlate the data. A description of these experiments is given in the following sections.

4.4.3 *Data collection and presentation.* Observations were made at the Arecibo Observatory during two periods: 11-28 January 1974, and 10-27 July 1975. Measurements of electron density using the pulse-compression technique were made in 1974. The same experiment was used again in 1975 together with a multiple-pulse experiment to measure ion drift velocities. Schedules of the two periods of observation, including the general features of the sporadic-E layers, are presented in Table 4.1 for 1974 and Table 4.2 for 1975.

The data-taking program and observational procedures were tested on 11 and 13 January 1974. Problems in recording the noise level in the scattered power were encountered and corrected. It was found that the system used for tracking astronomical objects with the radio telescope could be used to scan the radar in azimuth at a predetermined rate. Controlling the horizontal velocity of the point of intersection of the radar beam and a sporadic-E layer by adjusting the zenith angle of the radar was also considered. However, it was decided that required integration times were sufficiently short that the maximum angular velocity of the radar beam ($\sim 23 \text{ deg min}^{-1}$) at the maximum usable zenith angle was feasible. Considering the reduction in signal of the radar at large zenith angles, and on the advice of the observatory staff, a fixed zenith angle of 15 deg was used. Sporadic-E layers are expected to move with a velocity of the

TABLE 4.1

Observations during January, 1974, at Arecibo, P. R.

Date	Starting Time (AST)	Ending Time (AST)	Zenith Angle of beam (deg)	Speed of beam (deg/min)	Sweep Pattern (Azimuth)	Max f^bEs (MHz)	Max f^tEs (MHz)	Remarks
11	1620	1708	15	18	60°-120°-180°-240°	2.5	3.2	test of procedure
11	1823	1858	8.5	23	180° (Hold)-270°-90°	2.5	3.5	test of procedure
13	1600	1717	15	20	60°-120°	2.5	3.2	test of procedure
13	1719	1743	12	23	360°-540°-180°	0	0	test of procedure
14	1411	1503	12	23	90°-630°-90°-150°	7	9	Scan full circle
17	2006	2215	12	23	60°-120°	1.8	2.8	Night - 60° scan
18	1238	1402	12	23	60°-120°	5.2	8.0	Scan 60° arc
19	1253	1305	12	23	150°-210°	4.9	6.0	Scan 60° arc
19	1421	1456	12	23	150°-210°	5.0	6.0	Layer died away and built back up
24	1803	1901	0	--	Stationary	2.7	4.7	Two layers on ionogram
28	1237	1510	12	23	210°-270°	6.0	8.9	Recorded layer build-up

Table 4.2

Observations during July, 1975, at Arecibo, P. R.

<u>DATE</u>	<u>TIME (AST)</u>	<u>MODE*</u>	<u>MAX f_bE_s</u>	<u>MAX f_tE_s</u>	<u>REMARKS</u>
10	11:34-13:33	W	5.2	5.7	Test of programs.
16	12:14-18:58	W	8.4	11.0	Winds were measured that morning by R. M. Harper.
17	03:33-06:16	P	2.9	6.9	Scan between 270 and 310 deg. Intense layer formed at 04:30.
17	06:40-08:20	W	5.3	7.1	Large uncertainties, small electron density.
19	09:05-10:55	W	5.0	6.3	Problem with set-up. Measurement at 270 and 360 deg only.
19	11:45-14:22	P	> f _o F ₂	12.8	Scan between 265 and 275 deg. Observed irregularity with [e ⁻] > 5.4 x 10 ⁶ cm ⁻³ .
20	10:55-12:07	W	5.0	7.0	Large zonal component in ion drift.
20	12:17-13:37	P	3.9	4.6	Scan between 90 and 130 deg.
20	13:51-15:23	W	4.3	5.3	E _s layer not at v _z = 0.
21	19:52-21:00 and 21:38-24:00	P	2.4	6.0	Scan between 270 and 310 deg. Transmitter failure at 21:00 E _s layer formed at 21:30.
23	06:10-08:05	W	2.8	3.3	No power profiles measured between first two positions.
24	N/A	W			Noise measurement. Antenna on load.
26	09:07-09:42	P	3.4	4.2	Scan between 270 and 310 deg. E _s on ionogram but not on profile.
26	10:10-11:25	W	5.1	8.8	Smoothly-spiraling hodograph, no E _s layer.
26	11:33-14:50	P	5.4	6.2	Scan between 90 and 130 deg. Periodic enhancement of layer.
26	15:03-16:47	W	3.4	4.0	Large northward velocities below 111 km.
26	19:44-21:37	P	2.5	3.1	Scan between 180 and 220 deg. Two weak layers merge at 94 km.
27	11:25-15:02	P	3.9	4.3	Scan between 180 and 220 deg. E _s layers at 95 and 110 km.
27	15:12-16:56	W	3.6	4.3	Large errors in data. Possible problem with patch panel.

* W = Five-pulse measurement of ion drift with power profiles measured by a single-pulse technique during scans.

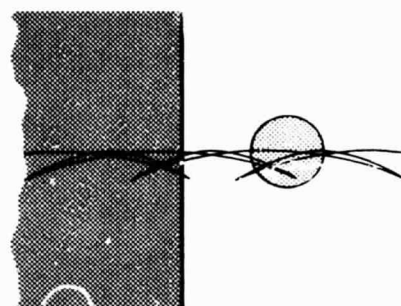
P = Power profiles measured using Barker-coded pulses.

order of 50 m sec^{-1} . At a zenith angle of 15° , the horizontal velocity of the intersection of the radar line of sight with a layer at an altitude of 100 km is 190 m sec^{-1} , when the radar is scanning in azimuth at $23^\circ \text{ min}^{-1}$.

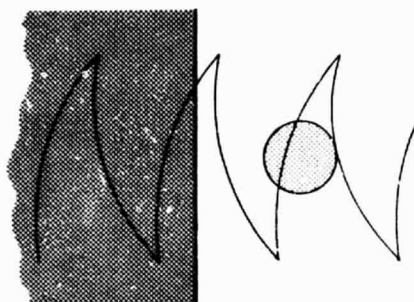
It is apparent that due to the small beamwidth ($\sim 300 \text{ m}$ at sporadic-E altitudes) only a small fraction of the sporadic-E layer is actually sampled in the experiment. Figure 4.7 illustrates how a circular patch 10 km in diameter and an edge of a large patch might appear in the data. In this example the beam is scanning in azimuth at the maximum rate, $23^\circ \text{ min}^{-1}$, and is held at a constant zenith angle of 15° . The sporadic-E layer is at an altitude of 100 km and is moving at a speed of 50 m sec^{-1} . The motion of the layer is tangent to the center of the scan in the upper diagram and radial to the center of the scan in the lower diagram. The drawings on the left show the patterns traced by the intersection of the beam and the sporadic-E layer. The diagrams on the right are a convenient representation of the data. Each scan is plotted as a function of azimuth with the points where the beam encounters a target represented by shaded areas. The direction of the beam is opposite in adjacent scans. It can be seen that the size and position of the patch, as well as its velocity, have a large effect on the appearance of the patch on the data map.

Another method of representing the data is shown in Figure 4.8. Arrays of successive electron-density profiles, similar to the one shown on the left of the figure, are printed by a computer. Contours of equal electron density are then drawn, giving the impression of a vertical cross section of the ionization. This plot can be converted to distance coordinates in both vertical and horizontal axes by noting that, at a zenith angle of 15° ,

Projection of Radar Beam on Ionosphere



→
wind velocity = 50 m/sec



→
wind velocity = 50 m/sec

Data Map

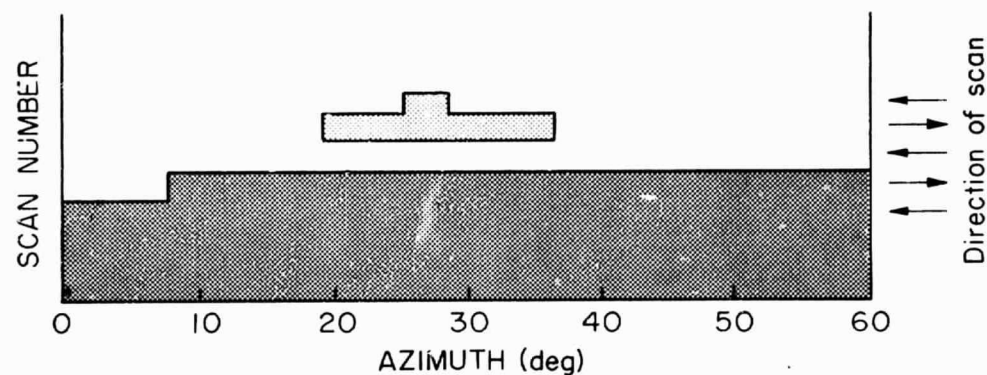
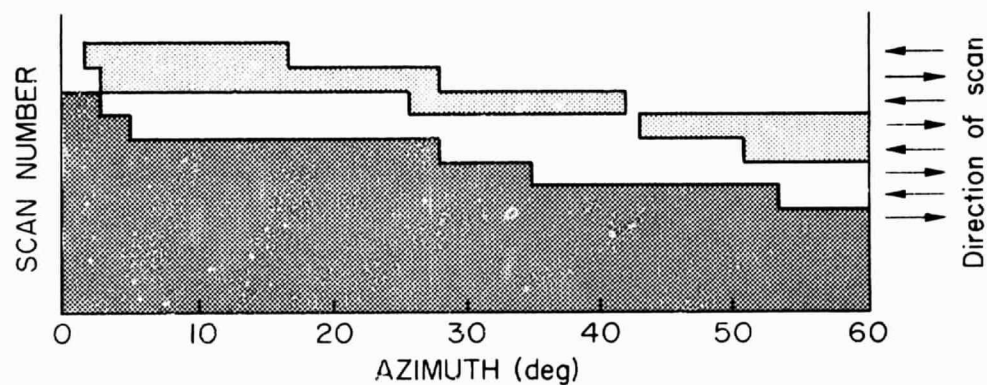


Figure 4.7 An illustration of the method used in the experiment and the effects of winds on the data [Miller and Smith, 1975].

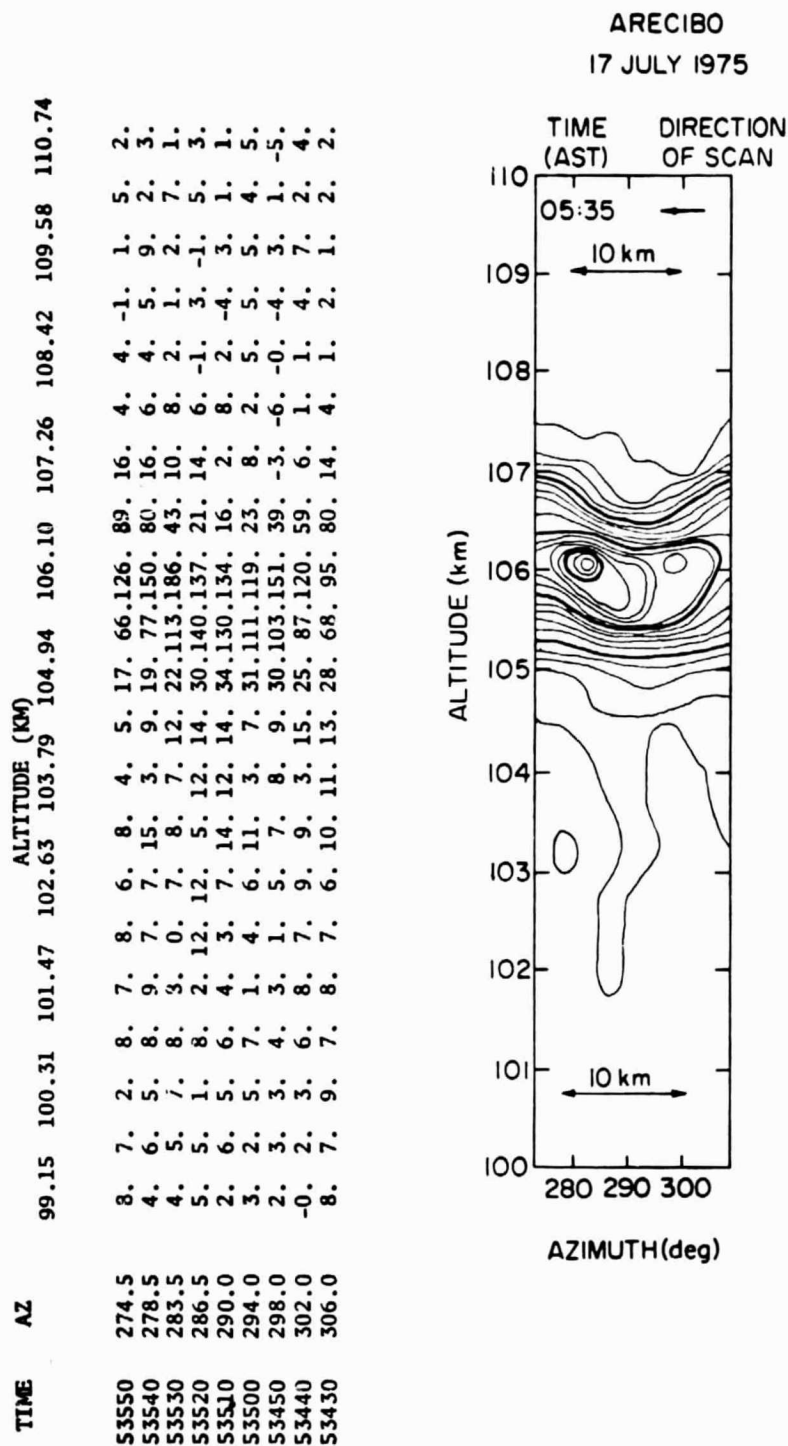


Figure 4.8 Illustration of a scan of the radar by drawing contours on a computer array of electron densities printed as functions of altitude and azimuth.

one degree in azimuth represents 468 m of horizontal distance along an arc at an altitude of 100 km. The horizontal distance per degree increases linearly with height. The azimuth scale is found to be slightly nonlinear because of changes in the angular velocity of the radar.

4.5 *Observations*

4.5.1 *Introduction.* A feature that becomes immediately obvious in examining the data taken by the incoherent-scatter radar is that sporadic-E layers are as variable in structure as they are unpredictable in occurrence. Some have a simple vertical structure and are uniform in the horizontal plane, consistent with rocket observations. Others have complex vertical and horizontal structure as has been implied by the radio reflection observations. Because of the variety of features which were found in a total of 29 observing periods in 18 days it has been decided to first present the individual periods in chronological order, pointing out the features of each, and later to discuss the implications of these observations in the formation of sporadic-E layers.

Where appropriate, data are presented using the representations described in Section 4.43, as well as more conventional methods. Time is given as Atlantic Standard Time (AST) which is UT minus 4 hr. When data from ionograms are presented, the reflection characteristics of the part of the signal with ordinary polarization are examined by plotting values of f_oE_s instead of f_tE_s . In all cases, f_oE_s is determined by subtracting half the gyrofrequency from f_tE_s .

4.5.2 *14 January 1974, 14:11-15:03 AST.* Several methods of scanning the radar beam were tested. It was decided that the optimum mode was to scan repeatedly through arcs of 60 deg or less. In the course of the observation, the radar was scanned through one and a half revolutions in

azimuth, starting at 90 deg and continuing clockwise. The scan was then reversed.

A sporadic-*E* layer appears to have drifted into the field of view at the end of the first scan (270 deg azimuth) and was seen again in the second scan. Contours of electron density observed during parts of the two scans are shown in Figure 4.9 as a function of azimuth and altitude. Figure 4.10 shows that while *foEs* remained nearly constant, there was an increase in *fbEs* between 14:30 and 14:40 AST as the sporadic-*E* layer passed overhead.

4.5.3 17 January 1974, 20:06-22:15 AST. This observation was made to gain experience with the system at night. A map of the data, similar to the example of Figure 4.7, is shown in Figure 4.11. The plot is of the peak electron density of the sporadic-*E* layer during successive scans as a function of azimuth. In this case the electron density is determined by a parabolic fit to the three points defining the layer. To aid in visualizing the variations, contours of electron density have been drawn, giving the impression of a map of the layer. This map may be considerably distorted as a result of the movement of the layer.

The structure of this sporadic-*E* layer is relatively simple compared with subsequent nighttime observations. Correspondingly the variation in *fbEs* and *ftEs*, plotted in Figure 4.12, is relatively smooth, with *ftEs* reaching a maximum of 3.3 MHz at 20:50 AST. By allowing roughly 25 min for the sporadic-*E* ionization to move the 30 km from the field of view of the ionosonde (0 deg zenith angle) to that of the radar (15 deg zenith angle), the peaks in *foEs* (Figure 4.12) are found to coincide with the observation of enhanced electron-density irregularities (Figure 4.11).

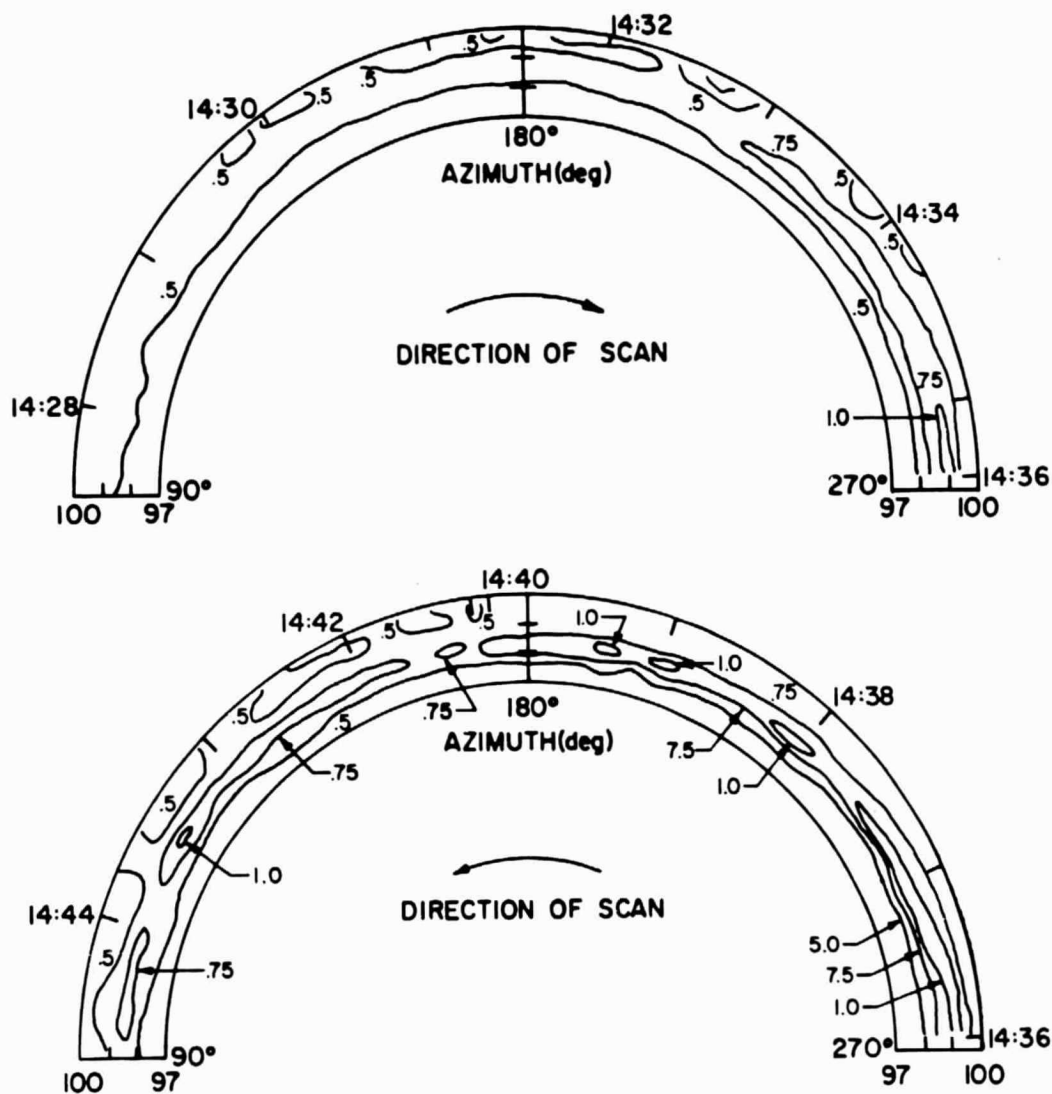


Figure 4.9 Electron density (10^5 cm^{-3}) of a sporadic-E layer observed during successive 90 deg scans on 14 January 1974. The motion of the radar beam is clockwise in the first scan and counterclockwise in the second.

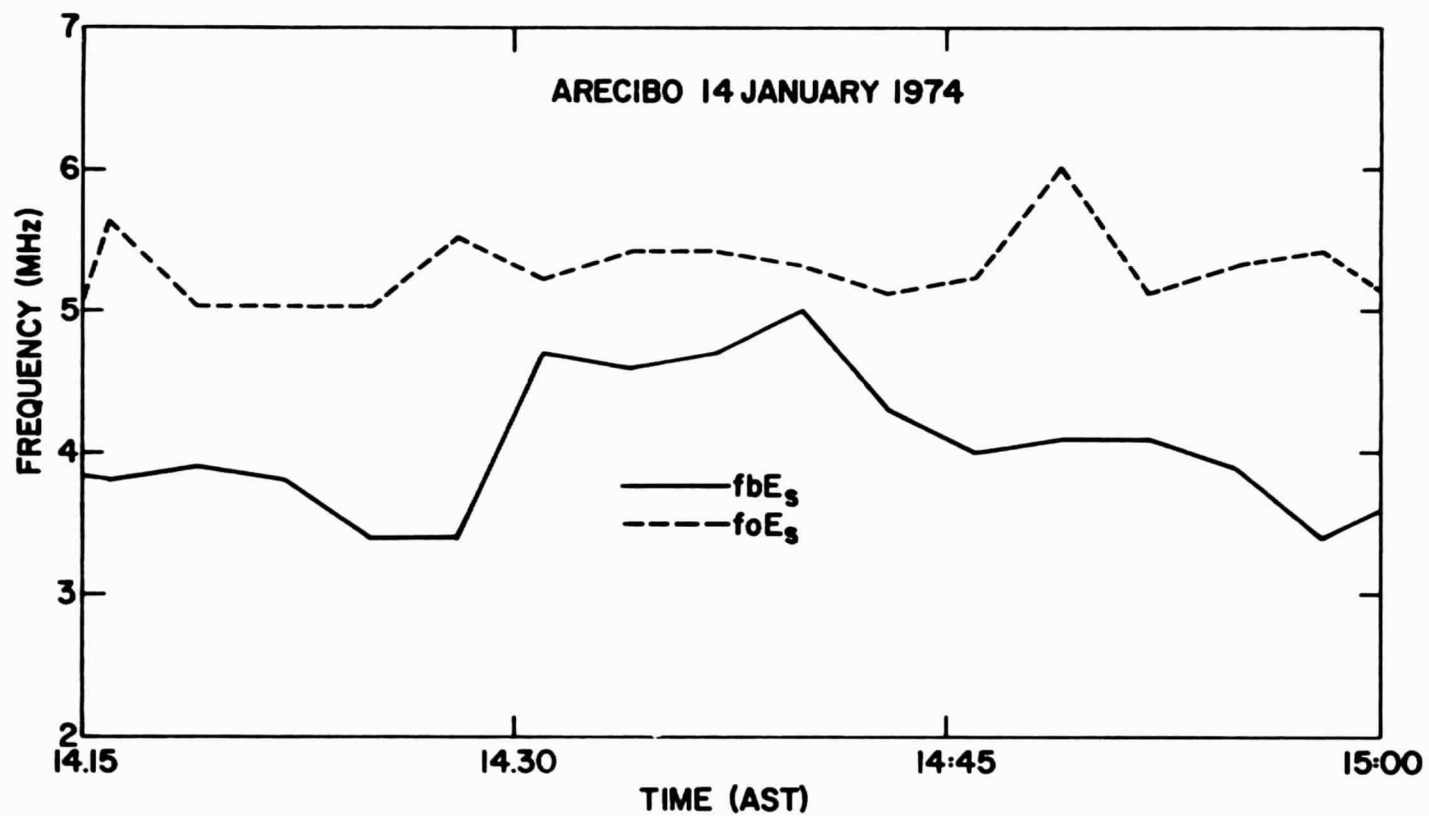


Figure 4.10 fbE_s and foE_s on 14 January 1974.

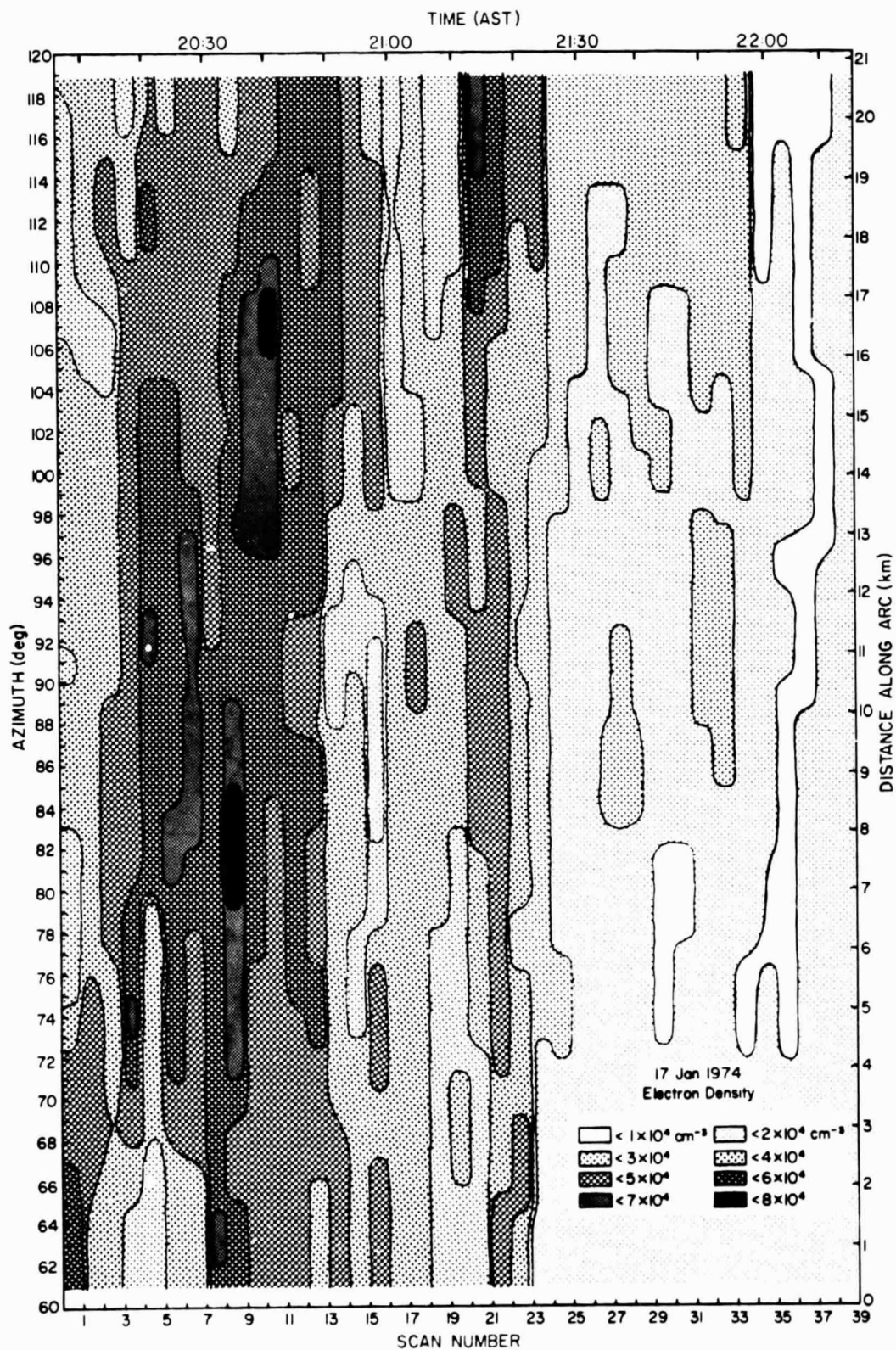


Figure 4.11 Representation of maximum density of the sporadic-E layer observed on 17 January 1974. The altitude of the layer is 97 km. The direction of odd numbered scans is toward lower values of azimuth; even numbered scans toward greater azimuth.

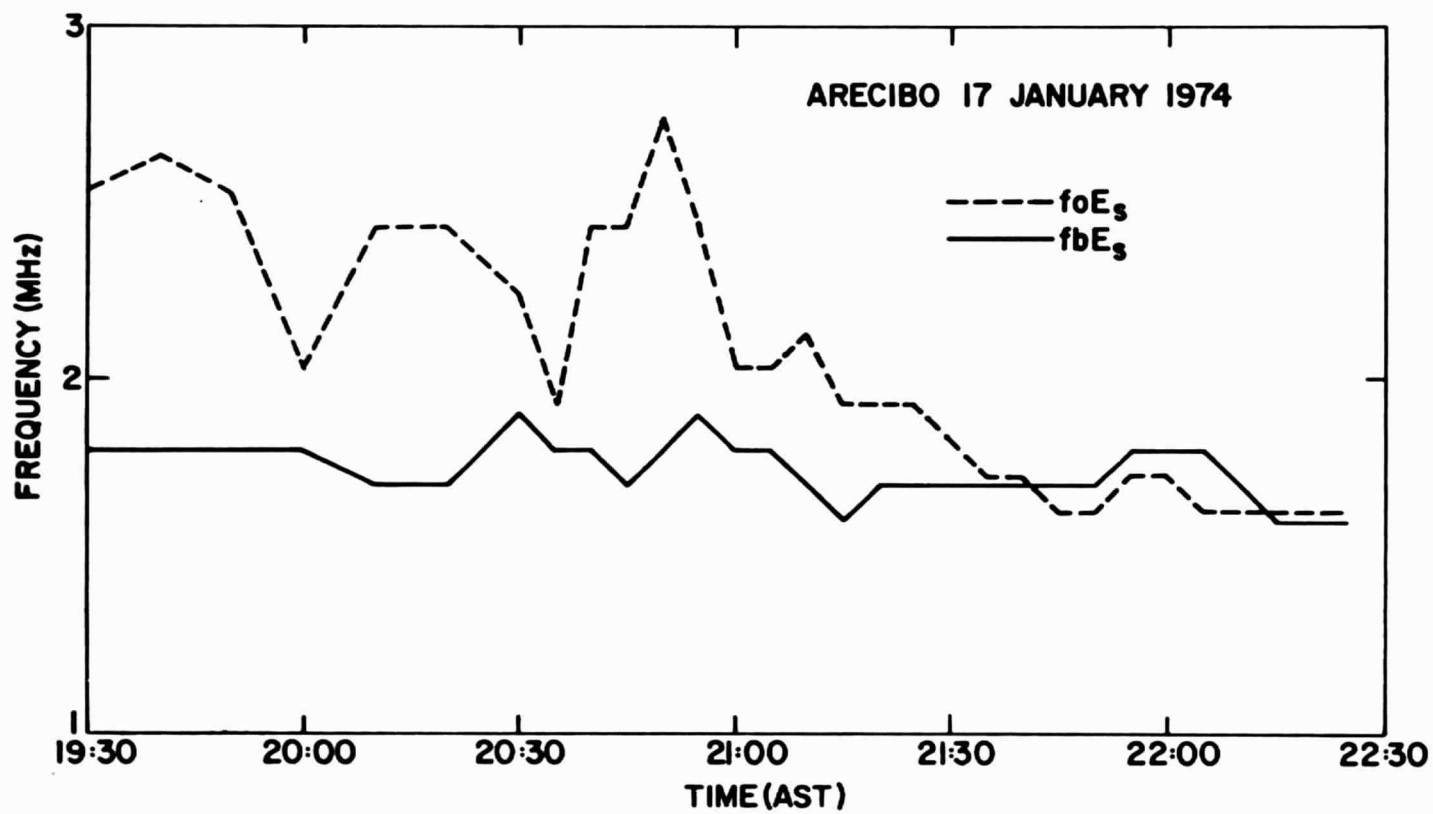


Figure 4.12 $fbEs$ and $foEs$ on 17 January 1974.

4.5.4 18 January 1974, 12:38-14:02 AST. In this and the remaining cases of January 1974 the observation was initiated on the basis of indication of the presence of sporadic *E* by the ionosonde. The layer appears to be made up of discrete patches of ionization separated by regions where no sporadic-*E* ionization was observed. The passage of one of these patches is shown in Figure 4.13. The discrete nature of the patches may not indicate a discontinuous metallic ion layer, but rather a variable layer with ionization densities in small regions becoming large enough to be observed above the ambient ionization.

What appears to be three patches on the right side of the fifth scan in Figure 4.13 is the result of the electron density being averaged into two height gates at certain altitudes (compare with Figure 4.6). This effect is expected for both a tilted layer and a descending horizontal layer. In this case it is identified as a tilted layer, as the implied descent velocity would otherwise be excessive.

The range of peak plasma frequencies derived from incoherent-scatter data is compared with $f_b E_s$ and $f_o E_s$ in Figure 4.14. Two sporadic-*E* traces were observed on the ionograms. The difference in the frequencies from the two measurements is interpreted as being the result of volume-averaging by the radar. In this figure, the similarities between the variation of the lower $f_o E_s$ trace and the upper edge of the shaded area and between the variation of $f_b E_s$ and the lower edge of the shaded area are apparent. This is consistent with the interpretation of $f_o E_s$ as being the largest value and $f_b E_s$ the smallest value of the peak plasma frequency in the sporadic-*E* layer above the ionosonde.

4.5.5 19 January 1974, 12:53-14:56 AST. Between 14:21 and 14:25 AST a double sporadic-*E* layer with peaks at about 100 and 101.5 km was seen

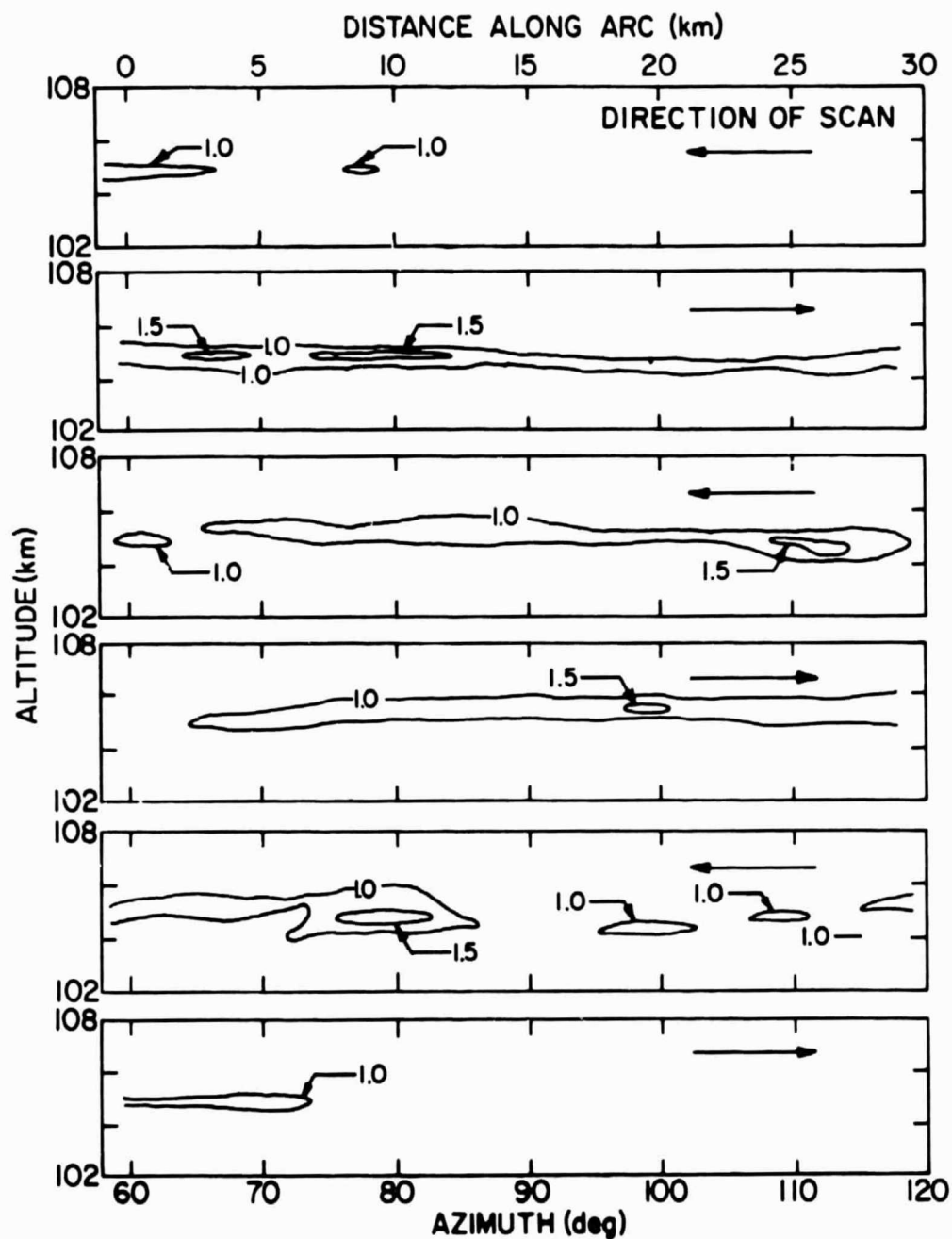


Figure 4.13 Electron density (10^5 cm^{-3}) above Arecibo, 18 January 1974, between 12:59 and 13:13 AST. Each scan represents approximately 3 min.

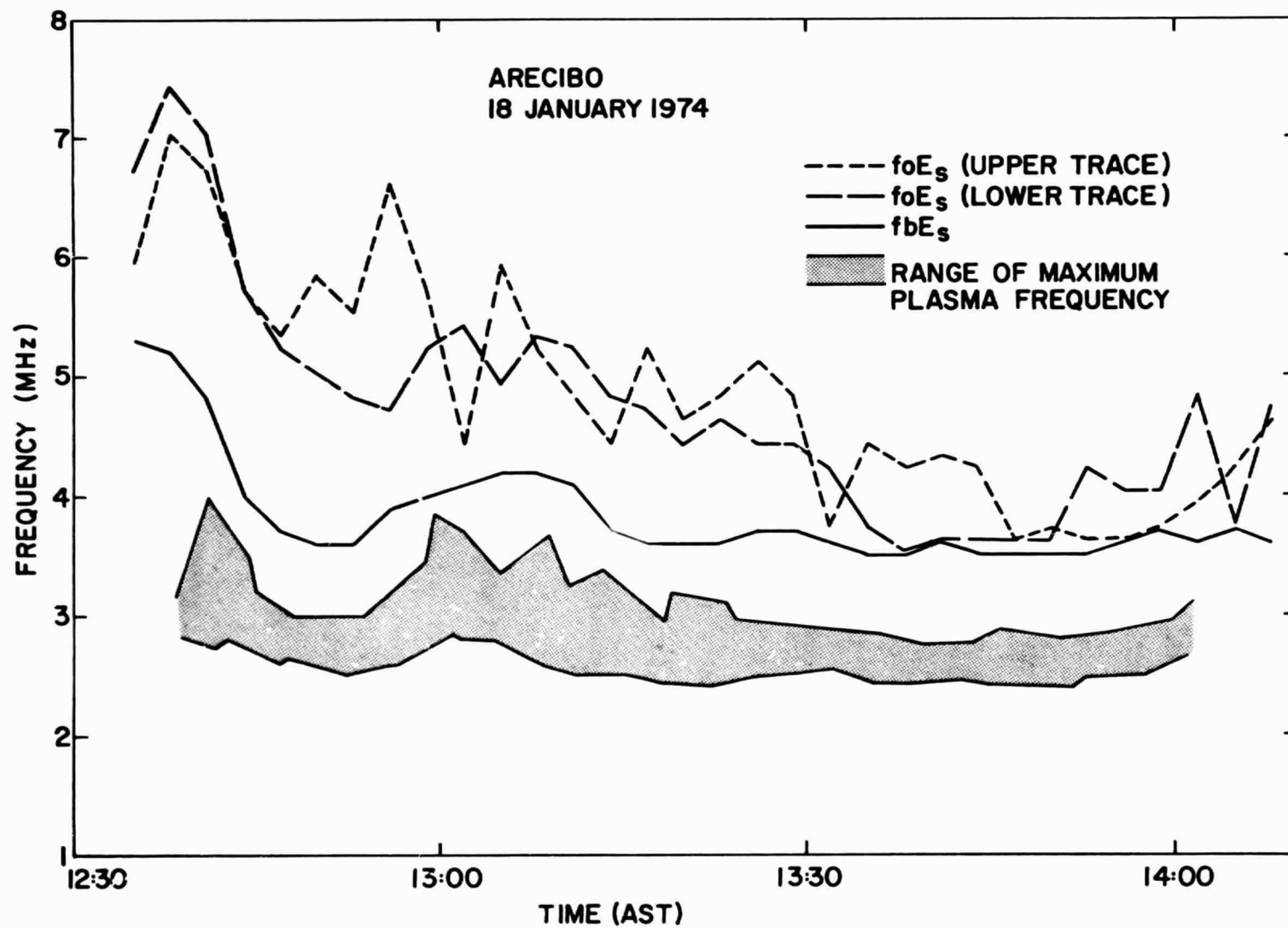


Figure 4.14 f_bE_s and f_oE_s on 18 January 1974. Shaded area represents limits of plasma frequencies derived from incoherent-scatter data.

(Figure 4.15). A transmitter failure occurred during this observation. The upper layer was not as intense as the lower. No relative vertical motion was apparent between the two layers. Neither layer was observed after the scan shown at the bottom of Figure 4.15, although a much weaker layer formed at an altitude of 99 km after 14:40 AST. Two sporadic-E traces, closely spaced in virtual height, were recorded on ionograms during this observation.

4.5.6 *24 January 1974, 18:03-19:01 AST.* On this occasion the radar beam was held in a vertical position and a sporadic-E layer observed. Figure 4.16 shows the excess electron column density of the layer. The length of the column (1.8 km) is defined by the three height gates centered on the layer. The electron densities above and below the layer show a smooth decrease in ionization throughout the experiment. They were averaged to determine the background ionization. The background is a small part of the total ionization in this region and varied from $0.94 \times 10^9 \text{ cm}^{-2}$ at the beginning of the observation to $0.38 \times 10^9 \text{ cm}^{-2}$ at the end. During the one-hour period of observation the solar zenith angle changed from 95 to 105 deg.

The peak of the layer is observed initially to be at about 100 km and descends during the period by about 200 m, based on the parabolic fit. The signals have been averaged over 20,000 samples, a period of approximately 64 sec. The error bars represent statistical errors based on the number of samples averaged and the signal-to-noise ratio, as described by equation (4.13).

The variation in excess electron column density is interpreted to be a spatial variation and not a variation in time, since no major redistribution in altitude of the ionization is apparent in the vertical

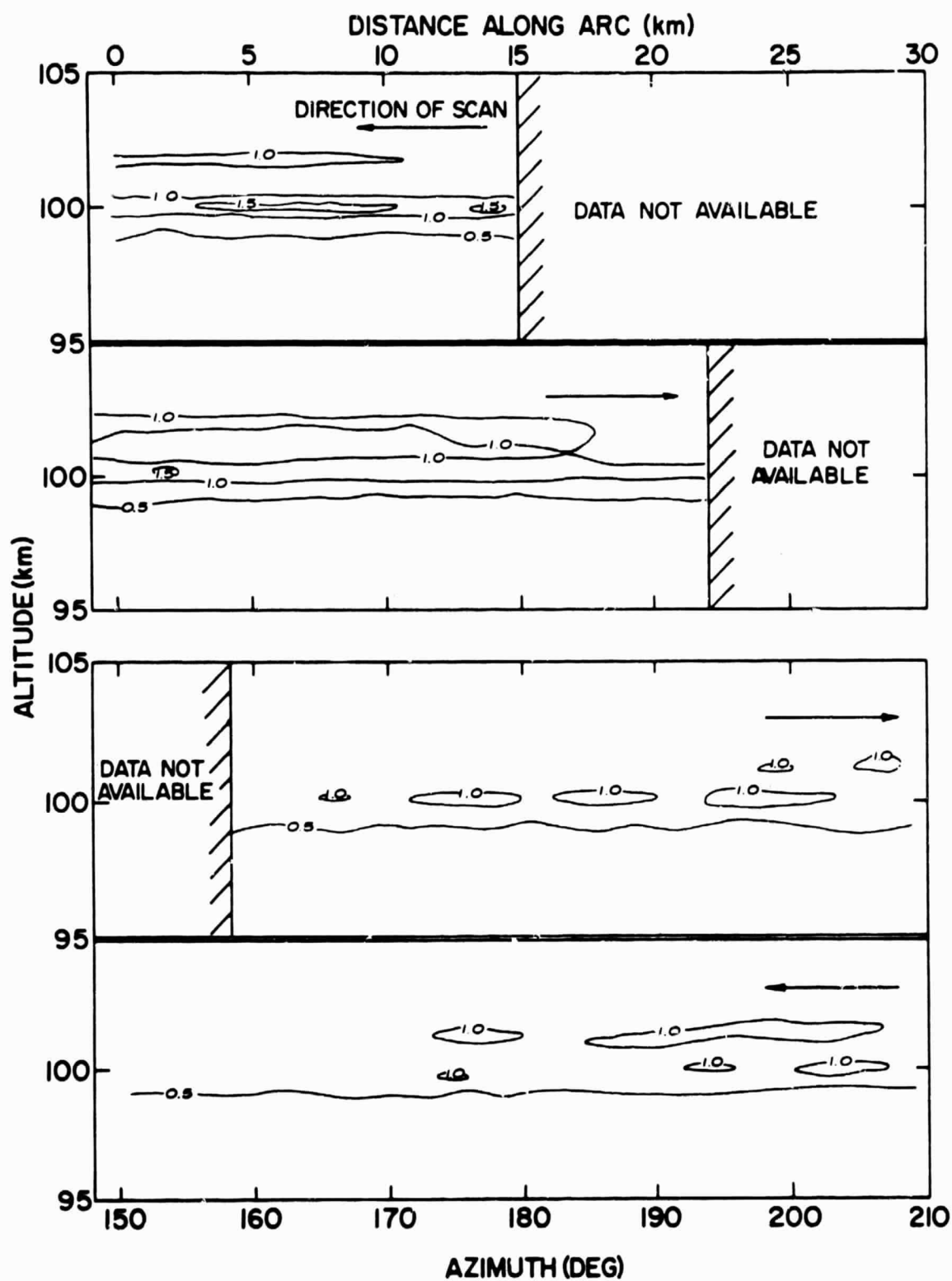


Figure 4.15 Electron density (10^5 cm^{-3}) above Arecibo, 19 January 1974, between 14:21 and 14:25 AST (upper two scans) and between 14:29 and 14:32 AST (lower two scans). Each scan represents approximately 3 min.

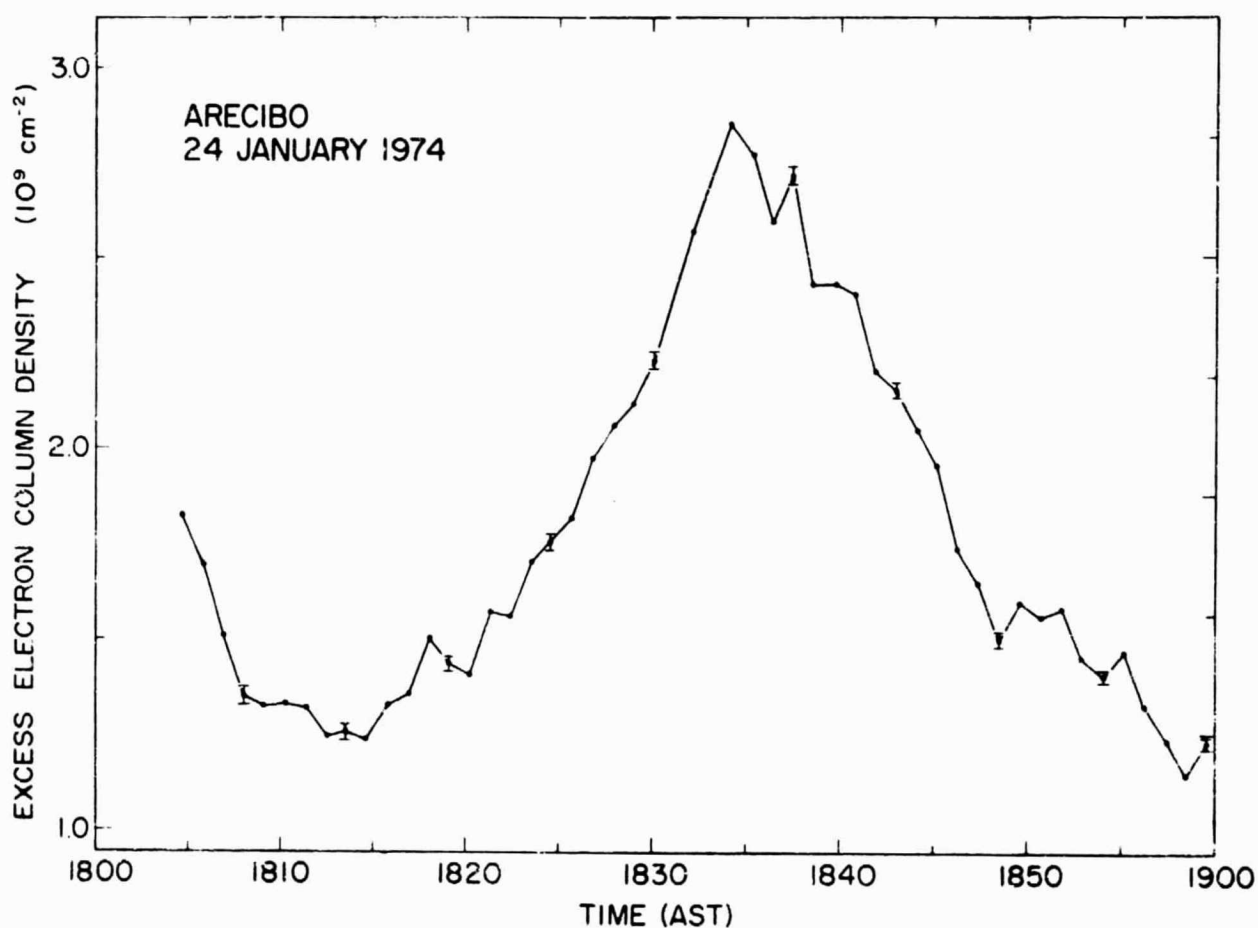


Figure 4.16 Electron column densities through a sporadic-E layer at an altitude of 100 km observed on 24 January 1974. The radar beam was held in a fixed vertical position [Miller and Smith, 1975].

electron-density profiles. If a wind speed of 50 m s^{-1} is assumed, this layer has a horizontal extent of 165 km. In this observation, very little small-scale structure is seen.

Figure 4.17 shows the values of $f_b E_s$ and $f_o E_s$ from ionograms taken during this experiment. It may be noted that $f_b E_s$ and $f_o E_s$ are approximately equal on this occasion. The temporal variation of the column electron density shown in Figure 4.16 is quite similar to that of the blanketing and critical frequencies shown in Figure 4.17.

In examining the data from 24 January 1974, an interesting feature was noted which illustrates the variability that can be present in the E region at sunset without appreciably affecting a sporadic- E layer. A sequence of electron-density profiles of the E region is shown in Figure 4.18. These profiles show what appears to be a layer of ionization ascending rapidly from 125 to 155 km. The time between profiles is approximately 3 min. During the observation, the solar zenith angle increased from 95 deg to 105 deg. There is also a rapid decrease in the ionization density of the E region which is better illustrated in Figure 4.19. The apparent upward movement of the layer below 150 km appears to be the result of both recombination and vertical transport, and does not necessarily represent only the bulk motion of the ionization.

The display of incoherent-scatter electron-density data by staggering vertical profiles, as in Figure 4.18, is very popular in the literature. The comparison of these two figures emphasizes that care must be taken in the interpretation of features related to the electron density in such plots.

4.5.7 28 January 1974, 12:52-14:58 AST. On this occasion a complete sporadic- E event was observed, including both build-up and decay. The layer was observed at an altitude of 105 km. A map of peak electron densities

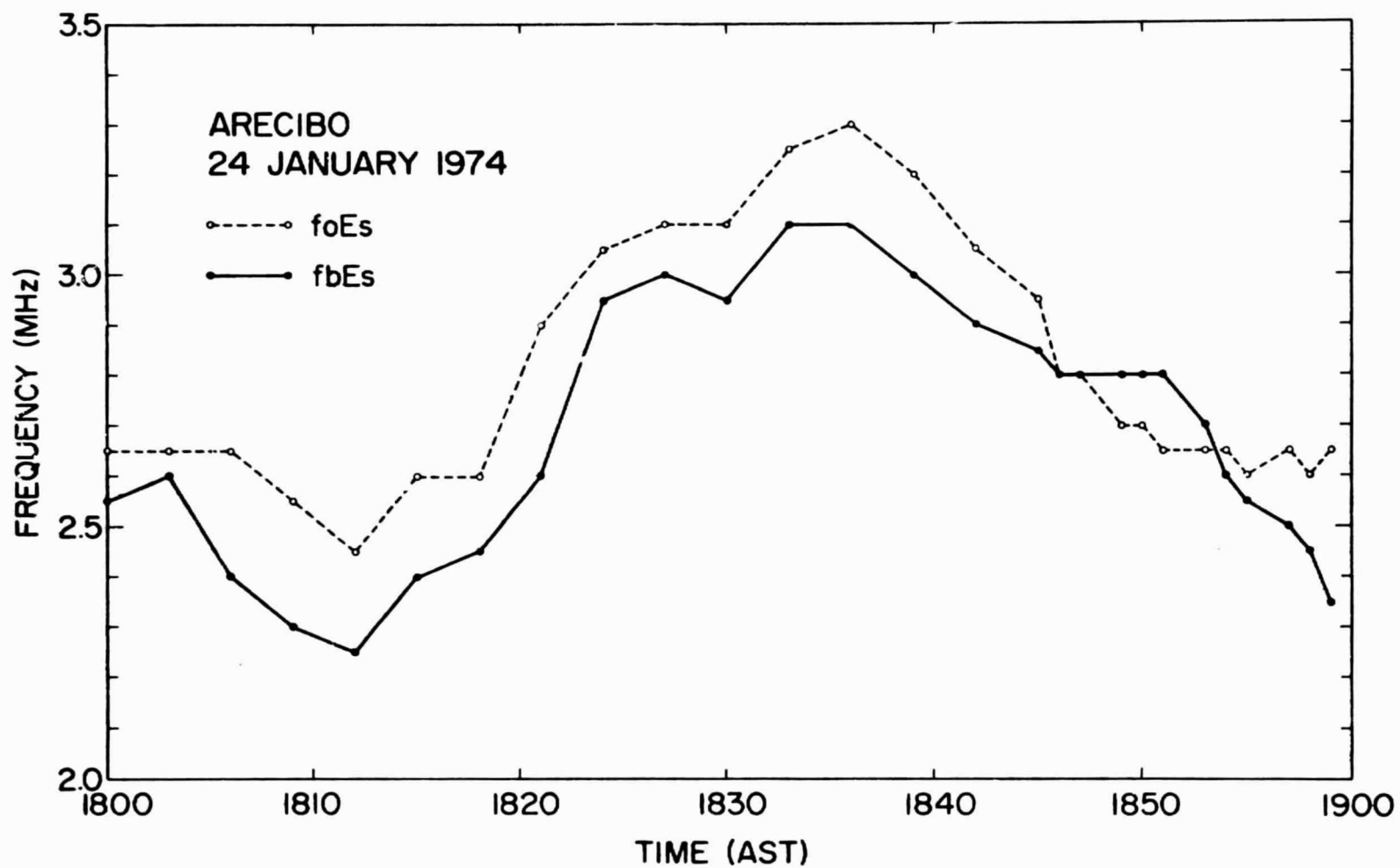


Figure 4.17 *fbEs* and *foEs* on 24 January 1974 [Miller and Smith, 1975].

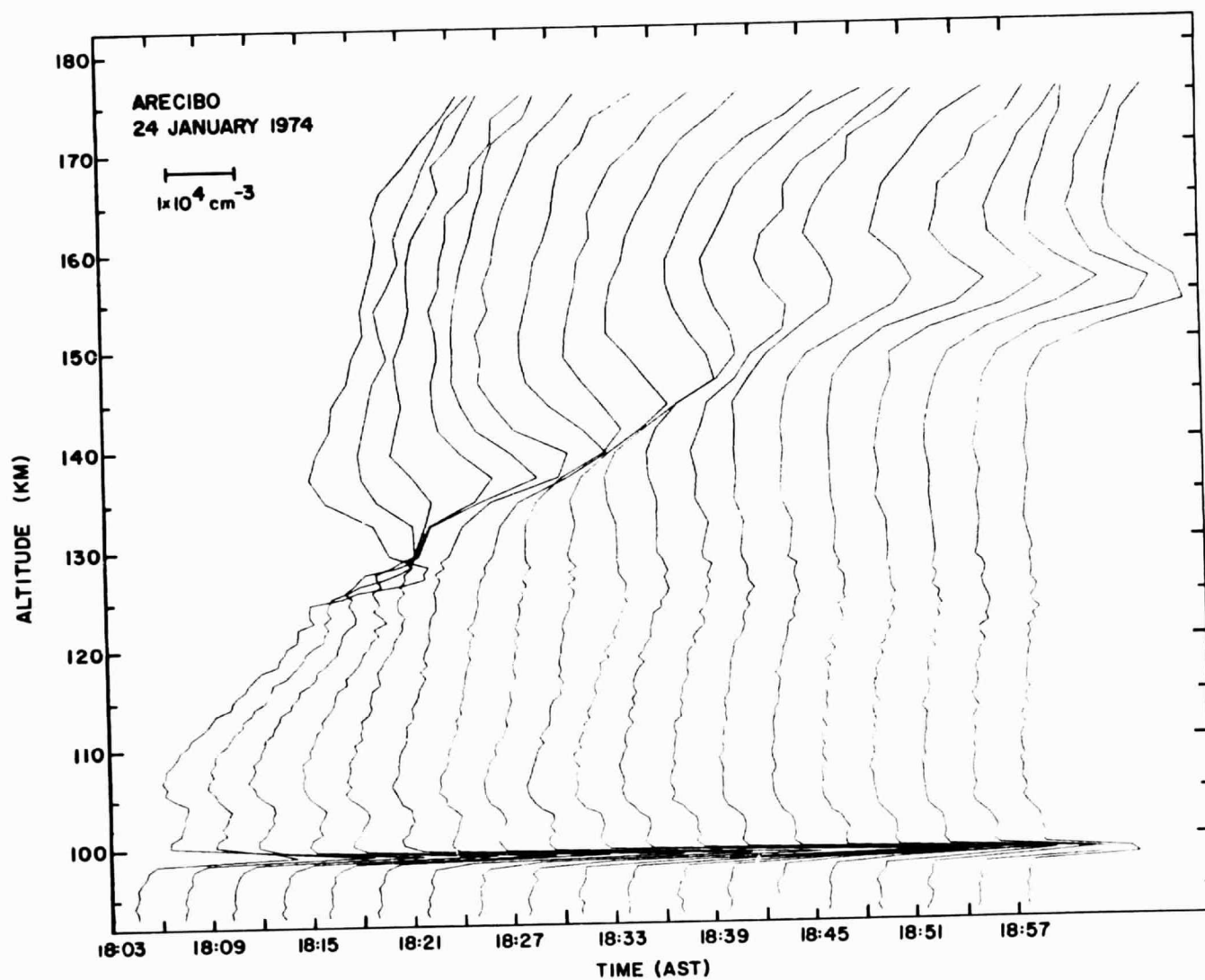


Figure 4.18 Electron-density profiles observed on 24 January 1974.

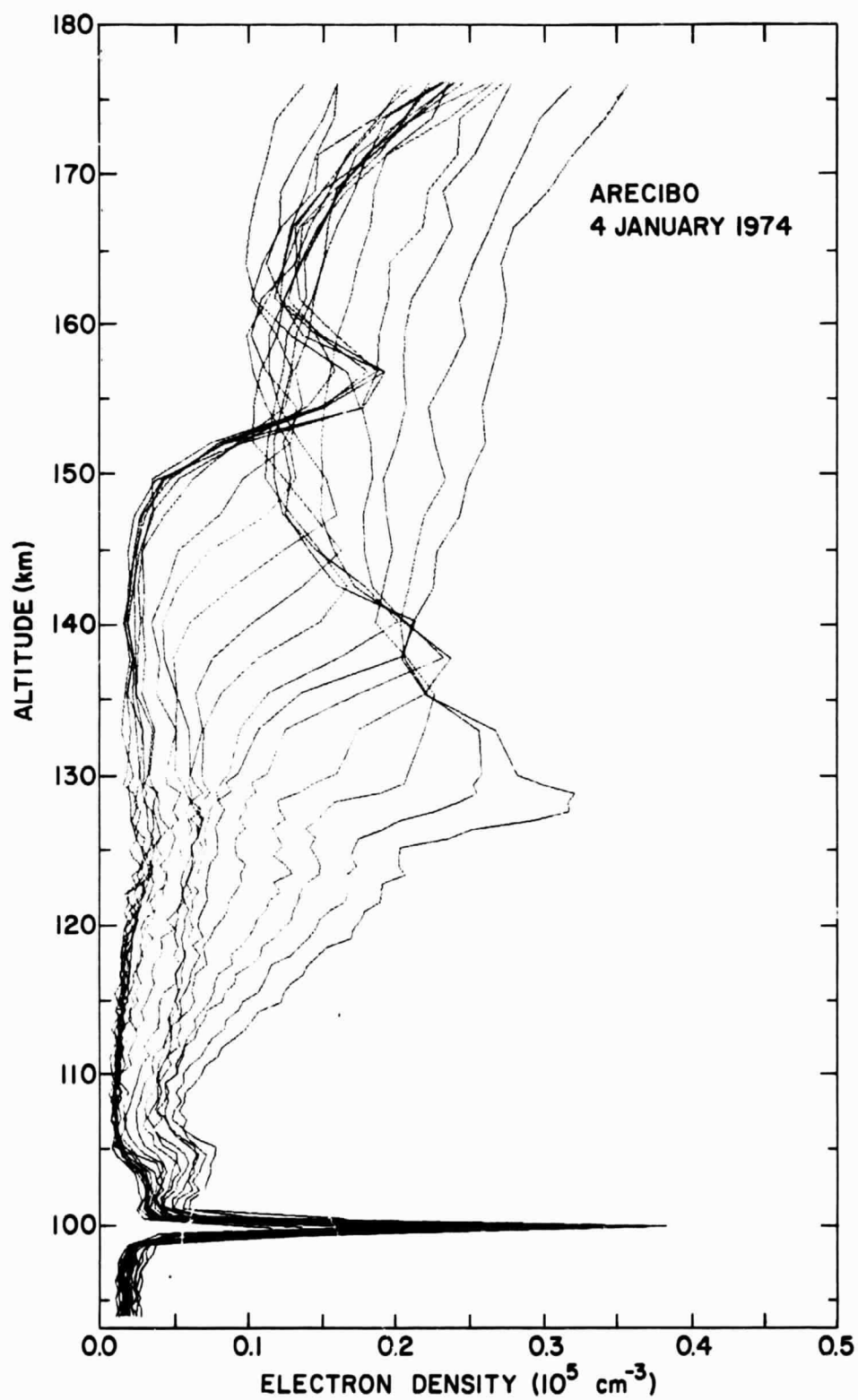


Figure 4.19 Electron-density profiles observed between 18:00 and 19:00 AST on 24 January 1974.

based on a parabolic fit is shown in Figure 4.20. The contours are slightly oblique with respect to the scans, indicating that the movement of the sporadic-*E* layer is in a direction essentially tangent to the scan. Figure 4.20 shows two regions containing patchy structure with electron densities higher than the surrounding layer. The first, between 13:45 and 13:50 AST includes the highest electron density recorded: $3.1 \times 10^5 \text{ cm}^{-3}$; the second, between 14:10 and 14:25 AST has a maximum electron density of $2.3 \times 10^5 \text{ cm}^{-3}$.

Vertical-electron-density profiles show that the column electron density of the sporadic-*E* layer increases when an increased peak electron density is observed, indicating that the irregularities are not caused by redistribution of the ionization in altitude. This is demonstrated by Figures 4.21 and 4.22, in which contours of electron density are plotted as a function of azimuth and altitude. The two regions where irregularities are observed are illustrated in these figures, which correspond, respectively, to scans in Figure 4.20 numbered 17-21 and 29-33. The thickening of the sporadic-*E* layers at the regions of enhanced electron density is apparent.

The values of *fbEs* and *foEs* during the time of observation are shown in Figure 4.23. For part of the time two sporadic-*E* echoes are present; both are shown in Figure 4.23. The higher trace was seen to descend quite rapidly, possibly the result of off-vertical reflections. However, at no time was the virtual height of the higher trace observed to increase. The electron-density profile shows only one layer to be present. Rocket observations by *Smith* [1970] similarly showed that not all sporadic-*E* echoes are associated with identifiable features of the electron-density profile.

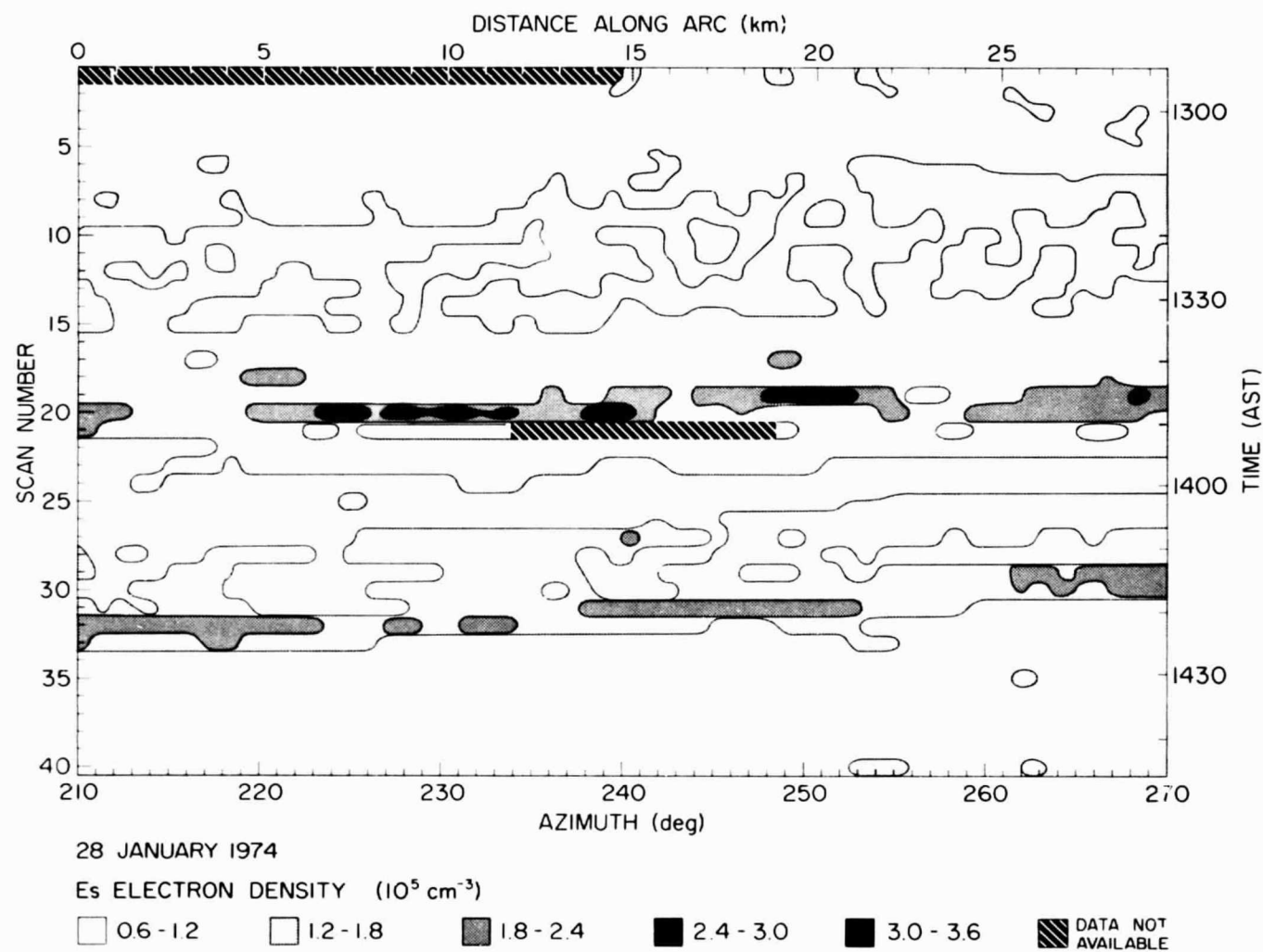


Figure 4.20 Representation of maximum density of the sporadic-E layer observed on 28 January 1974 between 12:52 and 14:58 AST. The altitude of the layer is 105 km. The direction of odd-numbered scans is from left to right, even-numbered scans from right to left [Miller and Smith, 1975].

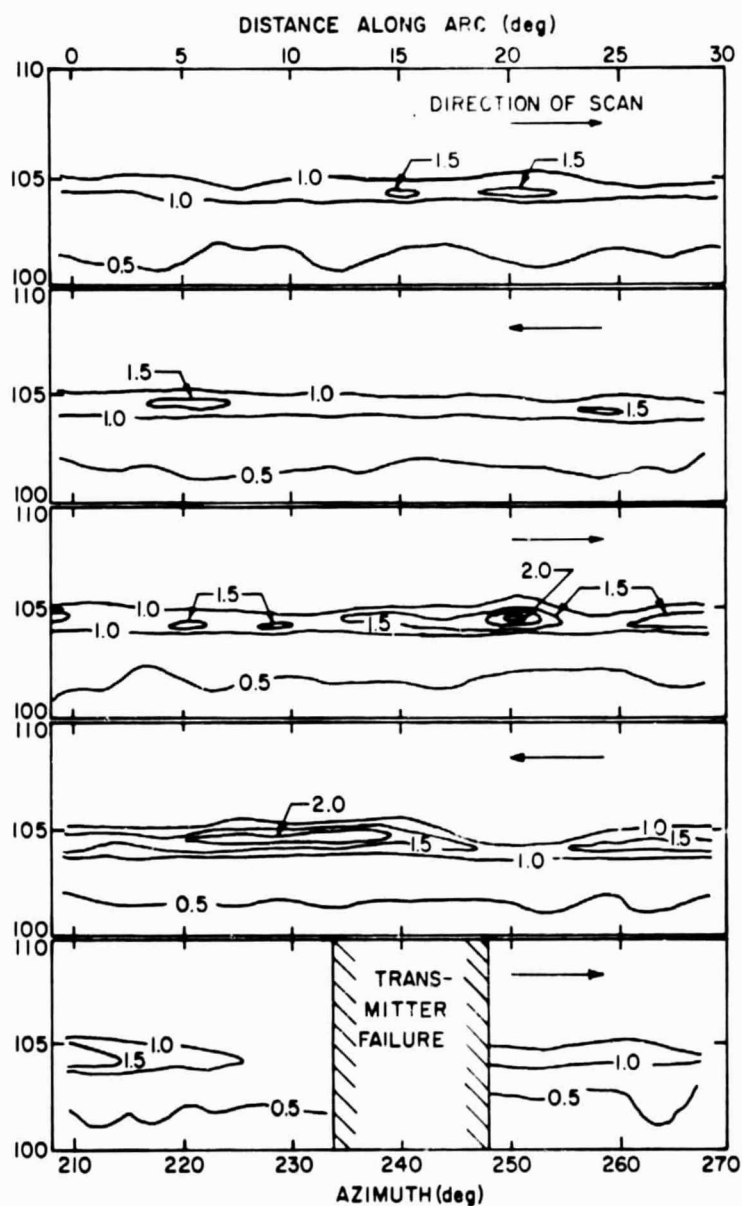


Figure 4.21 Electron density (10^5 cm^{-3}) above Arecibo, 28 January 1974, between 13:40 and 13:54 AST. Each scan represents approximately 3 min.

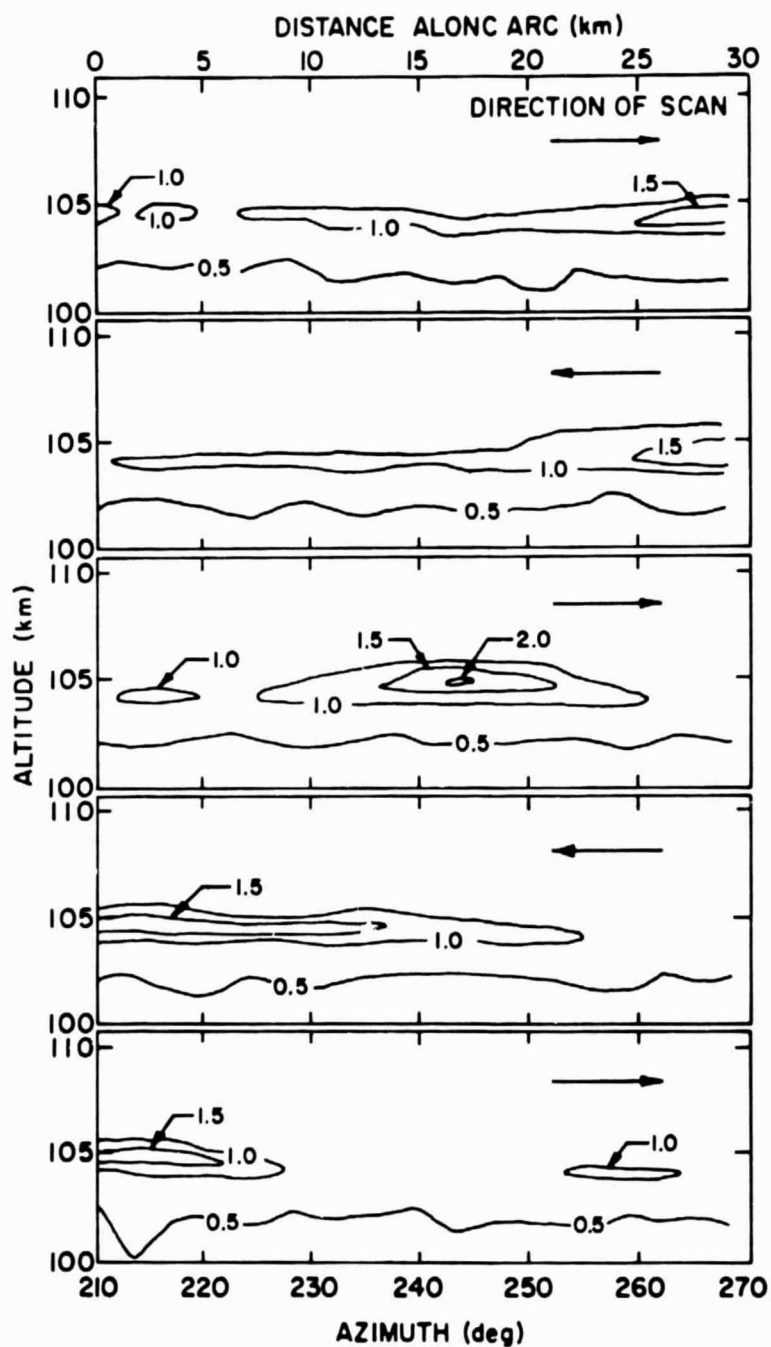


Figure 4.22 Electron density (10^5 cm^{-3}) above Arecibo, 28 January 1974, between 14:14 and 14:28 AST. Each scan represents approximately 3 min.

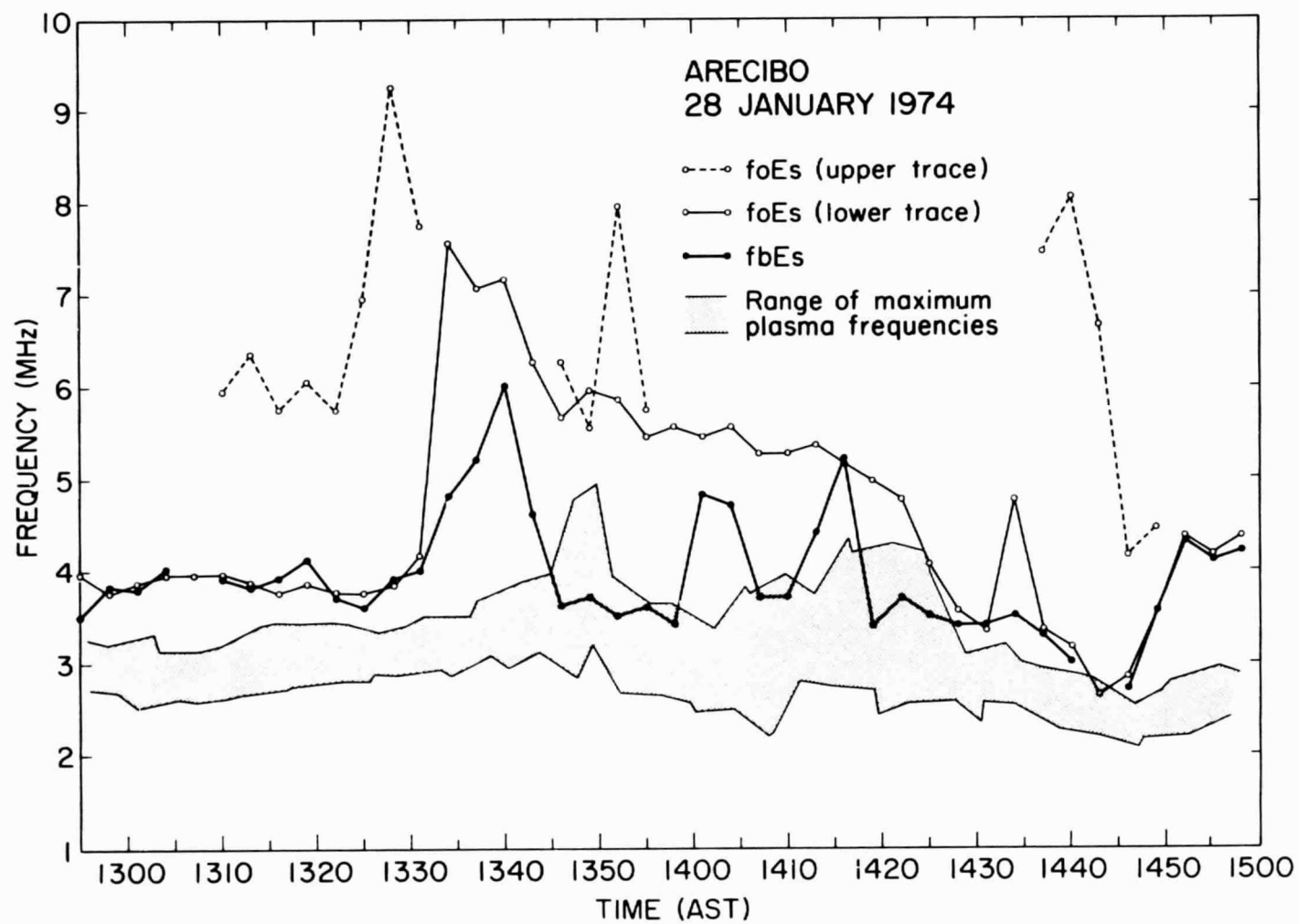


Figure 4.23 *fbEs* and *foEs* on 28 January 1974. Shaded area represents limits of plasma frequencies derived from the incoherent-scatter data [Miller and Smith, 1975].

The shaded area in Figure 4.23 is bounded by the plasma frequencies derived from the maximum and minimum values of the peak electron density of the layer during each scan in the incoherent-scatter data. The blanketing and maximum frequencies from the ionosonde data are both seen to be generally higher than the plasma frequencies derived from the incoherent scatter data, an effect of volume averaging.

4.5.8 10 July 1975, 11:31-13:33 AST. The first observation of the second series was devoted to a test of the data-taking program for the multiple-pulse ion drift experiment. Ion drifts were measured with the radar at azimuths of 180, 270, 360, and again at 180 deg. These positions will be identified as 1, 2, 3, and 4, respectively.

As described in Section 4.4.2 the three components of ion velocity can be obtained by combining measurements from positions 1, 2 and 3 or from positions 2, 3 and 4. Hodographs of the horizontal ion drift velocities and the corresponding profile of vertical ion drift derived separately from measurements at the two sets of positions are shown in Figure 4.24. The results from both sets of data would be identical if the velocity components were constant and errors in measurement of velocity were negligible. It is seen that there was in fact a significant change in the ion drift velocity in the 1.5 hr required to make the measurements. As a result of this test observation an interpolation procedure was developed which allows for slow changes in the wind structure. This will be illustrated in subsequent examples.

While moving between the four positions electron-density profiles were obtained with an altitude resolution of 1.2 km. These show a sporadic-E layer at a constant altitude of 109.5 km. As indicated in Figure 4.24 this layer occurs near a convergence point in the vertical

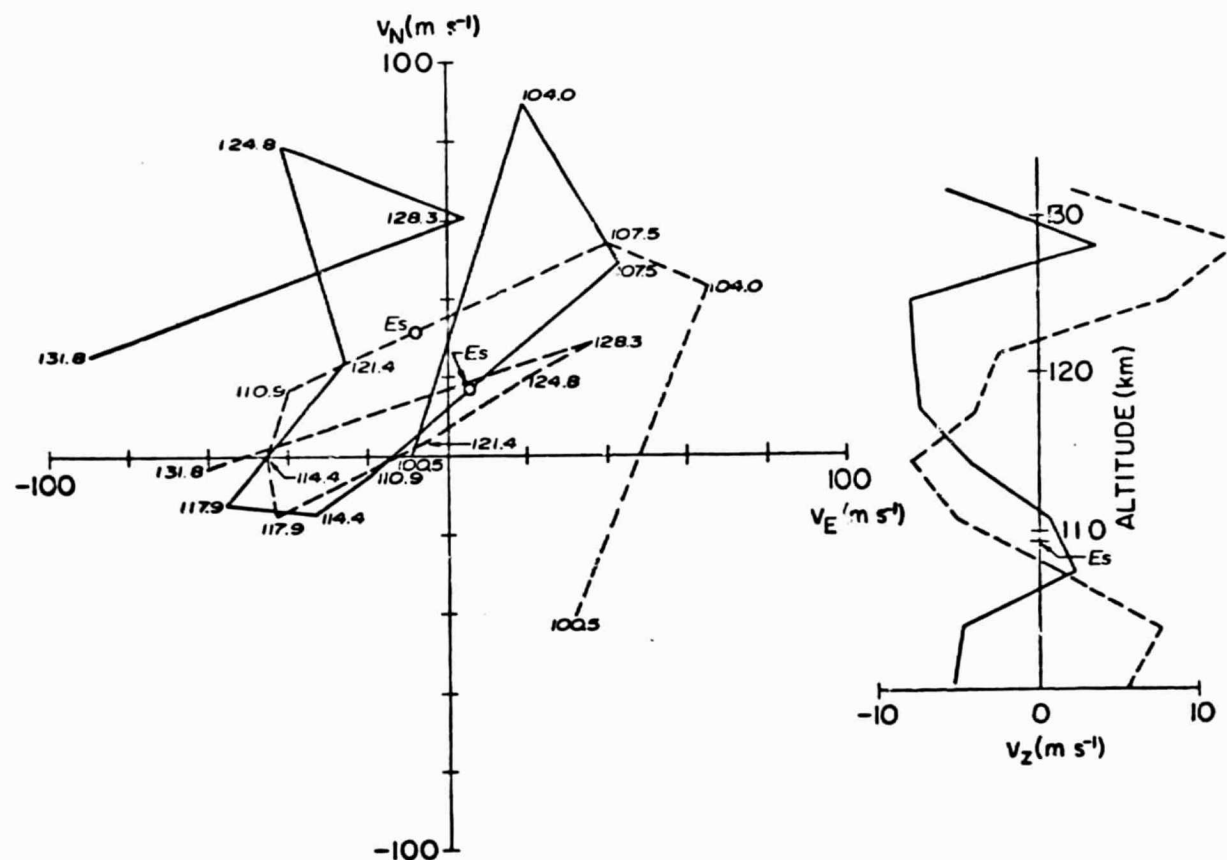


Figure 4.24 Ion drift velocities, 10 July 1975. The solid line shows velocities from incoherent-scatter measurements between 11:31 and 12:39 AST, the dashed line from measurements between 11:56 and 13:07 AST.

ion drift velocity. During this observation, ionosonde measurements showed f^oE_s to be approximately equal to fE_s , and vary between 3.6 and 5.2 MHz.

4.5.9 16 July 1975, 12:14-18:58 AST. On this day, an extended observation of ion drift velocities was made. Values of f^oE_s and fE_s from the ionograms are plotted in Figure 4.25. An intense sporadic-E event commenced at about 11:45 AST. No incoherent-scatter data were taken until 12:14 AST. At 12:59 AST, the value of fE_s reached a peak of 11.0 MHz, but by the time a third wind vector was measured and ion drift velocities determined, it was 13:22 AST, and fE_s had dropped to 7.0 MHz. The sporadic-E layer persisted throughout the afternoon with values of fE_s ranging between 4.5 and 7.6 MHz. The experiment was continued until 18:58 AST.

The ion velocities measured at each position of the radar were interpolated to a common time in order to minimize the effect of the changing velocities. This is justified by the continuity apparent between measurements. Figure 4.26 shows the line-of-sight ion velocities at altitudes of 100.4, 104.0 and 107.5 km, measured at each position of the radar and plotted at the corresponding time. The error bars are based on the fit of the measured autocorrelation function to a theoretical autocorrelation function. The relative magnitude of the error bars to the Cartesian velocity components is illustrated in the wind profile shown in Figure 4.27, which is based on values interpolated to 13:12 AST.

Figure 4.28 shows the components of the ion drift velocity as a function of time. The changing position of the sporadic-E layer is indicated. In spite of the presence of a sporadic-E trace on the

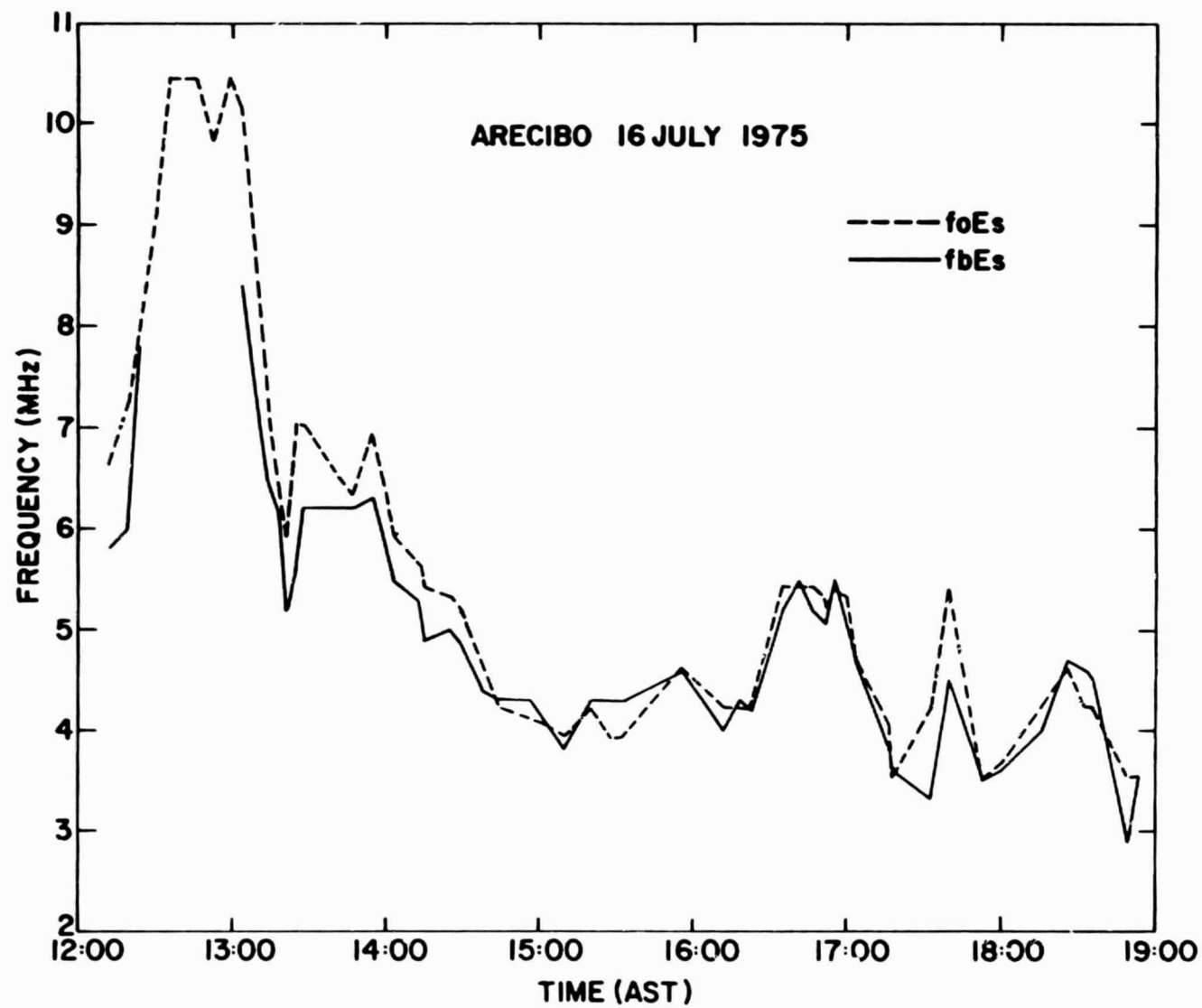


Figure 4.25 $fbEs$ and $foEs$ on 16 July 1975.

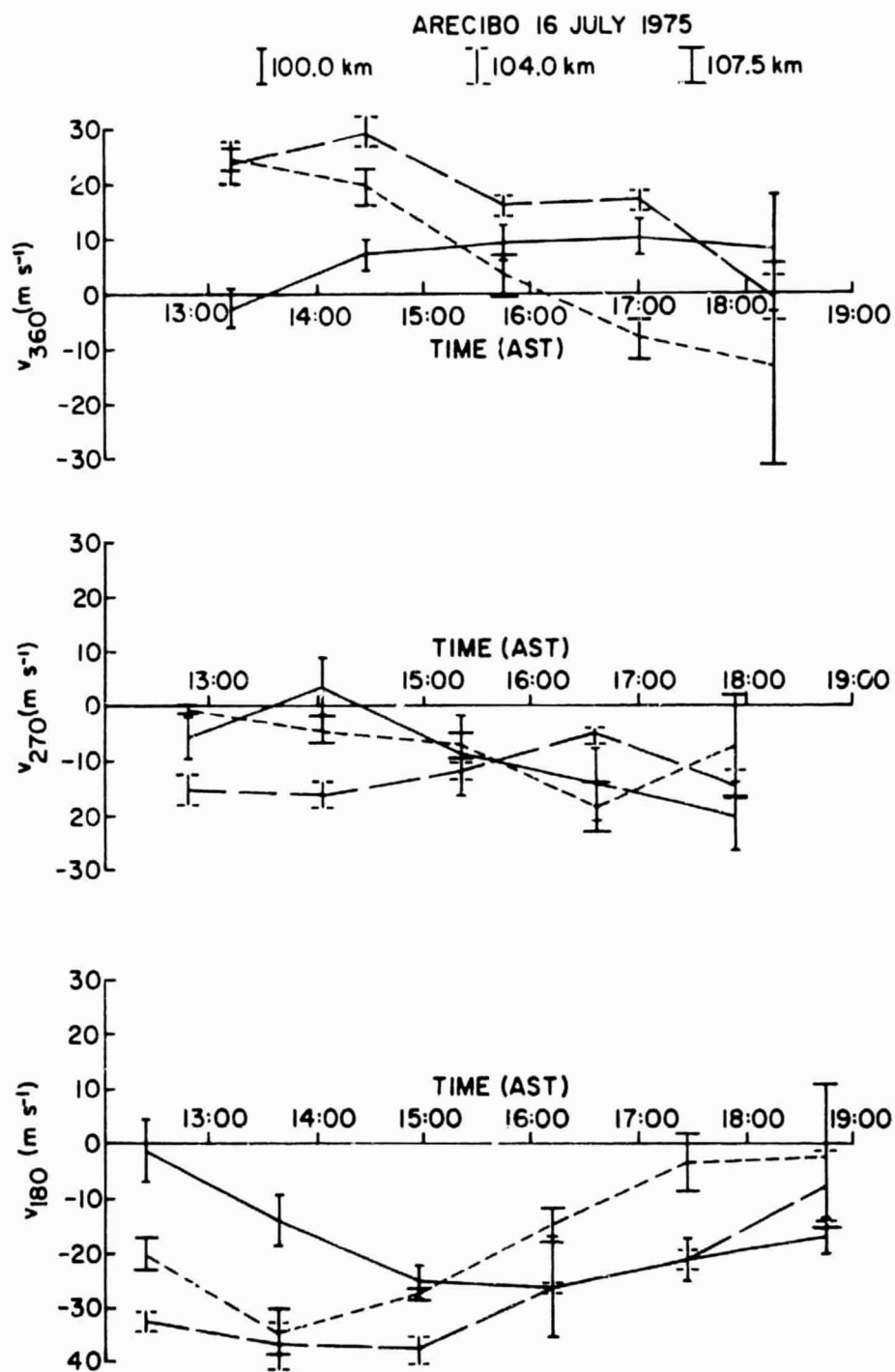


Figure 4.26 Line-of-sight ion drift velocities at altitudes of 100.4, 104.0 and 107.5 km, measured by incoherent-scatter radar on 16 July 1975.

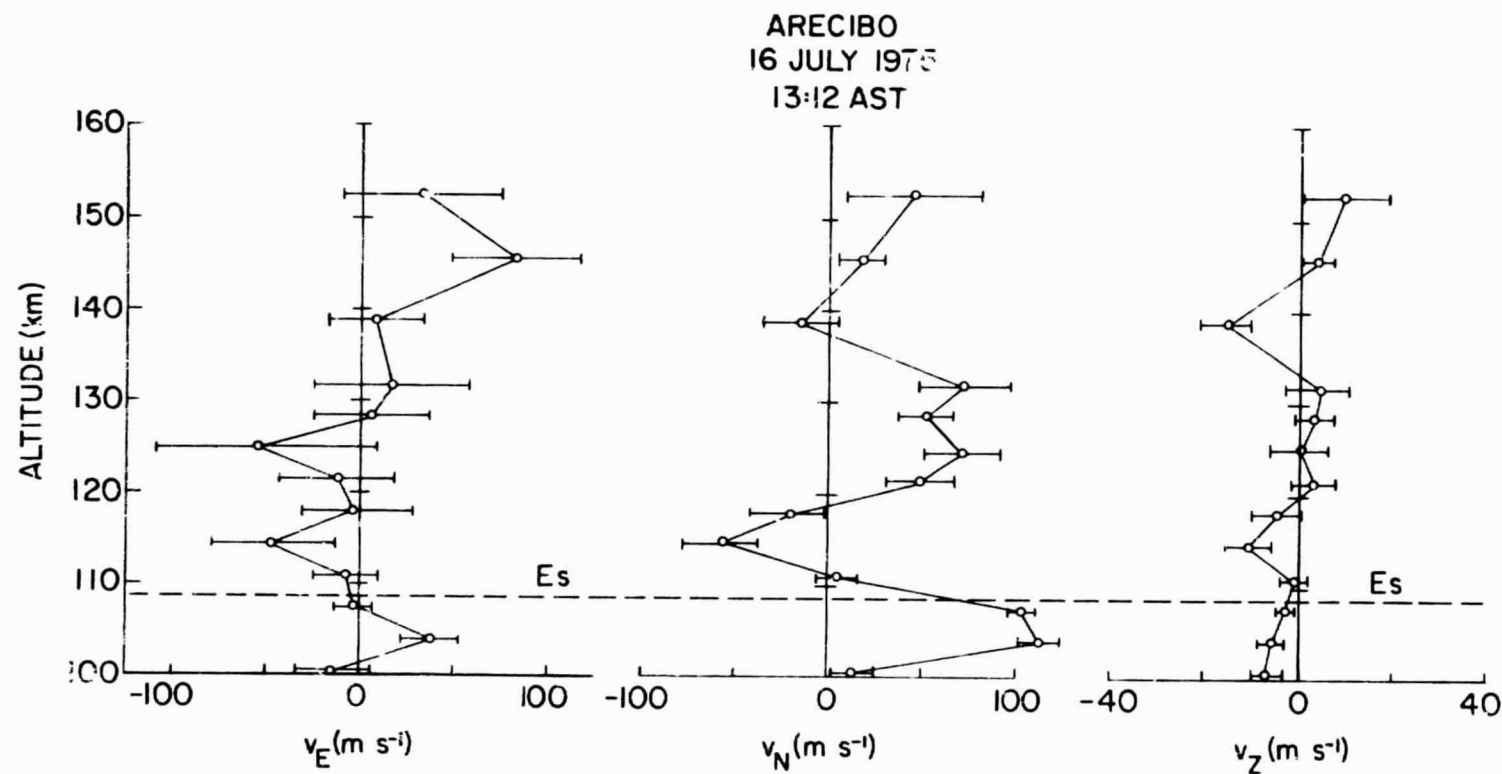


Figure 4.27 Components of the ion drift velocity at 13:12 AST, 16 July 1975. Uncertainties are based on least-squares fit of the data to theoretical autocorrelation functions.

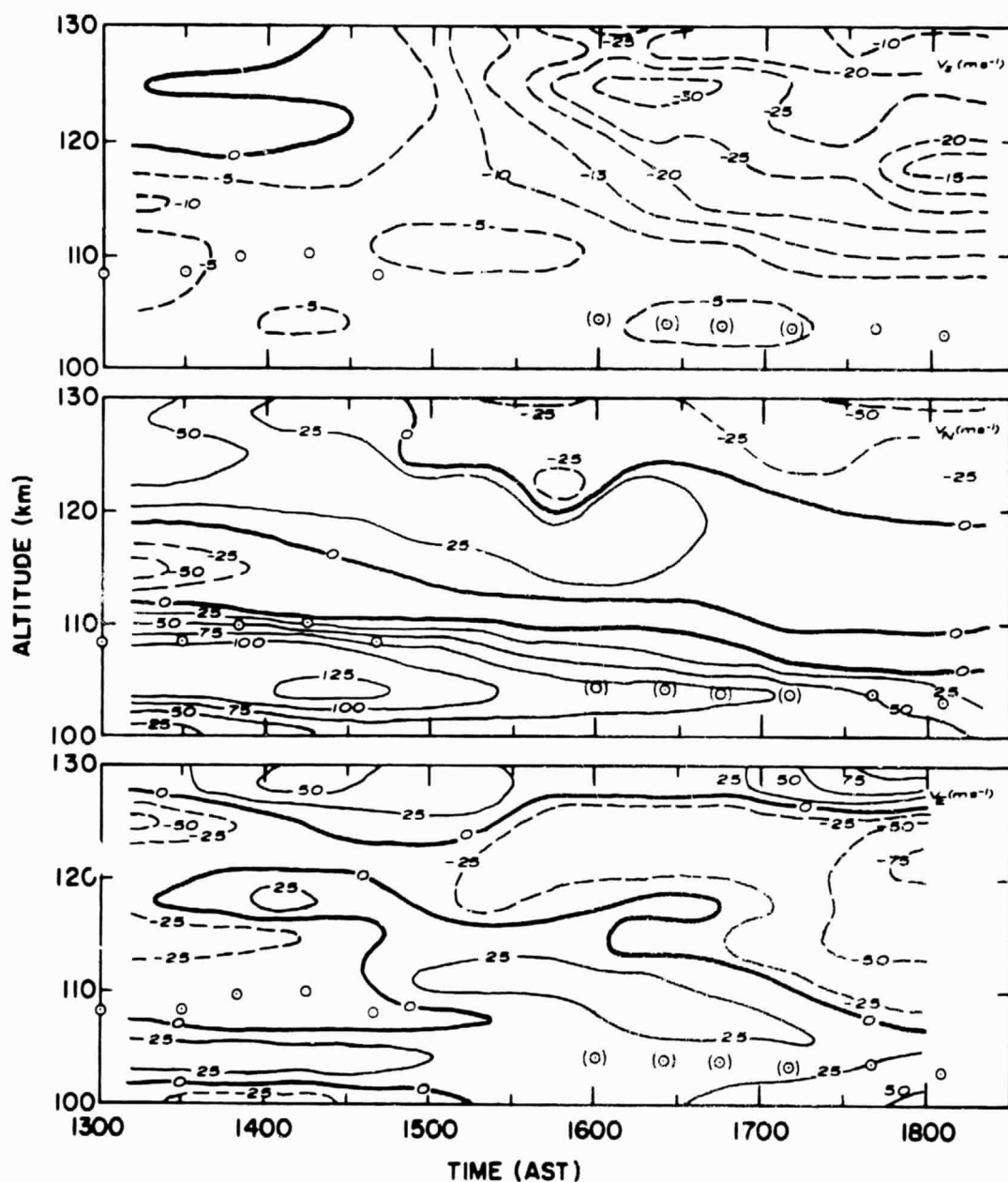


Figure 4.28 Ion drift velocities, 16 July 1975. The altitude of a sporadic-E layer is indicated by the circled points. Parentheses indicate a weak layer.

ionograms, no layer was detected by the incoherent-scatter experiment between about 14:40 and 16:00 AST.

It is also apparent in this figure that the sporadic-E layer is not at an altitude at which the vertical ion drift converges. The general downward velocity is probably the result of an inaccurate estimate of an internal frequency bias in the system [Harper *et al.*, 1975; 1976]. Correction of this bias would not produce vertical convergence at the altitude of the layer. However it will be shown later that the altitude of the layer is consistent with wind shear theory.

4.5.10 17 July 1975, 03:33-08:20 AST. Electron density was measured using phase-coded pulses until 06:16 AST, followed by an ion drift velocity measurement.

Figure 4.29 shows a sequence of scans where contours of electron density are drawn on a plot of altitude and azimuth. The contours represent values of electron density of 1×10^4 and $1 \times 10^5 \text{ cm}^{-3}$. Each scan covers a range of azimuth of approximately 40 deg and is centered on 290 deg. The vertical and horizontal scales in each frame do not give a true spatial representation of the region. The 40 deg range in azimuth represents a distance along the arc of 18.7 km at an altitude of 100 km, and 24.3 km at an altitude of 130 km. Beginning with the first frame in the upper left-hand corner of Figure 4.29, the actual motion of the radar beam is from right to left in the odd-numbered scans, and from left to right in the even-numbered scans.

The most striking feature of Figure 4.29 is the complex structure exhibited by the layers of ionization. At the beginning of the sequence, layers are observed at altitudes of 123 and 108 km. The upper layer remains at a constant altitude for approximately 20 min, and then begins

Figure 4.29 Electron density observed on 17 July 1975. Contours are at 10^4 and 10^5 cm^{-3} . Each scan of the radar beam was between approximately 270° and 310° azimuth.



to descend dissipating at 04:35 AST at an altitude of about 116 km. If the descent is extrapolated, it intercepts the lower layer at 04:40 AST corresponding with an intensification of the lower layer, which, however, remains at constant altitude. The peak electron density in this lower layer is dramatically enhanced, and the profile shows evidence that the layer becomes unstable. Another layer is seen to descend into the layer at 108 km between 04:12 and 04:26 AST, with less effect. The diffuse patch of ionization located just above the lower layer at 03:52 AST may also be noted. Each of these intensifications can be identified with increases in $f_b E_s$ and $f_o E_s$ as shown in Figure 4.30.

An attempt was made to measure the ion velocities between 06:40 and 08:12 AST to aid in the interpretation of the electron-density measurements. However, it was found that the low electron density at that time resulted in large uncertainties and improbably large velocities and no useful data were obtained.

4.5.11 19 July 1975, 11:05-14:22 AST. Perhaps the most dramatic evidence of patchiness in a layer associated with a high value of $f_o E_s$ is found in data taken this day using Barker-coded pulses. A particularly intense sporadic-E layer was present for the entire period. The range of plasma frequencies derived from the maximum and minimum peak electron densities during each scan is compared with $f_b E_s$ and $f_o E_s$ in Figure 4.31. In this experiment, the beam was scanned through approximately 10 deg in azimuth centered at 270 deg.

The irregularity which is represented by the high plasma frequencies near 12:55 AST is shown in more detail in Figure 4.32. The electron-density configuration is shown for twelve successive scans. The azimuth scale has been adjusted so that horizontal and vertical distances

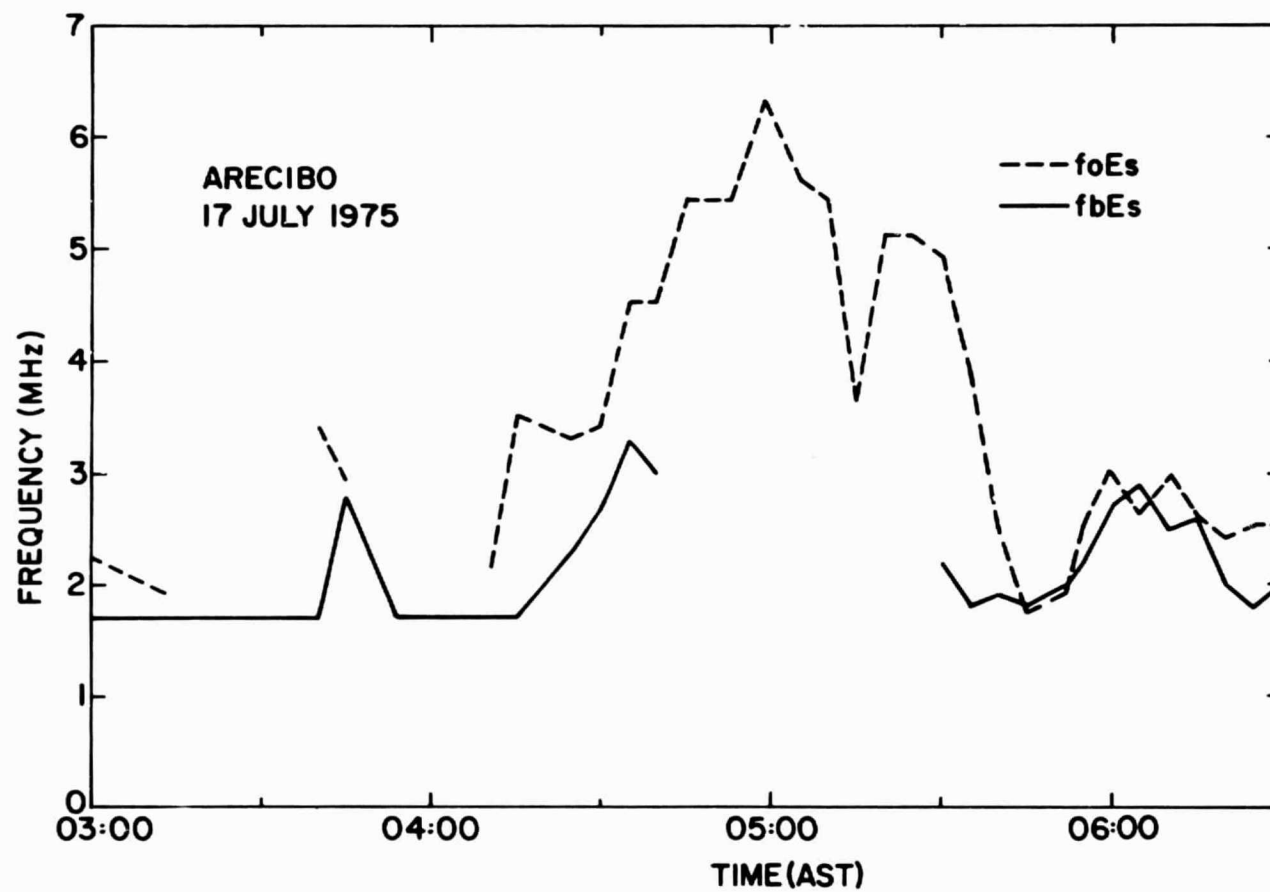


Figure 4.30 $f_b E_s$ and $f_o E_s$ on 17 July 1975.

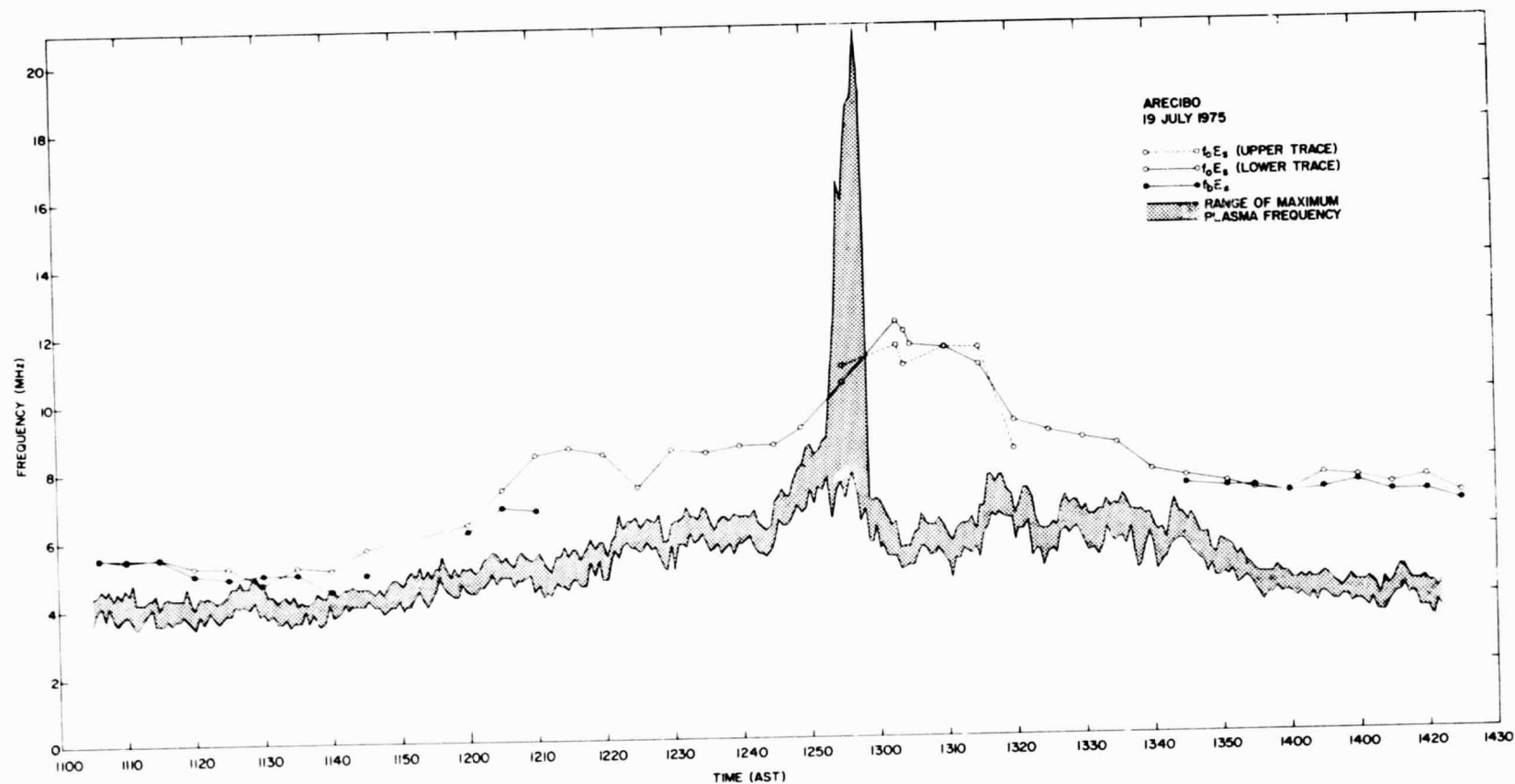


Figure 4.31 f_bE_s and f_oE_s on 19 July 1975. Shaded area represents limits of plasma frequencies derived from incoherent-scatter data.

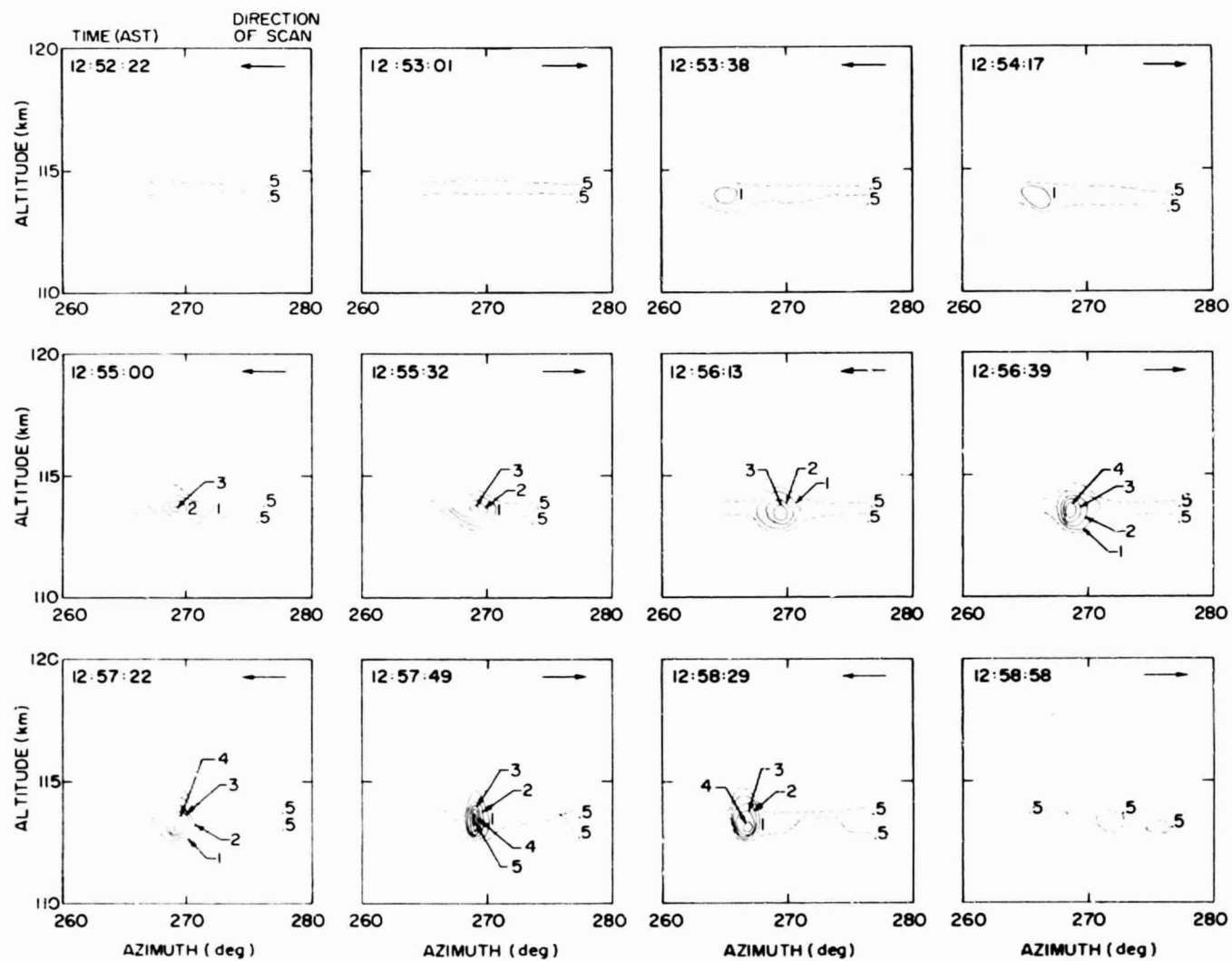


Figure 4.32 Electron density (10^6 cm^{-3}) from a sequence of 12 scans of the radar beam on 19 July 1975. The horizontal distance represented in each frame is approximately 10 km.

represented in the plots are approximately equal. At the time of this observation, the electron density of the *E* region adjacent to the sporadic-*E* layer varied between 9×10^4 and $1.3 \times 10^5 \text{ cm}^{-3}$. In Figure 4.32 the dashed line represents an electron density contour of $5 \times 10^5 \text{ cm}^{-3}$; the solid lines are contours at intervals of $1 \times 10^6 \text{ cm}^{-3}$.

Figure 4.32 shows a very localized irregularity either forming and dissipating rapidly, or drifting through the radar beam. The map of the irregularity as a function of azimuth and scan number is presented in Figure 4.33. Here the volume-averaged electron density recorded by the incoherent scatter is used, without attempting to estimate the maximum electron density. The short scan used in this experiment (~ 10 deg) shows the motion of the irregularity along the arc intersected by the radar beam. However, lack of detailed knowledge of ion drift velocities makes it uncertain whether the apparent motion is the result of a changing velocity of the irregularity in a direction tangent to the scan, or whether the velocity is radial and the irregularity has an elongated shape.

The irregularity is not resolved by the radar and is no larger than either the width of the radar beam (300 m) or the range resolution (600 m). The effect is that the peak electron density of the irregularity cannot be determined. The irregularity is recorded in two gates, part in one at 113.05 km and part in one at 113.63 km. The volume-averaged values at these gates at 12:57:42 AST are 5.41×10^6 and $5.18 \times 10^6 \text{ cm}^{-3}$, respectively. The peak electron density must be greater than, and may be much greater than, the larger of these two values.

4.5.12 20 July 1975, 10:55-15:23 AST. Ion drift velocity measurements using the multiple-pulse experiment were made from 10:55 to 12:07 and from

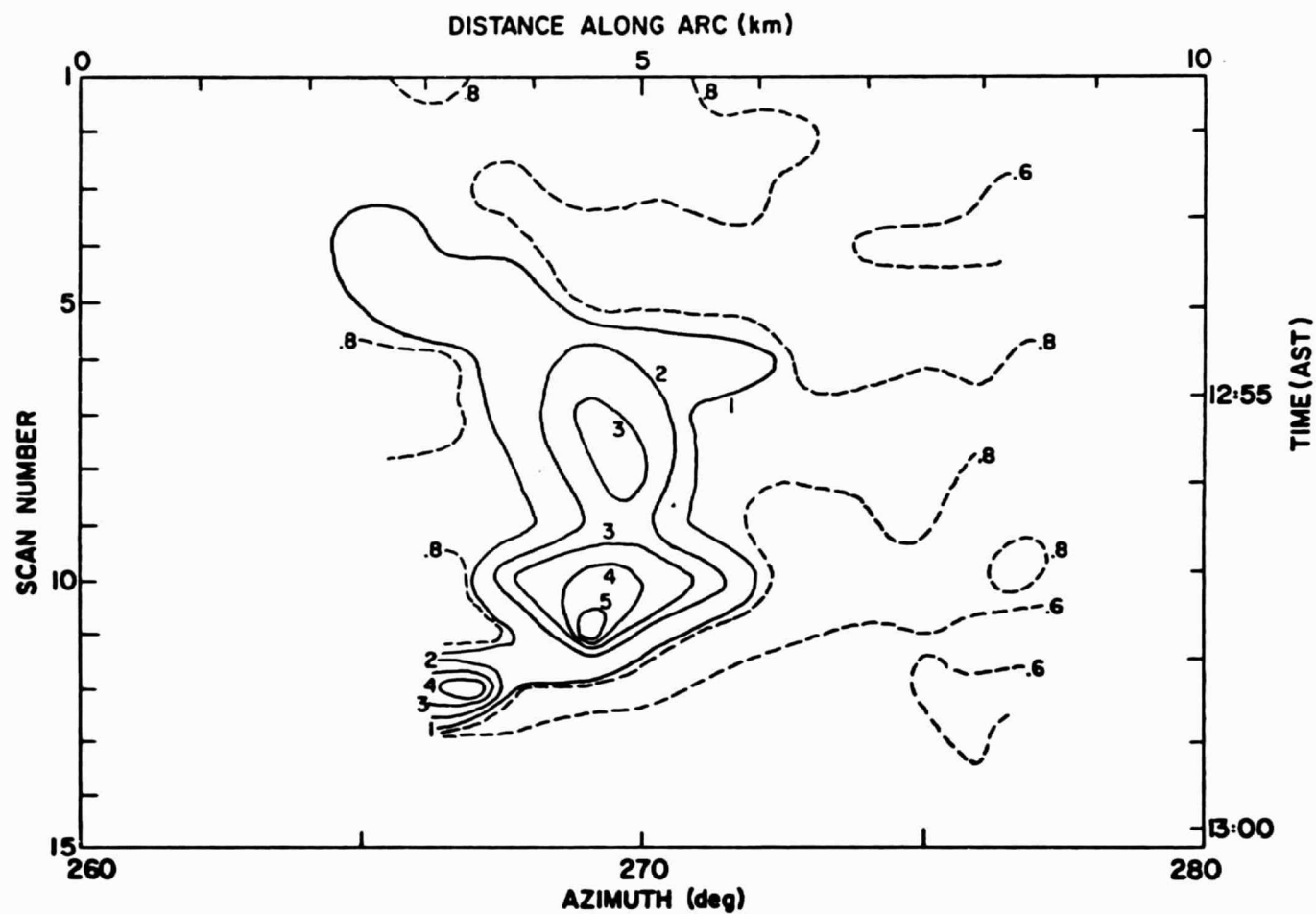


Figure 4.33 Representation of maximum density (10^6 cm^{-3}) of a portion of the sporadic-E layer observed on 19 July 1975 between 12:52 and 13:00 AST. The direction of the odd-numbered scans are toward decreasing azimuth.

13:51 to 15:23 AST. Hodographs of the horizontal velocities are shown in Figure 4.34, together with a profile of vertical velocities. The zonal (east-west) component is seen to be predominant, especially during the morning observation.

Sporadic-*E* layers were observed at altitudes of about 102 km in the morning and 103 km in the afternoon. In both cases, the layers were located on a strong east-west shear in the ion drift velocity. However as in the earlier case described in Section 4.5.9, their positions do not correspond to locations of vertical convergence.

Electron-density profiles were observed by Barker-coded pulses between 12:17 and 13:37 AST. The sporadic-*E* layer was found to be centered at an altitude of 102.5 km. The structure observed in this layer is illustrated in Figure 4.35. The interval between contours is $2.5 \times 10^4 \text{ cm}^{-3}$. This observation is an example of rather minor irregularities in a sporadic-*E* layer.

4.5.13 21 July 1975, 19:52-24:00 AST. The observation was begun at 19:52 with no sporadic *E* indicated in the data from the ionosonde, shown in Figure 4.36. The transmitter was inoperative between 21:00 and 21:38 AST. During this interval *ftEs* built up to 6 MHz. By the time the observations were begun again, *ftEs* had dropped to 4.2 MHz, and continued to decrease until the sporadic-*E* trace disappeared at 22:05 AST. The incoherent-scatter radar detected a sporadic-*E* layer with a thickness of about 4 km centered at an altitude of 112 km. The peak electron density of this layer decreased steadily until 22:06 AST after which it was not detected.

Later, starting at 22:27 AST, a layer was observed which developed unusual structure. Consecutive scans are shown in Figure 4.37. The

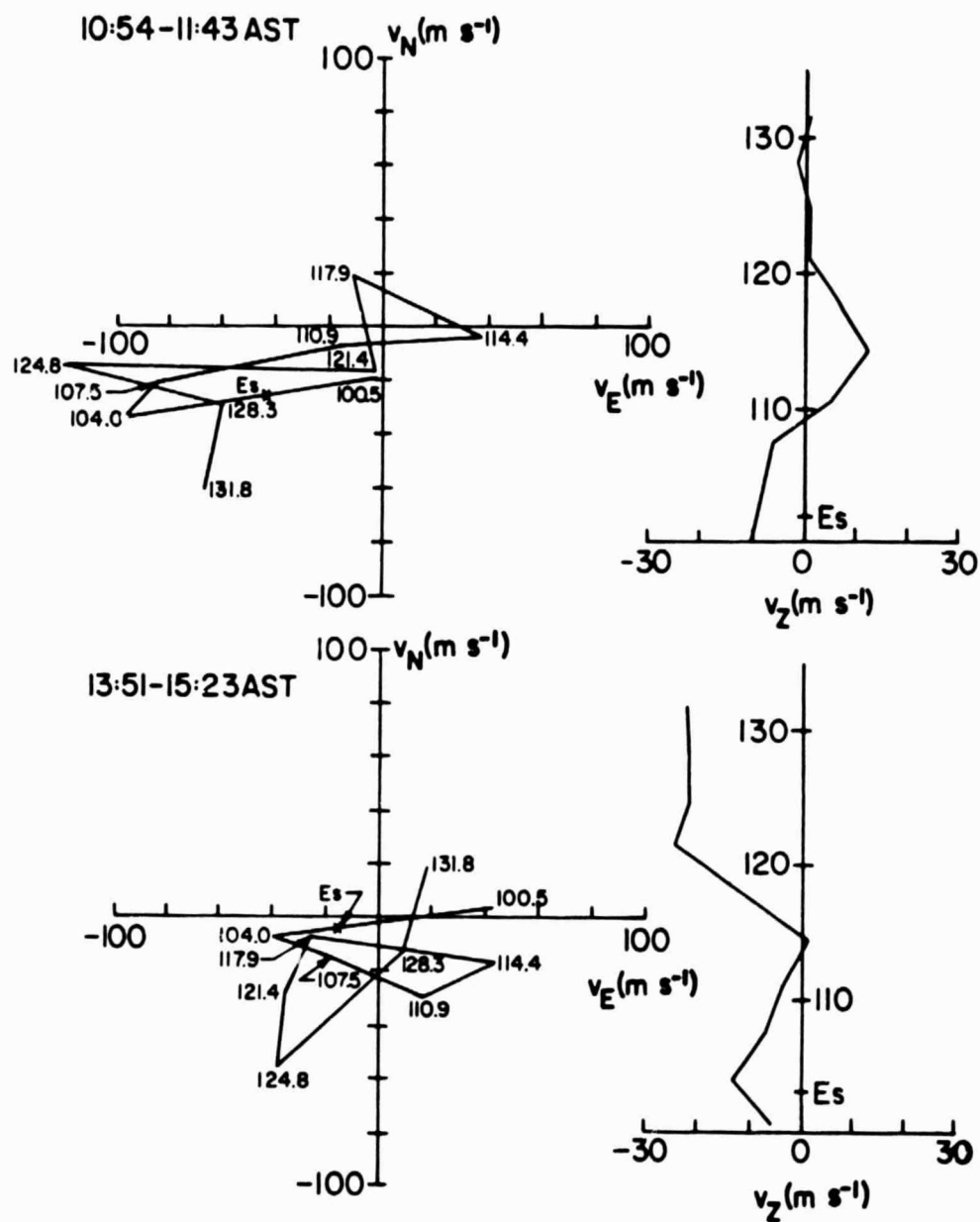


Figure 4.34 Ion drift velocities, 20 July 1975.

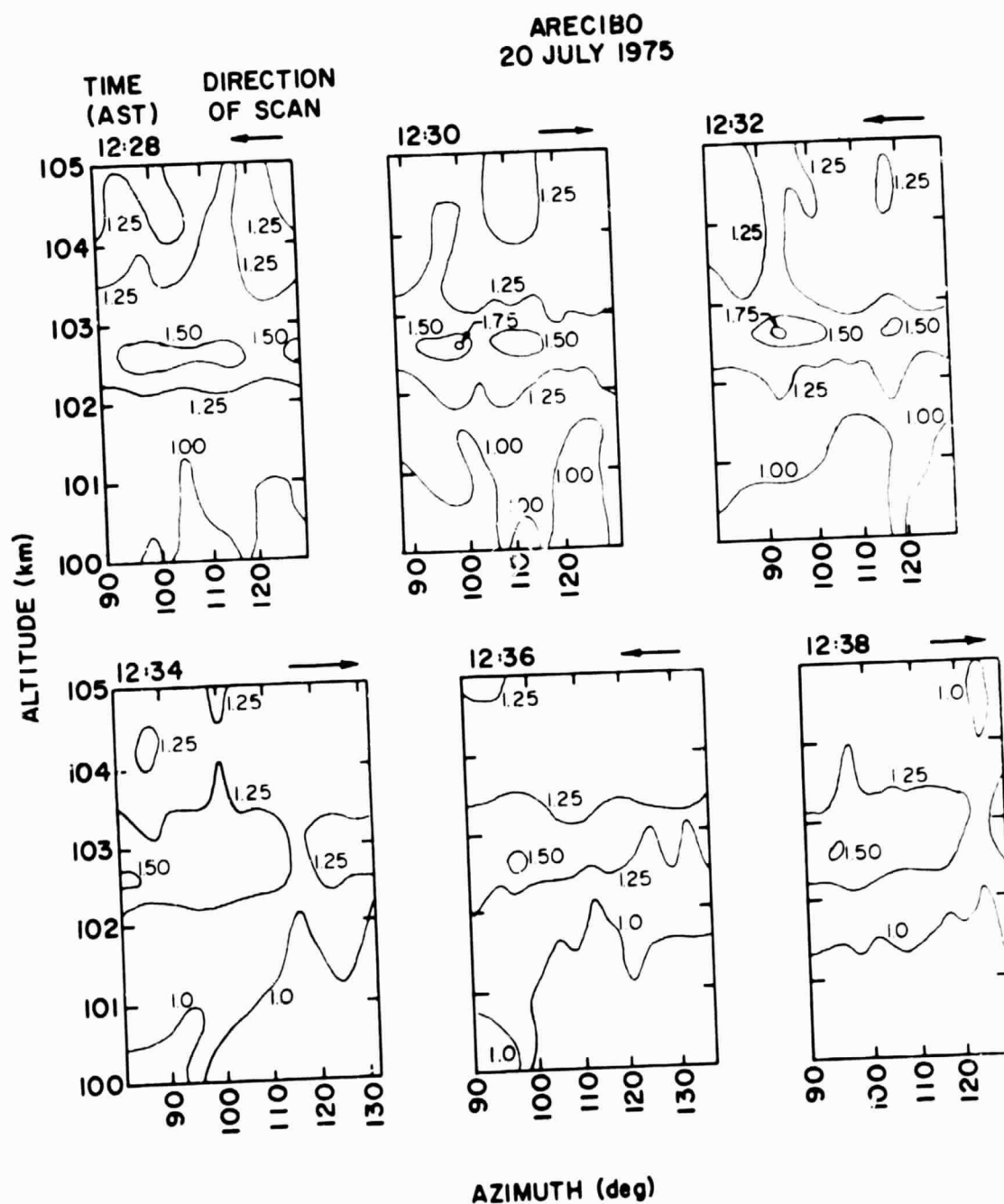


Figure 4.35 Electron density (10^5 cm^{-3}) from a sequence of scans of the radar beam on 20 July 1975.

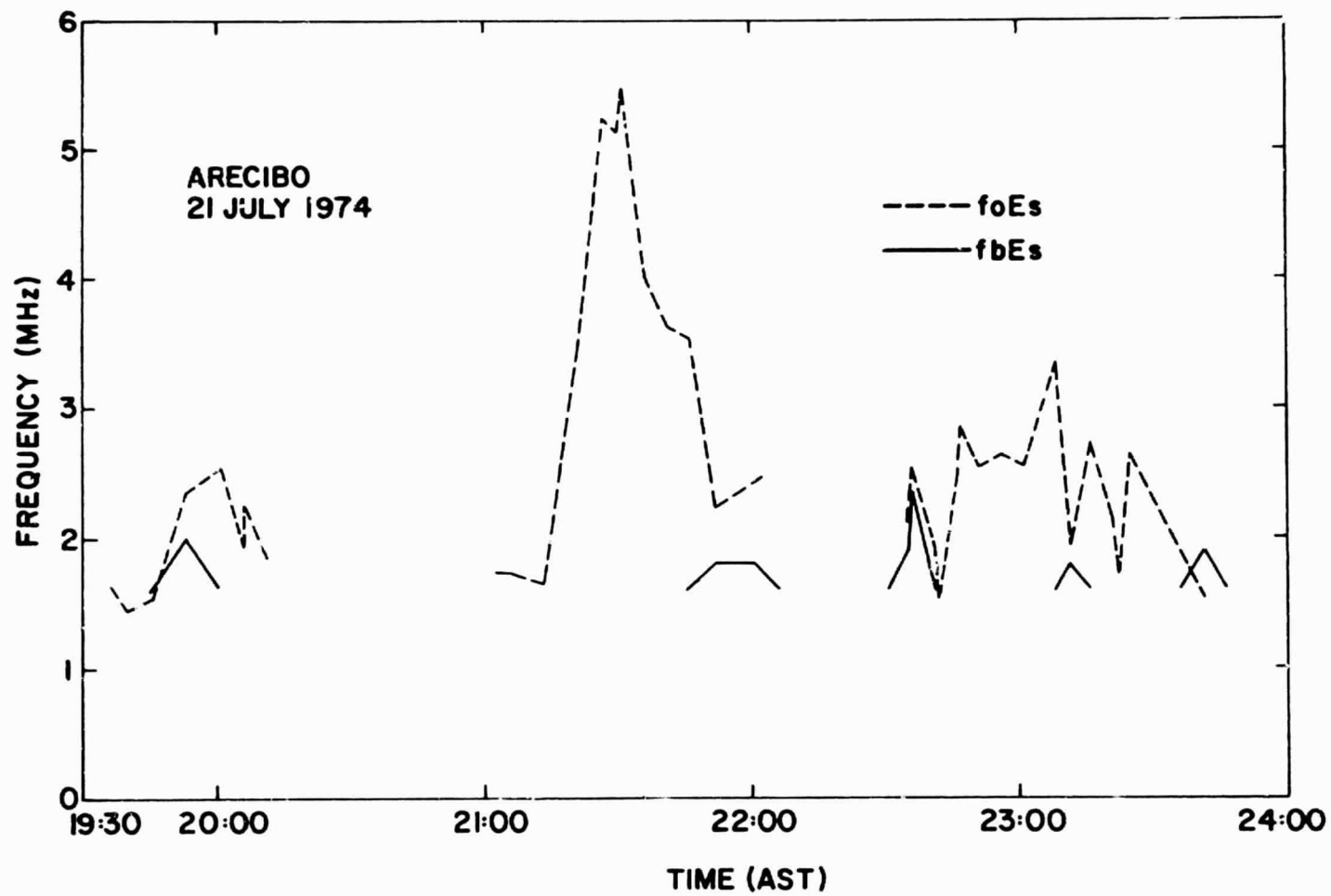


Figure 4.36 *fbEs* and *foEs* on 21 July 1975.

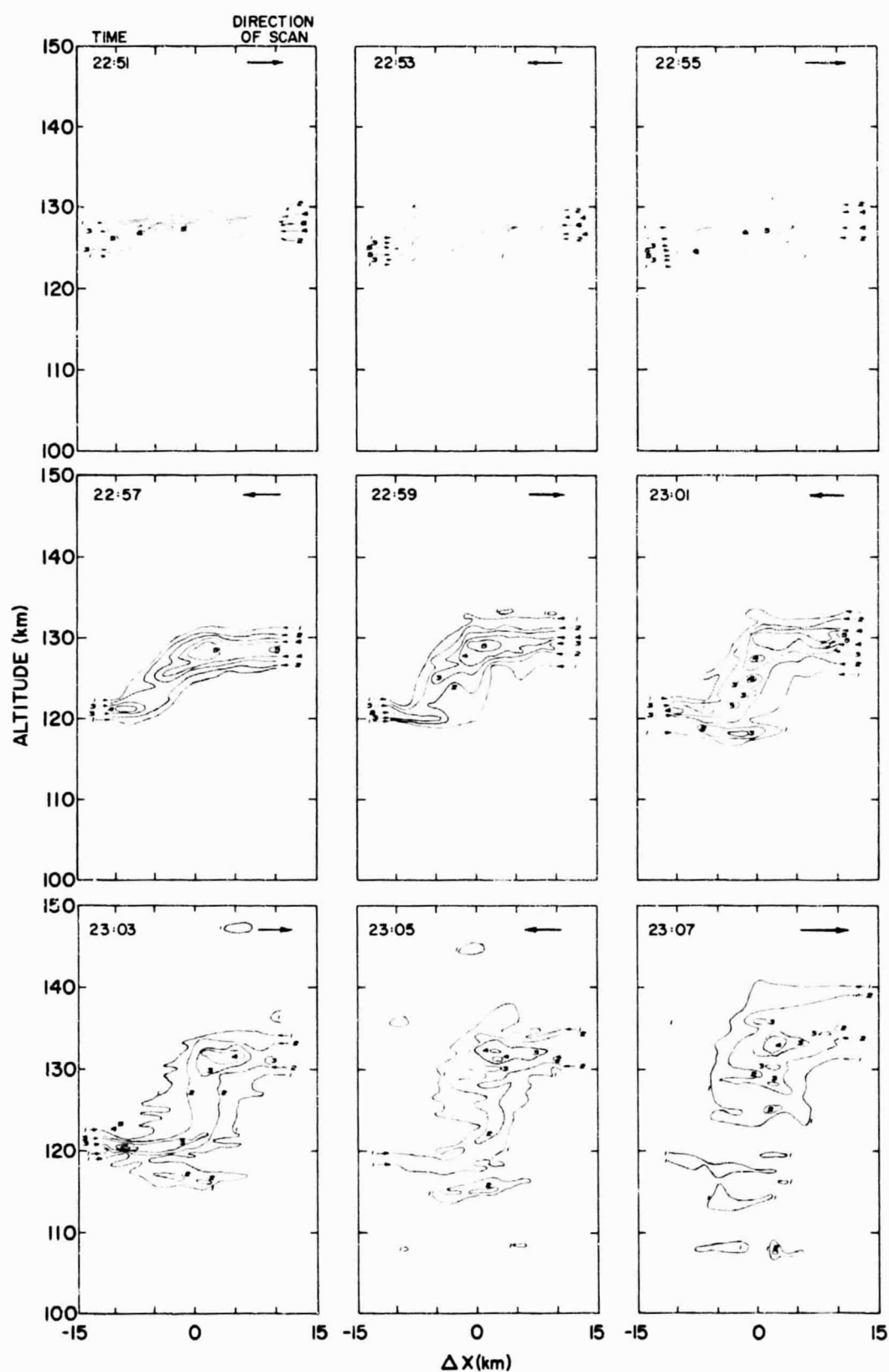


Figure 4.37 Electron density (10^4 cm^{-3}) from a sequence of scans of the radar beam on 21 July 1975.

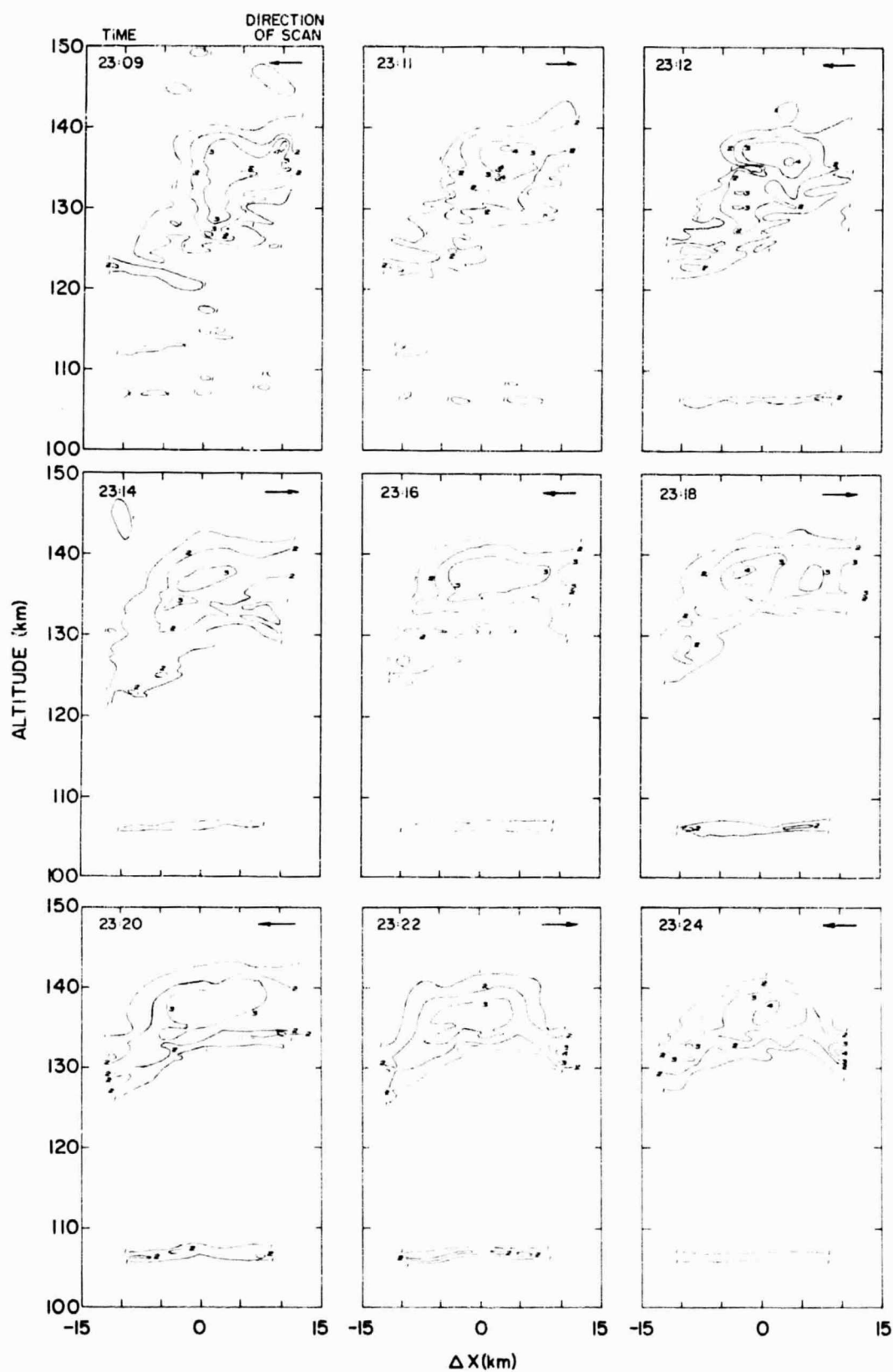


Figure 4.37 (Continued).

range of scan is 40 deg, centered on 290 deg. The layer of ionization had formed at an altitude of 127 km. The ionization at one end of the region being observed suddenly began to descend. By 23:12 AST, this ionization had re-formed into a layer at 106 km. At the same time, the part of the layer at the other end ascended to 135 km.

4.5.14 23 July 1975, 03:11-08:05 AST. Electron-density profiles were measured from 03:11 to 06:00 AST with no sporadic-E layer being observed. The ion drift velocities, measured between 06:10 and 08:05 AST, have large uncertainties. However, the magnitudes of the velocities, shown in Figure 4.38, are not unreasonable. A sporadic-E layer was observed during the multiple-pulse experiment at an altitude of 101.5 km, which was also near a convergence point of the vertical motion.

4.5.15 26 July 1975, 09:07-16:47 AST. It had been noticed that ionograms often showed sporadic-E traces in the midmorning as was the case on this day. The data on f_oE_s and f^bE_s are shown in Figure 4.39. An incoherent-scatter-radar observation was made from 09:07 to 09:42 AST. Although f^tE_s reached 4.2 MHz, no sporadic-E layer was detected by the incoherent-scatter radar. However, the vertical-electron-density profiles appeared to have a very irregular structure. A profile measured at 09:12 AST, a maximum of f^tE_s , is shown in Figure 4.40. Any irregularities observed in the vertical profile on this occasion were of limited horizontal extent, and do not represent layering. This is the only occasion when electron-density observations were attempted in midmorning and structure of this type was not seen at other times of day.

Ion drift velocities were measured during two periods, 10:10 to 11:25 AST and 15:03 to 16:47 AST. Horizontal and vertical velocities for both periods are shown in Figure 4.41. Data from the morning observation

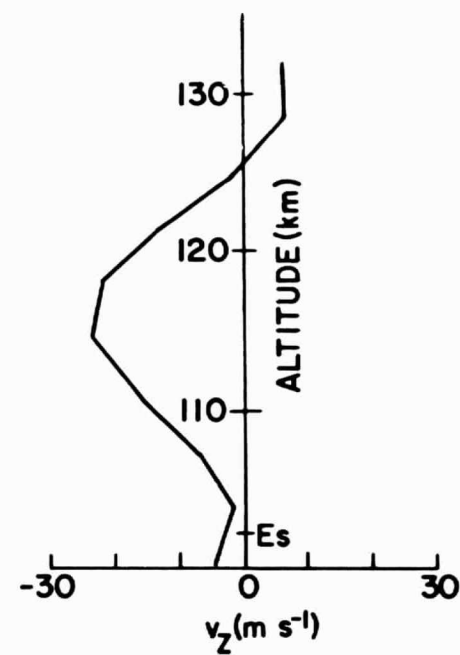
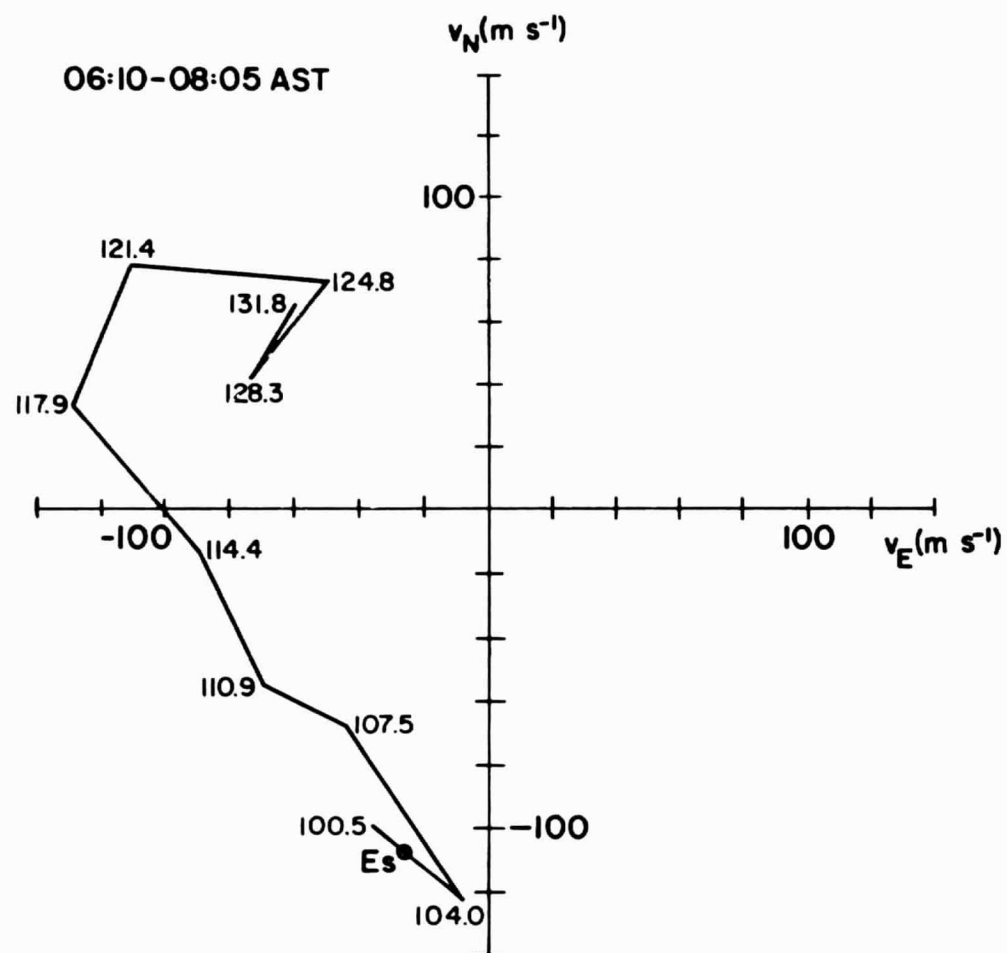


Figure 4.38 Ion drift velocity, 23 July 1975.

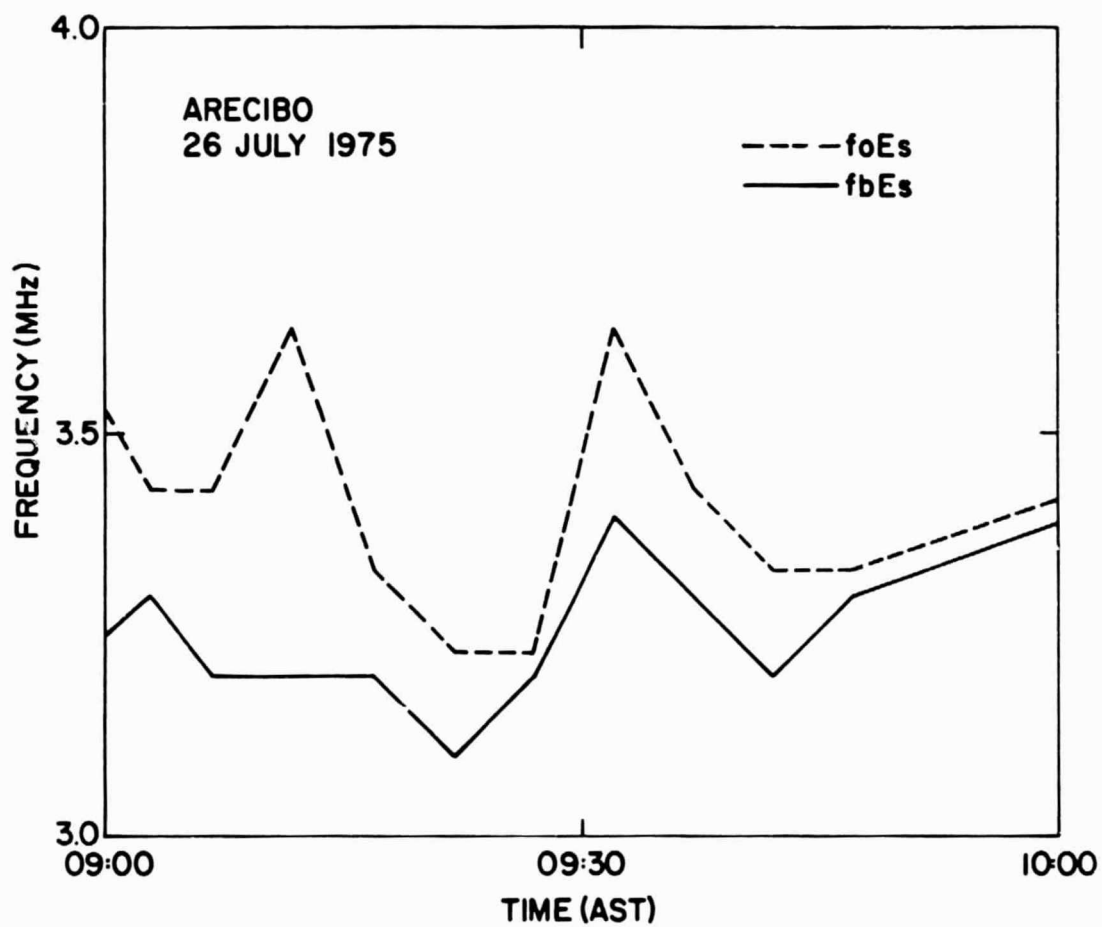


Figure 4.39 $fbEs$ and $foEs$ on 26 July 1975.

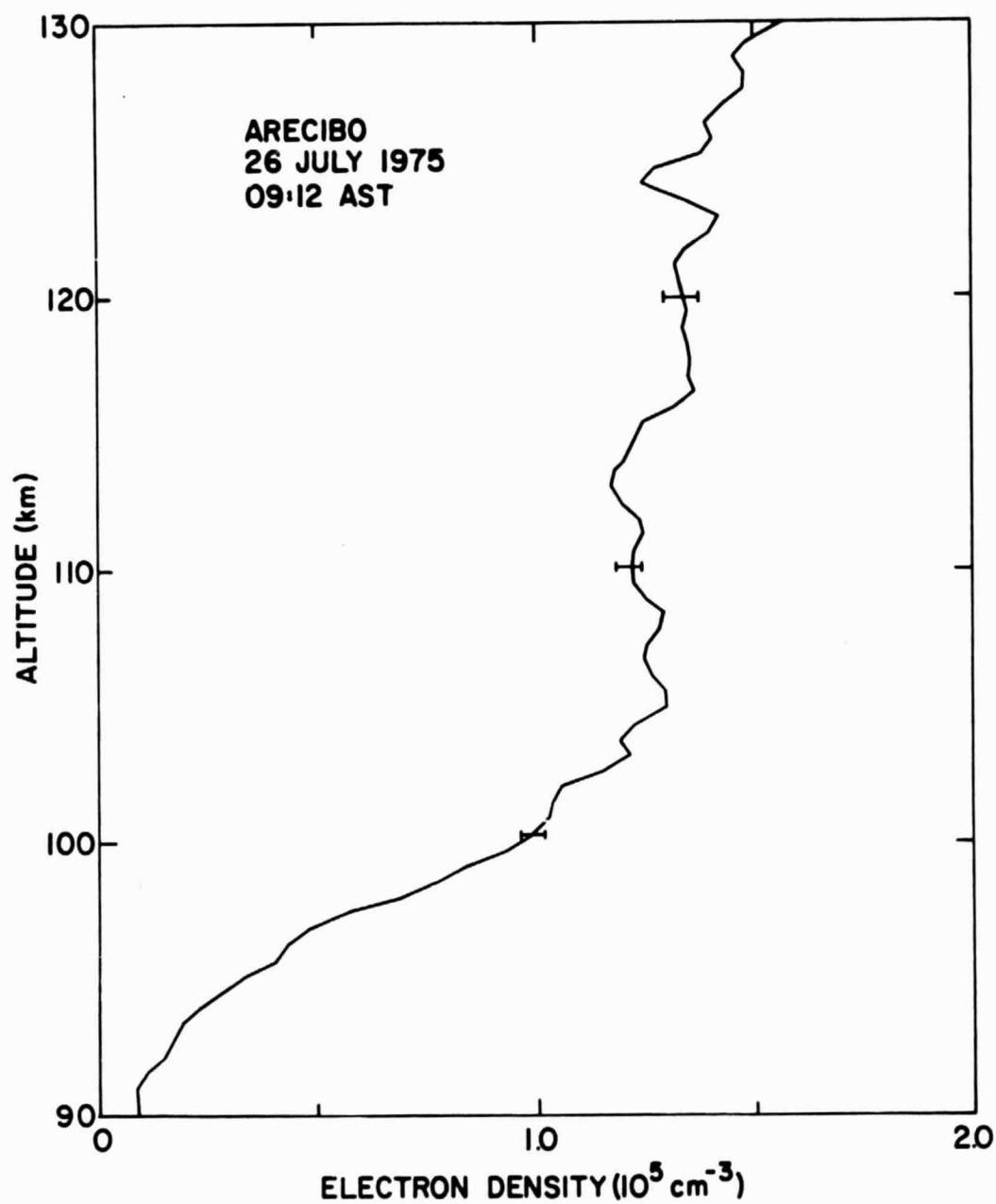


Figure 4.40 Electron-density profile measured by incoherent scatter radar at 09:12 AST on 26 July 1975. A three point weighted average was used to smooth the profile.

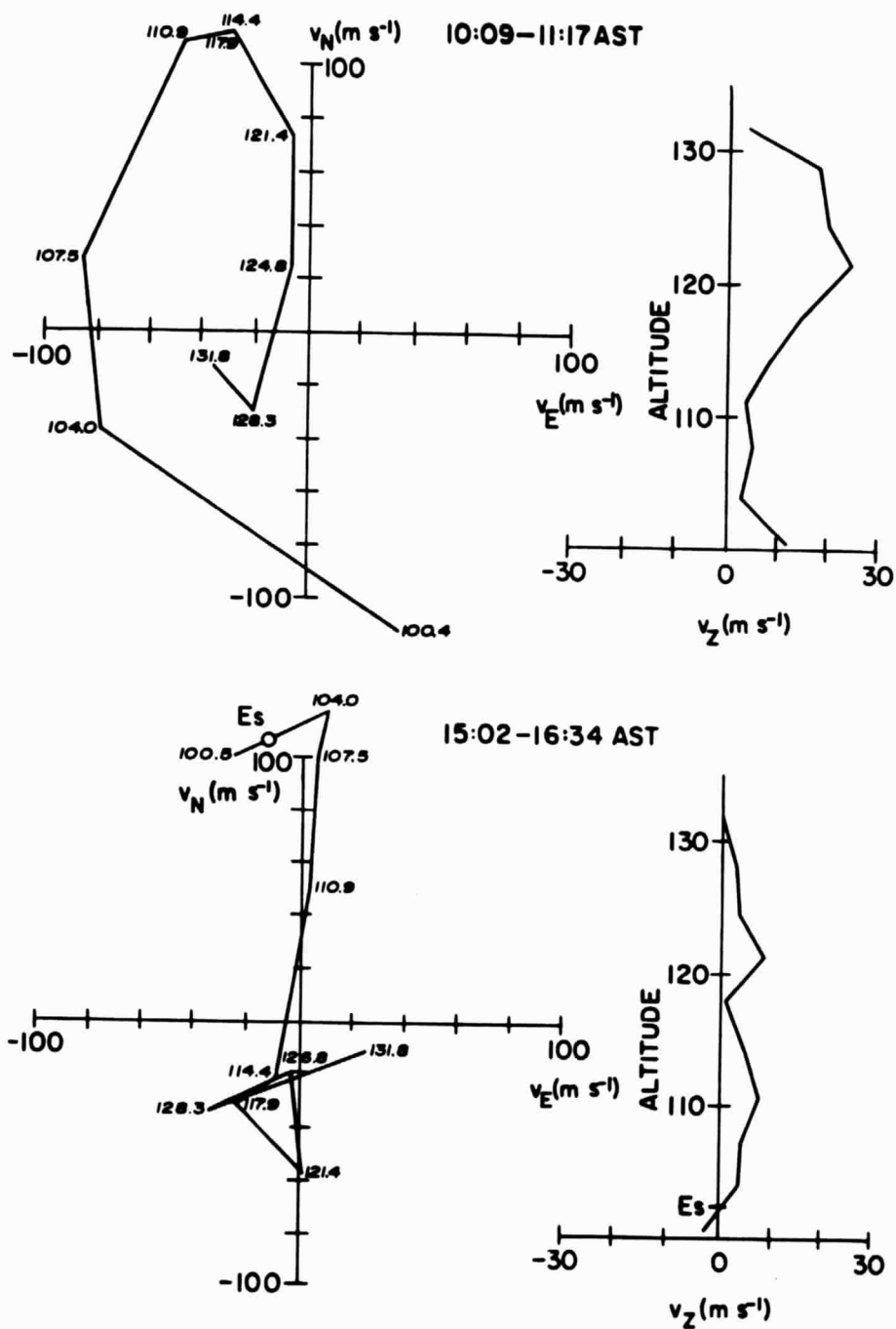


Figure 4.41 Ion drift velocities, 26 July 1975.

shows a smoothly spiraling hodograph and no nulls in the vertical-ion-velocity profile. No sporadic-*E* layer was present in scattered-power profiles, although the ionosonde showed $fbEs \approx 3.5$ MHz and $ftEs \approx 4.0$ MHz.

The afternoon ion drift velocity measurement shows strong velocities to the north at the lower altitudes, ceasing abruptly at about 111 km. A sporadic-*E* layer at 101.5 km is on shear in the east-west ion velocity. However, both the sense of the shear and the vertical velocity information indicate that the ionization should diverge at that altitude.

Between the two velocity measurements electron density was observed, from 11:33 to 14:50 AST, using Barker-coded pulses. A weak sporadic-*E* layer was found at an altitude of 97 km. Plasma frequencies of the maximum and minimum peak electron densities are compared with $fbEs$ and $foEs$ in Figure 4.42. Enhancements of the layer with a periodicity of approximately 15 or 20 min are apparent in the sporadic-*E* layer. The enhancement of the electron density of the layer is accompanied in most cases by development of wave-like structure. Six scans showing the enhancement at 13:39 AST are presented in Figure 4.43.

4.5.16 26 July 1975, 19:44-21:37 AST. Electron-density profiles were again measured between 19:44 and 21:37 AST. A very weak sporadic-*E* layer was observed at an altitude of 93 km. A second layer begins to form at 97 km at 20:40 AST. The two layers, shown in Figure 4.44, merge at 21:09 AST and form a 4-km thick layer centered at about 96 km. The layer then descended slowly, until at the end of the observation it was centered at 94 km.

4.5.17 27 July 1975, 11:25-15:02 AST. Electron-density profiles recorded between 11:25 and 15:02 AST showed weak layers near 95 and 120 km. The profile at 12:55 AST is shown in Figure 4.45. No significant small-scale horizontal structure was observed. Although a weak *F*-region

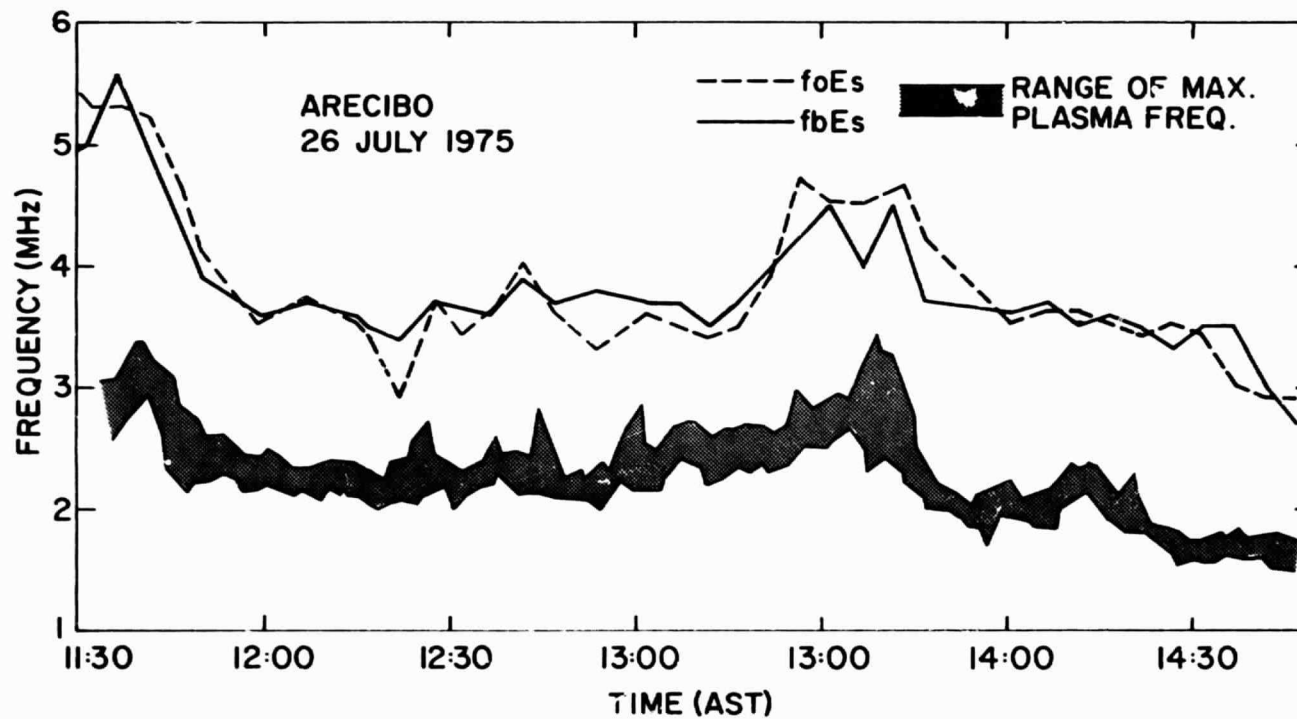


Figure 4.42 *fbEs* and *foEs* on 26 July 1975. Shaded area represents limits of plasma frequencies derived from incoherent-scatter data.

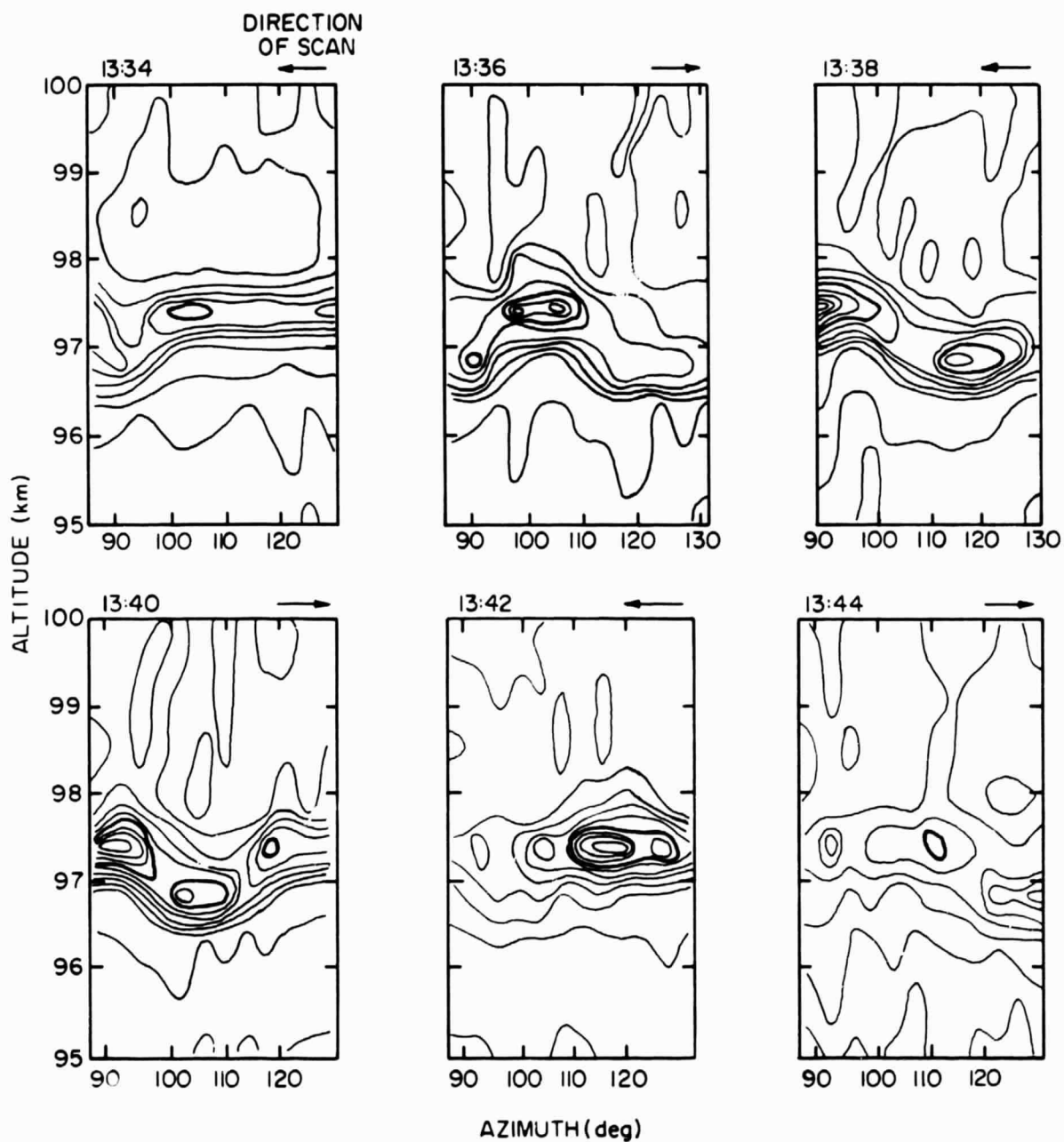


Figure 4.43 Electron density from a sequence of scans of the radar beam on 26 July 1975. Contours are at intervals of $1 \times 10^4 \text{ cm}^{-3}$ in electron density. The contour at $1 \times 10^5 \text{ cm}^{-3}$ has been darkened.

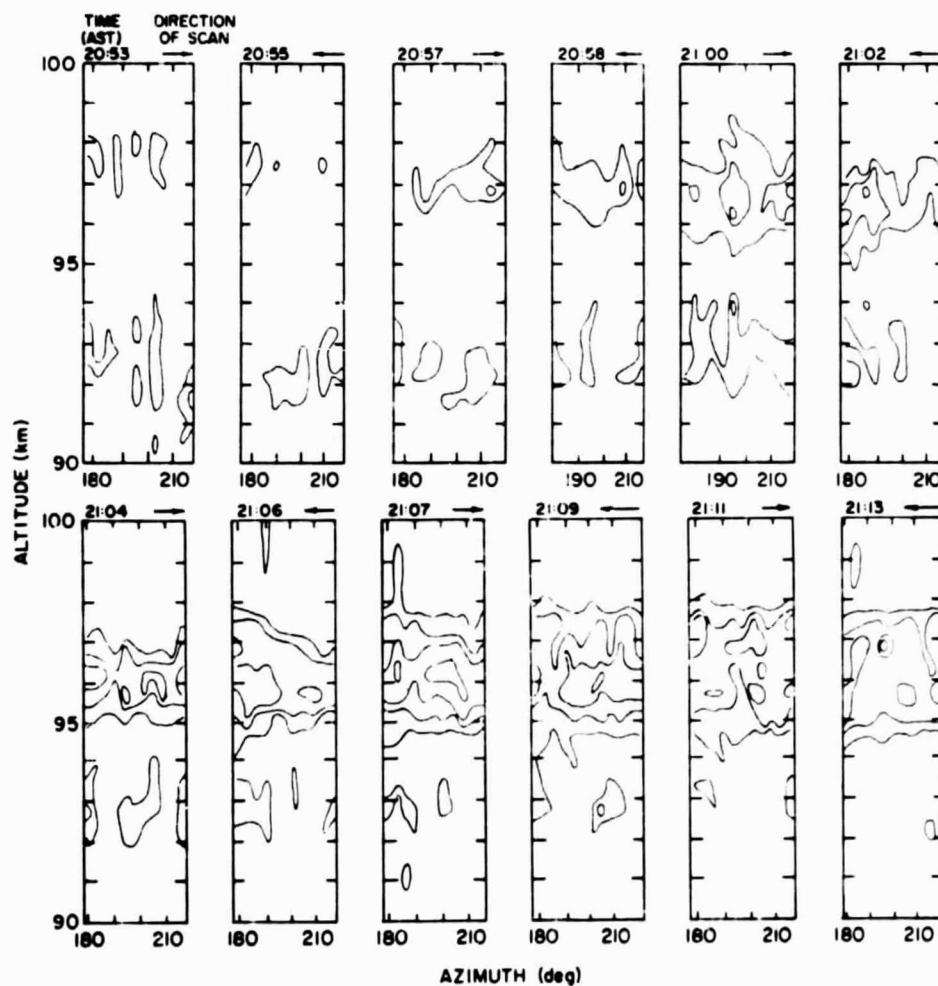


Figure 4.44 Electron density from a sequence of scans of the radar beam on 26 July 1975. Contours are at intervals of $5 \times 10^5 \text{ cm}^{-3}$.

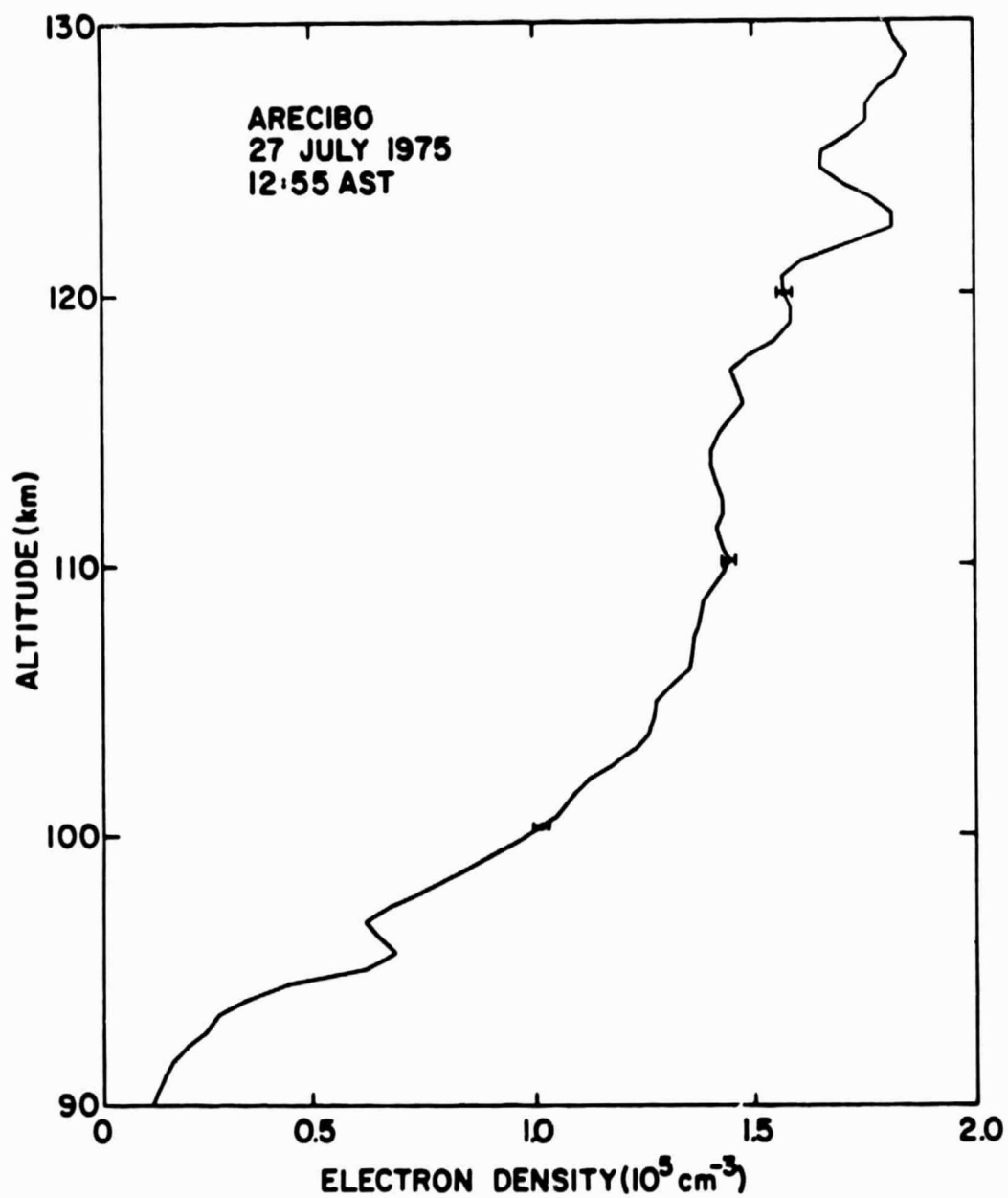


Figure 4.45 Electron-density profile measured by incoherent-scatter radar at 12:55 AST on 27 July 1975. A three-point weighted average was used to smooth the profile.

trace on ionograms made determination of $f_b E_s$ impossible, $f_t E_s$ remained nearly constant at 3.9 MHz.

4.6 *Comparison of Ionosonde and Incoherent-Scatter-Radar Observations*

4.6.1 *Effect of volume averaging.* The horizontal variation seen in the sporadic- E layers discussed in Section 4.5 shows a correlation between the presence of small regions of enhanced electron density and the partial transparency of sporadic- E layers at frequencies greater than $f_b E_s$ when allowance is made for a time delay resulting from a separation of the regions of the layer being sampled by the incoherent-scatter radar and ionosonde (see Figures 4.12, 4.14, 4.23, 4.30, 4.31, and 4.36). In Figure 4.31, the F region was blanketed by the sporadic- E layer so that $f_b E_s$ could not be determined during the time when the intense irregularity was observed. However, a large increase in $f_o E_s$ occurred at that time when the irregular structure was observed.

In the observations presented here, the peak electron density given by incoherent scatter is less than the peak electron density implied by the ionosonde observations. In the case of the layer observed on the evening of 24 January 1974, Section 4.5.6, the magnitude of the electron density at the peak of the layer given by the incoherent-scatter experiment is 28 percent of the density derived from the blanketing frequency. This can be explained by postulating that the thickness of the layer is less than the altitude resolution of the radar (600 m). A triangular sporadic- E profile that is approximately 300 m in total thickness would reconcile the data from the ionosonde with the data from incoherent scatter. It is apparent that with such thin layers the present method of investigation is unable to determine accurately the exact peak electron density of the layer.

The layers with large values of peak electron density were found to be substantially thicker than the evening layer just described, usually contributing to the electron density in three successive height gates. Peak electron densities appear to be about 70 percent of densities indicated by the ionosonde data. In Section 4.4.1, using electron-density profiles for rockets, it was shown that the effect of volume averaging in the incoherent-scatter data is to give peak electron densities which are between 50 and 90 percent of the actual peak electron density, the variation depending on the actual location of the range gate relative to the layer. This effect accounts for the range of plasma frequencies (i.e., the shaded area in the figures) being below the region bounded by f^oEs and fEs .

4.6.2 *Effect of limited sampling.* Although small regions with relatively high electron densities were observed, for example, on 28 January 1974 (Figure 4.23), the highest density was $3.1 \times 10^5 \text{ cm}^{-3}$, whereas an electron density of $7.1 \times 10^5 \text{ cm}^{-3}$ is required to explain fEs on the basis of total reflection. This apparent low electron density is, in part, the result of volume averaging. Interpretation of the data must also take account of the percentage of the layer actually being sampled by the incoherent-scatter radar. An estimate of the motion of the layer observed on 28 January 1974 can be made from the rate of drift of the patches across the data map shown in Figure 4.20 and from the time lag apparent in Figure 4.23 between features in the fields of view of the ionosonde and the radar. The sporadic-E layer appears to be moving at approximately 85 m s^{-1} on an azimuth of 190 deg. The scan pattern of the beam, Figure 4.46, is confined to a strip 17.5 km in width. The beam, 300 m in diameter at 100 km altitude, samples 4.5% of the total area of the strip.

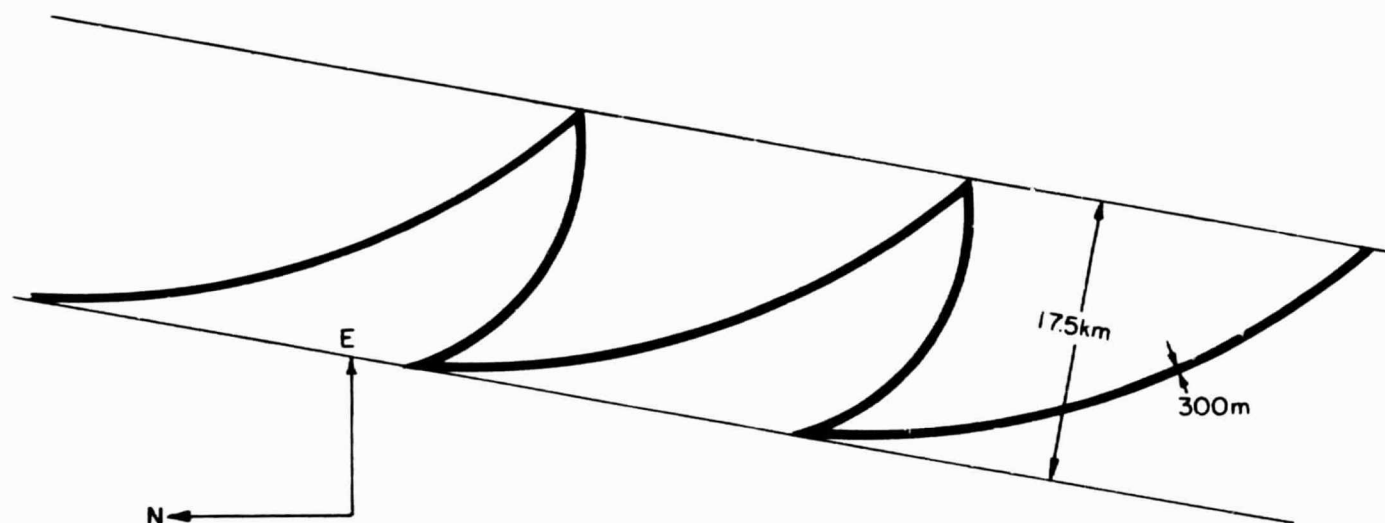


Figure 4.46 Beam pattern in the reference frame of the sporadic-E layer observed on 28 January 1974. Motion of the layer is 85 m s^{-1} at an azimuth of 190° . The radar is scanning between 210° and 270° .

A statistical analysis was made of the data taken on 28 January 1974 between 13:45 and 13:52 AST, when electron-density irregularities were observed. A histogram of the number of observations of peak electron densities in intervals of $3 \times 10^4 \text{ cm}^{-3}$ is shown in Figure 4.47. Each observation is the result of integrating 3000 samples and represents an average electron density in approximately 4 s of time or 2 km of horizontal distance. The frequency of occurrence of electron densities greater than $1.4 \times 10^5 \text{ cm}^{-3}$ decreases exponentially with increasing electron density, indicating the possibility that higher electron densities were present within the layer, but not observed.

As was mentioned, only about 4.5% of the region is actually sampled by the incoherent-scatter measurement. If it were possible to measure electron densities in the entire region, the number of observations in Figure 4.47 would presumably be increased by a factor of $(0.045)^{-1}$. The extended exponential decrease of observations with electron density shown in Figure 4.47 would then predict one observation at the electron density where the present curve is equal to 0.045.

If it is accepted that the values of electron density shown in Figure 4.20 are underestimated by a factor of 0.7 because of volume averaging, then an electron density of $7 \times 10^5 \text{ cm}^{-3}$, corresponding to the maximum value of f_oE_s in the ionogram (7.5 MHz), would appear as an electron density of $4.9 \times 10^5 \text{ cm}^{-3}$ in the incoherent-scatter data.

Following the above line of reasoning, a point has been included in Figure 4.47 at an electron density of $4.9 \times 10^5 \text{ cm}^{-3}$ and a number of observations equal to 0.045, as predicted by the ionosonde observation. There is good agreement between this point and the extension of a least-squares fit to the incoherent-scatter data. Thus, it is probable that an

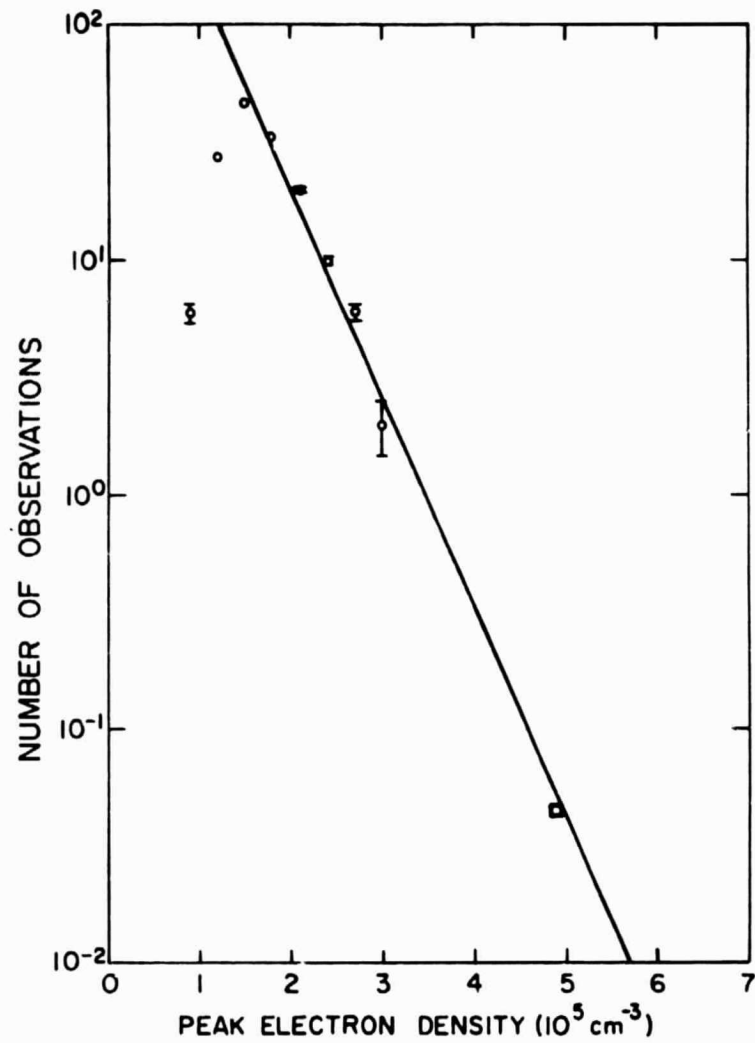


Figure 4.47 Frequency of occurrence of peak electron densities between 13:45 and 13:50 AST on January 1974 (circles), and prediction based on maximum f^oF_2 (square).

electron-density irregularity existed in the sporadic-*E* layer with a peak density of $7 \times 10^5 \text{ cm}^{-3}$, corresponding to the maximum value of *foEs*.

The observation of 19 July 1975 shows the converse effect in which, between 12:50 and 13:00 AST, the peak electron densities observed by incoherent scatter were much greater than expected on the basis of *foEs*. Two factors may have prevented the ionosonde from observing the echoes at 21 MHz, indicated in Figure 4.31. First, the section of the sporadic-*E* layer observed by incoherent scatter was not in the field of view of the ionosonde. Second, highly-ionized irregularities comprise only a small fraction of the sporadic-*E* layer. It was stated in Chapter 3 that the ionosonde would record reflected radiation from a sporadic-*E* layer only if the reflection coefficient of the layer were greater than approximately 1×10^{-3} . This means that at least 0.1% of the field of view of the ionosonde would have to contain a high enough electron density to reflect radiation of a given frequency before an echo at that frequency would be recorded on the ionogram. The fact that only one irregularity was observed, although there were probably others in the vicinity, indicates that they are scattered quite thinly throughout the region. This is evidently the reason that these regions of high electron density have not been detected in data from sounding rockets.

4.7 Summary

These series of experiments have demonstrated the value and limitations of the incoherent-scatter technique in the study of the horizontal structure of sporadic-*E*. The observations show that considerable horizontal structure does exist in some intense midlatitude sporadic-*E* layers. The size of this structure ranges from hundreds of kilometers down to the spatial resolution of the radar beam, about 300 m at a range of 100 km, with implications of

even smaller structure. Small regions were observed with densities much greater than the maximum electron densities in the surrounding sporadic-*E* layer. The occurrence of the irregularities was correlated in time with the detection by the ionosonde of partially transparent echoes from the layers. The magnitude of the irregularities was also found in each case to be consistent with the values of $f_b E_s$ and $f_o E_s$, when the effects of volume averaging and limited sampling by the radar are considered.

The observations have interesting implications for the explanation of the formation of sporadic-*E* layers. If, as appears likely, sporadic-*E* layers are formed by the vertical drift of metallic ions under the influence of the neutral wind system, then it is necessary to postulate either horizontal convergence of the ionization or an irregular source of the metallic ions.

5. DISCUSSION

5.1 *Introduction*

It was shown in Chapter 4 that, based on data from incoherent-scatter radar, there is small-scale structure of sufficient magnitude to account for the partial transparency of sporadic-E echoes seen in ionograms. The causes of sporadic-E irregularities will be discussed in this chapter.

The irregular structure observed in sporadic-E layers requires either that the ionization present is subject to an irregular forcing mechanism, or that there is an irregular source of ionization. The effects of motions of the neutral atmosphere on sporadic-E ionization are investigated. In particular, it is shown that many of the irregular features observed in sporadic-E layers may be caused by internal gravity waves. The possible proximity of a sporadic-E layer to a critical level of a dominant gravity-wave mode is discussed as a source of intense ionization irregularities. Evidence is shown of the peak ionization density in a layer being limited by a fluid instability. Other effects of motions of the neutral atmosphere which could give rise to small-scale irregularities in sporadic-E layers are discussed.

A possible irregular source of ionization from ablating meteors is also considered. It is shown that under specific and rather rare conditions an ionized meteor trail can be converged by the action of the neutral wind into an irregularity of relatively small dimensions.

5.2 *Ion Drift Velocity and the Formation of Sporadic-E Layers*

Some of the features of sporadic-E layers predicted by wind-shear theory were discussed in Chapter 2. Although, in general, observations of sporadic-E layers support the conclusions of wind-shear theory, not all of the problems have been resolved [Layzer, 1964a, b, 1972; Whitehead, 1964,

1971b; Axford, 1964]. It is, therefore, of interest to examine the results of this study for features either characteristic of or in contrast to the predictions of wind-shear theory.

It was found in describing sporadic-*E* profiles by mathematical functions, as described in Chapter 3, that most layers had a Gaussian shape. As discussed in Section 2.2.4, this is consistent with wind-shear theory for a linear shear if the layers are diffusion limited, as would be the case for metallic ions.

The concept of diffusion-limited layers may provide an explanation of one of the apparent discrepancies between the results of this study and the predictions of wind-shear theory. In Section 4.5.9 an experiment was described in which the ion velocities in the region of a sporadic-*E* layer were measured for an extended period. Figure 4.28 showed the ion velocities and also the location of a sporadic-*E* layer. It will be noted that no convergence in the vertical ion drift was measured in the vicinity of the sporadic-*E* layer. In fact the ionization seems to be moving uniformly downward at a speed of approximately 5 m s^{-1} . The apparent downward motion is likely to be due to an uncertainty in the internal bias of the radar [Harper *et al.*, 1976]. However, correcting for this velocity bias does not create a convergence of ionization.

The effect on the velocity components of an incorrect estimate of the internal bias of the radar can be easily found. The ion velocity vectors whose components are plotted in Figure 4.28 are calculated from measured velocities parallel to the lines of sight of the three positions of the radar by the relations given by equations (4.16) through (4.18). Since the velocity bias affects the measured velocities equally in each position, its effect is doubled in the vertical velocity, but cancels in the horizontal

velocities. The horizontal velocities are therefore not affected by the internal bias.

Given the horizontal ion velocities (v_x and v_y), the vertical component of ion drift (v_z) can be calculated using the equations of Chapter 2. If u_z is equal to zero in equation (2.17), ion drift velocity components are given by

$$v_x = \frac{1}{(1+\rho_i^2)} [(\Gamma_x^2 + \rho_i^2)u_x + (\Gamma_x\Gamma_y + \rho_i\Gamma_z)u_y] \quad (5.1)$$

$$v_y = \frac{1}{(1+\rho_i^2)} [(\Gamma_x\Gamma_y - \rho_i\Gamma_z)u_x + (\Gamma_y^2 + \rho_i^2)u_y] \quad (5.2)$$

$$v_z = \frac{1}{(1+\rho_i^2)} [(\Gamma_x\Gamma_z + \rho_i\Gamma_y)u_x + (\Gamma_y\Gamma_z - \rho_i\Gamma_x)u_y] \quad (5.3)$$

Equations (5.5) and (5.6) can be solved in terms of u_x and u_y and substituted into equation (5.7) to give

$$v_z = \frac{1}{\rho_i} (\Gamma_y v_x - \Gamma_x v_y) \quad (5.4)$$

The vertical ion drift velocities deduced in this fashion from the data of Figure 4.24 below 115 km are shown in Figure 5.1.

The position of the layer observed in the electron-density profiles is in good agreement with the calculated values of v_z . The layer is situated near a convergence point, and then dissipates at 14:40 AST when convergence is no longer indicated. However, there is a weak layer at 104 km between 15:30 and 17:40 AST. Although the vertical ion drift does not change direction at this altitude, there is some suggestion, on a finer scale than is shown in Figure 5.1, of a slowing down of the upward ion drift velocity that may be responsible for the convergence of ionization. At 17:40 AST the layer is quite

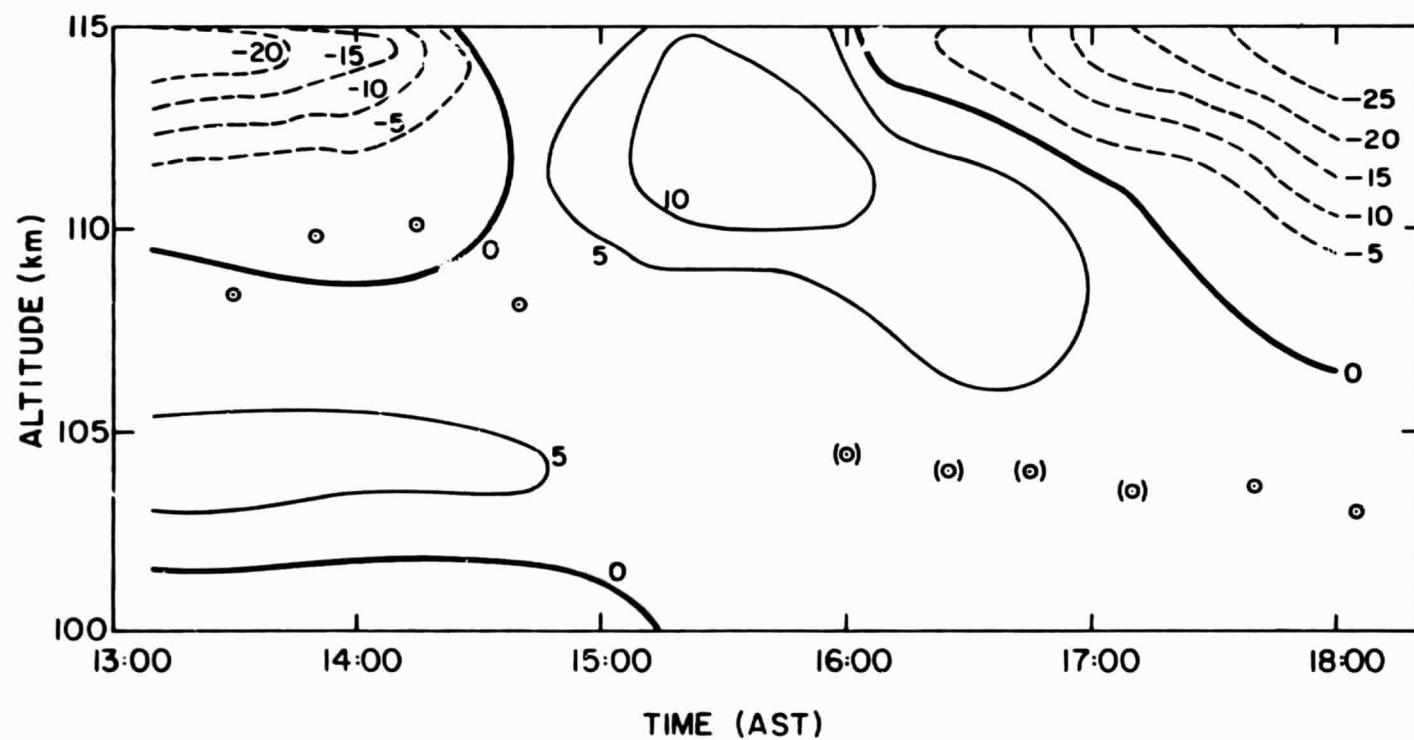


Figure 5.1 Vertical ion drift velocities (m s^{-1}) deduced from the horizontal components of the ion drift velocity measured on 16 July 1974 by incoherent-scatter radar.

intense again and begins to descend. This is probably due to the strong convergence level which is descending into the region.

The fact that there is no convergence in the vertical ion velocity measured by the incoherent-scatter radar is evidence of the predominance of metallic ions in sporadic-E layers. In a diffusion-limited layer, the convergent velocity of the ions is exactly balanced by a divergent velocity due to diffusion. Thus, the mean velocity, which is measured in the incoherent-scatter experiment, is equal to zero.

The vertical ion drifts necessary to maintain a diffusion-limited layer can be found using equation (2.22). This has been done for the profiles shown in Figures 3.10 and 3.14. The respective shears in the vertical ion drift velocities are 0.2 and $1.0 \text{ m s}^{-1} \text{ km}^{-1}$. Using values for ρ_i from *Wright and Fedor* [1970], the vertical drifts would result from vertical shears in the east-west neutral wind of 13 and $18 \text{ m s}^{-1} \text{ km}^{-1}$, which compare closely with the values observed by *Rosenberg* [1968] as illustrated in Figure 2.2. This analysis can only be valid in regions where the production and loss processes of the predominant ions involved are negligibly small, as in the case of metallic ions.

5.3 Altitudes of Sporadic-E Layers

5.3.1 *Combined effects of gravity waves and tides.* The magnitudes of tides and gravity waves are roughly the same [*Hines*, 1963]. However, the persistence of the tidal winds and the random nature of the gravity-wave spectrum indicates that long-term features of sporadic-E layers should be dominated by the tidal modes. This is supported by the observations of the rate of descent of intense sporadic-E layers which is at most a few km per hour (Figure 5.2).

It is possible that, on some occasions, gravity-wave modes of comparative

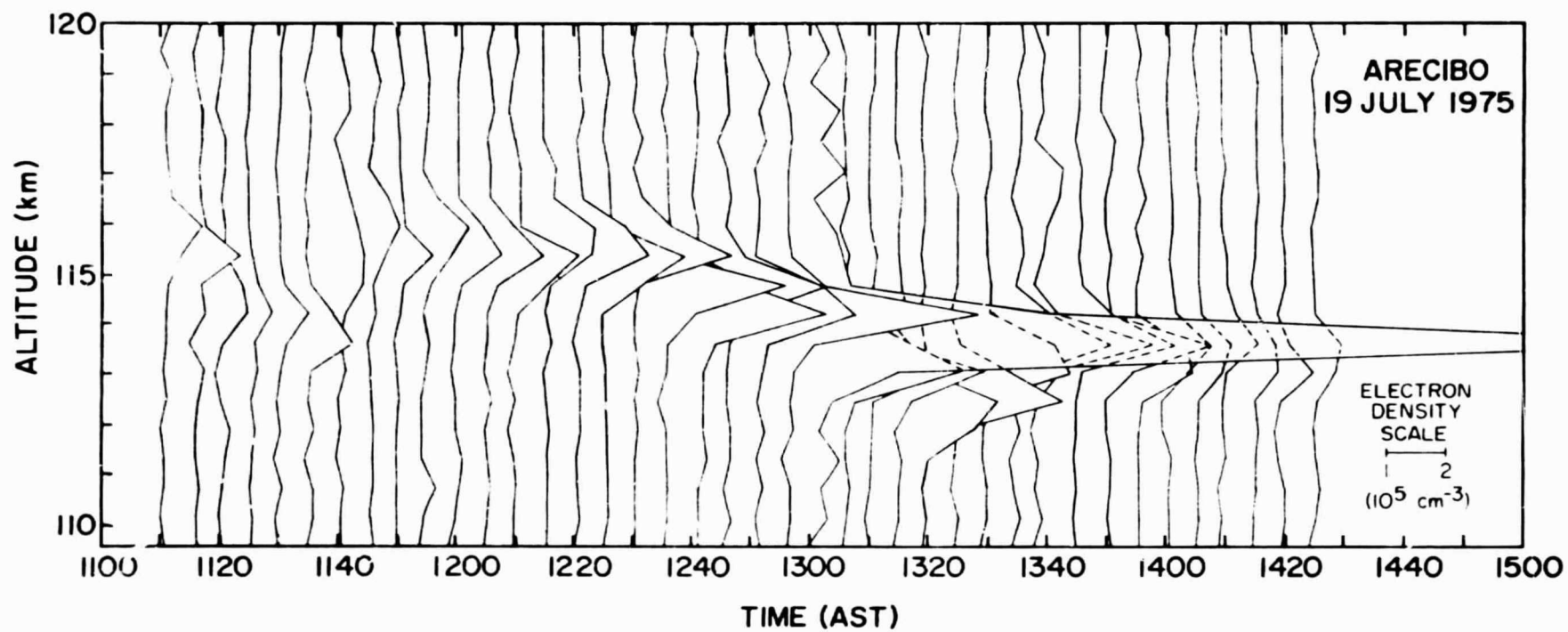


Figure 5.2 Electron-density profiles observed at Arecibo, 19 July 1975.

intensity would interfere with the tidal modes, affecting the behavior of the sporadic-E layer. *Chimonas* [1971] maintains that since the horizontal extent of tidal winds is much larger than that of sporadic-E layers, and since these winds are very regular, a resonance of the tidal modes with gravity waves is necessary to produce the sporadic nature and the required dimensions of sporadic-E layers.

Interference between tides and gravity waves would also have a pronounced effect on the vertical position and the local ionization density of a sporadic-E layer. For example, destructive interference caused by an active gravity-wave mode would prevent a layer from forming at a point where there would ordinarily be vertical convergence of the ionization by a shear in the tidal wind. If the phase of the gravity wave were descending more rapidly than that of the tidal mode, points of strong convergence could appear and disappear. This would be further complicated by the direction of propagation of the gravity wave with respect to the tidal winds.

Figure 5.3 illustrates vertical ion drift due to the interaction of two waves with different phase velocities. The sinusoidal east-west wind has constant phase and a wavelength of 10 km while a north-south sinusoidal wind has a wavelength of 12.5 km and has a downward phase velocity. Layering of the ionization would occur at points of convergence where v_z vanishes. In the sequence illustrated in Figure 5.3, the convergence of ionization at 123 km ceases between the fifth and sixth curve. The actual structure of the winds is never simple, but the model is used to demonstrate what may be occurring in the data shown in Figure 4.29. A layer is observed to form at an altitude of 123 km. This layer remains at a constant altitude for a period of time and then begins to descend, at which time the convergence of ionization seems to have ceased. In the situation represented in Figure 5.3,

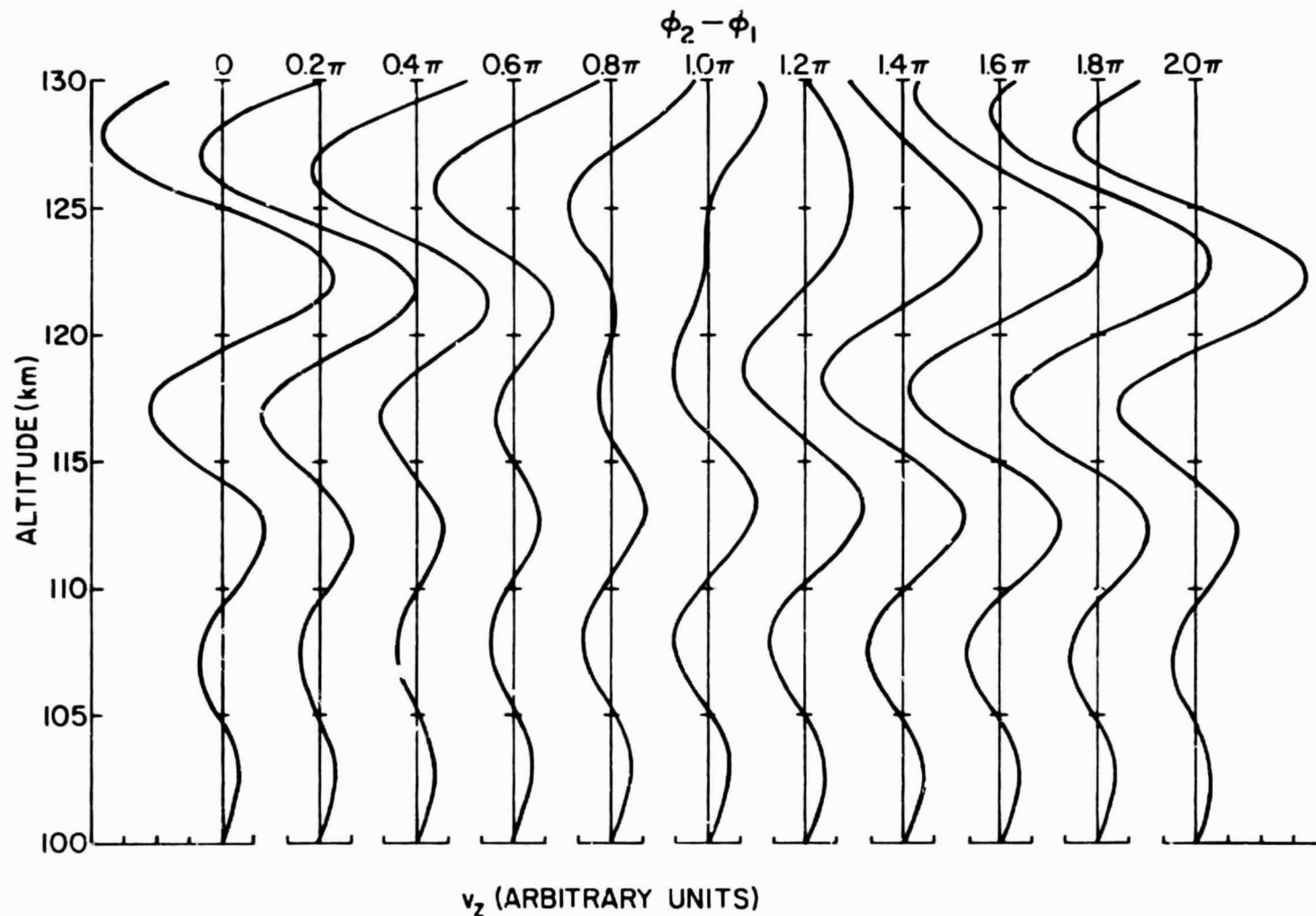


Figure 5.5 Vertical ion drift caused by two superimposed sinusoidal wind systems: one in the east-west plane with a vertical wavelength of 10 km and a constant phase, the other with a vertical wavelength of 12.5 km and a downward phase velocity. The phase of the second wave changes by 2π radians in the sequence shown.

this effect is enhanced by the fact that the vertical transport of ionization is dominated by the north-south winds at the higher altitudes, and by the east-west at the lower altitudes.

5.3.2 *Components of tidal modes.* The relative importance of the east-west and north-south velocity components can have an effect on the altitude of a sporadic-E layer when the only important winds are due to a regular, slowly-descending tidal mode. *Chimonas* [1973] showed that a layer that is initially located near a node in the north-south wind will descend at essentially the phase velocity of the node until the effect of the east-west wind becomes appreciable. Within a relatively short vertical distance in the neighborhood of 130 km, the convergence due to the north-south wind shear fails and the layer is "released" to descend rapidly to the node in the east-west wind. This is a more compelling model than that of interference with gravity waves described in the preceding section, since it is unlikely that any isolated wave will dominate the gravity-wave spectrum to the necessary degree. However, it seems to require that sporadic-E layers descend steadily above 130 km, and below an east-west node near 115 km, with the observation of a well-defined layer being improbable between these altitudes. In fact, the layer in Figure 4.29 seems to have descended in a discontinuous manner to the 123 km level before stepping to 108 km.

If the release of a layer from a north-south node is indeed as abrupt as is indicated in the work by *Chimonas* [1973], it could possibly account for the behavior of the sporadic-E layer observed on the night of 21 July 1975 and shown in Figure 4.37. The layer would have initially been located at a node in the north-south wind at 127 km. Then, possibly as a result of a horizontally-propagating gravity wave, the altitude of the left side of the scan decreased below the point where the layer was released from the

C-3

north-south wind shear. The ionization in this part of the layer then descended to the next point of convergence, which was at 107 km. At the same time, the ionization in the part of the layer at the right side of the scan was lifted by the action of the wave, and remained in the region where the north-south shear was effective.

5.3.3 *Standing waves.* As a wave propagates upward through the atmosphere, it will eventually reach a point where, because of changing temperature and background winds, the vertical wavelength becomes very large and the wave is reflected [Pitteway and Hines, 1965]. This condition could set up standing waves, with nodes separated by a few kilometers and remaining at a relatively constant altitude. The effect of standing waves on the ionization may explain evidence that sporadic-E layers form in "preferred" altitude intervals [Seddon, 1962; Smith and Mechtly, 1972]. If there were a fairly consistent source of atmospheric waves which were reflected by a similarly consistent mechanism above the region of sporadic-E formation, nodes would form in the standing wave pattern near certain altitudes, leading to the apparent preferred altitudes of the sporadic-E layers.

Standing waves may also be responsible for the discrete levels of layer formation where there is no relative motion between the layers, as illustrated in Figures 4.15 and 4.29. The former example shows two well-defined layers observed on 19 January 1974 between 14:21 and 14:32 AST. The two layers appear to be moving with the same velocity relative to the incoherent-scatter radar, and have trailing edges that coincide with each other. Neither layer was detected during the scan following the ones illustrated in the figure. This is interpreted to show that they are not two merging layers controlled by different atmospheric waves, but are parts of the same dynamic system.

5.3.4 *Quasi-stagnation levels.* A gravity wave propagating through the

ionosphere will collect metallic ions near its velocity nodes, causing them to move downward with the phase velocity of the wave [Chimonas and Axford, 1968]. This phenomenon has been called the "corkscrew" effect. As a result of the altitude dependence of the ion-neutral collision frequency, levels exist where the vertical ion motion can be shown to vanish independently of the phase of the wave inducing the motion resulting in "quasi-stagnation levels" [Hooke, 1971].

Quasi-stagnation levels may have a direct bearing on the discontinuous nature of the descent of a sporadic-*E* layer through the lower *E* region (see Figures 4.29 and 4.37). The spectrum of gravity waves is expected to be quite broad, with each Fourier component subject to its own stagnation level. This could lead to a series of levels at which ions following the downward phase of a wave are trapped. It could also mean, however, that no components of the wave would dominate the spectrum to a great enough extent for a stagnation level to affect the vertical motion of the ions.

The levels of stagnation can be found by solving equation (2.17) for the vertical ion drift. It is convenient to fix the coordinate system with respect to the direction of propagation of the wave, such that

$$u_y = 0 \quad (5.5)$$

Thus,

$$v_z = \frac{1}{1 + \rho_i^2} [(\rho_i \Gamma_y + \Gamma_x \Gamma_z) u_x + (\rho_i^2 + \Gamma_z^2) u_z] \quad (5.6)$$

Hines [1960] showed that for low frequency internal waves

$$\frac{u_z}{u_x} \cong - \frac{k_x}{k_z} \quad (5.7)$$

where k_x and k_z are the horizontal and vertical wave numbers, respectively. If this is substituted into equation (5.6), it is found that the vertical ion velocity vanishes when

$$\rho_i = \frac{k_z}{2k_x} \left\{ \Gamma_y \pm \left[\Gamma_y^2 - \frac{4k_x}{k_z} \left(\frac{\Gamma_z^2 k_x}{k_z} - \Gamma_x \Gamma_z \right) \right]^{\frac{1}{2}} \right\} \quad (5.8)$$

Hooke [1971] treats the case of an east-west (geomagnetic coordinates) wave propagation, so that $\Gamma_x = 0$, and the stagnation level occurs where

$$\rho_i = \frac{\Gamma_y k_z}{2k_x} \left\{ 1 \pm \left[1 - \left(\frac{2\Gamma_z k_x}{\Gamma_y k_z} \right)^2 \right]^{\frac{1}{2}} \right\} \quad (5.9)$$

The requirement that ρ_i is real and positive restricts the possible values of k_x and k_z .

This equation can be solved if the wave numbers are known. In the analysis by *Hooke*, a value of $k_x/k_z = 0.1$ is used, corresponding to a wave with a period of approximately one hour. At Arecibo, the magnetic dip angle is 50 deg, giving ρ_i equal to 6.3 and 0.093 for the two solutions. The corresponding heights of the stagnation layers, from a table of ρ_i versus height by *Wright and Fedor* [1970], are approximately 106 and 155 km. A similar calculation for conditions at Wallops Island (magnetic dip = 70 deg) gives $\rho_i = 3.1$ and 0.28, corresponding to altitudes of 110 and 134 km.

A major difficulty in relating this theory to the observed sporadic-E layers is the location of the expected stagnation levels. The period of the wave described above is relatively short with respect to the usual rate of descent of sporadic-E layers. Yet the levels of stagnation, at 106 and 155 km, are respectively too low and too high to be applied to the observations at Arecibo. Examination of equation (5.9) shows that for waves with longer periods, the respective stagnation levels would occur at even lower and

higher altitudes.

5.4 *Boundaries of Sporadic-E Layers*

An interesting feature observed in the sporadic-E layer of 17 July 1975 (Figure 4.29) is the well-defined trailing edge of the layer. Electron-density contours observed during the three scans of the radar beam as the edge was passing through the viewing region are shown in Figure 5.4. In this figure, the electron-density contours are on a linear scale, at intervals of 10^4 cm^{-3} . Contours at intervals of $5 \times 10^4 \text{ cm}^{-3}$ are indicated by thick lines. Note that the vertical and horizontal distance scales are not equal.

The abruptness of the edge of this layer is difficult to explain in terms of atmospheric waves. When compared with the normal horizontal scale sizes of the ionosphere, it would appear as a discontinuity. The column electron density is also greater where the layer is present, indicating that the edge of the layer is not a result of a change in the vertical-convergence mechanism. *Anderson and Barth* [1971] made a similar observation in an experiment which measured the dayglow from the ionized and neutral magnesium of a sporadic-E layer. The rocket carrying the instrumentation apparently passed below the edge of a sporadic-E layer. Within a horizontal distance of about 6 km the 2800Å dayglow, which is an indication of the column density of Mg^+ , increased from 0.5 to 5.0 kR.

A clue to the mechanism sustaining this large horizontal gradient is found in the less intense layer that is located on the right side of the apparent discontinuity and approximately 4 km lower in altitude than the intense layer. The structure of the electron density shown in Figure 5.4 suggests that boundaries exist in the lower E region between masses of air with different static and dynamic properties, as in tropospheric frontal systems, with the wind components parallel to, and on either side of this

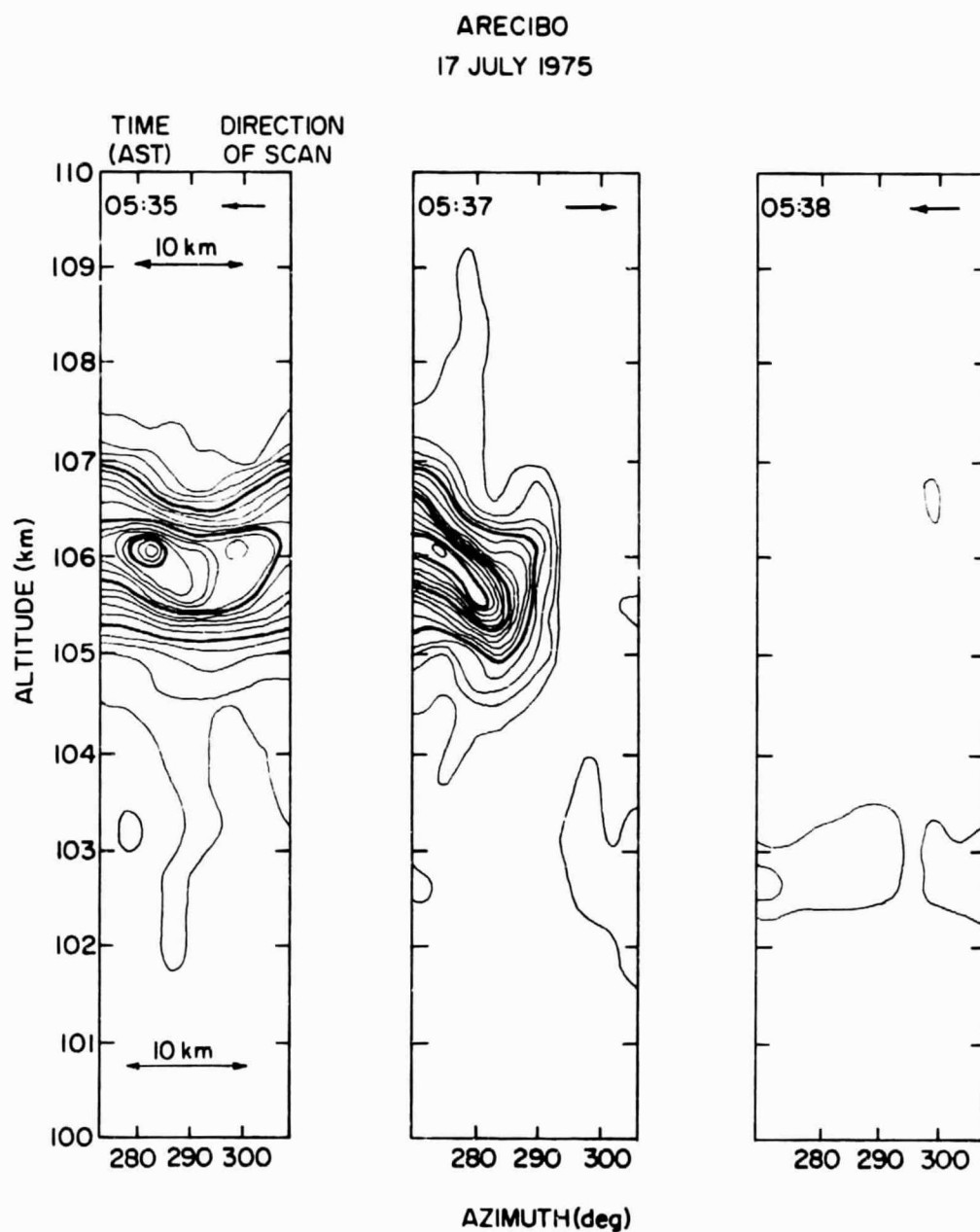


Figure 5.4 Electron density observed on 17 July 1975 (see Figure 4.29). Contours are at intervals of $1 \times 10^4 \text{ cm}^{-3}$, with contours at multiples of $5 \times 10^4 \text{ cm}^{-3}$ darkened.

"front", exhibiting different characteristics. For example, let the boundary at the "front" be a vertical east-west plane. Suppose wind systems on either side are similar, with the exception that the position of the null in the east-west wind is 4 km lower on the north side of the boundary than on the south. This is shown schematically in Figure 5.5. The drawing on the left, (Figure 5.5a), shows the direction of the neutral winds with respect to the boundary and to the geomagnetic field. The position of the nulls in the wind profiles coincide with the sporadic-*E* layers, and are indicated by *Es*.

The ion drift velocities in the north-south plane are shown in Figure 5.5b. It is seen that horizontal ion motions in the region of the boundary tend to oppose the horizontal diffusion of ionization from the edges of the layers. This would produce horizontal gradients, as seen in Figure 5.4.

The required horizontal ion drift is not great. If the layer is assumed to be diffusion limited so that equation (2.22) applies the ion drift which would maintain the observed gradient can be found by the methods described in the previous section. Assuming an ambipolar diffusion coefficient of $70 \text{ m}^2 \text{ s}^{-1}$ [Kaiser *et al.*, 1969] it is found that a horizontal ion drift of 0.02 m s^{-1} would be sufficient to maintain the edge of the layer for steady-state conditions. Bounded wind systems may also be responsible for the noticeably different dynamics in the two sides of the region observed on 21 July 1975 and shown in Figure 4.32.

There is evidence of rapid changes in horizontal velocities in data from incoherent scatter used in this study (see Figure 4.24) and in data from the University of Illinois meteor radar [G. C. Hess, personal communication, 1976]. However, the poor time resolution of these wind-measuring techniques precludes the observation of small-scale discontinuous effects of the type mentioned here.

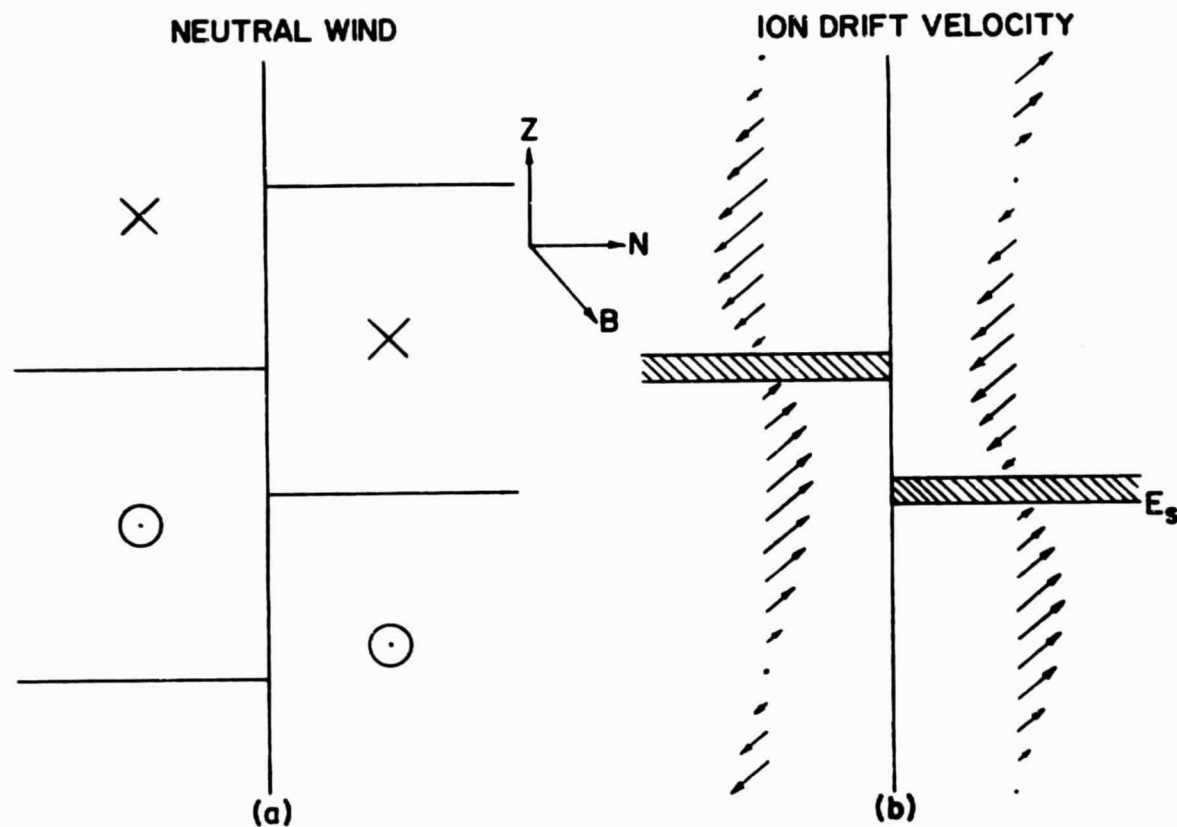


Figure 5.5 Sketch of possible configuration of winds producing the electron-density distribution shown in Figure 5.4. (a) Direction of sinusoidal east-west horizontal winds, (b) Ion drift velocities and locations of sporadic-E layers.

5.5 Wave-like Structure in Sporadic-E Layers

The existence of wave-like structure in the ionosphere has been known and studied for many years [Ratcliffe, 1959]. Experiments using ionospheric sounders operating at a fixed frequency and using spaced receivers show apparent random velocities superimposed on a relatively constant background motion associated with tidal modes [Hines, 1974]. The random velocity components observed by spaced ionosondes are possibly the effect of dominant gravity-wave modes propagating through the region where the radio wave was reflected. The observed random "velocities" would be the superimposed phase velocities of a near continuum of waves, and not an actual bulk motion of ionization.

Rapid changes in the observed "velocities", and even changes in direction, might be observed as a result of the introduction of one wave train or the loss of another [Hines, 1974, postscript to Paper 33]. The irregularities may be in the form of changes in the altitude of the reflecting level, or actual changes in the ionization density.

Various mechanisms have been suggested for the horizontal convergence of ionization by gravity waves. These include changes in the ion chemistry resulting from changes in neutral density and temperature [Hooke, 1969], the effects of vertical air motions and the geomagnetic field on ions [Wright and Fedor, 1969], and resonance between tidal and gravity-wave modes [Chimonas, 1971].

Wave-like motions of sporadic-E layers were observed on several occasions during this study, ranging from periods of a few hours to a few seconds. Because of the nature of the data and the inability to resolve motions in more than one horizontal direction, it is impossible to separate variations in time from spatial variations, and therefore difficult to determine frequencies

and wave numbers. Where possible, wavelengths or periods are estimated and compared to calculations by *Hines* [1960] of allowed gravity-wave modes.

Electron-density profiles in the vicinity of a sporadic-*E* layer are plotted at 5 min intervals in Figure 5.2. Evidence of short term variations in altitude is seen in parts of the data. However, the dominant oscillation seems to have a period of approximately two hours. Assuming the atmosphere at the sporadic-*E* layer to be essentially at rest with respect to the ground, the allowed gravity-wave modes of this period, according to the calculations of *Hines* [1960], must have horizontal wavelengths of between approximately 100 and 1000 km, and vertical wavelengths between 10 and 50 km in order to have propagated from the lower atmosphere and not be dissipated by viscous effects.

Another example of wave-like structure in sporadic-*E* height variations was observed on 26 July 1975 (Figure 4.43). In this case, the horizontal wavelength was comparable to the distance through which the radar beam was scanned, approximately 20 km. According to the calculations of *Hines* [1960] and assuming no net motion of the layer, these waves could propagate with periods of between 10 and 160 sec and vertical wavelengths of from 1 to 50 km.

Wave-like structure is evident in the form of electron-density fluctuations in the data from the single-pulse experiment on 16 July 1975. Figure 5.6 shows contours of electron density as a function of altitude and azimuth. The altitude resolution is about 1.2 km. Contours of electron density greater than $1.5 \times 10^5 \text{ cm}^{-3}$ are accented and regions where the average electron density is greater than $1.75 \times 10^5 \text{ cm}^{-3}$ have been darkened to emphasize variations within the sporadic-*E* layer. The main component appears to have a wavelength of 5 km. According to calculations by *Hines* [1960], a wave of such short wavelength could have originated in the lower

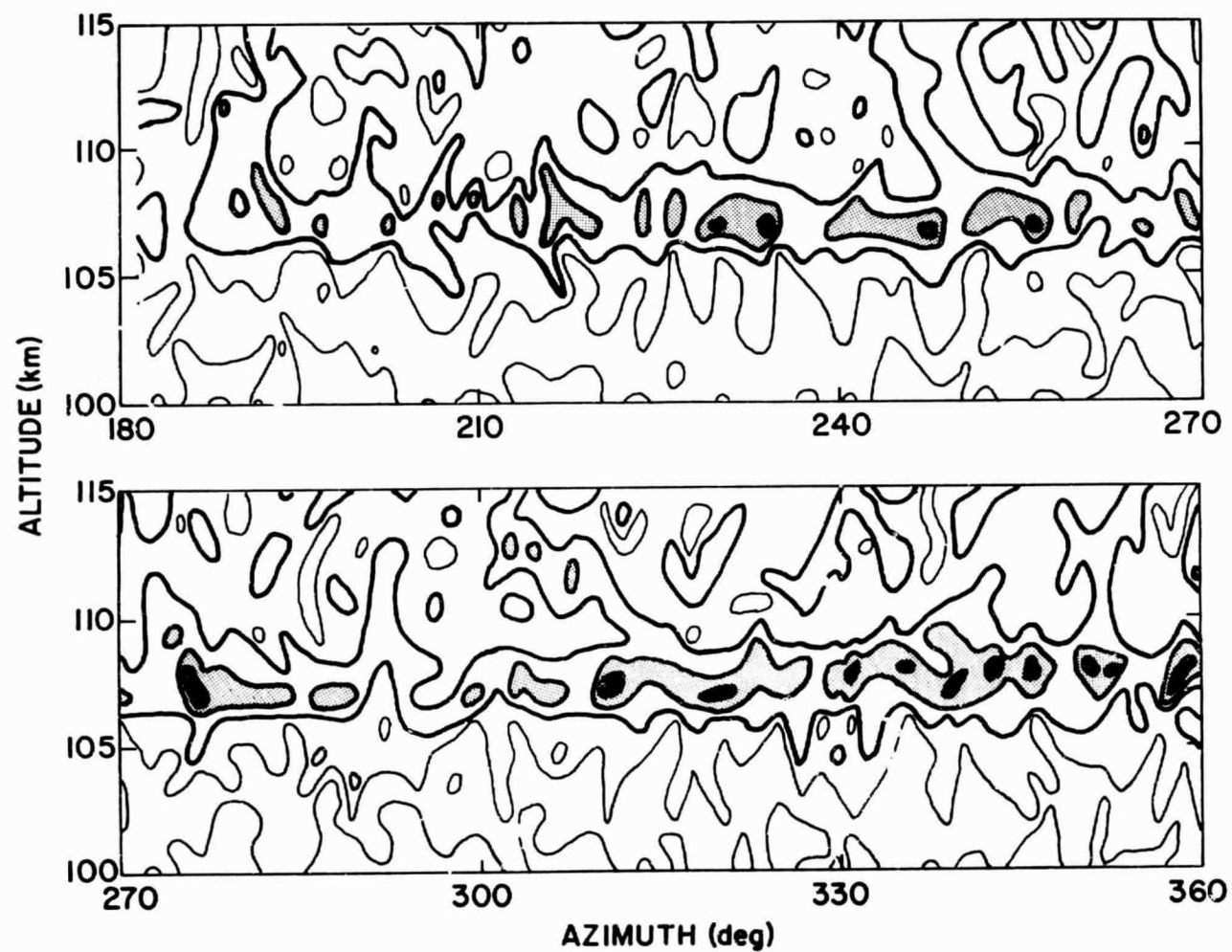


Figure 5.6 Electron density (10^5 cm^{-3}) observed by a single-pulse experiment on 16 July 1975 between 14:37 and 14:47 AST. The direction of scan is from right to left.

atmosphere only if the period is about 10 sec and the vertical wavelength is about 2 m, which are inconsistent with the data. A possible explanation lies in a source of the gravity wave in the middle or upper atmosphere.

5.6 *Irregular Structure Associated with Critical Levels*

5.6.1 *Introduction.* The main purpose of this study is to describe the horizontal structure of sporadic-E layers. This has been done in the above sections for small-amplitude perturbations in terms of atmospheric gravity waves. However, none of the mechanisms described can satisfactorily account for the very localized regions of enhanced ionization shown in Figures 4.21 and 4.32. This section will demonstrate that a plausible explanation of these intense irregularities lies in their proximity to critical levels of internal gravity waves.

5.6.2 *Critical levels.* A wave propagating through a region where there is a shear in the background wind is unable to propagate through a level where the Doppler-shifted frequency of the wave is zero in the rest frame of the moving atmosphere. This is known as a critical level, and may be a cause of instability and turbulence.

Some of the characteristics of critical levels were derived by *Hines* [1968], beginning with first order equations, including the vertical variation of the scale height, and making no assumptions about the vertical dependence of the wave parameters. The perturbation pressure, density, and horizontal velocity can be eliminated in this system of equations to give a second order differential equation describing vertical variations of the vertical perturbation velocity, w_z . In the limit as the Doppler-shifted frequency (Ω) of the gravity wave goes to zero, this equation becomes

$$\frac{d^2 w_z}{dz^2} + \frac{\omega_B}{\alpha^2 (z-z_0)^2} = 0 \quad (5.10)$$

where ω_B is the Brunt-Väisälä frequency, given by

$$\omega_B^2 = [\gamma - 1 + \gamma(dH/dz)]g/\gamma H \quad (5.11)$$

γ is the ratio of specific heats, H is the pressure scale height, and Ω has been expanded as

$$\Omega \cong \omega - k_x[w_{ox} + \alpha(z-z_o) + \dots] \quad (5.12)$$

A solution of equation (5.10) can be found in the form

$$w_z = A(z-z_o)^v \quad (5.13)$$

where

$$v = 1/2 \pm i \left(\frac{\omega_B^2}{\alpha^2} - \frac{1}{4} \right)^{1/2} \quad (5.14)$$

The ratio ω_B^2/α^2 is known as the Richardson number, and is an indicator of stability of a gas subject to a velocity shear.

It can be seen that as a gravity wave approaches a critical level, the vertical amplitude of the wave goes to zero as

$$|w_z| \sim (z-z_o)^{1/2} \quad (5.15)$$

By substituting the solution for w_z , the perturbation amplitudes of pressure, density, and horizontal velocity near the critical level are found to vary inversely with the square root of the distance from the critical level. The shears in the velocity of the neutral wind also become very large near the critical level, varying as

$$\left| \frac{\partial w_x}{\partial z} \right| \sim (z-z_o)^{-3/2} \quad (5.16)$$

$$\left| \frac{\partial w}{\partial y} \right| \sim (z - z_0)^{-1/2} \quad (5.17)$$

Under most conditions, the effect of critical levels on the atmosphere is not significant. A spectrum of all gravity waves at a point in the atmosphere would probably not be dominated by any particular frequency. It has been suggested, however, that if a wave were excited for an extended time by a reasonably coherent source, enough of the wave could become critical at a large wind shear to produce a measurable effect [Hines, 1968].

5.6.3 *Effect in sporadic-E layer formation.* Whitehead [1971a] suggested that, due to the increased vertical wind shear, intense sporadic-E layers would be most likely to form at or near the height of a critical level. Equation (5.17) suggests that there would also be an increase in the horizontal wind shear. A large horizontal shear in the neutral wind at a sporadic-E layer would cause the horizontal convergence or divergence of the ionization. This mechanism may be the source of intense electron-density irregularities with limited horizontal extent, such as was observed on 28 January 1974 (Figure 4.21) and 19 July 1975 (Figure 4.32).

In the following analysis, vertical and horizontal ion drift velocities will be found which, under steady-state conditions, would form an irregularity with the peak electron density observed on 19 July 1975. In this case, the vertical shear alone must produce a peak electron density of $8 \times 10^5 \text{ cm}^{-3}$, and the superposition of the vertical and horizontal shears produce a peak electron density of $6 \times 10^6 \text{ cm}^{-3}$ in order to account for the observed irregularity.

The peak ionization density in a diffusion-limited layer can be calculated using the continuity equation (2.22) when the vertical ion drift velocities are known by

$$\ln(n/n_o) = \int \frac{v_z}{D} dz \quad (5.18)$$

First consider the effect of vertical convergence in the absence of horizontal convergence. In particular, v_z will be assumed to be sinusoidal and D is assumed to increase exponentially with altitude. Integrating equation (5.18) then gives

$$n = n_o \exp \left\{ \frac{-v_{zm}}{D} \left(\frac{(1/H) \sin k_z(z-z_o) - k_z \cos k_z(z-z_o)}{(1/H^2) + k_z^2} \right) \right\} \quad (5.19)$$

where v_{zm} is the velocity amplitude of the wave, and n_o is the unperturbed metallic ion density. The ratio of the electron density at the peak of the layer to n_o is then

$$\frac{n_p}{n_o} = \exp \left\{ \frac{v_{zm} k_z}{D [(1/H^2) + k_z^2]} \right\} \quad (5.20)$$

Mass spectrometer measurements show the background metallic ion density to be of the order of 10^3 cm^{-3} [Narcisi, 1973; Zbinden et al., 1975]. Assuming a vertical wavelength of 10 km in v_z and a value of D of $230 \text{ m}^2 \text{ s}^{-1}$ at 115 km [Kaiser et al., 1969] (the altitude of the sporadic-E layer), with a scale height of 7 km [CIRA, 1972], the required maximum vertical ion drift to maintain a peak ionization density of $8 \times 10^5 \text{ cm}^{-3}$ is 1.0 m s^{-1} .

Next consider the case of vertical and horizontal convergence acting together. The continuity equation (2.22) is solved for this two-dimensional case by the method of separation of variables (x and z). For $v_x = -v_{xm} \sin [k_x(x-x_o)]$ the result is

$$\frac{n_p}{n_o} = \exp \left\{ \frac{v_{zm} k_z}{D [(1/H^2) + k_z^2]} + \frac{v_{xm}}{D k_x} \right\} \quad (5.21)$$

In order to explain the irregularity in Figure 4.32, the value of n_p/n_o must be of the order of 6×10^3 . If the vertical ion drift is assumed to be the value used previously and a horizontal wavelength of 50 km in v_x is assumed, a maximum horizontal drift of only 0.05 m s^{-1} , under steady-state conditions, is required.

At Arecibo, where the magnetic dip is 50 deg, east-west horizontal winds will produce vertical and north-south ion drifts of approximately the same magnitude. For a neutral wind of 100 m s^{-1} at an altitude of 115 km, each component of the ion drift velocity would be approximately 20 m s^{-1} . Horizontal convergence occurs only for the case of a shear in the east-west wind. The formation of irregularities by a horizontal shear in the north-south wind would be prohibited by the polarization electric field, in the same manner that sporadic-E layers are prohibited from forming at the magnetic equator. This is consistent with the suggestion that the irregularity shown in Figure 4.32 is elongated in the east-west direction.

The ion drifts derived in the above analysis are much less than those observed, and the widths of the corresponding layers are much greater than observed. The purpose of the preceding discussion is to show that the horizontal ion velocities required in such a model are not unreasonable, especially when considered to be the result of a gravity wave approaching a critical level. In his derivation of critical levels, Hines [1968] noted that their effects should be enhanced in a region where there is a large wind shear. Even if there is no dominant Fourier component, enough of the spectrum can go critical in a relatively small height interval to produce a pronounced effect on the ionization structure.

Further work is needed in evaluating the effect of critical levels on sporadic-E ionization, as the observed electron-density irregularities are

too highly enhanced for the approximations of the linear perturbation theory used here to be valid. However, on the basis of linear theory, it is concluded that horizontal convergence of ionization with sufficient magnitude to account for observed irregularities in sporadic-E layers can occur near the height of a critical level.

5.7 *Irregular Structure Caused by Fluid Instabilities*

An example of a fluid instability is seen in Figure 4.29. The very pronounced structure seen on the top side of the layer between 04:39 and 05:12 AST is characteristic of the Kelvin-Helmholtz instability which occurs in regions of large velocity shears [Corcos and Sherman, 1976; Patnaik et al., 1976]. The instability is driven by oscillations in the flow on either side of the shear having a horizontal phase difference of $\pi/2$. The boundary layer at the maximum shear, i.e. the location of the sporadic-E layer, then begins to exhibit wave-like characteristics which grow in amplitude until destroyed by turbulence.

This sequence of events is evident in Figure 4.29, and appears to be initiated by a wind pattern associated with the descent of the upper layer. At the approximate time that the upper layer would have reached the altitude of the lower layer, irregular wave-like structure begins to develop. The peak ionization density also increases, indicating that the shear in the neutral wind has increased. A more detailed plot of the layer at this time is shown in Figure 5.7. The electron-density contours are drawn at intervals of 10^4 cm^{-3} , with contours at intervals of $5 \times 10^4 \text{ cm}^{-3}$ accented.

The amplitude of the wave continues to grow until about 05:12 AST, when the layer thickens suddenly, probably at the onset of turbulence. Electron density during this time is shown in Figure 5.8. The decrease in the peak electron density of the layer at this time was also detected by the

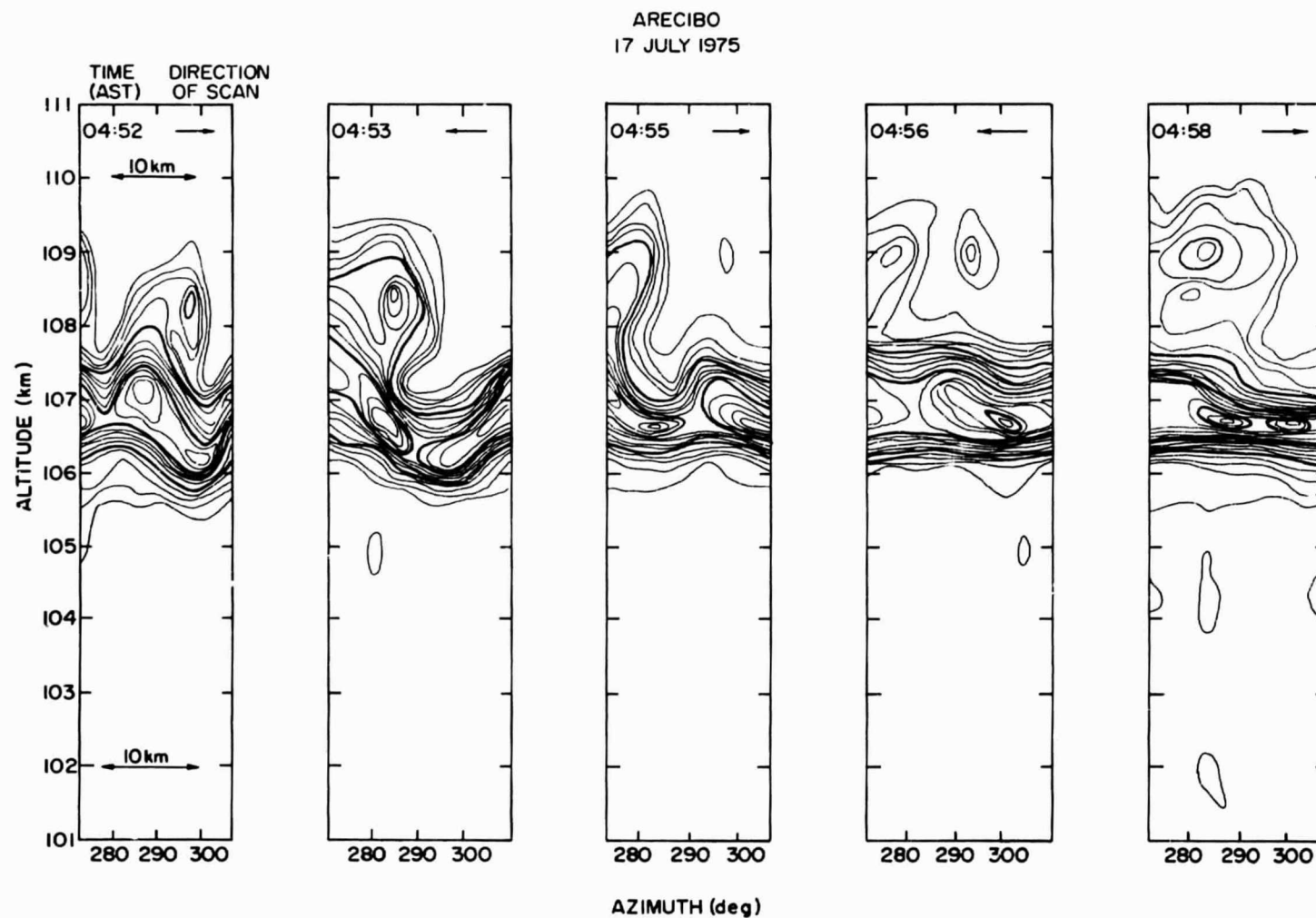


Figure 5.7 Electron density observed on 17 July 1975 (see Figure 4.29). Contours are at intervals of $1 \times 10^4 \text{ cm}^{-3}$ darkened.

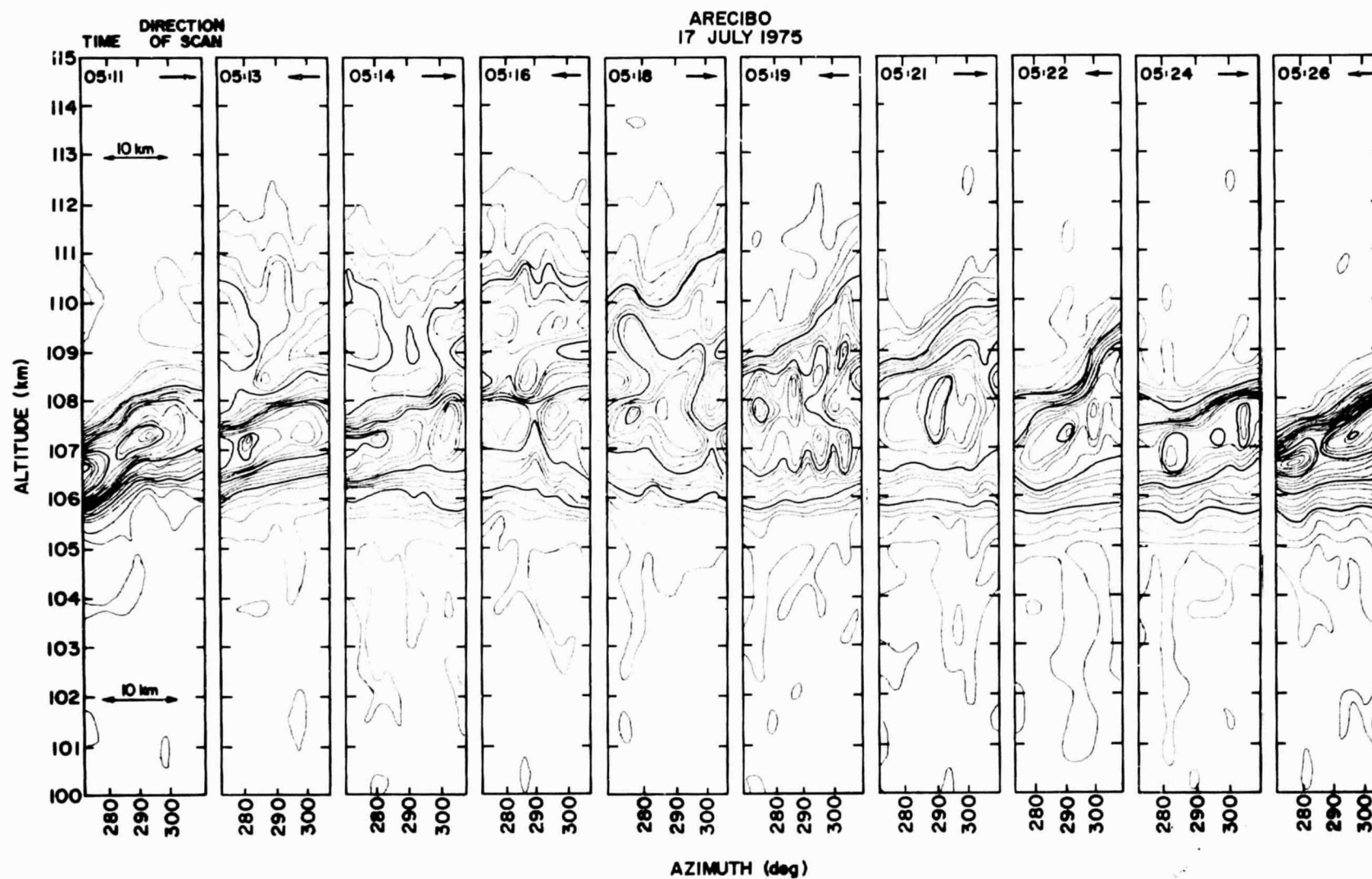


Figure 5.8 Electron density observed on 17 July 1975 (see Figure 4.29). Contours are at intervals of $1 \times 10^4 \text{ cm}^{-3}$, with contours at multiples of $5 \times 10^4 \text{ cm}^{-3}$ darkened.

ionosonde, Figure 4.30, whose field of view was separated from that of the radar by about 30 km.

5.8 Irregular Structure Caused by Plasma Instabilities

A theory that in the past has been advanced as an alternative to the formation of sporadic *E* by wind shears is that of instabilities in the ionospheric plasma [Clemmow and Johnson, 1959; Tsuda *et al.*, 1966; Tsuda and Sato, 1968]. The non-blanketing sporadic *E* that occurs at the magnetic equator is caused by plasma instabilities in the electrojet [Farley, 1963a,b; Reid, 1968; Prakash *et al.*, 1971]. However, the existence of plasma instabilities in midlatitude sporadic *E* has not been established.

Whitehead [1967, 1968, 1970b] developed the theory of a gradient instability, assuming midlatitude conditions, that could occur on a Gaussian-type layer of ionization. He found that when the equation of motion and the continuity equation were solved together, assuming small perturbations in ionization density and electric potential, irregularities would form near the peak of the layer and persist for tens of seconds. The fastest growing irregularities were found to be partially aligned with the magnetic field, which is in agreement with some observations of small sporadic-*E* irregularities [Goodwin and Thomas, 1963; Goodwin, 1965]. Atkinson [1973], showed the irregularities to have time constants of 1 to 170 s and periods of from 10^{-2} to 17 s, corresponding to phase velocities of 5 to 500 m s⁻¹. Whitehead [1968] concluded that this instability would be unable to form sporadic-*E* layers, but could be responsible for irregularities with scale sizes of a few tens of kilometers within the layers. He showed that the maximum ratio of the perturbation ionization density to the unperturbed ionization density was about 0.1 or 0.2. At greater values, the perturbation electric field would exceed the ambient electric field, causing the

irregularities to self-destruct [Kato, 1963].

The intense irregularities perhaps most likely to be attributed to an unstable plasma are shown in Figures 4.21 and 4.32. In each case the irregularity was observed for more than five minutes before drifting out of the field of observation, and each had a peak ionization density that was greater than the peak density in the surrounding sporadic-E layer by at least a factor of two in contrast to the maximum relative perturbation amplitude of 0.2 mentioned above. Another consequence of the gradient instability discussed by Whitehead [1967] is that if a layer becomes less than about 1.5 km thick, it will be destroyed by turbulence. There was no evidence in this study of the breaking up of localized irregularities by turbulence.

5.9 *Irregular Structure Attributed to Meteor Trails*

5.9.1 *Irregular source function.* Preceding sections have considered the formation of irregularities in sporadic-E layers by the horizontal convergence of ionization by the action of the neutral wind. An alternative mechanism for the formation of localized enhancements of electron density is provided by the irregular source of metallic ions as a consequence of their origin in meteor trails.

First the immediate effect of a meteor trail on the incoherent-scatter radar observations is described. Then a mechanism is proposed which allows the convergence of the ionization of a meteor trail into a localized region of high electron density within the sporadic-E layer.

5.9.2 *Individual meteor trails.* In Chapter 2 it was noted that a significant number of metallic ions are left in the meteor trail when a meteoroid enters the atmosphere. A representative initial linear density of meteoric ions is 10^{14} cm^{-1} [Baggaley and Cumack, 1974; Poole and Nicholson, 1975]. This is only a small contribution to the ionization already present

in a sporadic-E layer. If such a meteor were to pass through the beam of the incoherent-scatter radar, it would raise the average electron density measured in a particular 600 m height gate by about $3 \times 10^5 \text{ cm}^{-3}$. An apparent meteor trail observed on 21 July 1975 is shown in Figure 4.5. The peak electron density is about $1.5 \times 10^5 \text{ cm}^{-3}$. The detection of an individual meteor trail is a rare event and, in any case, even more rarely would occur in a sporadic-E layer.

5.9.3 *Convergence of a meteor trail.* While the ionization density left initially in a meteor trail is not insignificant, it is not nearly enough to account for the irregularity with a peak electron density possibly as great as $6 \times 10^6 \text{ cm}^{-3}$ observed on 19 July 1975. A possible explanation lies in the convergence of a meteor trail by the wind shear mechanism. The trajectories of ions under the influence of both an external magnetic field and collisions with neutral particles in motion was derived in Chapter 2. It was shown that ion drift velocities are described by

$$\vec{v} = \frac{1}{1+\rho} \left[\rho^2 \vec{u} + \rho \vec{u} \times \hat{\Gamma} + (\vec{u} \cdot \hat{\Gamma}) \hat{\Gamma} \right] \quad (5.22)$$

An examination of the effect of various wind-shear configurations was made by letting the winds act on a line of ionization as described by equation (5.22). The effects of both the orientation of the line of ionization and the orientation of the winds with respect to the geomagnetic field were determined.

For most configurations the effect of the wind shear is to spread the ionization out horizontally as it converged onto a horizontal plane at the null point of the wind velocity. However, it is found that the effect on particular configurations is to converge the ions into a small, relatively dense region of ionization. This is illustrated in Figure 5.9, showing the initial and final configurations of an ionized meteor trail initially 15 deg

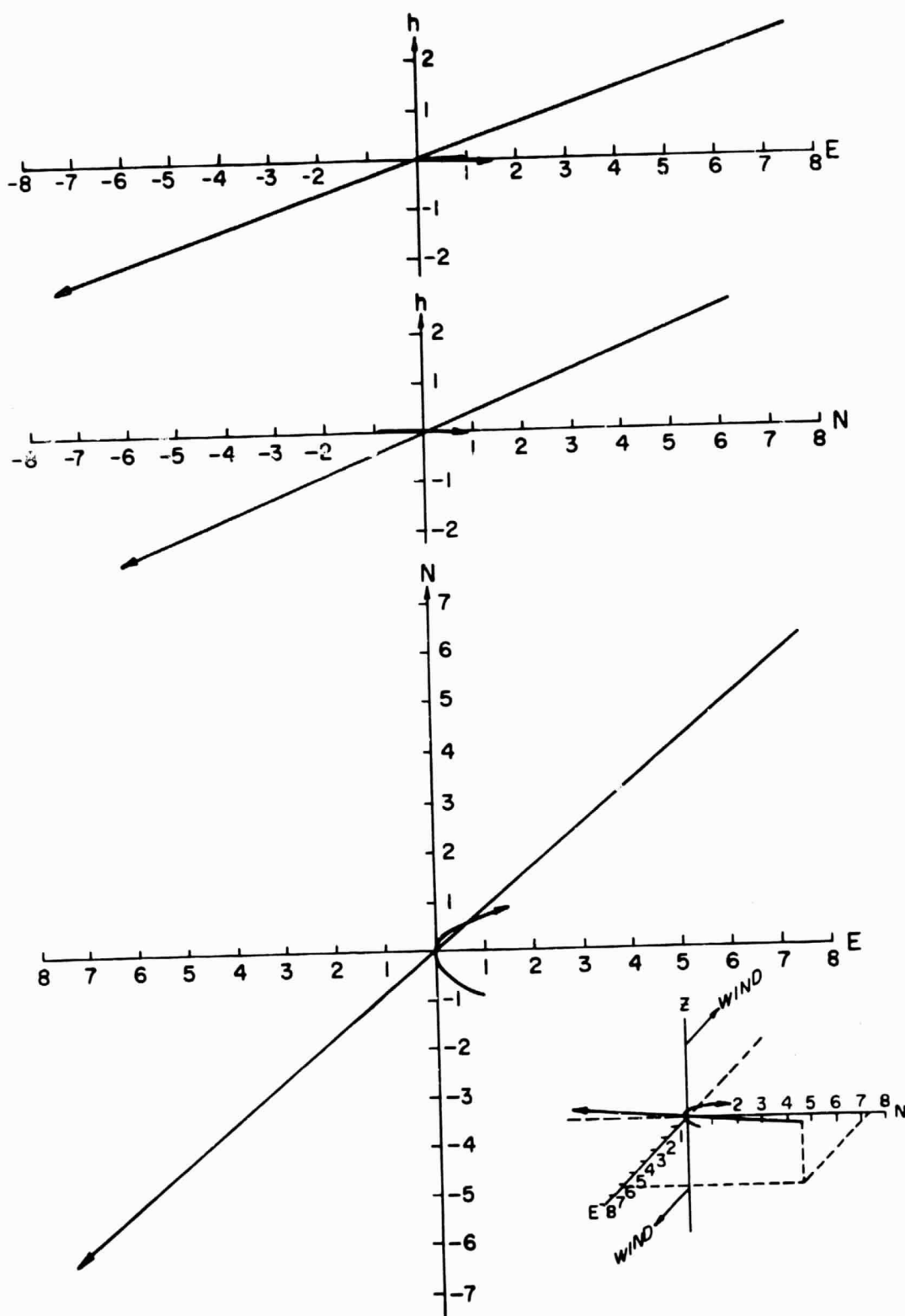


Figure 5.9 Initial and final configuration of an ionized trail in the presence of a wind shear.

from horizontal and at an azimuth of 230 deg. The wind has an east-west component only, and is represented by a sine wave with an amplitude of 100 m s^{-1} and a wavelength of 20 km. The ion-neutral collision frequency is assumed to decrease exponentially with height in such a way that ρ equals one at the altitude of the wind shear.

This analysis neglects many processes such as diffusion, production, and recombination. It does, however, demonstrate that the wind system is capable of converging ionized meteor trains into irregularities such as have been observed in the incoherent-scatter data. If the ionization from a 20 km meteor trail with a line density of 10^{14} cm^{-1} were converged by this mechanism and sampled in one height gate by the radar, the average electron density at that height would be increased by $4.7 \times 10^6 \text{ cm}^{-3}$, which agrees very well with the observation of 19 July 1975.

The time allowed for the convergence of the meteor trail in Figure 5.9 is 20 min, although the process is essentially complete after 10 min. Assuming an ambipolar diffusion coefficient of $35.6 \text{ m}^2 \text{ s}^{-1}$ [Kaiser et al., 1969] at an altitude of 102 km, the two-dimensional diffusion of a line of ions with an initial half-width of 1 m would result in a half-width of about 400 m after 20 min. The effect of diffusion is lessened somewhat by the restriction of movement perpendicular to the geomagnetic field. The duration of partial reflections from sporadic E at frequencies very much greater than the blanketing frequency seldom exceeds the 20 minutes used in the above example.

5.9.4 *Correlations with meteor activity.* Creation of irregularities in sporadic-E layers from ionization in individual meteor trails could account for the sporadic nature of the observed partial transparency, as these irregularities would form only under very specific conditions. Their

dependence on the action of the neutral wind shear would also give rise to the observed correlation between large frequency ranges of partial reflections and intense sporadic-*E* layers.

Two factors apparently not accounted for by this mechanism are the diurnal variation of *ftEs* and the lack of correlation with meteor activity. Top frequencies of 13 MHz, as in the case of the 19 July 1976 observation (Figure 4.28), and even greater, are observed at times in the daytime, but not at night. If convergence of the metallic ions left in meteor trails were the cause of irregularities, they would be as likely to form at night as in the day.

Many researchers have attempted to correlate sporadic-*E* occurrence with meteor activity with varying degrees of success [Fiocco, 1965; Kotadia and Jani, 1967; Wright, 1967; Whitehead, 1971b]. Hedberg [1975, 1976] showed that a dependence of *fbEs* on meteor rate can be shown if a time delay on the order of 6 hours is included. However, in the same study, no similar correlation of *ftEs* or *foEs* with meteor activity was found [A. Hedberg, personal communication, 1975]. Whitehead [1970a] suggested that only certain meteor showers may be responsible for the metallic ions present in sporadic-*E* layers. Shower meteors are travelling in essentially parallel trajectories and would, if properly aligned with respect to the wind shear, produce many irregularities. Trásková [1974] showed that the relationship between the occurrence of sporadic *E* and meteor activity might be better understood when considered together with changes in the zonal wind system.

Many of the attempts to correlate the occurrence of sporadic *E* with meteor activity have considered only the shower meteors. However, the majority of the metallic ions is introduced into the atmosphere by randomly-oriented sporadic meteors. Any wind shear which converges ionization vertically will

also converge into localized irregularities the fraction of sporadic meteors that are properly aligned with respect to that wind shear.

It is thus concluded that on some occasions, small-scale irregularities in electron density probably contain ionization from individual meteor trails which has been converged by the shear in the neutral wind.

5.10 *Summary*

In this chapter, observations of sporadic-*E* layers by incoherent-scatter radar have been discussed. Several features have been noted in the data that support the wind-shear mechanism of layer formation. Ion drift velocity measurements, when interpreted in terms of diffusion-limited metallic ion layers, showed the altitude of a sporadic-*E* layer to be near a point of convergence in the vertical ion drift. Preferred altitudes of occurrence of sporadic-*E* layers, as well as changes in altitude, are found to be consistent with the effects of wind shears caused by gravity waves and tides. The large horizontal gradient at the edge of a layer is indicative of a horizontal shear in the neutral wind, and is interpreted as being located at a boundary between wind systems.

The sporadic-*E* layers often contained pronounced small-scale structure, especially at times when partially transparent echoes were observed by the ionosonde. It was shown, based on several observations of wave-like structure, that internal gravity waves can be responsible for significant perturbations in the altitude and density of a sporadic-*E* layer. A sporadic-*E* layer at an altitude near a critical level of a gravity wave may be acted upon by highly enhanced vertical and horizontal shears in the neutral wind, creating small regions of high electron density. Irregular structure is also found to be generated by fluid instabilities in regions of large wind shears.

Small regions of enhanced electron density may also be an effect of the

irregular nature of the source of metallic ions. It was shown that under specific conditions the ions in a meteor trail will be converged by a shear in the neutral wind into a relatively small irregularity at the center of a sporadic-*E* layer.

In the observations of sporadic-*E* layers presented here, the small-scale horizontal structure has been emphasized. It is concluded that these small-scale irregularities are consistent with wind-shear theory when the combined effects of gravity waves, tides, and the irregular deposition of metallic ions are considered.

6. SUMMARY AND CONCLUSIONS

6.1 *Summary*

The objective of this study is to determine the source of the partially transparent echo from sporadic-*E* layers. The investigation is mainly concerned with two sporadic-*E* models that have been proposed to account for these reflections. In one model, the reflections are from the large electron-density gradients at the upper and lower boundaries of sporadic-*E* layers. The other holds that the radiation is reflected by small regions of enhanced ionization imbedded within the sporadic-*E* layer.

The basic theory of the formation of sporadic-*E* layers by wind shears is developed. Large wind shears are nearly always present in the region of the atmosphere where sporadic-*E* layers are observed, while, as the name suggests, the occurrence of sporadic-*E* layers is erratic. The role of metallic ions in sporadic-*E* formation is discussed and a model developed of the diurnal behavior of the metallic ions and atoms. It is found that a significant amount of metallic ionization is introduced into the ionosphere directly as a result of ablation from a meteoroid entering the atmosphere.

The importance of reflections of radio waves from electron-density gradients associated with sporadic-*E* layers is discussed in Chapter 3. A full-wave analysis is developed whereby reflection coefficients of sporadic-*E* electron-density profiles measured by rocket-borne probes is calculated. It is found that the frequency range of partial transparency is small both for layers causing partially transparent echoes on ionograms and those where no partially transparent echo is detected. It is thus concluded that large ranges of partial transparency in the echoes cannot be caused by electron-density gradients associated with the sporadic-*E* layer.

The small-scale horizontal structure of sporadic-*E* layers was investigated by a series of observations at the Arecibo Observatory in Puerto Rico. The observations were made during January, 1974, and July, 1975. Two basic experiments were used, one using phase-coded pulses to record electron-density profiles with a range resolution of 600 m, the other using multiple pulses to measure ion drift velocities. Highlights of each observation are summarized in Chapter 4. It is evident that sporadic-*E* layers contain small-scale irregularities of sufficient intensity to account for the partially transparent echoes observed by the ionosonde. Periods of intense irregularities and observations of partially transparent echoes are found to be well correlated.

Many interesting features observed in the incoherent-scatter data are discussed in Chapter 5. The observed structure of the sporadic-*E* layers is first considered with respect to motions of the neutral atmosphere. Various configurations consistent with wind-shear theory are discussed. Features indicating the presence of boundaries in wind systems similar to tropospheric fronts are also discussed, as well as the observation of the growth of a Kelvin-Helmholtz instability and its subsequent destruction by turbulence.

The irregular deposition of metallic ions by individual meteors is also considered as a source of irregularities. It is found that under specific conditions, ionization in a meteor trail will be converged by actions of a neutral wind shear into a small irregularity at the level where a sporadic-*E* layer will form.

The main conclusion of Chapter 5 is that sporadic-*E* layers are significantly influenced by strong Fourier components in the gravity-wave

waves are concluded to be the main source of the atmospheric motions affecting the small-scale structure of sporadic-E layers.

- (v) Intense localized irregularities indicate the proximity of critical levels in the internal-gravity-wave spectrum. Large horizontal-velocity gradients that occur near critical levels are suggested as the mechanism by which such irregularities are formed.

6.3 *Suggestions for Future Work*

Observations of neutral winds should be compared with ion drift velocities determined by the incoherent-scatter radar. This would provide a better check on the predictions of wind-shear theory than was possible in the analysis of Chapter 5. The two measurements might be made simultaneously using, for example, vapor trails from rockets launched from a site near the Arecibo Observatory.

Electron-density measurements are also needed that coincide with ion-drift-velocity measurements. In the multiple-pulse experiment described in Chapter 4, electron-density measurements were made only between ion-drift-velocity measurements, or during about 5 min of each 25 min period. Pulse-compression techniques can be developed to measure autocorrelation functions to give ion drift velocities with the height resolution necessary for studies of sporadic-E layers. An experiment could then be conducted in which scattered-power profiles would be recorded with good time resolution at the same time that autocorrelation functions are integrated to give the statistical accuracy required for the measurement of ion drift velocities.

Further research is needed in determining source functions and concentrations of metallic atoms and ions. The number of metallic particles being

spectrum. Wave-like structure is evident in many of the observations. It is shown that the most intense irregularities observed in this study can be produced by gravity-wave modes nearing critical levels as they encounter the sporadic-*E* ionization. Strong horizontal shears may be present at altitudes near a critical level which would converge the ionization of a sporadic-*E* layer into the observed irregularities.

6.2 Conclusions

The following are the main conclusions arrived at through this study:

- (i) Gradient reflections are not important in ionosonde observations of sporadic-*E*.
- (ii) Small-scale horizontal structure exists in midlatitude sporadic-*E* layers. The magnitude of the irregularities in electron density is strongly correlated with the observation of transparent echoes from the sporadic-*E* layer. Small regions of enhanced electron density provide an explanation for the occasions when $f^oE_s \gg f^xE_s$.
- (iii) The features of sporadic-*E* layers observed by incoherent-scatter radar are found to be consistent with layers composed of metallic ions being acted on by the motions of the neutral atmosphere as described by wind-shear theory. The dominant neutral motions are gravity waves and tidal modes.
- (iv) The irregular structure observed in midlatitude sporadic-*E* layers is mainly determined by the motions of the neutral atmosphere. This is especially evident in the case of nighttime sporadic-*E* layers where features in the structure at small electron densities can be observed. Internal gravity

deposited in the ionosphere and the fraction of these particles that are deposited directly as metallic ions needs to be determined. This should be done for both daytime and nighttime conditions.

More incoherent-scatter observations of sporadic-*E* layers are needed. The data presented in Chapter 4 represents a very limited sample. The sporadic-*E* layer in each observation was found to have features different from those in other layers observed, suggesting that there may be other effects that have not yet been detected.

The small-scale structure of sporadic-*E* layers should be considered in theoretical studies of atmospheric fluid instabilities and critical levels. In particular, the development of a non-linear theory which addresses itself to the observed irregularities is needed. The detailed information on the distribution of the electron density that is possible using pulse-compression techniques should be exploited in the study of non-linear processes associated with wind shears, as well as the onset of turbulence.

APPENDIX I

The Effect of the Polarization Electric Field on
the Formation of Sporadic-E Layers

When ionization is moved by the action of the neutral wind, the different charges and collision frequencies of electrons and ions cause them to move in different directions. Unless the plasma is infinite and uniform, this gives rise to a polarization electric field opposing their separation. Explicit expressions for the polarization electric field are developed here, following the work of *Whitehead* [1961]. These expressions are applied to a model of a region of large wind shears to obtain an estimate of the magnitude of the polarization field. It will be shown that the field is small at midlatitudes and can be neglected. However, at the magnetic equator, the polarization electric field becomes large and prevents the formation of layers by vertical shears in the horizontal wind.

The effect of the polarization electric field on the motion of the ionization can be found by solving equation (2.17) for both electrons and ions. Assuming no interaction between electrons and ions, with \vec{v}_i and \vec{v}_e as solutions of equation (2.17), the current resulting from their differing motions could be written as

$$\vec{j} = n e (\vec{v}_i - \vec{v}_e) \quad (\text{I.1})$$

where n is the electron density.

It is assumed that in a sporadic-E layer, any horizontal current caused by the relative motion of electrons and ions above the peak of the layer is complemented by another current in the opposite direction below the peak of the layer. Thus,

$$\int_{Es} j_x dz = e \int_{Es} n (v_{x_i} - v_{x_e}) dz = 0 \quad (\text{I.2})$$

$$\int_{Es} j_y dz = e \int_{Es} n(v_{y_i} - v_{y_e}) dz = 0 \quad (1.3)$$

where the integration is over the sporadic-E layer. It is also assumed that there are no vertical currents through the layer, so that

$$j_z = en(v_{z_i} - v_{z_e}) = 0 \quad (1.4)$$

In the following derivation, only the effects of horizontal winds and polarization electric fields, designated by \vec{E} , will be considered. The coordinate system will be oriented so the \vec{B} is in the y - z plane, and the x -axis is toward the east. Thus, equation (2.17) can be written

$$v_x = \frac{1}{(1+\rho^2)} \left[\rho^2 w_x + \rho \Gamma_z w_y + \rho \frac{E_x}{B_o} + \Gamma_z \frac{E_y}{B_o} \right] \quad (1.5)$$

$$v_y = \frac{1}{(1+\rho^2)} \left[-\rho \Gamma_z w_x + (\rho^2 + \Gamma_y^2) w_y - \Gamma_z \frac{E_x}{B_o} + \frac{(\rho^2 + \Gamma_y^2)}{\rho} \frac{E_y}{B_o} + \frac{\Gamma_y \Gamma_z}{\rho} \frac{E_z}{B_o} \right] \quad (1.6)$$

$$v_z = \frac{1}{(1+\rho^2)} \left[\rho \Gamma_y w_x + \Gamma_y \Gamma_z w_y + \Gamma_y \frac{E_x}{B_o} + \frac{\Gamma_y \Gamma_z}{\rho} \frac{E_y}{B_o} + \frac{(\rho^2 + \Gamma_z^2)}{\rho} \frac{E_z}{B_o} \right] \quad (1.7)$$

The corresponding components of the electric current are found by subtracting the electron velocities from the ion velocities. \vec{E} will be expressed in terms of its components parallel and perpendicular to the magnetic field, so that

$$E_y = \Gamma_y E_{||} + \Gamma_z E_{\perp} \quad (1.8)$$

$$E_z = \Gamma_z E_{||} - \Gamma_y E_{\perp} \quad (I.9)$$

where $E_{||}$ is the component parallel to \vec{B} , and E_{\perp} is the component in the y - z plane perpendicular to \vec{B} . Thus, by recalling that $\rho_i \gg \rho_e$, the difference between the drift velocities of the ions and electrons can be written as

$$v_{x_i} - v_{x_e} = \frac{\rho_i}{(1+\rho_i^2)} \left[\rho_i w_x + \Gamma_z w_y + \frac{E_x}{B_0} - \rho_i \frac{E_{\perp}}{B_0} \right] \quad (I.10)$$

$$v_{y_i} - v_{y_e} = \frac{\rho_i \Gamma_z}{(1+\rho_i^2)} \left[-w_x + \rho_i \Gamma_z w_y + \rho_i \frac{E_x}{B_0} + \frac{E_{\perp}}{B_0} \right] - \frac{\Gamma_y E_{||}}{\rho_e B_0} \quad (I.11)$$

$$v_{z_i} - v_{z_e} = \frac{\rho_i \Gamma_y}{(1+\rho_i^2)} \left[w_x - \rho_i \Gamma_z w_y - \rho_i \frac{E_x}{B_0} - \frac{E_{\perp}}{B_0} \right] - \frac{\Gamma_z E_{||}}{\rho_e B_0} \quad (I.12)$$

The condition that $j_z = 0$ requires that $v_{z_i} - v_{z_e} = 0$. Thus, $E_{||}$ can be eliminated between equation (I.11) and (I.12), giving

$$v_{y_i} - v_{y_e} = \frac{\rho_i}{(1+\rho_i^2)} \left[-\frac{1}{\Gamma_z} w_x + \rho_i w_y + \frac{\rho_i E_x}{\Gamma_z B_0} + \frac{1}{\Gamma_z} \frac{E_{\perp}}{B_0} \right] \quad (I.13)$$

Equations (I.10) and (I.13) are now substituted into equations (I.2) through (I.4), to give

$$\int_{Es} F \left(\Gamma_z w_y + \frac{E_x}{B_0} \right) dz = \int_{Es} G \left(w_x - \frac{E_{\perp}}{B_0} \right) dz \quad (I.14)$$

and

$$\int_{Es} F \left(\frac{w_x}{\Gamma_z} - \frac{E_{\perp}}{B_0 \Gamma_z} \right) dz = \int_{Es} G \left(w_y + \frac{E_x}{B_0 \Gamma_z} \right) dz \quad (I.15)$$

where

$$F = \frac{n \rho_i}{1 + \rho_i^2}$$

$$G = \frac{n \rho_i^2}{1 + \rho_i^2}$$

It can be assumed that E_x and E_{\perp} vary slowly with altitude and can be treated as constants. Equations (I.14) and (I.15) are then solved for E_x and E_{\perp} , giving

$$\frac{E_x}{B_0} = \frac{-1}{f^2 + g^2} \left[\Gamma_z (ff_y + gg_y) + (fg_x - gf_x) \right] \quad (I.16)$$

$$\frac{E_{\perp}}{B_0} = \frac{-1}{f^2 + g^2} \left[(ff_x + gg_x) - \Gamma_z (fg_y - gf_y) \right] \quad (I.17)$$

where

$$f = \int_{E_s} F dz$$

$$g = \int_{E_s} G dz$$

$$f_x = \int_{E_s} F w_x dz, \text{ etc.}$$

The vertical ion velocity can now be found by substituting equations (I.16) and (I.17) into equation (I.7). By setting equation (I.12) equal to zero, the parallel component of the polarization electric field is found to have a negligible effect on the vertical ion velocity. Thus,

$$v_z = \frac{\Gamma_y}{(1 + \rho_i^2)(f^2 + g^2)} \left\{ \left[\rho_i (w_x - \bar{w}_{x_F}) + \Gamma_z (w_y - \bar{w}_{y_F}) \right] f^2 + \left[\rho_i (w_z - \bar{w}_{x_G}) + \Gamma_z (w_y - \bar{w}_{y_G}) \right] g^2 + \left[(\bar{w}_{x_F} - \bar{w}_{x_G}) - \rho_i \Gamma_z (\bar{w}_{y_F} - \bar{w}_{y_G}) \right] fg \right\} \quad (I.18)$$

where

$$\bar{w}_{x_F} = \frac{f_x}{f}, \text{ etc.}$$

The field strength can be estimated for the conditions in the ionosphere. Suppose the ion density is constant above 80 km at a value of 10^5 cm^{-3} , and zero below 80 km. Also, let w_x be 100 m sec^{-1} between 110 and 120 km and zero elsewhere. w_y is set equal to zero everywhere. It can be assumed that ρ_i decreases exponentially with altitude, and has a value of 1 at 120 km. Thus,

$$\rho_i = \exp\left(\frac{z-120 \text{ km}}{H}\right) \quad (\text{I.19})$$

where H is the scale height of the neutral atmosphere, and is roughly equal to 10 km. By using these approximations, equations (I.16) and (I.17) give the following: $E_x \sim 10^{-4} \text{ V m}^{-1}$ and $E_{\perp} \sim 10^{-3} \text{ V m}^{-1}$. Equation (I.12) then gives $E_{||} \sim 10^{-5} \text{ V m}^{-1}$. In midlatitudes, therefore, the polarization electric field strength, and its effect on ion velocities, is negligibly small.

At the magnetic equator $\Gamma_z = 0$. The step in the above derivation which gives equation (I.13) involves a division by Γ_z , and cannot be used. Setting Γ_z equal to zero gives

$$v_{x_i} - v_{x_e} = \frac{\rho_i}{(1+\rho_i^2)} \left(\rho_i w_x + \frac{E_x}{B_0} - \rho_i \frac{E_{\perp}}{B_0} \right) \quad (\text{I.20})$$

$$v_{y_i} - v_{y_e} = \frac{-\Gamma_y}{\rho_e} \frac{E_{||}}{B_0} \quad (\text{I.21})$$

$$v_{z_i} - v_{z_e} = \frac{\rho_i \Gamma_y}{(1+\rho_i^2)} \left(w_x - \rho_i \frac{E_x}{B_0} - \frac{E_{\perp}}{B_0} \right) \quad (\text{I.22})$$

Setting $v_{z_i} - v_{z_e} = 0$,

$$\frac{E_{\perp}}{B_0} = w_x - \rho_i \frac{E_x}{B_0} \quad (\text{I.23})$$

so that

$$v_{x_i} - v_{x_e} = \rho_i \frac{E_x}{B_0} \quad (I.24)$$

Now, by applying the conditions in equations (I.2) through (I.4), that the integral of the currents be zero, it is seen that

$$\frac{E_x}{B_0} \int_{Es} n \rho_i = 0 \quad (I.25)$$

$$\frac{-\Gamma_y E_{||}}{\rho_e} \int_{Es} \frac{n}{\rho_e} = 0 \quad (I.26)$$

Since n and ρ_i are positive and finite, these equations can only be satisfied if E_x and $E_{||}$ are zero. Thus, from equation (I.23),

$$\frac{E_{||}}{B_0} = w_x \quad (I.27)$$

And, substituting into equation (I.7) the vertical ion velocity at the magnetic equator is

$$v_z(\Gamma_z = 0) = 0. \quad (I.28)$$

Thus, the vertical motion of ionization, and therefore the formation of sporadic- E layers by vertical shears in the horizontal wind, is prevented at the magnetic equator by the polarization electric field.

APPENDIX II.

APPROXIMATE DERIVATIONS OF REFLECTION COEFFICIENTS

II.1 *Approximation of a Layer by Multiple Thin Films*

A first approximation of the reflection coefficient is found by describing the reflecting medium by a series of vertically-thin layers of differing electron density. Within each layer the electron density, and therefore the refractive index, is assumed to be everywhere constant. A derivation of the reflection coefficient of multiple dielectric films can be found in many optics texts [ie. *Stone*, 1963].

Considering a boundary between two layers, Stokes theorem insures that the tangential E and H fields be continuous. Denoting the amplitudes of the incident, reflected, and transmitted fields by the subscripts i , r , and t respectively, this can be written

$$E_i + E_r = E_t \quad (II.1)$$

$$H_i + H_r = H_t \quad (II.2)$$

Or, expressing the spatial dependence explicitly,

$$H_i e^{ikn_1 z} + H_r e^{ikn_1 z} = H_t e^{-ikn_2 z} \quad (II.3)$$

Where n_1 and n_2 are the refractive indices of the two layers. From Maxwell's equations, it is seen that for the transverse components

$$H \propto \frac{dE}{dz} \quad (II.4)$$

Thus

$$n_1(E_i - E_r) = n_2 E_t \quad (II.5)$$

Equations (II.1) and (II.5) can be combined to give the Fresnel formulas for the reflection (R) and transmission (T) coefficients

$$R \equiv \frac{E_r}{E_i} = \frac{n_1 - n_2}{n_1 + n_2} \quad (\text{II.6})$$

$$T \equiv \frac{E_t}{E_i} = \frac{2n_1}{n_1 + n_2} \quad (\text{II.7})$$

If this layer is followed by another boundary and another layer with index of refraction n_3 , there are waves travelling in both directions on both sides of the initial boundary. Within the layer, the waves are denoted by E_+ and E_- . Thus equations (II.1) and (II.5) become

$$E_i + E_r = E_+ + E_- \quad (\text{II.8})$$

$$n_1(E_i - E_r) = n_2(E_+ - E_-) \quad (\text{II.9})$$

At the second boundary, the phase of the wave differs by kn_2d from the wave at the first boundary, where d is the width of the layer. Thus, the above equations are

$$E_+ e^{-ikn_2d} + E_- e^{ikn_2d} = E_t \quad (\text{II.10})$$

$$n_2(E_+ e^{-ikn_2d} - E_- e^{ikn_2d}) = n_3 E_t \quad (\text{II.11})$$

The fields between the boundaries can be eliminated and the result written in matrix form

$$\begin{bmatrix} E_i + E_r \\ n_1(E_i - E_r) \end{bmatrix} = \tilde{A} \begin{bmatrix} E_t \\ n_3 E_t \end{bmatrix} \quad (\text{II.12})$$

where

$$\tilde{A} = \begin{bmatrix} \cos(kn_2d) & \frac{i}{n_2} \sin(kn_2d) \\ in_2 \sin(kn_2d) & \cos(kn_2d) \end{bmatrix}$$

This process can be repeated for successive layers. If the index of refraction in the j^{th} layer is n_j , and in the region of the incident and

transmitted waves, n_i and n_t respectively, equation (II.12) can be generalized to give

$$\begin{bmatrix} E_i + E_r \\ n_i(E_i - E_r) \end{bmatrix} = A_1 A_2 \dots A_j \dots A_n \begin{bmatrix} E_t \\ n_t E_t \end{bmatrix} \quad (\text{II.13})$$

where

$$A_j = \begin{bmatrix} \cos(kn_j d) & \frac{i}{n_2} \sin(kn_j d) \\ in_2 \sin(kn_j d) & \cos(kn_j d) \end{bmatrix}$$

The product of the A 's can be written in the form of a two-by-two matrix

$$A_1 A_2 \dots A_n = \begin{bmatrix} a & b \\ c & d \end{bmatrix} \quad (\text{II.14})$$

from which reflection and transmission coefficients can be derived as

$$R = \frac{an_i + bn_i n_t - c - dn_t}{an_i + bn_i n_t + c + dn_t} \quad (\text{II.15})$$

$$T = \frac{2n_i}{an_i + bn_i n_t + c + dn_t} \quad (\text{II.16})$$

II.2 W.K.B. Solution

The wave equation for E_y can be written

$$\frac{d^2 E_y}{dz^2} + k^2 n^2 E_y = 0 \quad (\text{II.17})$$

In a varying medium, the refractive index is a function of z , making this a difficult equation to solve. The derivation of the W.K.B. solution is as follows [Budden, 1961]:

Let

$$\phi(z) = \pm i k n z \quad (\text{II.18})$$

so that

$$E_y = E_{y0} e^{i\phi(z)} \quad (\text{II.19})$$

This, substituted into the wave equation, (II.17), gives

$$\left[i \frac{d^2 \phi}{dz^2} - \left(\frac{d\phi}{dz} \right)^2 + k^2 n^2 \right] E_{y0} e^{i\phi} = 0 \quad (\text{II.20})$$

or

$$\left(\frac{d\phi}{dz} \right)^2 = k^2 n^2 + i \frac{d^2 \phi}{dz^2} \quad (\text{II.21})$$

It is assumed that $\frac{d^2 \phi}{dz^2}$ is small, and so, to a first approximation,

$$\frac{d\phi}{dz} \approx \pm k n \quad (\text{II.22})$$

This is differentiated to give

$$\frac{d^2 \phi}{dz^2} \approx \pm k \frac{dn}{dz} \quad (\text{II.23})$$

which is substituted back into (II.21) to give

$$\left[\frac{d\phi}{dz} \right]^2 \approx k^2 n^2 \pm i k \frac{dn}{dz} \quad (\text{II.24})$$

Then, by expanding the square root,

$$\frac{d\phi}{dz} \approx \pm k n \left(1 \pm \frac{i}{2 k n^2} \frac{dn}{dz} \right) \quad (\text{II.25})$$

The second sign in equation (II.25) is determined by the sign in equation (II.22). Therefore, if the two equations are consistent, both signs in equation (II.25) must be the same, or,

$$\frac{d\phi}{dz} \approx \pm k n + \frac{i}{2 n} \frac{dn}{dz} \quad (\text{II.26})$$

This may now be integrated to give

$$\phi = \pm k \int n dz + i \ln(n^{\frac{1}{2}}) \quad (\text{II.27})$$

so that

$$E_y = E_{y0} n^{-\frac{1}{2}} e^{\pm i k \int n dz} \quad (\text{II.28})$$

The reflection coefficient at a reflection point is given by the ratio of the downward travelling to the upward travelling wave.

$$|R| = \exp \left\{ -2k \int_0^{z_0} \chi dz \right\} \quad (\text{II.29})$$

where χ is the imaginary part of the refractive index and z_0 is the altitude where reflection occurs.

This approximation does not account for partial reflections from the ionized medium. If the frequency of the incident radiation is greater than the peak plasma frequency of the medium, the reflection coefficient derived by this method is zero.

An expression for the reflection coefficient where total reflection does not occur is suggested by *Yeh and Liu [1972]*. They solve the wave equation (11.17) for E_y using a Green's function to obtain

$$\begin{aligned} \frac{E_y(z)}{E_{y0}} &= \frac{1}{n(z)} \exp[-ik \int_0^z n(\tau) d\tau] \\ &+ \frac{1}{2n(z)} \exp[-ik \int_0^z n(\tau) d\tau] \left\{ \int_{-\infty}^z \frac{dn}{dz'} \exp[ik \int_0^{z'} n(\tau) d\tau] \frac{E_y(z')}{E_{y0}} dz' \right\} \\ &- \frac{1}{2n(z)} \exp[ik \int_0^z n(\tau) d\tau] \left\{ \int_z^{+\infty} \frac{dn}{dz'} \exp[-ik \int_0^{z'} n(\tau) d\tau] \frac{E_y(z')}{E_{y0}} dz' \right\} \end{aligned} \quad (\text{II.30})$$

where z' and τ are dummy height variables.

The first and second terms on the right-hand side describe upward-propagating waves, while the third term describes a downward-propagating

wave. As $z \rightarrow \infty$ the second term goes to zero and the upgoing and downgoing waves can be compared to give the reflection coefficient.

$$R = -\frac{1}{2} \int_{-\infty}^{\infty} \frac{dn}{dz} \exp[-ik \int_0^z n(\tau) d\tau] \frac{E_y(z)}{E_{y0}} dz \quad (\text{II.31})$$

Thus, by substituting the expression for E_y given by the W.K.B. method (II.28), an approximate expression for the reflection coefficient can be written in terms of known quantities.

$$R = -\frac{1}{2} \int_{-\infty}^{\infty} n^{-1/2} \frac{dn}{dz} \exp[-2ik \int_0^z n(\tau) d\tau] dz \quad (\text{II.32})$$

At $z = +\infty$, the third term on the right-hand side of equation (II.30) vanishes, leaving only upward propagating waves. This can be compared with the upgoing wave at $z = -\infty$ to give the transmission coefficient.

$$T = \frac{n(-\infty)}{n(+\infty)} \exp[-ik \int_{-\infty}^{\infty} n(\tau) d\tau] \times \left\{ 1 + \frac{1}{2} \int_{-\infty}^{\infty} n^{-1/2} \frac{dn}{dz} \exp[2ik \int_0^z n(\tau) d\tau] dz \right\} \quad (\text{II.33})$$

or

$$T = \frac{n(-\infty)}{n(+\infty)} \exp[-ik \int_{-\infty}^{\infty} n(\tau) d\tau] (1 - R) \quad (\text{II.34})$$

The expression for E_y , equation (II.28), can be substituted into the wave equation (II.17), giving

$$\left[\frac{3}{4} \left(\frac{1}{n} \frac{dn}{dz} \right)^2 - k^2 n^2 - \frac{1}{2} \frac{1}{n} \frac{d^2 n}{dz^2} \right] E_y + k^2 n^2 E_y = 0 \quad (\text{II.35})$$

This provides a condition for the region in which the W.K.B. approximation is valid. That is,

$$\left| \frac{3}{4} \left(\frac{1}{n} \frac{dn}{dz} \right)^2 - \frac{1}{2} \frac{1}{n} \frac{d^2 n}{dz^2} \right| \ll k^2 n^2$$

or

$$\frac{1}{k^2} \left| \frac{3}{4} \left(\frac{1}{n^2} \frac{dn}{dz} \right)^2 - \frac{1}{2} \frac{1}{n^3} \frac{d^2 n}{dz^2} \right| \ll 1 \quad (\text{II.36})$$

This condition is not violated in sporadic-E layers, except where the frequency of incident radiation approaches the reflection point in the medium. However, this fact makes it impossible to examine the reflection coefficient of sporadic-E layers by the W.K.B. method at frequencies near and below the peak plasma frequency of the layer.

II.3 Solution Using Hypergeometric Functions

This method assumes the ionization profile to be in the shape of a so-called Epstein profile [Budden, 1961]. For this case, exact algebraic expressions for the reflection and transmission coefficients can be derived [Brekhovskikh, 1960].

Consider the hypergeometric equation,

$$\frac{d^2 F}{d\xi^2} - \frac{(\alpha + \beta + 1)\xi - \gamma}{\xi(1 - \xi)} \frac{dF}{d\xi} - \frac{\alpha\beta}{\xi(1 - \xi)} F = 0 \quad (\text{II.37})$$

Now let

$$F = r(z) E_y \quad (\text{II.38})$$

$$\xi = \xi(z) \quad (\text{II.39})$$

where

$$r(z) = r_0 \xi^{-\gamma/2} (1 - \xi)^{\frac{1}{2}(\gamma - \alpha - \beta - 1)} \left(\frac{d\xi}{dz} \right)^{\frac{1}{2}} \quad (\text{II.40})$$

and $\xi(z)$ is an arbitrary function. Then equation (II.37) becomes

$$\frac{d^2 E_y}{dz^2} + g(z) E_y = 0 \quad (\text{II.41})$$

where

$$g(z) = \frac{1}{2} \frac{d^2}{dz^2} \left(\ln \frac{d\xi}{dz} \right) - \frac{1}{4} \left[\frac{d}{dz} \left(\ln \frac{d\xi}{dz} \right) \right]^2$$

$$- \left(\frac{d}{dz} \ln \xi \right)^2 \left[K_1 + K_2 \frac{\xi}{1-\xi} + K_3 \frac{\xi}{(1-\xi)^2} \right]$$
(II.42)

and

$$K_1 = \frac{1}{4} \gamma(\gamma-2)$$

$$K_2 = \frac{1}{4} [1 - (\alpha-\beta)^2 + \gamma(\gamma-2)]$$

$$K_3 = \frac{1}{4} [(\alpha+\beta-\gamma)^2 - 1]$$
(II.43)

For equations (II.41) to describe electromagnetic waves in the ionosphere, it is necessary that

$$g(z) = k^2 n^2$$
(II.44)

This is accomplished by letting

$$\xi(z) = -e^{mz}$$
(II.45)

Then,

$$g(z) = -\frac{m^2}{4} - m^2 \left[K_1 - K_2 \frac{e^{mz}}{(1+e^{mz})} - K_3 \frac{e^{mz}}{(1+e^{mz})^2} \right]$$
(II.46)

Now let m , M , and N be defined such that K_1 , K_2 , and K_3 can be expressed as

$$\begin{aligned} K_1 &= -\frac{k^2}{m^2} - \frac{1}{4} \\ K_2 &= -\frac{k^2}{m^2} N \\ K_3 &= -\frac{4k^2}{m^2} M \end{aligned} \quad (\text{II.47})$$

With this substitution, (II.44) and (II.46) can be combined to give

$$n^2 = 1 - N \frac{e^{mz}}{(1+e^{mz})} - 4M \frac{e^{mz}}{(1+e^{mz})^2} \quad (\text{II.48})$$

By setting either M or N equal to zero, equation (II.48) is the equation for either a symmetrical layer or a transition region between different refractive indices. This is illustrated in Figure 3.4.

The system of equations (II.43) can be solved for α , β , and γ giving

$$\begin{aligned} \gamma &= 1 \pm (1+4K_1)^{\frac{1}{2}} \\ \alpha-\beta &= \pm [-4K_2 + 1 + \gamma(\gamma-2)]^{\frac{1}{2}} \\ \alpha+\beta &= \pm (4K_3+1)^{\frac{1}{2}} + \gamma \end{aligned} \quad (\text{II.49})$$

To make the following derivation physically meaningful, the positive sign in the above equations will be retained. Thus,

$$\begin{aligned} \alpha &= \frac{1}{2} \{ 1 + (1+4K_1)^{\frac{1}{2}} + (1+4K_3)^{\frac{1}{2}} + [1+4(K_1-K_2)]^{\frac{1}{2}} \} \\ \beta &= \frac{1}{2} \{ 1 + (1+4K_1)^{\frac{1}{2}} + (1+4K_3)^{\frac{1}{2}} - [1+4(K_1-K_2)]^{\frac{1}{2}} \} \\ \gamma &= 1 + (1+4K_1)^{\frac{1}{2}} \end{aligned} \quad (\text{II.50})$$

This can be simplified by defining a relative thickness of the layer,

$$S = 2 \frac{k}{m} \quad (\text{II.51})$$

and substituting into equation (II.47):

$$\begin{aligned} (1+4K_1)^{\frac{1}{2}} &= iS \\ [1 + 4(K_1 - K_2)]^{\frac{1}{2}} &= iS(1-N)^{\frac{1}{2}} \\ (1+4K_3)^{\frac{1}{2}} &= (1-4S^2M)^{\frac{1}{2}} \end{aligned} \quad (\text{II.52})$$

Therefore

$$\begin{aligned} \alpha &= \frac{1}{2} \{ 1 + (1-4S^2M)^{\frac{1}{2}} + i \frac{S}{2} [1 + (1-N)^{\frac{1}{2}}] \} \\ \beta &= \frac{1}{2} \{ 1 + (1-4S^2M)^{\frac{1}{2}} + i \frac{S}{2} [1 - (1-N)^{\frac{1}{2}}] \} \\ \gamma &= 1 + iS \end{aligned} \quad (\text{II.53})$$

To solve for the reflected and transmitted wave fields, it is now necessary to find solutions to equation (II.41). This solution can be written in the form of a hypergeometric series,

$$\begin{aligned} F(\alpha, \beta, \gamma, \xi) &= 1 + \frac{\alpha\beta}{\gamma} \xi + \frac{\alpha(\alpha+1)\beta(\beta+1)}{2!\gamma(\gamma+1)} \xi^2 \\ &+ \frac{\alpha(\alpha+1)(\alpha+2)\beta(\beta+1)(\beta+2)}{3!\gamma(\gamma+1)(\gamma+2)} \xi^3 + \dots \end{aligned} \quad (\text{II.54})$$

It will be recalled that for the case in question, $\xi = -e^{mz}$. The hypergeometric equation (II.37) has poles at the points $\xi = 0, 1, \infty$. Solutions are sought where $z = \infty$ (or $\xi = -\infty$) and $z = -\infty$ (or $\xi = 0$). Near each pole there are two independent convergent hypergeometric series which are analytic functions. In the regions near each of these points,

Brekhovskikh [1960] gives the two convergent series as the following:

For $\xi \sim 0$

$$F_1 = F(\alpha, \beta, \gamma, \xi) \quad (\text{II.55})$$

$$F_2 = \xi^{1-\gamma} F(\alpha-\gamma+1, \beta-\gamma+1, 2-\gamma, \xi) \quad (\text{II.56})$$

For $\xi \sim 1$

$$F_3 = F(\alpha, \beta, \alpha+\beta-\gamma+1, 1-\xi) \quad (\text{II.57})$$

$$F_4 = (1-\xi)^{\gamma-\alpha-\beta} F(\gamma-\alpha, \gamma-\beta, \gamma-\alpha+\beta+1, 1-\xi) \quad (\text{II.58})$$

For $\xi \sim \pm \infty$

$$F_5 = \xi^{-\beta} F(\alpha, \alpha-\gamma+1, \alpha-\beta+1, \xi^{-1}) \quad (\text{II.59})$$

$$F_6 = \xi^{-\beta} F(\beta, \beta-\gamma+1, \beta-\alpha+1, \xi^{-1}) \quad (\text{II.60})$$

The solution in the region of $\xi = -\infty$ can be expressed in terms of F_1 and F_2 by the method of analytic continuation. This is done by solving the Barnes' contour integral for hypergeometric functions in the two regions [Whittaker and Watson, 1952],

$$I = \frac{1}{2\pi i} \int_{-\infty i}^{\infty i} \frac{\Gamma(a+s) \Gamma(b+s) \Gamma(-s)}{\Gamma(c+s)} (-\zeta)^s ds \quad (\text{II.61})$$

By Cauchy's Theorem, equation (II.57) can be expressed as a contour integral with the solution

$$I = 2\pi i \sum (\text{residues within the contour}). \quad (\text{II.62})$$

The poles in the gamma function occur where the argument of the function is equal to zero or a negative integer. The residue at a pole of the gamma function is

$$\text{residue } (\Gamma(-n)) = \frac{(-1)^n}{n!} \quad n = 0, 1, \dots \quad (\text{II.63})$$

The contour in (II.57) is closed about the right half of the complex plane

if $|\zeta| < 1$ and about the left half plane if $|\zeta| > 1$. Taking first the case of $|\zeta| < 1$,

$$I_1 = \lim_{N \rightarrow \infty} \sum_{n=0}^N \frac{\Gamma(a+n)\Gamma(b+n)}{\Gamma(c+n)} \frac{(-1)^n}{n!} (-\zeta)^n \quad (\text{II.64})$$

or

$$I_1 = \sum_{n=0}^{\infty} \frac{\Gamma(a+n)\Gamma(b+n)}{n! \Gamma(c+n)} \zeta^n \quad (\text{II.65})$$

This is proportional to the hypergeometric series,

$$I_1 = \frac{\Gamma(a)\Gamma(b)}{\Gamma(c)} F(a, b, c, \zeta) \quad (\text{II.66})$$

Now, the contour is closed about the left half plane ($|\zeta| > 1$). This includes poles in $\Gamma(a+s)$ and $\Gamma(b+s)$ at $s = -a-n$ and $s = -b-n$ respectively.

The solution is

$$I_2 = \lim_{N \rightarrow \infty} \left[\sum_{n=0}^N \frac{(-1)^n \Gamma(b-a-n)\Gamma(a+n)}{n! \Gamma(c-a-n)} (-\zeta)^{-a-n} \right. \\ \left. + \sum_{n=0}^N \frac{(-1)^n \Gamma(a-b-n)\Gamma(b+n)}{n! \Gamma(c-b-n)} (-\zeta)^{-b-n} \right] \quad (\text{II.67})$$

This can be rewritten in the form of (II.59) using the relation

$$\Gamma(s) \Gamma(1-s) = \frac{\pi}{\sin \pi s} \quad (\text{II.68})$$

Thus,

$$I_2 = \sum_{n=0}^{\infty} \frac{(-1)^n \Gamma(a+n)\Gamma(1-c+a+n)}{n! \Gamma(1-b+a+n)} \frac{\sin[\pi(c-a-n)]}{\sin[\pi(b-a-n)]} (-\zeta)^{-a-n} \\ + \sum_{n=0}^{\infty} \frac{(-1)^n \Gamma(b+n)\Gamma(1-c+b+n)}{n! \Gamma(1-a+b+n)} \frac{\sin[\pi(c-b-n)]}{\sin[\pi(a-b-n)]} (-\zeta)^{-b-n} \quad (\text{II.69})$$

or, by again using equation (II.68),

$$I_2 = \frac{\Gamma(a)\Gamma(b-a)}{\Gamma(a-b)} (-\zeta)^{-a} F(a, 1-c+a, 1-b+a, \zeta^{-1}) \\ + \frac{\Gamma(b)\Gamma(a-b)}{\Gamma(c-b)} (-\zeta)^{-b} F(b, 1-c+b, 1-a+b, \zeta^{-1}) \quad (\text{II.70})$$

The expressions I_1 and I_2 can be expressed in the form developed earlier by making the following substitutions:

$$\begin{aligned} a &= \alpha \\ b &= \alpha - \gamma + 1 \\ c &= \alpha - \beta + 1 \\ \zeta &= \xi^{-1} \end{aligned} \quad (\text{II.71})$$

so that, recalling equations (II.55), (II.56), and (II.59), setting I_1 equal to I_2 gives

$$F_5 = (-1)^{-\alpha} \frac{\Gamma(\alpha-\beta+1)\Gamma(1-\gamma)}{\Gamma(\alpha-\gamma+1)\Gamma(1-\beta)} F_1 + (-1)^{\gamma-1-\alpha} \frac{\Gamma(\alpha-\beta+1)\Gamma(\gamma-1)}{\Gamma(\alpha)\Gamma(\gamma-\beta)} F_2 \quad (\text{II.72})$$

The function F is related to the electric field through (II.38).

Making use of the fact that $\frac{d\xi}{dz} = m\xi$,

$$E_y = \frac{F}{r(z)} = r_0^{-1} m^{-\frac{1}{2}} \xi^{\frac{1}{2}(\gamma-1)} (1-\xi)^{\frac{1}{2}(1+\alpha+\beta-\gamma)} F \quad (\text{II.73})$$

When $\xi \rightarrow \infty$ (or $z \rightarrow \infty$), the first term of F_5 is dominant, so that, by recalling equation (II.45),

$$\lim_{z \rightarrow \infty} E_y = r_0^{-1} m^{-\frac{1}{2}} (-1)^{\frac{1}{2}(\gamma-1)-\alpha} \exp[-m(\alpha-\beta)z] \quad (\text{II.74})$$

When $\xi \rightarrow 0^+$ (or $z \rightarrow -\infty$), the right side of equation (II.72) is used.

Again, only the first term in each series remains.

$$\begin{aligned} \lim_{z \rightarrow -\infty} E_y &= r_0^{-1} m^{-\frac{1}{2}} (-1)^{\frac{1}{2}(\gamma-1)-\alpha} \\ &\times \left[\frac{\Gamma(\alpha-\beta+1)\Gamma(1-\gamma)}{\Gamma(\alpha-\gamma+1)\Gamma(1-\beta)} e^{\frac{1}{2}m(\gamma-1)z} + \frac{\Gamma(\alpha-\beta+1)\Gamma(\gamma-1)}{\Gamma(\alpha)\Gamma(\gamma-\beta)} e^{-\frac{1}{2}m(\gamma-1)z} \right] \end{aligned} \quad (\text{II.75})$$

If, as required by (II.53), the expressions $(\alpha-\beta)$ and $(\gamma-1)$ are chosen to be purely imaginary and positive, equation (II.74) becomes an expression for a plane wave at $z = \infty$ travelling in the $+z$ direction. Equation (II.75) can be interpreted as two plane waves at $z = -\infty$, one travelling in the $+z$ direction and the other in the $-z$ direction. Thus, (II.75) can be considered to be the incident and reflected waves below the ionized region; and (II.74), the transmitted wave above the region. The reflection and transmission coefficients are given by ratios of these waves,

$$R = \frac{\Gamma(\alpha-\beta+1)\Gamma(1-\gamma)}{\Gamma(\alpha-\gamma+1)\Gamma(1-\beta)} \cdot \frac{\Gamma(\alpha)\Gamma(\gamma-\beta)}{\Gamma(\alpha-\beta+1)\Gamma(\gamma-1)}$$

$$= \frac{\Gamma(1-\gamma)}{\Gamma(\alpha-\gamma+1)} \frac{\Gamma(\alpha)\Gamma(\gamma-\beta)}{\Gamma(1-\beta)\Gamma(\gamma-1)} \quad (\text{II.76})$$

$$T = \frac{\Gamma(\alpha)}{\Gamma(\alpha-\beta+1)} \frac{\Gamma(\gamma-\beta)}{\Gamma(\gamma-1)} \quad (\text{II.77})$$

By substituting the appropriate values of α , β , and γ into (II.77), the reflection coefficient for a transition or a symmetrical layer are found.

For a transition layer, $M = 0$, $N \neq 0$, and

$$\alpha = 1 + \frac{iS}{2} [1 + (1-N)^{\frac{1}{2}}]$$

$$\beta = 1 + \frac{iS}{2} [1 - (1-N)^{\frac{1}{2}}] \quad (\text{II.78})$$

$$\gamma = 1 + iS$$

From which,

$$R = \frac{\Gamma(-iS)\Gamma\{1 + \frac{iS}{2}[1 + (1-N)^{\frac{1}{2}}]\} \Gamma\{\frac{iS}{2}[1 + (1-N)^{\frac{1}{2}}]\}}{\Gamma(iS)\Gamma\{1 - \frac{iS}{2}[1 - (1-N)^{\frac{1}{2}}]\} \Gamma\{-\frac{iS}{2}[1 - (1-N)^{\frac{1}{2}}]\}} \quad (\text{II.79})$$

Thus, from equation (II.68),

$$|R| = (RR^*)^{\frac{1}{2}} = \frac{\sinh \left\{ \frac{\pi S}{2} [1 - (1-N)^{\frac{1}{2}}] \right\}}{\sinh \left\{ \frac{\pi S}{2} [1 + (1-N)^{\frac{1}{2}}] \right\}} \quad (\text{II.80})$$

From (II.48) it is seen that the index of refraction a great distance above the transition, n_{∞} , is given by

$$n_{\infty} = (1-N)^{\frac{1}{2}} \quad (\text{II.81})$$

Whence,

$$|R| = \frac{\sinh \left[\frac{\pi k}{m} (1-n_{\infty}) \right]}{\sinh \left[\frac{\pi k}{m} (1+n_{\infty}) \right]} \quad (\text{II.82})$$

For a symmetrical layer, $M \neq 0$, $N = 0$, and

$$\begin{aligned} \alpha &= \frac{1}{2} + iS + (\frac{1}{4} - S^2 M)^{\frac{1}{2}} \\ \beta &= \frac{1}{2} + (\frac{1}{4} - S^2 M)^{\frac{1}{2}} \\ \gamma &= 1 + iS \end{aligned} \quad (\text{II.83})$$

and

$$R = \frac{\Gamma(-iS) \Gamma(\frac{1}{2} + d + iS) \Gamma(\frac{1}{2} - d + iS)}{\Gamma(iS) \Gamma(\frac{1}{2} + d) \Gamma(\frac{1}{2} - d)} \quad (\text{II.84})$$

where $d = (\frac{1}{4} - S^2 M)^{\frac{1}{2}}$.

If $4S^2 M < 1$, d is real, and

$$|R|^2 = \frac{\cos^2(\pi d)}{\cos^2(\pi d) \cosh^2(\pi S) + \sin^2(\pi d) \sinh^2(\pi S)} \quad (\text{II.85})$$

If $4S^2 M > 1$, d is imaginary, and

$$|R|^2 = \frac{\cosh^2(\pi d)}{\cos[\pi(d+S)] \cosh[\pi(d-S)]} \quad (\text{II.86})$$

REFERENCES

- Aiken, A. C. and R. A. Goldberg [1973], Metallic ions in the equatorial ionosphere, *J. Geophys. Res.* 78, 734-735.
- Allen, E. R. [1970], Chemical factors regulating free alkali metal atoms in the upper atmosphere, *J. Geophys. Res.* 75, 2947-2950.
- Anderson, J. G. and C. A. Barth [1971], Rocket investigation of the Mg I and Mg II dayglow, *J. Geophys. Res.* 76, 3723-3732.
- Antosiewicz, H. A. and W. Gautschi [1962], Numerical methods in ordinary differential equations, in *Survey of Numerical Analysis*, J. Todd (Ed.) McGraw-Hill, New York, 314-346.
- Armstrong, R. J. and T. Lue [1970], Some drift observations by radio reflections from Es, *J. Geophys. Res.* 75, 183-192.
- Atkinson, K. R. [1973], The gradient instability in Gaussian sporadic-E layers, *J. Atmos. Terr. Phys.* 35, 460-477.
- Axford, W. I. [1963], The formation and vertical movement of dense ionized layers in the ionosphere due to neutral wind shears, *J. Geophys. Res.* 68, 769-779.
- Axford, W. I. [1964], Comments on "Generalization and critique of the wind-shear theory of sporadic E" by David Layzer, *J. Geophys. Res.* 69, 5093-5097.
- Axford, W. I. and D. M. Cunnold [1966], The wind-shear theory of temperate zone sporadic E, *Radio Sci.* 1, 191-198.
- Baggaley, W. J. and C. H. Cumback [1974], Meteor train ion chemistry, *J. Atmos. Terr. Phys.* 36, 1759-1773.
- Balsley, B. B., A. Rey, and R. F. Woodman [1976], On the plasma instability mechanisms responsible for Esq, *J. Geophys. Res.* 81, 1391-1396.
- Bedinger, J. F., H. B. Kneflich, E. Manring and D. Layzer [1968], Upper-

- atmosphere winds and their interpretation - 1. Evidence for strong nonlinearity of the horizontal flow above 80 km, *Planet. Space Sci.* 16, 159-193.
- Behnke, R. A. and J. F. Vickrey [1975], Radar evidence for Fe^+ in a sporadic-E layer, *Radio Sci.* 10, 325-327.
- Bevington, P. R. [1969], *Data Reduction and Error Analysis for the Physical Sciences*, McGraw-Hill, New York, 210-213.
- Beynon, W. J. G. and J. C. Wright [1969], The analysis of ionospheric drift data in the closely spaced receiver method, *J. Atmos. Terr. Phys.* 31, 593-596.
- Booker, H. G. and W. E. Gordon [1950], A theory of radio scattering in the troposphere, *Proc. I.R.E.* 38, 401-412.
- Bowhill, S. A. [1966], A rocket experiment on the structure of sporadic E, *Radio Sci.* 1, 187-190.
- Bowles, K. L. [1958], Observation of vertical incidence scatter from the ionosphere at 41 Mc/sec, *Phys. Rev. Lett.* 1, 454-455.
- Bowles, K. L. [1964], Radio wave scattering in the ionosphere, *Advances in Electronics and Electron Physics* 17, L. Marton (Ed.), Academic Press, New York, 55-176.
- Bowles, K. L. and R. Cohen [1962], A study of radio wave scattering from sporadic E near the magnetic equator, *Ionospheric Sporadic E*, E. K. Smith and S. Matsushita (Eds.), MacMillan Co., New York, 51-77.
- Breit, G. and M. A. Tuve [1926], A test of the existence of the conducting layer, *Phys. Rev.* 28, 554-575.
- Brekhovskikh, L. M. [1960], *Waves in Layered Media*, Academic Press, New York.
- Brown, T. L. [1973], The chemistry of metallic elements in the ionosphere and mesosphere, *Chem. Rev.* 73, 645-667.

- Budden, K. G. [1961], *Radio Waves In The Ionosphere*, Cambridge University Press.
- Chapman, S. [1931], The absorption and dissociative or ionizing effect of monochromatic radiation in an atmosphere on a rotating earth, *Proc. Phys. Soc.* 43, 26-45.
- Chessell, C. I. [1971a], The numerical calculation of reflection and transmission coefficients for thin highly ionized layers including the effect of earth's magnetic field, *J. Atmos. Terr. Phys.* 33, 1515-1532.
- Chessell, C. I. [1971b], Results of numerical calculations of reflection and transmission coefficients for thin highly ionized layers and their application to sporadic-E reflections, *J. Atmos. Terr. Phys.* 33, 1803-1822.
- Chessell, C. I., J. A. Thomas and I. A. Bourne [1973], Experimental observations of the amplitudes of *Es* and *F*-region reflections and their comparison with the thin-layer model for *Es*, *J. Atmos. Terr. Phys.* 35, 545-561.
- Chimonas, G. [1971], Enhancement of sporadic *E* by horizontal transport within the layer, *J. Geophys. Res.* 76, 4578-4586.
- Chimonas, G. [1973], Wind component exchange and the rapid vertical movement of a sporadic *E* layer, *J. Geophys. Res.* 78, 5636-5639.
- Chimonas, G. and W. I. Axford [1968], Vertical movement of temperate-zone sporadic *E* layers, *J. Geophys. Res.* 73, 111-117.
- CIRA [1972], *COSPAR International Reference Atmosphere*, 450 pp., Akademie-Verlag, Berlin.
- Clemmow, P. C. and M. A. Johnson [1959], A contribution to the theory and the motion of weak irregularities in the ionosphere, *J. Atmos. Terr. Phys.* 16, 21-36.
- Corcos, G. M. and F. S. Sherman [1976], Vorticity concentration and the dynamics of unstable free shear layers, *J. Fluid Mech.* 73, 241-264.

- DeGregorio, J. F., J. W. Finney, K. Kildahl and E. K. Smith [1962], Recent sporadic-E experimental work in the United States, *Ionospheric Sporadic E*, E. K. Smith and S. Matsushita (Eds.), MacMillan Co., New York, 131-142.
- Donahue, T. M. and R. R. Meier [1967], Distribution of sodium in the daytime upper atmosphere as measured by a rocket experiment, *J. Geophys. Res.* 72, 2803-2829.
- Dungey, J. W. [1956], The influence of the geomagnetic field on turbulence in the ionosphere, *J. Atmos. Terr. Phys.* 8, 39-42.
- Dungey, J. W. [1959], Effect of a magnetic field on turbulence in an ionized gas, *J. Geophys. Res.* 64, 2188-2191.
- Evans, J. V. [1967], Midlatitude F-region densities and temperatures at sunspot minimum, *Planet. Space Sci.* 15, 1387-1405.
- Evans, J. V. [1969], Theory and practice of ionosphere study by Thomson scatter radar, *Proc. IEEE* 57, 496-530.
- Evans, J. V. [1975], High-power radar studies of the ionosphere, *Proc. IEEE* 63, 1636-1650.
- Evans, J. V. and M. Loewenthal [1964], Ionospheric backscatter observations, *Planet. Space Sci.* 12, 915-944.
- Farley, D. T. [1963a], A plasma instability resulting in field-aligned irregularities in the ionosphere, *J. Geophys. Res.* 68, 6083-6097.
- Farley, D. T. [1963b], Two-stream plasma instability as a source of irregularities in the ionosphere, *Phys. Rev. Lett.* 10, 279-282.
- Farley, D. T. [1969], Incoherent scatter correlation function measurements, *Radio Sci.* 4, 935-953.
- Ferguson, E. E. [1972], Atmospheric metal ion chemistry, *Radio Sci.* 7, 397-401.
- Fiocco, G. [1965], Optical radar results and ionospheric sporadic E, *J. Geophys. Res.* 70, 2213-2215.

- Francis, S. H. [1975], Global propagation of atmospheric gravity waves: A review, *J. Atmos. Terr. Phys.* 37, 1011-1054.
- Gadsden, M. [1968], Sodium in the upper atmosphere: meteoric origin, *J. Atmos. Terr. Phys.* 30, 151-161.
- Gadsden, M. [1970], Metallic atoms and ions in the upper atmosphere, *Ann. Geophys.* 26, 141-149.
- Gadsden, M. [1972], Dayglow of Mg I and Mg II, *J. Geophys. Res.* 77, 1330-1331.
- Gill, S. [1951], A process for the step-by-step integration of differential equations in an automatic digital computing machine, *Proc. Cambridge Philos. Soc.* 47, 96-108.
- Goldberg, R. A. [1975], Silicon ions below 100 km: A case for SiO_2^+ , *Radio Sci.* 10, 329-334.
- Goodwin, G. L. [1965], Some aspects of direct backscatter echoes from sporadic E, *J. Atmos. Terr. Phys.* 27, 777-793.
- Goodwin, G. L. and R. N. Summers [1970], Es-layer characteristics determined from spaced ionosondes, *Planet. Space Sci.* 18, 1417-1432.
- Goodwin, G. L. and J. A. Thomas [1963], Field-aligned irregularities in the Es region, *J. Atmos. Terr. Phys.* 25, 707-719.
- Gordon, W. E. [1958], Incoherent scattering of radio waves by free electrons with applications to space exploration by radar, *Prod. IRE* 46, 1824-1829.
- Gray, R. W. and D. T. Farley [1973], Theory of incoherent-scatter measurements using compressed pulses, *Radio Sci.* 8, 123-131.
- Hagfors, T. [1961], Density fluctuations in a plasma in a magnetic field with applications to the ionosphere, *J. Geophys. Res.* 66, 1699-1712.
- Harper, R. M., R. H. Wand and J. D. Whitehead [1975], Comparison of Arecibo E-region data and sporadic-E theory: A measurement of the diffusion

- coefficient, *Radio Sci.* 10, 357-361.
- Harper, R. M., R. H. Wand, C. J. Zamlutti and D. T. Farley [1976], E-region ion drifts and winds from incoherent scatter measurements at Arecibo, *J. Geophys. Res.* 81, 25-35.
- Hedberg, Å. [1975], Sporadic-E as a function of meteor rate, *Kleinheubacher Berichte* 18, 261-268.
- Hedberg, Å. [1976], Seasonal variations in the correlation of meteors and sporadic E, *J. Atmos. Terr. Phys.* 38, 785-788.
- Heisler, L. H. and J. D. Whitehead [1960], Longitude effect in temperate zone sporadic E and the earth's magnetic field, *Nature* 187, 676-677.
- Heisler, L. H. and J. D. Whitehead [1962], Rapid variations in the sporadic-E region, *J. Atmos. Terr. Phys.* 24, 753-764.
- Heisler, L. H. and J. D. Whitehead [1964], The correlation between the occurrence of sporadic-E and the horizontal component of the earth's magnetic field, *J. Atmos. Terr. Phys.* 26, 437-444.
- Hines, C. O. [1960], Internal atmospheric gravity waves at ionospheric heights, *Can. J. of Phys.* 38, 1441-1481. (Correction in *Can. J. of Phys.* 42, 1425-1427, 1964).
- Hines, C. O. [1963], The upper atmosphere in motion, *Quart J. Roy. Meteorol. Soc.* 89, 1-42.
- Hines, C. O. [1966], Diurnal tide in the upper atmosphere, *J. Geophys. Res.* 71, 1453-1459.
- Hines, C. O. [1968], Some consequences of gravity-wave critical layers in the upper atmosphere, *J. Atmos. Terr. Phys.* 30, 837-843.
- Hines, C. O. [1974], *The Upper Atmosphere in Motion*, Heffernan Press, Inc., Worcester, Mass.
- Hines, C. O. and C. A. Reddy [1967], On the propagation of atmospheric gravity

- waves through regions of wind shear, *J. Geophys. Res.* 72, 1015-1034.
- Hooke, W. H. [1969], E-region ionospheric irregularities produced by internal atmospheric gravity waves, *Planet. Space Sci.* 17, 749-765.
- Hooke, W. H. [1971], Quasi-stagnation levels in the ion motion induced by internal atmospheric gravity waves at ionospheric heights, *J. Geophys. Res.* 76, 248-250.
- Hunsucker, R. D. [1975], Chatanika radar investigation of high latitude E-region ionization structure and dynamics, *Radio Sci.* 10, 277-288.
- Ioannidis, G. and D. T. Farley [1972], Incoherent scatter observations at Arecibo using compressed pulses, *Radio Sci.* 7, 763-766.
- Istomin, V. G. [1963], Ions of extra-terrestrial origin in the earth's ionosphere, *Space Res.* 3, 209-220.
- Johannessen, A. and D. Krankowsky [1972], Positive-ion composition measurement in the upper mesosphere and lower thermosphere at a high latitude during summer, *J. Geophys. Res.* 77, 2888-2901.
- Kaiser, T. R., W. M. Pickering and C. D. Watkins [1969], Ambipolar diffusion and motion of ion clouds in the earth's magnetic field, *Planet. Space Sci.* 17, 519-552.
- Kato, S. [1963], Theory of movement of irregularities in the upper atmosphere, *Planet. Space Sci.* 11, 823-830.
- Kato, S. [1966], Theoretical basis of the formation of sporadic E due to wind motion in the ionosphere, *Radio Sci.* 1, 226-234.
- Kochanski, A. [1964], Atmospheric motions from sodium cloud drifts, *J. Geophys. Res.* 69, 3651-3662.
- Kotadia, K. M. and K. C. Jani [1967], Sporadic E ionization and anomalous increase in the rate of radar meteor counts during 1963, *J. Atmos. Terr. Phys.* 29, 221-223.

- LaLonde, L. M. [1966], Incoherent backscatter observations of sporadic E, *J. Geophys. Res.* 71, 5059-5065.
- Layzer, D. [1964a], Generalization and critique of the wind-shear theory of sporadic-E, *J. Geophys. Res.* 69, 1853-1860.
- Layzer, D. [1964b], Reply, *J. Geophys. Res.* 69, 5098-5104.
- Layzer, D. [1972], Theory of midlatitude sporadic E, *Radio Sci.* 7, 385-395.
- Lebedinets, V. N. [1973], Ablation in meteors, *Evolutionary and Physical Properties of Meteoroids*, C. L. Hemenway, P. M. Millman and A. F. Cook (Eds.), NASA Scientific and Technical Information Office, Washington, D. C., 259-269.
- Lebedinets, V. N. and V. B. Shushkova [1970], Meteor ionization in the E-layer, *Planet. Space Sci.* 18, 1659-1663.
- Leighton, H. I., A. H. Shapley and E. K. Smith [1962], The occurrence of sporadic-E during the IGY, *Ionospheric Sporadic E*, E. K. Smith and S. Matsushita (Eds.), MacMillan Co., New York, 166-177.
- Link, F. [1973], Cosmic dust in the upper atmosphere, *Space Res.* 13, 1135-1138.
- MacLeod, M. A. [1966], Sporadic E theory - I. Collision-geomagnetic equilibrium, *J. Atmos. Sci.* 23, 96-109.
- MacLeod, M. A., T. J. Keneshea and R. S. Narcisi [1975], Numerical modelling of a metallic ion sporadic-E layer, *Radio Sci.* 10, 371-388.
- Miller, K. L. and L. G. Smith [1975], Horizontal structure of midlatitude sporadic-E layers observed by incoherent scatter radar, *Radio Sci.* 10, 317-323.
- Mozer, F. S. [1972], Simultaneous electric-field measurements on nearby balloons, *J. Geophys. Res.* 77, 6129-6132.
- Narcisi, R. S. [1966], Ion composition measurements and related ionospheric processes in the D and lower E region, *Ann. Geophys.* 22, 224-234.

- Narcisi, R. S. [1968], Processes associated with metal-ion layers in the E-region of the ionosphere, *Space Res.* 8, 360-369.
- Narcisi, R. S. [1973], Mass spectrometer measurements in the ionosphere, *Physics and Chemistry of Upper Atmospheres*, B. M. McCormac (Ed.), D. Reidel Publ. Co., Dordrecht, Holland, 171-183.
- Narcisi, R. S. and A. D. Bailey [1965], Mass spectrometric measurements of positive ions at altitudes from 64 to 112 km, *J. Geophys. Res.* 70, 3687-3700.
- Patnaik, P. C., F. S. Sherman and G. M. Corcos [1976], A numerical simulation of Kelvin-Helmholtz waves of finite amplitude, *J. Fluid Mech.* 73, 215-240.
- Pitteway, M. L. V. [1965], The numerical calculation of wave-fields, reflexion coefficients and polarizations for long radio waves in the lower ionosphere - I., *Phil. Trans. A* 257, 219-241.
- Pitteway, M. L. V. and C. O. Hines [1965], The reflection and ducting of atmospheric acoustic-gravity waves, *Can. J. of Phys.* 43, 2222-2243.
- Poole, L. M. G. and T. F. Nicholson [1975], The effect of ionic processes on the characteristics of radio-echoes from meteor trains, *Planet. Space Sci.* 23, 1261-1277.
- Prakash, S., S. P. Gupta and B. H. Subbaraya [1971], Experimental evidence for cross-field instability in the equatorial ionosphere, *Space Res.* 11, 1139-1145.
- Ratcliffe, J. A. [1959], Ionizations and drifts in the ionosphere, *J. Geophys. Res.* 64, 2102-2111.
- Ratcliffe, J. A. [1972], *An Introduction to the Ionosphere and Magnetosphere*, Cambridge University Press, Cambridge.
- Rawer, K. [1939], Elektrische Wellen in einem geschichteten Medium, Zur Frage der partiellen Reflexion und zur Berechnung der scheinbaren

- Höhe von Ionosphärenschichten, *Ann. d. Physik* 35, 385-416.
- Rawer, K. [1962], Structure of Es at temperate latitudes, *Ionospheric Sporadic E*, E. K. Smith and S. Matsushita (Eds.), MacMillan Co., New York, 292-343.
- Reddy, C. A. [1968], Physical significance of the Es parameters fbEs, fEs and foEs - 2. Causes of partial reflections from Es, *J. Geophys. Res.* 73, 5627-5647.
- Reddy, C. A. and M. Mukunda Rao [1968], On the physical significance of the Es parameters fbEs, fEs and foEs, *J. Geophys. Res.* 73, 215-224.
- Reid, G. C. [1968], The formation of small-scale irregularities in the ionosphere, *J. Geophys. Res.* 73, 1627-1640.
- Rishbeth, H. and O. K. Garriott [1969], *Introduction to Ionospheric Physics*, Academic Press, New York.
- Rosenberg, N. W. [1968], Statistical analysis of ionospheric winds - II., *J. Atmos. Terr. Phys.* 30, 907-917.
- Rosenberg, N. W. and S. P. Zimmerman [1972], Ionospheric winds and viscous dissipation, *Radio Sci.* 7, 377-380.
- Rowe, J. F. Jr. [1974], Downward transport of nighttime Es-layers into the lower E-region at Arecibo, *J. Atmos. Terr. Phys.* 36, 225-234.
- Schutz, S., G. J. Adams and F. S. Mozer [1973], Probe electric field measurements near a midlatitude ionospheric barium release, *J. Geophys. Res.* 78, 6634-6642.
- Seddon, J. C. [1962], Sporadic-E as observed with rockets, *Ionospheric Sporadic-E*, E. K. Smith and S. Matsushita (Eds.), MacMillan Co., New York, 78-88.
- Sida, D. W. [1969], The production of ions and electrons by meteoric processes, *Mon. Not. Roy. Astron. Soc.* 143, 37-47.

- Smith, E. K. [1957], Worldwide occurrence of sporadic E, *N.B.S. Circ.* 582, U.S. Government Printing Office.
- Smith, E. K. [1968], Do intense blobs exist in temperate-latitude sporadic E, *Proc. Conf. Struct. Causes Sporadic E*, Vail, Colorado.
- Smith, L. G. [1966], Rocket observations of sporadic E and related features of the E region, *Radio Sci.* 1, 178-186.
- Smith, L. G. [1969], Langmuir probes in the ionosphere, *Small Rocket Instrumentation Techniques*, North-Holland Publ. Co., Amsterdam, 1-15.
- Smith, L. G. [1970], A sequence of rocket observations of nighttime sporadic-E, *J. Atmos. Terr. Phys.* 32, 1247-1257.
- Smith, L. G. and E. A. Mechtly [1972], Rocket observations of sporadic-E layers, *Radio Sci.* 7, 367-376.
- Stanton, R. G. [1961], *Numerical Methods for Science and Engineering*, Prentice-Hall, Inc., Englewood Cliffs, New Jersey, 151-154.
- Stone, J. M. [1963], *Radiation and Optics*, McGraw-Hill, New York, 388-417.
- Sugar, G. R. [1964], Radio propagation by reflection from meteor trails, *Proc. IEEE* 52, 116-136.
- Swider, W., Jr. [1969], Processes for meteoric elements in the E-region, *Planet. Space Sci.* 17, 1233-1246.
- Tao, K. and J. R. Wait [1962], Reflection mechanisms for sporadic E, *Ionospheric Sporadic E*, E. K. Smith and S. Matsushita (Eds.), Macmillan Co., New York, 13-27.
- Thomas, J. A. and E. K. Smith [1959], A survey of the present knowledge of sporadic-E ionization, *J. Atmos. Terr. Phys.* 13, 295-314.
- Trřsková, L. [1974], On the seasonal variation in the temperate Es occurrence, *J. Atmos. Terr. Phys.* 36, 861-869.
- Tsuda, T. and T. Sato [1968], Structure of plasma turbulence due to non-

- linear cross-field instability, *Phys. Fluids* 11, 676-678.
- Tsuda, T., T. Sato and K. Maeda [1966], Formation of sporadic *E* layers at temperate latitudes due to vertical gradients of charge density, *Radio Sci.* 1, 212-225.
- URSI [1972], *Handbook of Ionogram Interpretation and Reduction*, second edition, W. R. Piggot and K. Rawer (Eds.), U.S. Dept. of Commerce, N.O.A.A., Environmental Data Service, Asheville, North Carolina.
- Whitehead, J. D. [1961], The formation of the sporadic-*E* layer in the temperate zones, *J. Atmos. Terr. Phys.* 20, 49-58.
- Whitehead, J. D. [1964], Comments on "Generalization and critique of the wind-shear theory of sporadic *E*" by David Layzer, *J. Geophys. Res.* 69, 5091-5092.
- Whitehead, J. D. [1967], Instabilities in a gradient of ionization and sporadic-*E*, *J. Atmos. Terr. Phys.* 29, 1285-1297.
- Whitehead, J. D. [1968], Low frequency plasma instabilities in the ionosphere, *J. Atmos. Terr. Phys.* 30, 1563-1579.
- Whitehead, J. D. [1970a], Production and prediction of sporadic *E*, *Rev. Geophys. Space Phys.* 8, 65-144.
- Whitehead, J. D. [1970b], The gradient instability in bounded ionospheric layers, *J. Atmos. Terr. Phys.* 32, 1283-1304.
- Whitehead, J. D. [1971a], Ionization disturbances caused by gravity waves in the presence of an electrostatic field and background wind, *J. Geophys. Res.* 76, 238-241.
- Whitehead, J. D. [1971b], Difficulty associated with wind-shear theory of sporadic-*E*, *J. Geophys. Res.* 76, 3127-3135.
- Whitehead, J. D. [1972a], The structure of sporadic *E* from a radio experiment, *Radio Sci.* 7, 355-358.

- Whitehead, J. D. [1972b], Winds in E region, *Radio Sci.* 7, 403-404.
- Whittaker, E. T. and G. N. Watson [1952], *A Course of Modern Analysis*, University Press, Cambridge, 286-289.
- Whitten, R. C. and I. G. Poppoff [1971], *Fundamentals of Aeronomy*, John Wiley and Sons, Inc., New York.
- Woodman, R. F. [1970], Vertical drift velocities and east-west electric fields at the magnetic equator, *J. Geophys. Res.* 75, 6249-6259.
- Wright, J. W. [1967], Sporadic E as an indicator of wind structure in the lower ionosphere and the influx of meteors, *J. Geophys. Res.* 72, 4821-4829.
- Wright, J. W. [1968], The interpretation of ionospheric radio drift measurements - I. Some results of experimental comparisons with neutral wind profiles, *J. Atmos. Terr. Phys.* 30, 919-930.
- Wright, J. W. and L. S. Fedor [1969], The interpretation of ionospheric radio drift measurements - II. Kinesonde observations of microstructure and vertical motion in sporadic-E, *J. Atmos. Terr. Phys.* 31, 925-942.
- Wright, J. W. and L. S. Fedor [1970], Errata, *J. Atmos. Terr. Phys.* 32, 451-452.
- Yeh, K. C. and C. H. Liu [1972], *Theory of Ionospheric Waves*, Academic Press, New York, 270-276.
- Young, J. M., C. Y. Johnson and J. C. Holmes [1967], Positive ion composition of a temperate-latitude sporadic E layer as observed during a rocket flight, *J. Geophys. Res.* 72, 1473-1479.
- Zamlutti, C. J. and D. T. Farley [1975], Incoherent scatter multiple-pulse measurements at Arecibo, *Radio Sci.* 10, 573-580.
- Zbinden, P. A., M. A. Hidalgo, P. Eberhardt and J. Geiss [1975], Mass spectrometer measurements of the positive ion composition in the D- and E-regions of the ionosphere, *Planet. Space Sci.* 23, 1621-1642.